

Remote tree-ring proxies: methods, opportunities, and limitations for reconstructing South Pacific climate

Author:

Higgins, Philippa

Publication Date:

2022

DOI:

<https://doi.org/10.26190/unsworks/24634>

License:

<https://creativecommons.org/licenses/by/4.0/>

Link to license to see what you are allowed to do with this resource.

Downloaded from <http://hdl.handle.net/1959.4/100927> in <https://unsworks.unsw.edu.au> on 2024-05-02

Remote tree-ring proxies: methods, opportunities, and limitations for reconstructing South Pacific climate

Philippa Higgins

A thesis in fulfilment of the requirements for the degree of
Doctor of Philosophy



School of Civil and Environmental Engineering

Faculty of Engineering

August 2022

ORIGINALITY STATEMENT

☒ I hereby declare that this submission is my own work and to the best of my knowledge it contains no materials previously published or written by another person, or substantial proportions of material which have been accepted for the award of any other degree or diploma at UNSW or any other educational institution, except where due acknowledgement is made in the thesis. Any contribution made to the research by others, with whom I have worked at UNSW or elsewhere, is explicitly acknowledged in the thesis. I also declare that the intellectual content of this thesis is the product of my own work, except to the extent that assistance from others in the project's design and conception or in style, presentation and linguistic expression is acknowledged.

COPYRIGHT STATEMENT

☒ I hereby grant the University of New South Wales or its agents a non-exclusive licence to archive and to make available (including to members of the public) my thesis or dissertation in whole or part in the University libraries in all forms of media, now or here after known. I acknowledge that I retain all intellectual property rights which subsist in my thesis or dissertation, such as copyright and patent rights, subject to applicable law. I also retain the right to use all or part of my thesis or dissertation in future works (such as articles or books).

For any substantial portions of copyright material used in this thesis, written permission for use has been obtained, or the copyright material is removed from the final public version of the thesis.

AUTHENTICITY STATEMENT

☒ I certify that the Library deposit digital copy is a direct equivalent of the final officially approved version of my thesis.

INCLUSION OF PUBLICATIONS

☒ The candidate has declared that their thesis has publications - either published or submitted for publication - incorporated into it in lieu of a Chapter/s. Details of these publications are provided below..

Publication Details #1

Full Title:	One Thousand Three Hundred Years of Variability in the Position of the South Pacific Convergence Zone
Authors:	P. A. Higgins, J. G. Palmer, C. S. M. Turney, M. S. Andersen, and E. R. Cook
Journal or Book Name:	Geophysical Research Letters
Volume/Page Numbers:	47
Date Accepted/Published:	11/8/2020
Status:	published
The Candidate's Contribution to the Work:	Philippa Higgins conceptualised the study, designed the methods, undertook the analysis and prepared the manuscript under the supervision of all co-authors.
Location of the work in the thesis and/or how the work is incorporated in the thesis:	Chapter 2

Publication Details #2

Full Title:	Do Southern Hemisphere tree rings record past volcanic events? A case study from New Zealand
Authors:	Higgins, P. A., Palmer, J. G., Turney, C. S. M., Andersen, M. S., & Johnson, F.
Journal or Book Name:	Climate of the Past
Volume/Page Numbers:	18(5)
Date Accepted/Published:	24/5/2022
Status:	published
The Candidate's Contribution to the Work:	Philippa Higgins conceptualised the study, designed the methods, undertook the analysis and prepared the manuscript under the supervision of all co-authors.
Location of the work in the thesis and/or how the work is incorporated in the thesis:	Chapter 4

Publication Details #3

Full Title:	Unprecedented High Northern Australian Streamflow Linked to an Intensification of the Indo-Australian Monsoon
Authors:	Higgins, P. A., Palmer, J. G., Rao, M. P., Andersen, M. S., Turney, C. S. M., & Johnson, F.
Journal or Book Name:	Water Resources Research
Volume/Page Numbers:	58
Date Accepted/Published:	2/3/2022
Status:	published
The Candidate's Contribution to the Work:	Philippa Higgins conceptualised the study, designed the methods, undertook the analysis and prepared the manuscript under the supervision of all co-authors.
Location of the work in the thesis and/or how the work is incorporated in the thesis:	Chapter 5

Candidate's Declaration

I confirm that where I have used a publication in lieu of a chapter, the listed publication(s) above meet(s) the requirements to be included in the thesis. I also declare that I have complied with the Thesis Examination Procedure.

Abstract

Increasing population and resource demands, a changing hydroclimate, and increasing risks of extreme events means that sustainable water management is more important now than ever before. Water planners are increasingly recognising that short instrumental records are insufficient to understand fully natural trends and variability in climate. High resolution paleoclimate proxies, like tree rings, can provide long time series of observations prior to the instrumental period, to better understand instrumental and pre-instrumental variability, the occurrence, trends, and drivers of extreme events, and provide insights into possible future hydroclimatic scenarios. However, tree-ring proxies are not evenly distributed in the landscape, and the South Pacific has very few high-resolution paleoclimate proxies to develop detailed reconstructions of climate variability.

This thesis explores whether the relationships between tree-ring proxies in regions with strong teleconnections to the Pacific (i.e., ‘remote’ tree rings) can be exploited to reconstruct hydroclimatic indices across eastern Australia and the South Pacific Islands. Methods for hydroclimatic reconstruction are investigated, considering the unique challenges of the region: strong inter-annual and inter-decadal variability, very short data records, data gaps, and potential non-stationarities in climate teleconnections. Existing methods for tree-ring reconstructions have been successfully applied in the South Pacific (Chapter 2); however, overcoming the challenges posed by very short and non-continuous records required adaptations to existing methods (Chapter 3) and the development of new methods (Chapter 5). In the final two chapters, the thesis focuses on how catchment-scale tree-ring reconstructions can be most useful to water managers. In these chapters, methods of identifying, explaining, and representing extreme event frequency, return periods, and trends are explored, as are methods for using paleoclimate data along with climate model projections to help contextualise future risks of climate change.

Overall, this thesis highlights the enormous potential of remote tree-rings for improving our understanding of past climate in the South Pacific. The reconstructions consistently demonstrate that the instrumental period underestimates the full range of natural climate variability and shows how century-long records provided by tree rings can help us better understand past climate drivers, contextualise the instrumental period, and refine estimates of future climate risks. This thesis builds upon a growing body of work that demonstrates the considerable value of tree-ring based reconstructions for current and future water resource decision making, most notably in remote regions that are highly vulnerable to climate change but where there are limited instrumental records. Maximising the potential of tree-ring data for water management will require ongoing collaboration between dendrochronologists and water managers.

Acknowledgements

This is not the thesis I planned or started. Completing this thesis has been a long and, at times, extremely difficult journey. That it was completed at all is due to the enormous amount of support that I was given by so many people over the last four years.

I thank my four amazing supervisors for their constant encouragement, in particular: A/Prof Martin Andersen, for the many coffees, multiple field trips, not a small amount of counselling, and graciousness when we finally abandoned my first PhD topic. While this thesis work does not reflect our efforts in Vanuatu, I won't forget them. Dr Jonathan Palmer, for welcoming me to his home, and for his excessive patience as he taught me everything I now know about dendrochronology. You weren't expecting to supervise an entire PhD, but stepped up without complaint. A/Prof Fiona Johnson, who adopted me into her research group, and who I in turn adopted into my supervisory team. Thank you for providing a welcoming and supportive research group to brighten a long lock-down year. Last, but certainly not least, Prof Chris Turney, without whose enthusiasm I doubt there'd be a thesis at all. Thank you for celebrating all the wins, even the tiny ones.

No research is possible without the support of our wonderful administration staff. I would like to thank Patricia McLaughlin, Robert Steel, Patrick Vuong, Sunhee Lim, Andrea Heslin, and Ultra Benton for keeping the School of Civil and Environmental Engineering running. Thank you also to all my friends and colleagues at the Water Research Centre, for providing a wonderful working environment. You are too many to name individually, but a special mention to those friends who were there from the beginning and supported me through the worst times: Dr Clare Stephens, Dr Ademir Prata, Johan Visser, Dr Suresh Hettiarachchi, Dr Hung Pham, Dr Ruth Fisher, Dr Shuang Lui, Dr Song Thao Li, and Varsha Sivagurunathan.

To my husband, Marcos, who left Europe, and an amazing career, to move to Australia and support me while I undertook this PhD. There aren't enough words. Thank you.

I was able to undertake this research because dendrochronologists were willing to upload their data to the International Tree Ring Databank, publicly accessible and free of charge. Knowing the time and costs associated with collecting and processing that data, this is an enormous gift to the research community. The value of large networks of tree-rings cannot be overstated. I therefore thank Ed Cook, Dave Stahle, Mariano Morales, Jonathan Palmer, and all the scientists who contributed to the drought atlas collections, for their efforts. I was saddened to hear of the passing of Geert Jan van Oldenborgh, the developer of the KNMI climate explorer, which I heavily relied on in my work, in 2021. I never met Dr van Oldenborgh but will remember his huge contribution to accessibility in science.

List of Activities

Publications

Sharifazari, S., Palmer, J., **Higgins, P.**; Rao, M.; Johnson, F.; Turney, C., Martín-Benito, D., and Andersen, M. Using tree-ring chronologies to derive the first multi-centennial reconstruction of the Dez River discharge in Iran. Submitted.

Higgins, P. A., Palmer, J. G., Turney, C. S. M., Andersen, M. S., & Johnson, F. (2022). Do Southern Hemisphere tree rings record past volcanic events? A case study from New Zealand. *Climate of the Past*, 18(5), 1169–1188. <https://cp.copernicus.org/articles/18/1169/2022/>.

Higgins, P. A., Palmer, J. G., Rao, M. P., Andersen, M. S., Turney, C. S. M., & Johnson, F. (2022). Unprecedented high Northern Australian streamflow linked to an intensification of the Indo-Australian monsoon. *Water Resources Research*, 58, e2021WR030881. <https://doi.org/10.1029/2021WR030881>.

Higgins, P. Andersen, M., Holley, C., Howey, K., Johnson, F., Kearnes, M., Khan, S., Leslie, G., Molloy, S. (2021). Monitoring the monitor: a temporal synthesis of the McArthur River Mine Independent Monitor reports. *Technical Report*. Global Water Institute, University of New South Wales. ISBN: 978-0-7334-4044-1.

Johnson, F., **Higgins, P.**, & Stephens, C. (2021). Climate change and hydrological risk in the Pacific: a Humanitarian Engineering perspective. *Journal of Water and Climate Change*, 1–32. <https://doi.org/10.2166/wcc.2021.277>.

Higgins, P. A., Palmer, J. G., Turney, C. S. M., Andersen, M. S., & Cook, E. R. (2020). One Thousand Three Hundred Years of Variability in the Position of the South Pacific Convergence Zone. *Geophysical Research Letters*, 47(17), 1–11. <https://doi.org/10.1029/2020GL088238>.

Conference Presentations

Higgins, P. A., Palmer, J. G., Turney, C. S. M., Andersen, M. S., & Johnson, F. (2022). Do Southern Hemisphere tree rings record past volcanic events? AmeriDendro, Tree-ring Society, Montreal, Canada, July 2022.

Rao, M. P., **Higgins, P.**, Hung, N. T. T., Sharifazari, S., Cook, E. R., Cook, B., D'Arrigo, R., and Palmer, J. G. (2021). A wetter Brahmaputra River with greater flood risk. American Geophysical Union (AGU) Fall Meeting. New Orleans, USA, December 2021. (*Presented by M. P. Rao*).

Higgins, P. A., Palmer, J. G., Rao, M. P., Andersen, M. S., Turney, C. S. M., & Johnson, F. (2021). Recent increase in Northern Australian streamflow unmatched over the past 600 years. 24th International Congress on Modelling and Simulation (MODSIM), Sydney, Australia, December 2021.

Kearnes, M., **Higgins, P.**, Andersen, M., Holley, C., Howey, K., Johnson, F., Khan, S., Leslie, G., Molloy, S. (2021). Monitoring the monitor: A temporal synthesis of the McArthur River Mine independent monitor reports. Institute of Australian Geographers & New Zealand Geographical Society Combined Conference. Online. July 2021. (*Co-presented by M. Kearns and P. Higgins*).

Higgins, P. Andersen, M., Holley, C., Howey, K., Johnson, F., Kearnes, M., Khan, S., Leslie, G., Molloy, S. (2021). Monitoring the Monitor: an assessment of the McArthur River Mine. Environmental Law Doctoral Researchers' Workshop. Online. July 2021.

Higgins, P. A., Palmer, J. G., Turney, C. S. M., Andersen, M. S., & Cook, E. R. (2020). A 1300-year reconstruction of the South Pacific Convergence Zone using a Pacific-wide tree-ring network. European Geophysical Association (EGU) General Assembly, Online, May 2020.

Research-related Activities

31st Annual North American Dendroecological Fieldweek (NADEF), UQAT-UQAM, Rapide-Dansez, Quebec, June 2022.

Women in Leadership Development Programme, Australian School for Graduate Management, Sydney, 2021.

Authentic Communicator: Activating Presence, Australian School for Graduate Management, Sydney, August 2021.

Submission and expert testimony to the Senate Inquiry into the destruction of 46,000-year-old caves at the Juukan Gorge in the Pilbara region of Western Australia, June 2021.

5th summer school on Trends, Rhythms and Events in the Earth's Climate System – Past, Present and Future, Potsdam University (Online), May-June and Aug-Sep 2021.

Hydrogeological fieldwork, Port Vila, Vanuatu - Three campaigns, 2018/19.

Table of Contents

<u>Abstract.....</u>	<u>ii</u>
<u>Acknowledgements</u>	<u>vi</u>
<u>List of Activities.....</u>	<u>vii</u>
<u>Table of Contents</u>	<u>ix</u>
<u>List of Figures.....</u>	<u>xiii</u>
<u>List of Tables</u>	<u>xx</u>
<u>List of abbreviations</u>	<u>xxi</u>
<u>Chapter 1 <u>Introduction</u></u>	<u>1</u>
1.1 Rationale.....	1
1.2 Study region	3
1.3 Tree-ring chronologies	6
1.4 Thesis aims	8
1.5 Paleoclimate reconstructions	9
<u>Chapter 2 <u>One thousand three hundred years of variability in the position of the South Pacific Convergence Zone</u></u>	<u>12</u>
2.1 Abstract	12
2.2 Plain Language Summary.....	12
2.3 Introduction	13
2.4 Methods	14
2.4.1 The Instrumental SPCZ Index	14
2.4.2 Predictor Selection and Reconstruction.....	14
2.4.3 Calibration and Verification	16
2.5 Results and Discussion	17
2.5.1 Response to Volcanic and Solar Forcing.....	19
2.5.2 Paleoclimate Implications.....	21
2.6 Conclusions	21
2.7 Acknowledgments.....	21
2.8 Conflict of Interest.....	22
2.9 Data Availability Statement.....	22
<u>Chapter 3 <u>Towards a drought atlas for the South Pacific</u></u>	<u>23</u>
3.1 Abstract	23
3.2 Introduction	23
3.3 Data and methods	25

3.3.1	Climate data	25
3.3.2	Reconstruction method	27
3.3.3	Identifying ENSO-related droughts	30
3.4	Results.....	31
3.4.1	Model calibration and validation	31
3.4.2	Selected tree ring proxies and teleconnections to the Pacific	33
3.4.3	Drought anomalies during instrumental ENSO events.....	35
3.4.4	Drought anomalies during significant historical drought events	38
3.4.5	Characteristics of the reconstruction	40
3.4.6	Performance of the Random Forest classifier (RFC).....	41
3.4.7	Identification of extreme events	42
3.4.8	Comparison to other reconstructions	45
3.5	Wider Considerations.....	46
3.5.1	The need for independent verification	47
3.5.2	Length of the calibration period	49
3.5.3	Assumptions of stationarity	51
3.6	Conclusions	52
<u>Chapter 4 Do Southern Hemisphere tree rings record past volcanic events? A case study from New Zealand.....</u>		<u>54</u>
4.1	Abstract	54
4.2	Introduction	54
4.3	Data and methods	57
4.3.1	Tree-ring chronologies	57
4.3.2	Selection of volcanic events	59
4.3.3	Superposed epoch analysis	60
4.3.4	Temperature reconstructions	60
4.4	Results.....	62
4.4.1	Overall species volcanic responses.....	62
4.4.2	Within-species variability in volcanic response	63
4.4.3	Calibration and validation of the temperature reconstructions	64
4.4.4	Volcanic signals in the temperature reconstructions	66
4.5	Discussion	68
4.5.1	Volcanic responses recorded by New Zealand trees	68
4.5.2	A kauri growth benefit.....	70
4.5.3	Site-related volcanic responses.....	72
4.5.4	Implications for temperature reconstructions	73
4.6	Conclusions	76
4.6.1	Data availability.....	77
4.6.2	Supplement	77
4.6.3	Author contributions.....	77
4.6.4	Competing interests	77
4.6.5	Disclaimer.....	78
4.6.6	Special issue statement	78
4.6.7	Acknowledgements	78

4.6.8	Financial support	78
4.6.9	Review statement.....	78

Chapter 5 Unprecedented High Northern Australian Streamflow Linked to an Intensification of the Indo-Australian Monsoon 79

5.1	Abstract	79
5.2	Plain Language Summary.....	79
5.3	Introduction	80
5.4	Study area and data availability.....	82
5.4.1	The Daly catchment.....	82
5.4.2	Hydrological data	83
5.4.3	Historical flood records	84
5.4.4	Tree-ring proxy records.....	84
5.5	Methods	85
5.5.1	Streamflow reconstruction.....	85
5.5.2	Historical flood events.....	86
5.5.3	Extreme event analysis and climate forcing	86
5.6	Results and Discussion	87
5.6.1	Tree-ring predictor selection.....	87
5.6.2	Streamflow reconstruction.....	88
5.6.3	Historical comparisons	90
5.6.4	Extreme events	91
5.6.5	Regional coherency	94
5.7	Conclusions	96
5.8	Conflict of Interest.....	97
5.9	Data Availability Statement.....	97
5.10	Acknowledgments.....	97

Chapter 6 Combining paleoclimate data and future climate projections to predict hydrological drought risk..... 99

6.1	Abstract	99
6.2	Introduction	99
6.3	Past and future streamflow reconstructions from gridded PDSI.....	101
6.4	Case study catchment: the Murray-Darling Basin.....	102
6.4.1	Streamflow data.....	104
6.5	Streamflow reconstruction and projection.....	106
6.5.1	Streamflow reconstructions	106
6.5.2	Calibration and verification	107
6.5.3	Future streamflow projections from modelled PDSI.....	108
6.5.4	Future streamflow projections from downscaled runoff estimates.....	109
6.5.5	Analysis of drought risk	109
6.6	Results.....	111
6.6.1	Continuous past and future streamflow reconstructions.....	111

6.6.2	Analysis of past and future drought occurrence	121
6.7	Discussion	126
6.7.1	Implications for water management	126
6.7.2	Expanding gridded projections to a more extensive study and other future work.....	130
6.8	Conclusions	132
<u>Chapter 7</u>	<u>Conclusions</u>	<u>134</u>
7.1	Summary of main findings.....	134
7.2	Recommendations for future work	137
<u>References</u>		<u>139</u>
<u>Appendix A.</u>	<u>Supplementary information for Chapter 2</u>	<u>159</u>
<u>Appendix B.</u>	<u>Supplementary information for Chapter 3</u>	<u>166</u>
<u>Appendix C.</u>	<u>Supplementary information for Chapter 4</u>	<u>167</u>
<u>Appendix D.</u>	<u>Supplementary information for Chapter 5</u>	<u>182</u>
<u>Appendix E.</u>	<u>Supplementary information for Chapter 6</u>	<u>198</u>

List of Figures

Figure 1-1 The major climate features affecting eastern Australia, New Zealand, and the South Pacific Islands. The position of the Inter-tropical Convergence Zone and South Pacific Convergence Zone are based on the twentieth Century Reanalysis v3 data set Omega at 500 hPa (Lorrey et al., 2012). Predominant wind directions are depicted by arrows, after CSIRO et al. (2015).....	3
Figure 1-2 Publicly available tree-ring chronologies used in this thesis (black dots) compared to the typical ENSO-precipitation teleconnections during El Niño events. Regions with anomalous precipitation during El Niño events from 1951–2016 were derived from the probabilistic estimates of Lenssen et al. (2020). Further information on the seasonality of the teleconnections is provided in Figure 1 of Lenssen et al. (2020).	7
Figure 1-3 Publicly available tree-ring chronologies used in this thesis (black dots) compared to the typical ENSO-precipitation teleconnections during La Niña events. Regions with anomalous precipitation during La Niña events from 1951–2016 were derived from the probabilistic estimates of Lenssen et al. (2020). Further information on the seasonality of the teleconnections is provided in Figure 2 of Lenssen et al. (2020).	8
Figure 1-4 The five reconstructions explored in Chapters 2-6: 2) Variability in the position of the South Pacific Convergence Zone; 3) South Pacific Island drought; 4) New Zealand temperature response following volcanic eruptions; 5) A monsoon river reconstruction for the Daly River, Australia; 6) Past and future streamflow in the Murray-Darling Basin, Australia.	9
Figure 2-1 Location of the tree-ring predictors selected for the reconstruction (red circles) and the mean Nov-Apr position axis of low-level convergence (SPCZ, black dashed line) based on the twentieth Century Reanalysis v3 data set Omega at 500 hPa 1911–1998 (Lorrey et al., 2012). The black circles show the locations of Suva, Fiji, and Apia, Samoa, the MSLP stations used to calculate the instrumental SPCZI (Salinger et al., 2014).....	15
Figure 2-2 Comparison of the instrumental SPCZI and SPCZIr over the calibration period (1911–1998). The instrumental SPCZI is shown in black, SPCZIr is shown in red, and the grey bars show the 5–95% bootstrap confidence interval of the reconstruction.	16
Figure 2-3 (a) SPCZIr from 700 to 1998 CE. The red line shows the smoothed reconstruction using a 13-year Gaussian low pass filter, bands indicate the approximate timing of the MCA and LIA and triangles represent the timing of large volcanic eruptions; (b) wavelet spectrum of the SPCZI reconstruction (Torrence & Compo, 1998). Black contours indicate power above the 95% confidence interval when using an AR(1) red noise model.	18
Figure 2-4 Normalised SPCZIr SEA results for large tropical volcanic eruptions since 700 CE. Results are shown for the reconstruction presented in this paper (a), and for SPCZIr based on the subset of tree rings from the Northern Hemisphere (b) and Southern Hemisphere (c). The vertical bars show the 5th to 95th percentiles of the SPCZIr response based on 1,000 unique draws of key years, while the dashed horizontal lines indicate the threshold for epochal anomalies to be statistically significant using random bootstrapping. Positive values indicate an eastward-shifted SPCZ.....	19
Figure 3-1 Location of precipitation (top left) and temperature stations (top right) with data available during the baseline period 1960-1990. Filled diamonds indicate stations with less than 10% of monthly values missing over the baseline period. The total number of stations with data over time is also shown in bottom panel, with the baseline period indicated by the grey bar.	26

Figure 3-2 Locations of all tree-ring chronologies included in the initial predictor pool (red) and the CRU grid point reconstruction targets (blue). Five grid points were calculated from instrumental data not included in the CRU gridded products.	28
Figure 3-3 Precipitation (blue) and temperature (orange) data availability for two gauges with long records.....	30
Figure 3-4 Calibration period leave-one-out cross-validation reduction of error (CVRE) for each reconstructed grid point for the best-replicated nest.	32
Figure 3-5 Number of reconstructed grid points to which each tree-ring chronology contributes.	34
Figure 3-6 Proportional weighting of chronologies from each of the four regions (ANZDA – Australia and New Zealand, SADA – South America, MXDA – Central and North America, and MADA – Monsoon Asia) to the reconstruction by island group. The weighting for each island/island group is defined as the sum of the absolute value of beta weights of all chronologies from a region.	35
Figure 3-7 Instrumental (left) versus reconstructed (right) November-April SPEI during El Niño events during the data period (1950-2018 for instrumental, 1875-1998 for reconstruction). The average of all El Niño events is shown in the top row, and individual El Niño years in which the SPCZ took a zonal orientation are shown in the remaining two rows.	36
Figure 3-8 Instrumental (left) versus reconstructed (right) November-April SPEI during La Niña events during the data period (1950-2018 for instrumental, 1875-1998 for reconstruction). The average of all La Niña events is shown in the top row, and individual strong La Niña years are shown in the remaining two rows.	37
Figure 3-9 (Top) 50-year running Pearson correlation between the first principal component of reconstructed SPEI and the instrumental Niño-34 index with 95% confidence interval calculated from synthetic data. (Bottom) Spatial correlation between SPEI and Niño-34 for overlapping 50-year periods. Correlations not significant at $p < 0.05$ are greyed out.	38
Figure 3-10 November-April SPEI during known historical droughts: the Mexican Year of Hunger (1785-86), the Australian Settlement Drought (1791-93), the Vanuatu drought (1865-66), and the Great Drought (1876-78).	40
Figure 3-11 Percentage of area under severely dry ($\text{SPEI} < -1$, orange) and extremely dry ($\text{SPEI} < -2$, red) conditions, and for severely wet ($\text{SPEI} > 2$, light blue) and extremely wet ($\text{SPEI} > 4$, blue) conditions over the whole SPaDA domain. The dashed lines indicate 95% percentiles of the distribution. The black triangles indicate the occurrence of the four historical drought years and the seven ‘zonal’ El Niño years (1877/78 is common to both groups of events). Only years 1940/41 and 1991/92 do not have a substantial proportion of extremely wet/extremely dry grid points.....	41
Figure 3-12 Wavelet spectra of the first two (unrotated) principal components of the SPEI reconstruction (Torrence & Compo, 1998) a) PC1, and b) PC2. Black contours indicate power above the 95% confidence interval when using an AR(1) red noise model.	41
Figure 3-13 Summary of results of the Random Forest classification for pre-instrumental years 1640 – 1874 CE. November-April SPEI during years classified as neutral (135 years), La Niña (61 years), El Niño (29 years), and Zonal (10 years).	43

Figure 3-14 Instrumental November-April SPEI during neutral, La Niña, and El Niño years for gauges with anomalous precipitation regimes during zonal El Niño events. Starred years indicate the zonal events demonstrating anomalous SPEI during the data period. Nauru is calculated from precipitation and temperature data with the other gauges taken as the nearest CRU grid point.....	44
Figure 3-15 Average reconstructed November-April SPEI during years classified as La Niña, and El Niño by the random forest model, with SPEI during the 13 zonal events plotted individually. Starred years indicate the zonal events demonstrating anomalous SPEI matching the gauge behaviour during the instrumental period.....	44
Figure 3-16 50-year running Pearson correlation between the SPaDA PC1 and the ENSO reconstructions of a) McGregor et al. (2010) over 1650-1977 CE and b) Li et al. (2013) over the period 1640-1998 CE All correlations are significant ($p < 0.01$).	46
Figure 3-17 Event-based comparison between the published reconstructions of a) Gergis and Fowler (2009) and b) Freund et al. (2019) with c) events identified by the RFC model as El Niño (blue) and zonal El Niño (orange) for the period 1640-1875 CE. The calendar year events of Gergis and Fowler (2009) have been shifted forwards by one year for consistency with the other reconstructions. While Freund et al. (2019) report event amplitude, Gergis and Fowler presented a qualitative ENSO strength index. For potting purposes weak, medium, strong, very strong, and extreme events have been given amplitudes of 0.1, 0.25, 0.5, 0.75, and 1. Events identified in the SPaDA have similarly been given an amplitude of 0.5 (El Niño) or 1 (zonal El Niño).	46
Figure 3-18 50-year running Pearson correlation between the SPaDA PC1 and the ENSO reconstructions of Zhu et al., (2022): a) PC1 vs the multiproxy coral and tree-ring reconstruction, b) PC1 vs the coral only reconstruction, and c) the Zhu et al. reconstructions compared directly. Grey bars indicate periods where correlations are not significant ($p > 0.05$).	49
Figure 3-19 Power in the decadal (10-20 years, orange) and multidecadal (> 20 years, blue) frequency bands as a proportion of total power in 50-year moving windows for all reconstructions of Apia, Samoa calibrated using 40 or 60 years of instrumental data.	51
Figure 4-1 Distribution of tree-ring chronologies in New Zealand. Elevation data sourced from the LINZ Data Service and licensed for reuse under CC BY 4.0.	57
Figure 4-2 Selection of volcanic events based on thresholds of peak modelled stratospheric atmospheric optical depth (Toohey and Sigl, 2017), averaged over 30–50 °S, greater than 0.04 (blue) and 0.08 (red). Known eruptions are labelled.	60
Figure 4-3 Mean chronology departures 5 years before and 5 years after the 13 largest eruption years (year 0), separated by tree species. The chronologies contributing to the species-wide composite are shown in black, with the number of chronologies indicated in parentheses. The sensitive chronology composite is shown in blue and the number of contributing chronologies is shown in brackets. Significance bands (dotted grey lines) are the 1st, 5th, 95th, and 99th percentile of 10 000 random samples of non-event years from the species-wide composite.	63
Figure 4-4 a) Results of k-means clustering of New Zealand cedar chronologies. b–f) Mean chronology departures 5 years before and after eruption years (year 0), separated by cluster, and the 95th and 99th significance levels calculated by generating 10 000 random samples of non-event years from the group composite. The map in a) was made with Natural Earth free vector map data, which are available at http://naturalearthdata.com (last access: 17 November 2021).65	65

Figure 4-5 New Zealand average DJF temperature reconstructions. Unfiltered (black) and filtered (20-year spline; blue) mean DJF reconstruction with 90% uncertainty interval (grey) between 1400 and 2018 CE for a) NZall and b) NZsens. Reconstruction fit to instrumental temperature (red) over the full calibration period 1911–1990 CE for c) NZall and d) NZsens. The 90% uncertainty interval was calculated from 300 maximum entropy bootstrap replications.

..... 66

Figure 4-6 Mean anomalies 5 years before and after 21 eruption years with SAOD > 0.04 a, c) and 13 eruption years with SAOD > 0.08 b, d) for both the NZall (blue) and NZsens (red) reconstructions. The mean response from an ensemble of seven climate models to the same set of events is shown in black. The 90th percentile bootstrap confidence intervals were constructed from 1000 replicates of either 15 or 9 event years at random.

..... 67

Figure 4-7 Distribution of tree rings used in a) the NZall temperature reconstruction and b) the NZsens temperature reconstruction. Larger, darker red markers represent chronologies with greater relative weighting in the multiple regression. Made with Natural Earth free vector map data available at <http://naturalearthdata.com> (last access: 17 November 2021).

..... 68

Figure 5-1 The Daly catchment showing the location of the four selected stream gauges (blue triangles with gauge numbers). The inset map shows the location of the Daly catchment (grey) and Burdekin catchment (beige) within the Australian tropical monsoon region (light blue), and the locations of *Callitris intratropica* and *C. columellaris* tree-ring chronologies within and proximal to the monsoon region (black diamonds). The approximate southern monsoon region boundary was adapted from the Australian Bureau of Meteorology climate classification.

..... 82

Figure 5-2 (a) Catchment average annual water year (September–August) rainfall (mm) from 1896 to 2018, with the long-term trend shown in red; (b) Boxplots showing monthly discharge (km³/month, left axis) for the instrumental period (1961–2018) at gauge G8140040, Daly River at Mount Nancar, with catchment average monthly rainfall (mm, right axis) plotted in blue.

.... 83

Figure 5-3 Schematic overview of the reconstruction methodology. ¹Partial information correlation.

..... 85

Figure 5-4 Left: Spatial Pearson correlation fields comparing average Daly catchment (red square) GPCP rainfall and GPCP rainfall over Australia, the South-east Asian Monsoon and Asian Monsoon regions during the northern Australia dry season (May–Sept) between 1979 and 2020. Right: Same figure for the northern Australia wet season (Nov–Apr). Correlations not significant at $p < 0.1$ are greyed out. Black diamonds represent the location of the 63 tree-ring chronologies with a significant correlation to at least three of four Daly catchment streamflow gauges after variance transformation.

..... 88

Figure 5-5 (a) Instrumental (black) versus reconstructed (blue) streamflow in km³/year for Daly River gauge G8140040 over the instrumental period 1961–2018. (b) Reconstructed flow at G8140040 from 1413 to 2005 CE with the 90% confidence interval for the reconstruction shown in light blue.

..... 89

Figure 5-6 (a) Relationship between maximum five-day rainfall and total annual (September–August) rainfall at Katherine for all years on record (blue) and historical flood years (red). The blue line shows the significant positive trend ($r = 0.60$; $p < 0.001$) between the variables within the 95% confidence interval. (b) Superposed epoch analysis showing that Katherine River streamflow is significantly ($p < 0.01$) higher than expected by chance during historical flood years.

..... 91

Figure 5-7 Kernel density estimate plots of 30,000 bootstrapped replications of instrumental Niño3.4 DJF SST anomalies from 1875–2005 showing the co-occurrence of extremes in the

reconstructed streamflow and El Niño (a, b) and La Niña (c, d) events. The number of extreme low and high flow events in the reconstruction associated with each ENSO phase is shown in black and compared to the bootstrap mean (dashed lines); significant values lying outside the 95% bias-corrected bootstrap confidence interval are shown in red. The average December to January (DJF) SST anomalies during low flow years (e) and high flow years (f) are also shown, with the approximate location of the Daly catchment indicated by the black square. 93

Figure 5-8 Extreme high flow/low flow event years and the time-varying frequency of the occurrence of these events between 1413 and 2018 for the a) Daly River at G8140040 and b) Katherine River at G8140001. A kernel smoothing method was used with a bandwidth of 38 years (solid lines), with dashed lines showing the adjusted frequency curve if instrumental data is appended to the reconstruction after 2005. In c) the frequency of extremes between 1648 and 2018 for the Burdekin River coral reconstruction of Lough (2015) is plotted with a bandwidth of 38 years, with instrumental data appended to the reconstruction after 2011. The shaded areas (blue and orange) represent the 95% confidence intervals based on 1,000 bootstrap simulations. 96

Figure 6-1 a) Location of the study sites, the Darling River at Wilcannia (blue dot), located in the upper Murray-Darling Basin (green), and the Murray River at Lock-7 (red dot), located in the lower Murray-Darling Basin (grey); Historical (1961-1990 CE) average annual rainfall (mm; b) and Morton point potential evapotranspiration (mm; c) over the MDB. Data from the SILO gridded database (QLD Government, last accessed 14/7/2022). 102

Figure 6-2 a) Time series of naturalised average monthly streamflow (blue) compared to gauged average monthly streamflow (brown) in the Darling River at Wilcannia (1970-2022). Decreasing trends (dashed lines) in both gauge (1973-2022) and naturalised (1970-2019) streamflow are significant (Mann-Kendall trend test, $p < 0.05$); b) Comparison of the proportion of annual streamflow occurring in each month at Wilcannia, for the naturalised (blue) and gauged (brown) streamflow; c) Average monthly naturalised streamflow in the Darling River at Wilcannia; d) Average monthly naturalised streamflow in the Murray River at Lock-7. Data from the Murray-Darling Basin Authority (2020). 105

Figure 6-3 Stylised plot of streamflow anomalies (standard deviation units) in blue showing how drought duration, magnitude, and peak are defined for each drought event. 111

Figure 6-4 Correlation between seasonally averaged, transformed Darling River streamflow and the first four principal components of the four drought atlases a) ANZDA, b) MADA, c) SADA, and d) MXDA. Significant correlations based on 1000 bootstrap replications are shown in bold circles/lines, correlations not significant ($p > 0.05$) by light circles/dashed lines. The hatched periods correspond to the seasonal reconstruction targets of each drought atlas (a, c – DJF; b, d – JJA). 112

Figure 6-5 Correlation between seasonally averaged, transformed Murray River streamflow and the first four principal components of the four drought atlases a) ANZDA, b) MADA, c) SADA, and d) MXDA. Significant correlations based on 1000 bootstrap replications are shown in bold circles/lines, correlations not significant ($p > 0.05$) by light circles/dashed lines. The hatched periods correspond to the seasonal reconstruction targets of each drought atlas (a, c – DJF; b, d – JJA). 113

Figure 6-6 Drought atlas grid points selected as predictors for the gridded reconstruction based on a) significant ($p < 0.05$) correlation with transformed Darling July-Dec streamflow at Wilcannia and b) significant ($p < 0.05$) correlation with transformed water year Murray streamflow at Lock-7. 114

Figure 6-7 Reconstructed (blue) versus instrumental (black) Darling July-Dec naturalised streamflow over the full calibration period (1897-2000) for a) the reconstruction based on tree-ring chronologies and b) the reconstruction based on gridded drought atlas outputs. The uncertainty interval (light blue shading) is based on 300 maximum entropy bootstrap replications.	115
Figure 6-8 Reconstructed (blue) versus instrumental (black) Murray water year naturalised streamflow over the full calibration period (1897-2000) for a) the reconstruction based on tree-ring chronologies and b) the reconstruction based on gridded drought atlas outputs. The uncertainty interval (light blue shading) is based on 300 maximum entropy bootstrap replications.	116
Figure 6-9 Residuals for the full calibration period (1897-2000) for a) the reconstruction of July-Dec Darling streamflow based on gridded drought atlas outputs and b) the reconstruction of water year Murray streamflow based on gridded drought atlas outputs. The top 10% of overpredicted values are shown in red, the top 10% of underpredicted values are shown in brown, and the remaining 80% of values are shown in blue.	117
Figure 6-10 Boxplots of a) July-Dec streamflow at Wilcannia and b) Water year streamflow at Lock-7 in the reconstruction period (1500-2019 CE; light blue) and each year from 2020-2099. The 30 projections based on gridded PDSI (brown) are compared to the four simulations from the AWO bias-corrected model outputs (purple), with the mean of each simulation shown as a red diamond.	118
Figure 6-11 The average percent change in streamflow over 2020-2099 in the projections compared to the 1961-2019 instrumental period used for scaling for a) projected July-Dec streamflow at Wilcannia and b) projected water year streamflow at Lock-7. Projections based on gridded PDSI are shown in brown and derived from the AWO bias-corrected model outputs in purple.	119
Figure 6-12 Reconstructed Darling River July-Dec streamflow for each year between 1500 and 2000 CE as a departure from the ‘historical’ period mean (1500-2019 CE; blue and brown bars, with 90% confidence interval as light shaded bars), along with the 30-year low-pass filtered reconstruction (black) highlighting multi-decadal variability. The instrumental Darling dry season streamflow between 1897 and 2019 CE is shown as black bars. Projected streamflow modelled using PDSI derived from the multi-model CMIP5 RCP8.5 ensemble (Table E-1) during the ‘future’ (2001–2099 CE) simulation period of these runs is shown as the grey lines. The 30-year low-pass filtered projected streamflow is shown as bold brown (median), dashed red (25th percentile), and dashed blue lines (75th percentile).	120
Figure 6-13 Reconstructed Murray River water year streamflow for each year between 1500 and 2000 CE as a departure from the ‘historical’ period mean (1500-2019 CE; blue and brown bars, with 90% confidence interval as lightly shaded bars), along with the 30-year low-pass filtered reconstruction (black) highlighting multi-decadal variability. The instrumental Murray streamflow between 1897 and 2019 CE is shown as black bars. Projected streamflow modelled using PDSI derived from the multi-model CMIP5 RCP8.5 ensemble (Table E-1) during the ‘future’ (2001–2099 CE) simulation period of these runs is shown as the grey lines. The 30-year low-pass filtered projected streamflow is shown as bold brown (median), dashed red (25th percentile), and dashed blue lines (75th percentile).	121
Figure 6-14 The top 30 ranked droughts during the historical period (1500-2019 CE) for the Darling River at Wilcannia compared to selected quantiles of the conditional distribution for a) drought duration and magnitude and b) drought duration and peak. The colours indicate the century when the drought began, and points are jittered for display purposes.	123

Figure 6-15 The top 30 ranked droughts during the historical period (1500-2019 CE) at Murray River Lock-7 compared to selected quantiles of the conditional distribution for a) drought duration and magnitude and b) drought duration and peak. The colours indicate the century when the drought began, and points are jittered for display purposes. 124

Figure 6-16 The top 30 ranked droughts during the historical period (1500-2019 CE; blue) compared to the highest ranked drought for each streamflow projection (2020-2099 CE; red) for the Darling River at Wilcannia for a) drought duration and magnitude and b) drought duration and peak. The dark blue dots indicate the Millennium and recent droughts. The dashed black lines represent selected quantiles of the conditional distribution based on historical data, the dashed brown lines represent the median quantiles for the conditional distribution of historical and projected streamflow for each of the 30 gridded PDSI projections, and the yellow bands represent the full range of projected quantiles from the gridded projections. Points are jittered for display purposes and may appear in slightly different locations to the points in Figure 6-14. 125

Figure 6-17 The top 30 ranked droughts during the historical period (1500-2019 CE; blue) compared to the highest ranked drought for each streamflow projection (2020-2099 CE; red) for the Murray River at Lock-7 for a) drought duration and magnitude and b) drought duration and peak. The dark blue dots indicate the Millennium and recent droughts. The dashed black lines represent selected quantiles of the conditional distribution based on historical data, the dashed brown lines represent the median quantiles for the conditional distribution of historical and projected streamflow for each of the 30 gridded PDSI projections, and the yellow bands represent the full range of projected quantiles from the gridded projections. Points are jittered for display purposes and may appear in slightly different locations to the points in Figure 6-15. 126

List of Tables

Table 3-1 Calibration and verification intervals for each island/island group. Refer to Figure 3-6 for a spatial reference of island/island group names.	28
Table 3-2 Verification statistics for selected island grid points based on long instrumental records. Year refers to the earliest year of reconstruction validity using a cut-off of VRE and $VCE > 0$	32
Table 3-3 Calibration and verification statistics for Apia and Tahiti for reconstructions models using different calibration period lengths. The mean and standard deviation are provided for each statistic across all iterations of a calibration period length.	33
Table 3-4 Testing results for the Balanced Random Forest classifier.....	42
Table 3-5 Probability of a zonal El Niño event according to Random Forest classification of MEboot replications of reconstructed drought.....	45
Table 4-1 Distribution, reported climate sensitivities, and key references for New Zealand dendrochronological species.	58
Table 5-1 Selected streamflow gauges in the Daly catchment.	84
Table 5-2 Calibration and verification statistics for the best-replicated nest (1895-2005) and median values for the whole reconstruction interval (1413-2005) for the four Daly catchment gauges.	89
Table 6-1 List of the ten “strongest” drought episodes in the Darling River and Murray River reconstructions over the period 1500-2019 CE. Bold events are coherent in both the upper and lower MDB. The final rank score was derived from the sum of the individual rank scores for duration, peak, and magnitude (not shown) thus ties are possible. The higher the score, the stronger the event.	121

List of abbreviations

ANZDA	Eastern Australia and New Zealand Drought Atlas
AR1	First Order Autoregressive Model
AWO	Australian Water Outlook
AWRA-L	Australian Water Resource Assessment Landscape Model
BCA	Bias-corrected and Accelerated Bootstrap
BOM	Australian Bureau of Meteorology
CC	Creative Commons
CE	Common Era
CMIP5	Coupled Model Intercomparison Project 5
CRSQ	Calibration Period Coefficient of Multiple Determination
CRU	University of East Anglia Climatic Research Unit
CVRE	Cross-validation Reduction of Error
DJF	December to February
ENSO	El Niño-Southern Oscillation
EOF	Empirical Orthogonal Function
ERSST	Extended Reconstructed Sea Surface Temperature
GCM	General Circulation Models
GPCP	Global Precipitation Climatology Project
hPA	Hectopascal
IASM	Indo-Australian Summer Monsoon
IOD	Indian Ocean Dipole
IPO	Inter-decadal Pacific Oscillation
IQR	Interquartile Range
ITCZ	Intertropical Convergence Zone
ITRDB	International Tree Ring Data Bank
JJA	July to August
LIA	Little Ice Age

LINZ	Land Information New Zealand
MADA	Monsoon Asia Drought Atlas
MAM	March to May
MCA	Medieval Climate Anomaly
MDB	Murray-Darling Basin
MEboot	Maximum Entropy Bootstrap
ML	Megalitres
MRNBC	Multivariate Recursive Nested Bias Correction
MSLP	Mean Sea Level Pressure
MTM	Multi-taper Method Spectral Analysis
MXD	Maximum Latewood Density
MXDA	Mexican Drought Atlas
NIWA	New Zealand National Institute of Water and Atmospheric Research
NZ	New Zealand
PC	Principal Component
PCA	Principal Component Analysis
PDSI	Palmer Drought Severity Index
PPR	Point-to-Point Regression
RCP	Representative Concentration Pathway
RFC	Random Forest Classifier
SADA	South American Drought Atlas
SAM	Southern Annular Mode
SAOD	Stratospheric Aerosol Optical Depth
SDU	Standard Deviation Units
SEA	Superposed Epoch Analysis
SON	September to November
SPaDA	South Pacific Drought Atlas
SPCZ	South Pacific Convergence Zone

SPCZI	South Pacific Convergence Zone Index
SPCZIr	Reconstructed South Pacific Convergence Zone Index
SPEI	Standardized Precipitation Evapotranspiration Index
SST	Sea Surface Temperatures
Tg	Teragrams
VCE/CE	Verification Period Coefficient of Efficiency
VRE/RE	Verification Period Reduction of Error
VSSI	Volcanic Stratospheric Sulphur Injection
WASP	WAvelet System Prediction

Chapter 1 Introduction

1.1 Rationale

Increasing population and demands on water resources, and a changing hydroclimate regime, means there is an urgent need for sustainable water management. Increasingly, water planners are recognising that the relatively short instrumental (historic) records of hydrological observations are insufficient to fully understand, natural trends, variability, and climate drivers. The analysis of multi-centennial-long hydroclimate-sensitive tree ring series allow us to extend the records further back in time (Ljungqvist et al., 2020; Turney & Fogwill, 2021). Variability in the width of annual tree rings and other wood properties are influenced by climate conditions during the growing season; most notably a combination of temperature and soil moisture (Fritts, 1991). Reconstruction of climate and/or hydrology from tree rings can therefore provide detailed information on sub-annual to annual climate variability, extending the instrumental record from the eighteenth and nineteenth centuries, back potentially millennia (Jones & Mann, 2004). These long records can be used to better understand instrumental and pre-instrumental variability, the occurrence, trends, and drivers of extreme events, and provide insights into possible future hydroclimatic scenarios (Neukom et al., 2019). In this way, tree rings can contribute to robust water resource planning that considers both the plausible range of natural hydrologic variability and climate change impacts (Meko & Woodhouse, 2011).

The South Pacific is a region that could greatly benefit from longer datasets of climate information. South Pacific Island countries are highly vulnerable to extreme events such as droughts and floods. Their small size and remote location provides limited opportunities to naturally buffer the resilience of populations in the face of climate variability (Johnson et al., 2021). Meteorological records from these countries are typically very short, often only a few decades long, whilst pervasive multidecadal variability is considered to play an important role in the spatial and temporal patterns of climate and extremes (McGree et al., 2016); the latter a characteristic of Australia and New Zealand, while of very different size and socio-economic circumstances to the South Pacific islands. For the region as a whole, characterising natural hydroclimatic variability is challenging due to the short duration of the instrumental record (Deser & Phillups, 2017). This leaves a substantial gap in our understanding of long-term natural climate variability, which is a requirement for reasonable estimates of potential future changes.

While ‘paleo-reconstructions’ can help fill this knowledge gap, tree rings are not evenly distributed across the region, and the South Pacific has very few local, high-resolution paleoclimate proxies to develop hydroclimatic reconstructions. Only New Zealand has a high-density spatial coverage of tree-ring chronologies (Palmer et al., 2015). In Australia, tree rings are primarily restricted to the island state of Tasmania, with a dearth of chronologies available

over much of the mainland. The small land area, and difficulty in finding tropical tree species with annual growth rings (Rozendaal & Zuidema, 2011), have prevented the development of chronologies from the South Pacific Islands. In the absence of local proxies, tree-ring chronologies from regions that have strong teleconnections to the South Pacific can be used to reconstruct climate variables of interest (Buckley et al., 2019; Li et al., 2013; Lough & Fritts, 1985; MacDonald & Case, 2005; Stahle et al., 1998).

The standard approach for tree-ring climate reconstructions is to use statistical models to determine the relationship between the instrumental record and the chronology during the period of overlap (Hernández et al., 2020; Jaume-Santero et al., 2020; Jones & Mann, 2004; Neukom et al., 2019). This calibration process provides a transfer function that enables the proxy to be used as a surrogate for past climate. A significant source of uncertainty in paleoclimate reconstructions is that the relationship between tree-rings and climate is not perfect. The methodological challenge, therefore, is to filter the climate signal from multiple noisy proxies whilst addressing the limitations of short calibration periods and decreasing numbers of proxies going back in time (Riedwyl et al., 2009).

Additional methodological considerations exist for reconstructions based largely or entirely on remote tree-rings. Using tree rings from a single teleconnection region can bias the reconstruction toward the influence of the climate driver on that region, which will be different from the signal in the tropical Pacific (Woodhouse, 1997). Another important consideration is whether the relationship between the Pacific and the teleconnection region is stationary (stable) over time (Mann, 2000). Non-stationary relationships between the climate and the teleconnected region can result from changes in the ocean-atmosphere linkages (Hernández et al., 2020; Power et al., 1999) or due to local climate factors which weaken the climate driver-proxy relationship (Cook et al., 2018). Using networks of tree rings from multiple teleconnection regions can resolve or partially resolve these issues. The common climate signal identified amongst proxies from separate teleconnected regions must be the common expression of the climate driver. Using proxies from different geographical regions also minimises the potential impact of non-stationarities between a climate driver and any single region on the reconstruction (Batehup et al., 2015). The network approach has produced remarkably robust reconstructions of Pacific climate variability despite the remote location of the tree-ring predictors from the tropics (e.g., Buckley et al., 2019; Cook et al., 2018; Li et al., 2013; Stahle et al., 1998).

This thesis explores the potential and limitations of networks of remote tree-ring proxies (i.e., proxies from regions with strong teleconnections to the South Pacific) to reconstruct the hydroclimate across the South Pacific region. Through a series of regional to catchment-scale case studies, the thesis investigates existing and new methods for hydroclimatic reconstructions

considering the unique challenges of the South Pacific region: strong inter-annual and inter-decadal variability, multi-decadal (or shorter) instrumental records, data gaps, and potential non-stationarities in climate teleconnections. In the final chapters, the thesis focuses on how these reconstructions can be most helpful to water managers. Methods of identifying, explaining, and representing extreme event frequency, return periods, and trends are explored, as are methods for using paleoclimate data to help contextualise future risks of climate change.

1.2 Study region

This thesis investigates the potential of remote tree-ring reconstructions over the broad South Pacific region, which includes eastern Australia, New Zealand, and the South Pacific Islands. The large-scale atmospheric circulation patterns which cause sub-annual variability in climate, and the climate drivers primarily responsible for inter-annual regional climate variability, are shown in (Figure 1-1). Here, a brief introduction is provided on the most important climate features for the reconstructions; further details on the climate specific to each case study are provided in their respective chapters.

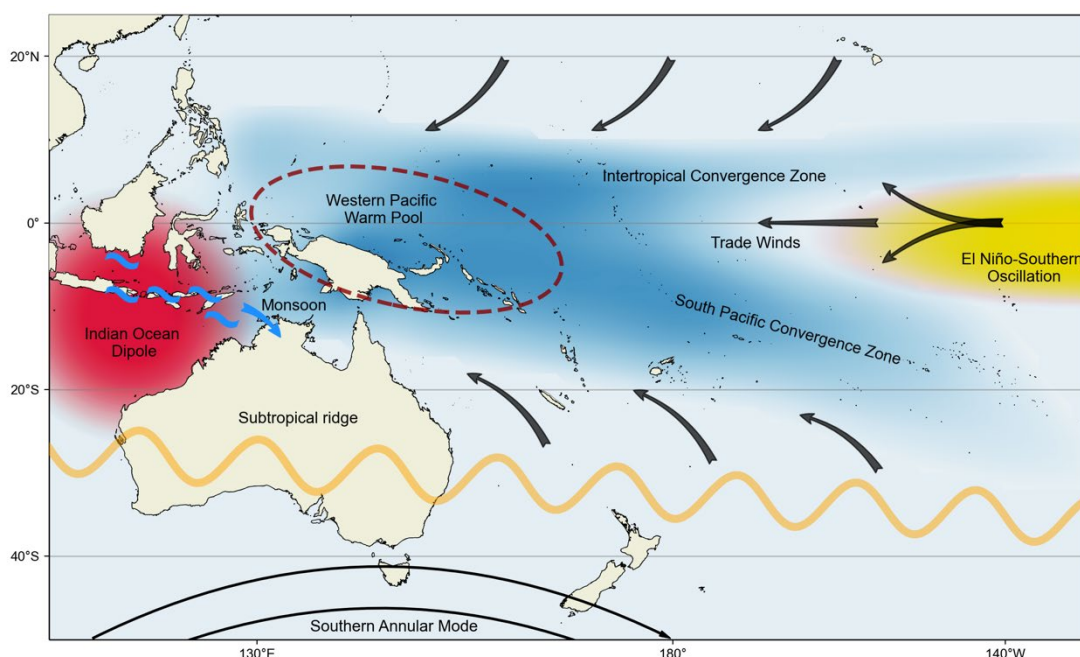


Figure 1-1 The major climate features affecting eastern Australia, New Zealand, and the South Pacific Islands. The position of the Inter-tropical Convergence Zone and South Pacific Convergence Zone are based on the twentieth Century Reanalysis v3 data set Omega at 500 hPa (Lorrey et al., 2012). Predominant wind directions are depicted by arrows, after CSIRO et al. (2015).

Precipitation across the Pacific varies spatially due to the position and strength of two large bands of cloudiness and precipitation, the Intertropical Convergence Zone (ITCZ) and the South Pacific Convergence Zone (SPCZ) (CSIRO et al., 2015). Seasonal movement of the convergence zones results in the wet/dry seasonality experienced by the South Pacific Islands. The ITCZ is a zonal rain band driven by the collision of the northerly and southerly trade winds near the

equator (Byrne et al. 2018). The mean location of the ITCZ is a few degrees north of the Equator (Gruber, 1972), because of hemispheric differences in energy transport and therefore mean temperature (Schneider et al., 2014). The ITCZ typically follows the seasonal solar cycle toward the warming hemisphere, resulting in a Northern Pacific wet season from May to October (CSIRO et al., 2015; Schneider et al., 2014).

The SPCZ is a persistent, convective cloud band that stretches from Papua New Guinea in a south-easterly direction toward French Polynesia. In the north-western sector, the SPCZ merges with the ITCZ over the western equatorial Pacific warm pool (Vincent, 1994). The presence and northwest-southeast orientation of the SPCZ is controlled by underlying sea surface temperature (SST) gradients (van der Wiel et al., 2016; Widlansky et al., 2011), which determine the near-surface wind conditions that result in low-level moisture convergence (Ganachaud, 2014). The southwest Pacific wet season occurs from November to April when the westerly duct is present over the equatorial Pacific, leading to heightened activity in the SPCZ (Matthews, 2012; van der Wiel et al., 2016), and tropical cyclone activity for the southwest Pacific Islands and northeastern Australia (Magee et al., 2020).

The northern Australian wet season also occurs from November to April (austral summer) due to the influence of the Indo-Australian monsoon (Wang et al., 2014). From June to August the high-pressure zone moves over southern Australia, the south-east trade winds are over the South Pacific, and the SPCZ is weaker, bringing dry conditions to northern Australia and the southwest Pacific Islands (Vincent, 1994). In contrast, austral winter is southern and eastern Australia's wettest period of the year for, with precipitation resulting from extra-tropical weather systems (Gallant et al., 2012; Wright, 1997).

The Southern Annular Mode (SAM) describes (non-seasonal) variations in the position of the Southern Hemisphere mid-latitude (~ 40 – 50° S) storm track (Renwick & Thompson, 2006). During its positive phase, the SAM contracts poleward and is associated with relatively light winds and lower rainfall in New Zealand. In the opposite (negative) phase, the westerlies increase over New Zealand with greater windiness and storm activity (Renwick & Thompson, 2006). The relationship between the phases of SAM and southern Australian rainfall depends on the season and the latitude. Positive phases enhance summer rainfall over south-eastern and eastern Australia, and winter rainfall over eastern Australia, but suppress winter rainfall over south-eastern Australia. The reverse pattern occurs during negative phases (Gallant et al., 2012).

On inter-annual time scales, the climate of the region is influenced by the phases of the El Niño-Southern Oscillation (ENSO) and the Indian Ocean Dipole (IOD). For the Pacific Islands, periods of extreme wet and extreme dry are correlated to strengthening (La Niña) or weakening (El Niño) of the atmospheric pressure gradient (and associated trade winds) between the east and west

tropical Pacific (CSIRO et al., 2015). The SPCZ and ITCZ move away from the equator during La Niña events when zonal sea surface temperature gradients are strengthened, bringing dry conditions to the north-eastern Pacific Islands (van der Wiel et al. 2016; Werner et al. 2017). The southwest Pacific Islands and eastern Australia experience higher rainfall and more frequent tropical cyclones (Magee et al., 2020). For New Zealand, north-easterly wind patterns become more common bringing rainy conditions to northeastern areas of the North Island and reduced rainfall to the lower and western South Island (Thompson, 2006).

The ITCZ and SPCZ migrate equatorward during El Niño events when warm water from the warm pool moves eastward and decreases the zonal sea surface temperature gradient (van der Wiel et al. 2016). The southwest Pacific and eastern Australia experience dry conditions and tropical cyclones more frequently occur in the northeast Pacific (Magee et al., 2020). The relationship between eastern Australian rainfall anomalies and the strength of ENSO events is not linear, so the strength of a La Niña episode has a much greater influence on the occurrence of extreme high rainfall events than the strength of an El Niño episode on extreme low rainfall events (Gallant et al., 2012; King et al., 2013). For New Zealand, westerly winds in summer bring dry conditions to the east and more rain in the west during El Niño events (Thompson, 2006).

The Indian Ocean Dipole (often abbreviated to IOD), is an intrinsic interannual fluctuation in Indian Ocean sea surface temperatures, tends to occur synchronously with ENSO (Luo et al., 2010) and has been linked to the occurrence of extreme ENSO events (Hameed et al., 2018). Precipitation anomalies are enhanced over eastern Australia when La Niña/negative IOD (increased rainfall) or El Niño/positive IOD (suppressed rainfall) periods co-occur (Cleverly et al., 2016; Holgate et al., 2022). The IOD also affects northern Australian rainfall, with positive phases linked to decreased winter-spring rainfall, but minimal impact on the peak of the monsoon (Jourdain et al., 2013).

Large volcanic eruptions are a key source of global temperature variability on interannual to decadal timescales (Robock, 2005; Sigl et al., 2015). Changes in radiation due to volcanic emissions also affect the hydroclimate, suppressing the global water cycle (Robock, 2000; Timmreck, 2012), causing an El Niño-like sea surface temperature response in the Pacific (Stevenson et al., 2016) and weakening monsoon circulation (Liu et al., 2016; Man et al., 2014).

At longer timescales South Pacific climate is modulated by the Inter-decadal Pacific Oscillation (IPO), a low frequency (approximately 15-30 years) variation in Pacific sea surface temperatures and basin-wide circulation (Power et al., 1999), similar to the Pacific Decadal Oscillation (King et al., 2013). Changes in the phase of the IPO have been linked to significant changes in climate regimes across the wider Pacific Ocean. For example, the rapid transition from a negative (lower than average sea surface temperatures, a south-westerly shift of the SPCZ) to a positive IPO phase

(higher than average SST, north-easterly change of the SPCZ) during the mid-1970s was associated with a transition to an El Niño dominated period (McGree et al., 2016) with more severe droughts occurring southwest of the SPCZ (Ludert et al., 2018).

The IPO modulates the ENSO-extreme rainfall teleconnection over eastern Australia (Power et al., 1999). During IPO-negative phases, the relationships between La Niña events and extreme high rainfall and El Niño events and low rainfall, strengthen over eastern Australia. However, during IPO-positive phases, these relationships break down (King et al., 2013). During IPO-positive phases New Zealand experiences conditions similar to an El Niño event, with a climate more ‘La Niña-like’ during IPO-negative phases (Thompson, 2006). Several plausible mechanisms have been proposed to explain Pacific multidecadal variability, including slow westward propagating oceanic Rossby waves, changing concentrations of anthropogenic aerosols, and tropical-extratropical coupling of atmospheric and oceanic processes (Henley, 2017). However, recent studies have questioned the very existence of intrinsic low-frequency oscillations in SSTs, as distinguishable from climatic noise (Mann et al., 2020).

A significant contributing factor to the uncertainty around low-frequency Pacific climate variability is the relatively short and asymmetric coverage of observations (Henley, 2017); meteorological and oceanic data records are too short to fully capture multidecadal variability. Centuries-long tree-ring reconstructions can help us understand long-term multidecadal natural climate variability in South Pacific climate. The short meteorological data record does not only hamper efforts to identify low-frequency variability. Relatively little is known about historical and recent trends in hydroclimate, particularly for extreme events, due to the lack of records longer than a few decades. Again, tree-ring reconstructions can fill this gap by providing information on the occurrence, trends, and drivers of extreme events.

1.3 Tree-ring chronologies

The large-scale climate drivers described in Section 1.2 (ENSO, IOD, IPO) not only impact the climate of the South Pacific but are major drivers of precipitation variability worldwide (da Silva et al., 2011; Gershunov & Barnett, 1998; Lenssen et al., 2020; Rifai et al., 2019; Williams & Hanan, 2011). Pacific and Indian Ocean sea surface temperature variability affects the climate in different regions of the world via teleconnections - atmospheric or oceanic ‘bridges’ between climate variability in non-contiguous areas (Yang et al., 2018). In this thesis, teleconnections are leveraged to utilise remote tree-ring chronologies to reconstruct South Pacific hydroclimatic variability. In most of the following chapters, ENSO is the major driver of inter-annual variability in the case study region, and tree-ring chronologies are selected from regions that experience changes in climate during El Niño (Figure 1-2) and La Niña (Figure 1-3) phases of ENSO. However, as will be discussed in Chapter 5, remote tree-rings from the region are also impacted

by the Indian monsoon, which has a strong anti-correlation to precipitation in the Indo-Australian monsoon, providing climate insights beyond ENSO (Wang et al., 2014).

The tree-ring chronologies used in this thesis are nearly all publicly available¹ chronologies previously used in the development of the Monsoon Asia Drought Atlas (MADA; Cook et al., 2010), Eastern Australia and New Zealand Drought Atlas (ANZDA; Palmer et al., 2015), Mexican Drought Atlas (MXDA; Stahle et al., 2016), and South American Drought Atlas (SADA; Morales et al., 2020). These four regions all experience climate variability in response to ENSO phases. Climate variability in monsoon Asia has further been linked to phases of the IOD (Ummenhofer et al., 2013) whilst the South American climate is influenced by SAM (Morales et al., 2020).

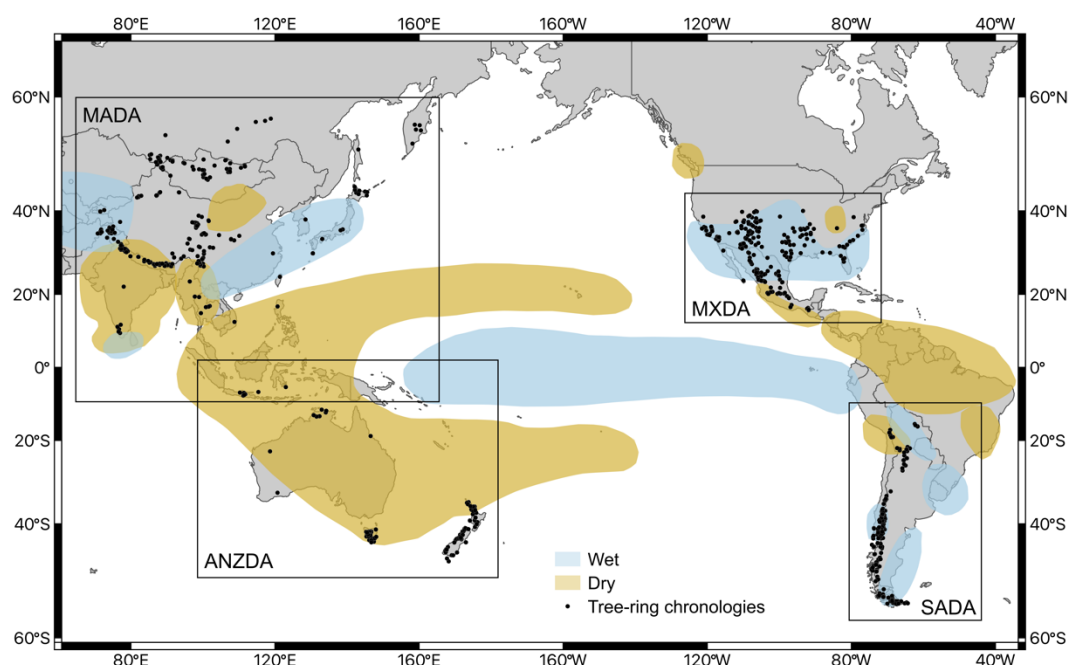


Figure 1-2 Publicly available tree-ring chronologies used in this thesis (black dots) compared to the typical ENSO-precipitation teleconnections during El Niño events. Regions with anomalous precipitation during El Niño events from 1951–2016 were derived from the probabilistic estimates of Lenssen et al. (2020). Further information on the seasonality of the teleconnections is provided in Figure 1 of Lenssen et al. (2020).

¹ Unpublished chronologies incorporated into the reconstructions are listed in the relevant chapters.

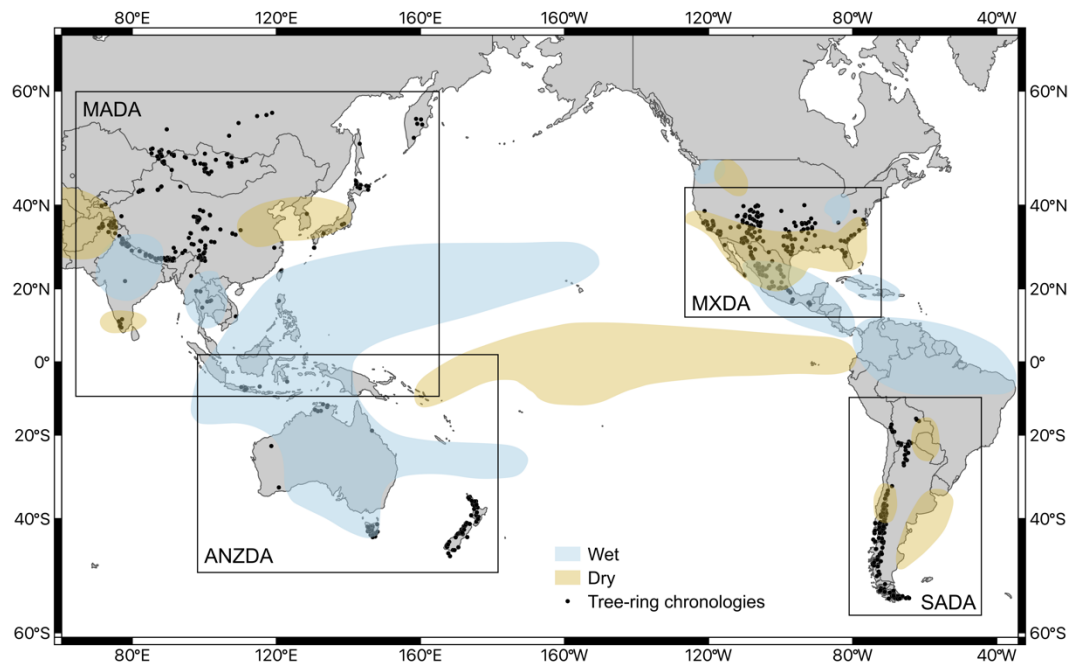


Figure 1-3 Publicly available tree-ring chronologies used in this thesis (black dots) compared to the typical ENSO-precipitation teleconnections during La Niña events. Regions with anomalous precipitation during La Niña events from 1951–2016 were derived from the probabilistic estimates of Lenssen et al. (2020). Further information on the seasonality of the teleconnections is provided in Figure 2 of Lenssen et al. (2020).

1.4 Thesis aims

This thesis aims to reconstruct past climate in the South Pacific region using tree-ring chronologies. However, these climate reconstructions are underpinned by relatively short instrumental climate records. This then requires the careful examination of the associated uncertainty around past and future trends in hydroclimate, and the occurrence of extremes. Specifically, the thesis addresses this uncertainty around past and future climate trends and extreme events by:

- i. Investigating existing and novel methods to reconstruct hydroclimatic variables in Australia and the South Pacific considering the region's unique challenges.
- ii. Describing past climate in Australia and the South Pacific using tree-ring reconstructions and assessing results in terms of major climate drivers.
- iii. Identifying the occurrence and frequency of extreme events in the paleoclimate record to contextualise extremes in the instrumental period.
- iv. Demonstrating the value of tree-ring reconstructions for water management by translating paleoclimate data into decision-relevant formats.

1.5 Paleoclimate reconstructions

Five examples of paleoclimate reconstructions (Chapters 2-6) are used to address the specific aims of this thesis. Each case study develops, describes, and analyses a tree-ring reconstruction of an aspect of the South Pacific hydroclimate. The geographical target of each case study, in relation to the climate drivers of the region described in Section 1.2, is shown in Figure 1-4.

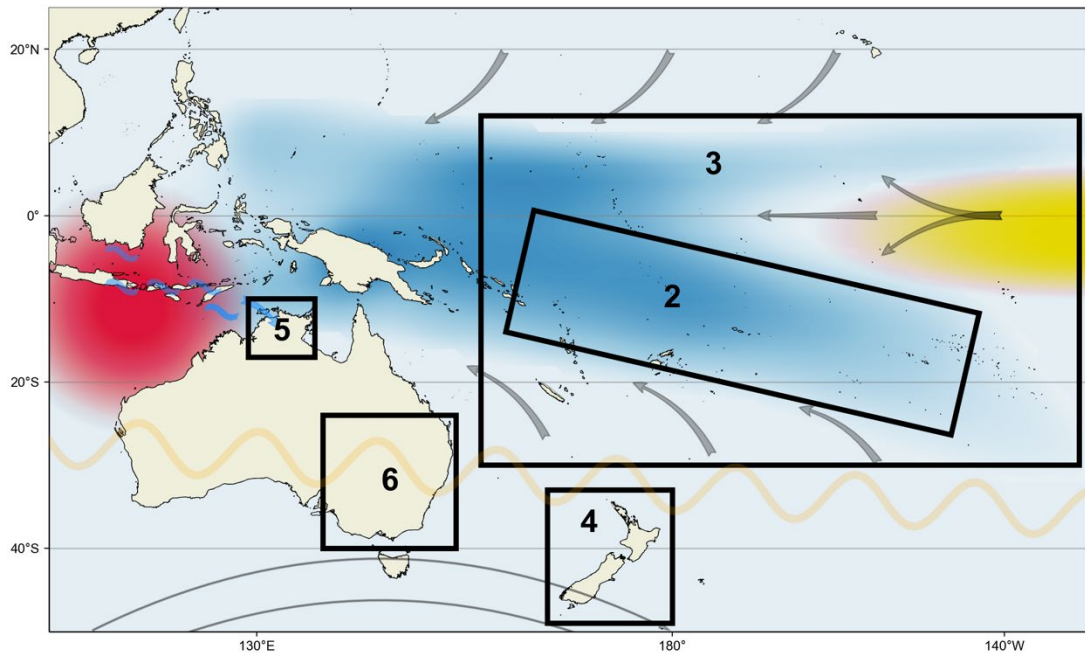


Figure 1-4 The five reconstructions explored in Chapters 2-6: 2) Variability in the position of the South Pacific Convergence Zone; 3) South Pacific Island drought; 4) New Zealand temperature response following volcanic eruptions; 5) A monsoon river reconstruction for the Daly River, Australia; 6) Past and future streamflow in the Murray-Darling Basin, Australia.

Chapters 2 to 4 utilise existing methods for tree-ring reconstructions and consider how they can best be applied to the South Pacific region, considering the unique challenges of very short data records, data gaps, and the lack of annually resolved terrestrial proxies. The past climate of the South Pacific is described and assessed in terms of major climate drivers.

- South Pacific Island communities experience significant rainfall variability between seasons and years, due to changes in the average position and intensity of the South Pacific Convergence Zone (SPCZ), the largest rain belt in the Southern Hemisphere. Lower frequency variability is also present in the SPCZ; however, this variability is poorly understood because data records from the region are too short. **Chapter 2** presents a millennial-length reconstruction of the SPCZ and explores potential drivers of multidecadal variability over the past 1300 years including volcanic eruptions and solar forcing. The SPCZ reconstruction provides a ‘proof of concept’ for using a trans-Pacific network of remote tree-ring proxies for reconstructing hydroclimatic variables for the South Pacific region.

- Following on from this work, in **Chapter 3** the remote tree-ring methodology is extended, exploring spatial drought reconstructions for the South Pacific Islands using a circum-Pacific network of tree rings. Small Pacific Islands are particularly susceptible to droughts compromising water availability, food security, public health, and economic activity. A major cause of droughts is shifts in the mean position of the convergence zones, modulated by interannual fluctuations in ENSO. The chapter analysis shows how spatial reconstructions can be used to inform on past climatic variability using a supervised machine learning algorithm, focusing on extreme El Niño events. If successful, the drought reconstructions would represent the only continuous pre-1950s climate data available for many Pacific Islands, providing a unique opportunity to both contextualise the instrumental data period and address some of the uncertainties resulting from the short data record.
- Large volcanic eruptions can have a major impact on temperature and hydroclimate variability on interannual to decadal timescales. However, little is known about their impact on the climate of the low to mid-latitudes of the Southern Hemisphere. In Chapter 2, a small but observable volcanic signal was identified in tree rings from New Zealand, conflicting with previous studies which found no volcanic impact. In **Chapter 4**, this finding is investigated in detail. The study explores potential species and site-specific factors that influence the expression of volcanic signals in tree rings from eight New Zealand dendrochronological species. The influence of large eruptions on New Zealand's average temperature is also explored through two new tree-ring temperature reconstructions. This case study contributes to the broader question of how large volcanic eruptions impact Southern Hemisphere climate, which is key to understanding existing discrepancies between paleo-reconstructions and climate models.

The final two technical chapters focus on how remote tree-ring reconstructions can provide decision-relevant information for water managers, producing paleo-streamflow reconstructions for two important catchments in Australia. New methods are proposed to address some of the limitations identified for applying existing methods for climate reconstructions in the South Pacific region.

- Streamflow in Australia's northern rivers has been steadily increasing since the 1970s, most likely due to increased intensity in the Indo-Australian monsoon. However, because of limited data availability, it is hard to assess this recent trend and therefore contextualise potential future climatic changes. **Chapter 5** considers how local and remote tree-ring proxies can be used in conjunction to reconstruct monsoon streamflow for the Daly River, incorporating a novel pre-reconstruction step that adjusts the variance spectra of the tree

rings to that of streamflow. As the available gauge data records are short and non-continuous, we developed our streamflow reconstructions using Hierarchical Bayesian Regression and a ‘moving-block’ calibration and verification scheme. These methodological advancements resolve some of the challenges discussed for the drought reconstructions in Chapter 3. The 600-year record of paleo-streamflow is used to contextualise the very short instrumental period and to highlight the risk associated with determining future water allocations using only recent data.

- Chapter 5 demonstrates the benefits of using paleo data for water management. The natural extension of this work is to combine paleo-reconstructions with climate model outputs to better understand the potential impacts of climate change on water resources. **Chapter 6** proposes a method for producing both past reconstructions and future projections of streamflow from gridded records of the Palmer drought severity index. The chapter analysis demonstrates how paleoclimate reconstructions can be used to contextualise the severity of past drought events and help understand how the likelihood of such events may change in the future due to climate change. Joint distribution models are used to derive numerical probability statements about drought occurrence which can help inform science-based management and policy decisions.

Finally, **Chapter 7** provides a summary and conclusions of the body of work and outlines the future research opportunities. Chapters 2, 4, and 5 are reproduced, with minor formatting changes, from a series of published journal articles; the data, methods, results, and analysis undertaken for each case study are presented in the associated chapters. Along with this introduction, a chapter-specific literature review is presented at the beginning of each chapter.

Chapter 2 One thousand three hundred years of variability in the position of the South Pacific Convergence Zone

The content in this chapter has been reproduced (with reformatting) from the following journal paper:

Higgins, P. A., Palmer, J. G., Turney, C. S. M., Andersen, M. S., & Cook, E. R. (2020). One Thousand Three Hundred Years of Variability in the Position of the South Pacific Convergence Zone. *Geophysical Research Letters*, 47(17), 1–11. <https://doi.org/10.1029/2020GL088238>.

2.1 Abstract

The South Pacific Convergence Zone (SPCZ) is the largest rain belt in the Southern Hemisphere and a key driver of precipitation variability, impacting South Pacific island communities. Our millennial-long reconstruction is based on a trans-Pacific tree-ring network, containing chronologies sensitive to changes in the SPCZ because of its pervasive nature, spatial extent, and link to the El Niño-Southern Oscillation. The reconstruction explains 58% of variance in the instrumental SPCZ index from 1911–1998. El Niño-Southern Oscillation cycles are identified throughout the reconstruction period. Multidecadal periodicities wax and wane, coinciding with a sustained eastward shift during the Medieval Climate Anomaly (~1000–1200 CE). We find large volcanic eruptions increased the tendency for the SPCZ to be displaced eastward. The reconstruction helps improve our understanding of past hydroclimatic behaviour in the southwest Pacific and can be used to validate general circulation model projections for Pacific Island communities and the wider region in the 21st century.

2.2 Plain Language Summary

South Pacific Island communities experience significant variability in their rainfall between seasons, across years, and between decades. This variability is due to changes in the average position and intensity of the South Pacific Convergence Zone (SPCZ), the largest rain belt in the Southern Hemisphere. The SPCZ tends to move from east to west in response to changes in sea surface temperatures and winds that accompany the El Niño-Southern Oscillation. Lower frequency variability is also present in the SPCZ; however, this variability is poorly understood because data records from the region are too short. In this research, we extended the record of SPCZ variability back in time to 700 CE using a statistical model based on moisture-sensitive tree-ring records from both sides of the Pacific. We analysed the SPCZ reconstruction during periods when the average climate conditions were different from today and assessed the impact that changes in solar output and volcanic eruptions may have had during these periods.

This research helps us to understand the long-term behaviour of the SPCZ, which is essential to understand how it may change under future climate conditions.

2.3 Introduction

The South Pacific Convergence Zone (SPCZ), a convective cloud band stretching from the Western Pacific Warm Pool toward French Polynesia (Trenberth, 1976; Vincent, 1994), is the largest rain band in the world during austral summer (December–February). The extensive and pervasive nature of this climate feature means the SPCZ plays a major role in South Pacific cyclogenesis and rainfall (Vincent et al., 2011) and a significant role in global-scale circulation (Vincent, 1994), influencing the ocean freshwater budget, cross-equatorial flow (Lorrey et al., 2012; Matthews, 2012), and circulation patterns across the southern oceans (Clem et al., 2019; Clem & Renwick, 2015). The presence and northwest-southeast orientation of the SPCZ is controlled by underlying sea surface temperature (SST) gradients (van der Wiel et al., 2016; Widlansky et al., 2011), which determine the near-surface wind conditions that result in low-level moisture convergence (Ganachaud, 2014). Precipitation in the SPCZ is triggered by transient Rossby waves originating from the Australian subtropical jet, which are deflected toward the upper tropospheric westerlies in the equatorial eastern Pacific, elongating in a northwest-southeast direction and triggering convection, forming the distinctive “diagonal” component of the rain band (Matthews, 2012; van der Wiel et al., 2016; Widlansky et al., 2011).

Due to strong precipitation gradients in the vicinity of the SPCZ, even small shifts in its mean position can result in dramatic changes in precipitation across the region, impacting the small, South Pacific islands communities under its influence (Vincent et al., 2011). The position and intensity of the SPCZ are moderated by the El Niño-Southern Oscillation (ENSO) on interannual timescales (Harvey et al., 2019; van der Wiel et al., 2016; Vincent, 1994). During strong El Niño events the SPCZ can shift up to 10° of latitude toward the equator, becoming zonally orientated (Cai et al., 2012). For instance, during the 1997–1998 El Niño event, record low streamflow was recorded in Fiji, along with widespread and sustained damage to agriculture (Terry & Raj, 2002), while the strong 2010–2012 La Niña was associated with severe water shortages, crop failure, and economic impacts for Tuvalu, hundreds of kilometres to the north (McGree et al., 2016).

On decadal to multidecadal timescales variation in Pacific SSTs related to the Interdecadal Pacific Oscillation (IPO) modulates ENSO teleconnections within the SPCZ region (Folland et al., 2002; McGree et al., 2016). Changes between the positive (El Niño-like) and negative (La Niña-like) phases of the IPO influence the mean SPCZ position and thus decadal climate variability in region, both in terms of average precipitation and the frequency of extremes (Salinger et al., 2014). However, there is little knowledge of SPCZ variability prior to the start of meteorological

observations at ~1890 CE. The data record does not fully capture multidecadal variability, leading to considerable uncertainty around past and future SPCZ behaviour and impacts.

Climate models suggest increased drying in the south-eastern branch of the SPCZ under emission scenarios SRES A1B and RCP8.5 and moderate ($\sim 1\text{--}2^\circ\text{C}$) SST warming (Dutheil et al., 2019; Widlansky et al., 2013), increased ENSO-driven precipitation variability (Power et al., 2017), and an increase in the frequency of extreme zonal SPCZ events (Cai et al., 2014, 2012). However, many models exhibit large biases in western Pacific SSTs, influencing the modelled position and movement of the SPCZ, thus limiting confidence in projections (Brown et al., 2013, 2015; Dutheil et al., 2019; Grose et al., 2014). In the absence of instrumental records, there is a need for SPCZ proxy reconstructions extending back to periods with different climate conditions to the instrumental period (Partin et al., 2013) which can provide a constraint on climate models. Here we present the first millennial-length paleoclimate proxy network reconstruction of the SPCZ, providing a record of variability in the southwest Pacific, capturing behaviour during both the periods described as the Medieval Climate Anomaly (MCA; ~1000 to 1200 CE) and Little Ice Age (LIA; (~1450 to 1850 CE).

2.4 Methods

2.4.1 The Instrumental SPCZ Index

The SPCZ index (SPCZI; Salinger et al., 2014) is a mean sea level pressure-based (MSLP) index which captures monthly east-west variations in the position of the SPCZ. The SPCZI is derived from the MSLP difference between Apia, Samoa ($13^\circ 48'\text{S}$, $171^\circ 48'\text{W}$), and Suva, Fiji ($18^\circ 9'\text{S}$, $178^\circ 26'\text{E}$), normalised to the 1933–1992 period. The index is positive when the SPCZ moves east of its mean position toward Apia during El Niño events and IPO positive years, and negative when it is displaced westward toward Suva during La Niña events and IPO negative years. The SPCZI replaced the older SPCZ position index (SPI; Folland et al., 2002) based on the same station pair, using higher quality MSLP data and extending the index forward in time from 1999 to 2019. As a point index, the SPCZI does not capture the full extent of zonal El Niño events when significant north-south movement occurs (Salinger et al., 2014; E. M. Vincent et al., 2011).

2.4.2 Predictor Selection and Reconstruction

Climate proxies were selected from a trans-Pacific network of 428 precipitation-sensitive tree-ring chronologies underlying two recently published drought atlases—the Eastern Australia and New Zealand Drought Atlas (ANZDA; Palmer et al., 2015) and the Mexican Drought Atlas (MXDA; Stahle et al., 2016). The tree-ring network includes chronologies from Australia, New Zealand, and Indonesia on the south-western border of the Pacific, and from Mexico, the southern United States and western Guatemala to the east, two clusters from approximately opposite sides of the Pacific Ocean. Both atlases have been shown to have strong teleconnections to the South

Pacific region (Figure A-1), with drought in the ANZDA strongly linked to El Niño events and, conversely, La Niña events associated with drought in the MXDA (Cook et al., 2018). To reconstruct the November to April (Nov-Apr) SPCZI, we used a nested, principal components-based regression method, point-by-point regression (PPR; Cook et al., 1999, 2007, 2010). The Nov-Apr window was selected to coincide with the tropical South Pacific wet season, when the westerly duct is present over the equatorial Pacific, leading to heightened activity in the SPCZ (Matthews, 2012; van der Wiel et al., 2016). The reconstruction window aligns within the Austral warm growing season and to winter-spring precipitation in Mexico, which is modulated by Pacific SSTs (Cleaveland et al., 2003; Stahle et al., 2016).

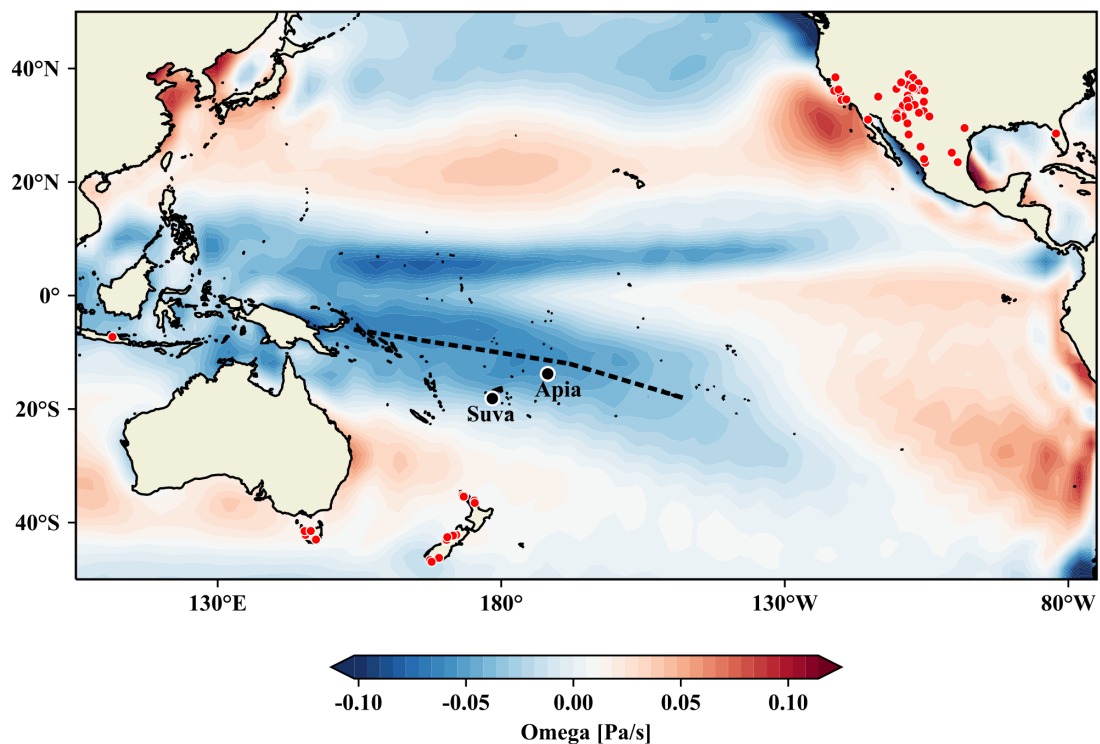


Figure 2-1 Location of the tree-ring predictors selected for the reconstruction (red circles) and the mean Nov-Apr position axis of low-level convergence (SPCZ, black dashed line) based on the twentieth Century Reanalysis v3 data set Omega at 500 hPa 1911–1998 (Lorrey et al., 2012). The black circles show the locations of Suva, Fiji, and Apia, Samoa, the MSLP stations used to calculate the instrumental SPCZI (Salinger et al., 2014).

While other paleoclimate records (such as Antarctic ice cores, e.g., Vance et al., 2015; and coral, e.g., Linsley et al., 2006; and speleothem records, e.g., Partin et al., 2013; from the SPCZ region) may provide predictors of the SPCZ position, only replicated chronologies precisely dated at absolute annual resolution were included in the predictor pool. Reconstructions based on PPR typically include a search radius limiting predictor selection to those closely located to the reconstruction target (Cook et al., 1999; Stahle et al., 2016). The lack of tree-ring chronologies from the South Pacific region necessitated the removal of the search radius from the predictor selection. Remote tree-ring proxies have been shown to skilfully reconstruct major climate drivers

(Buckley et al., 2019; Cook et al., 1999; Palmer et al., 2015), but implicitly assume that local-remote climate teleconnections are stationary. Predictors were limited to tree-ring chronologies with a significant relationship ($P \leq 0.1$) to instrumental SPCZI. The final reconstruction was based on 95 tree-ring chronologies, 59 from the MXDA and 36 from the ANZDA (Figure 2-1).

2.4.3 Calibration and Verification

The SPCZI reconstruction (SPCZI_r) captures 58% of the variation in the instrumental SPCZI (Figure 2-2) as estimated by the PPR regression model fitted to the entire instrumental period (1911–1998). The last year of the calibration period was limited to 1998 which is the end date of many of the New Zealand tree-ring chronologies. Using the entire instrumental period follows a similar approach described by Briffa et al. (1990) and is better able to capture twentieth century SPCZI extremes. Those same selected tree-ring chronologies were then subjected to standard 50/50 split calibration and verification tests (Figure A-2, Table A-1). The verification tests included the reduction of error (RE) and coefficient of efficiency (CE; Cook & Kairiukstis, 1990). In general, RE and CE values greater than zero indicate some reconstruction skill (Fritts, 1991). The very strong RE and CE test results clearly demonstrate that despite the remoteness of the tree-ring proxies from the Southwest Pacific, they are able to capture east-west movement in the SPCZ. The reconstruction was then independently verified against composite local coral proxy records from the SPCZ region (Bagnato et al., 2005; Linsley et al., 2006, 2008; Table A-2). The reconstruction shows good fidelity with coral records during both the instrumental and pre-instrumental periods (Table A-2), further demonstrating the ability of the reconstruction to represent local hydroclimate.

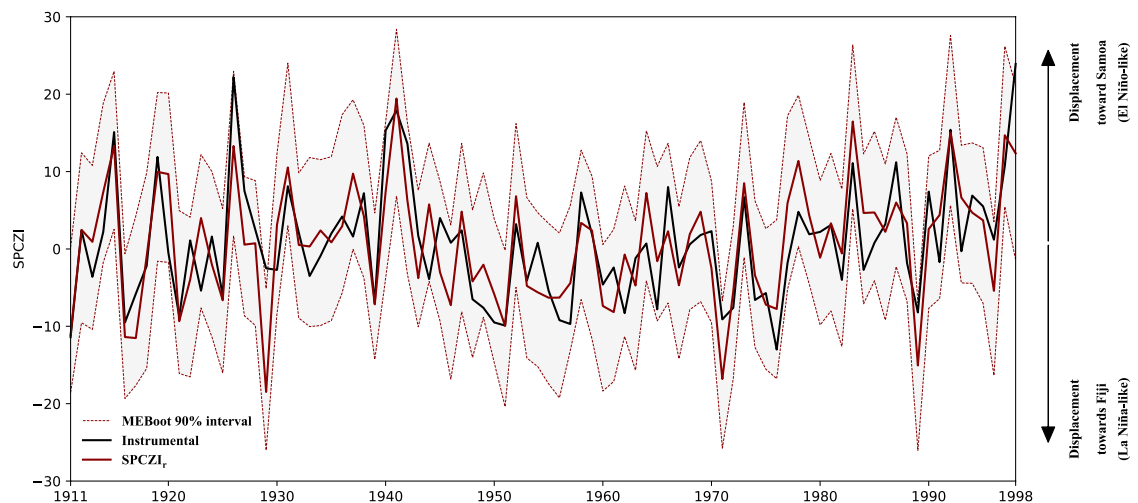


Figure 2-2 Comparison of the instrumental SPCZI and SPCZI_r over the calibration period (1911–1998). The instrumental SPCZI is shown in black, SPCZI_r is shown in red, and the grey bars show the 5–95% bootstrap confidence interval of the reconstruction.

The reconstruction has a strong and statistically significant correlation to the Nov-Apr Niño-3.4 index ($R = 0.71$, $P < 0.001$), IPO index ($R = 0.73$, $P < 0.001$), and the Henley et al. (2015) tripole IPO index ($R = 0.75$, $P < 0.001$). These correlations are of similar magnitude and significance as found between the instrumental SPCZI and climate indices (Salinger et al., 2014). Further verification is provided by the ability of the SPCZI reconstruction to accurately capture the regime shift from negative to positive IPO in 1977–1978. Regime shift analysis (Rodionov & Overland, 2005) also captures the earlier shift to negative IPO that occurred in 1943–1944, however, it is attributed to 1947 in the reconstruction.

2.5 Results and Discussion

Wavelet analysis (Figure 2-3; Torrence & Compo, 1998) reveals persistent concentrations of power in the inter-annual band corresponding to ENSO periodicities (~3–8 years), significant above an AR(1) red noise model ($P < 0.05$). Significant multidecadal periodicities (~55 years), with power concentrated between 1000 and 1400 CE in the wavelet spectrum, are also identified, corresponding to the core warming period (1000–1200 CE) of the MCA (Lüning et al., 2019), and the following two centuries. During this period, lower than average variance in the ENSO band can be observed, along with an increase in the frequency of both extreme, multiyear eastward and westward shifted SPCZ events (see Appendix A). The period ~1050–1130 CE, falling in the middle of the MCA, is a period of sustained anomalously high average SPCZI. This suggests that the MCA was characterised by an eastward shifted SPCZ and drier than average conditions in the southwest Pacific. The first 30 years of this eastward-SPCZ_r period (~1060–1090) has the second highest average values of the reconstruction, eclipsed only by the 20-year period from ~1310–1330 CE.

There are very few millennial-length paleoclimate proxy records from the Southern Hemisphere which can contribute to our understanding of the climate during the MCA (Emile-Geay et al., 2017; Lüning et al., 2019). Those available suggest the period was characterised by higher-than-average temperatures and predominantly positive IPO (Lüning et al., 2019; Vance et al., 2015). A relatively warm and dry southwest Pacific is consistent with sediment records from the eastern and western equatorial Pacific (Conroy et al., 2009; Moy et al., 2002; Tierney et al., 2010) which suggest an El Niño-like mean state during the MCA. However, this conflicts with noncontinuous coral records (Cobb et al., 2003; Y. Liu et al., 2017), sediment cores (Khider et al., 2011; Rein et al., 2004), and modelling studies (Mann et al., 2005) which found cool, La Niña-like eastern Pacific SSTs during the MCA, consistent with the “ocean thermostat” model of heating (Clement et al., 1996). Several possible explanations could account these discrepancies, including dating or analysis errors in some proxy records, misattribution of regional climate effects to global climate drivers, different seasonal reconstruction targets, or nonstationarity in the relationship between ENSO and past hydroclimate variability across the Pacific (Tierney et al., 2010). The basis of the

SPCZI reconstruction on a trans-Pacific network of tree-ring records gives us confidence that we capture basin-wide patterns of variability and not localised effects. However, we cannot discount that the shift in the axis of convergence of the SPCZ during the MCA could be the result of changes in ocean-atmospheric patterns unrelated to ENSO.

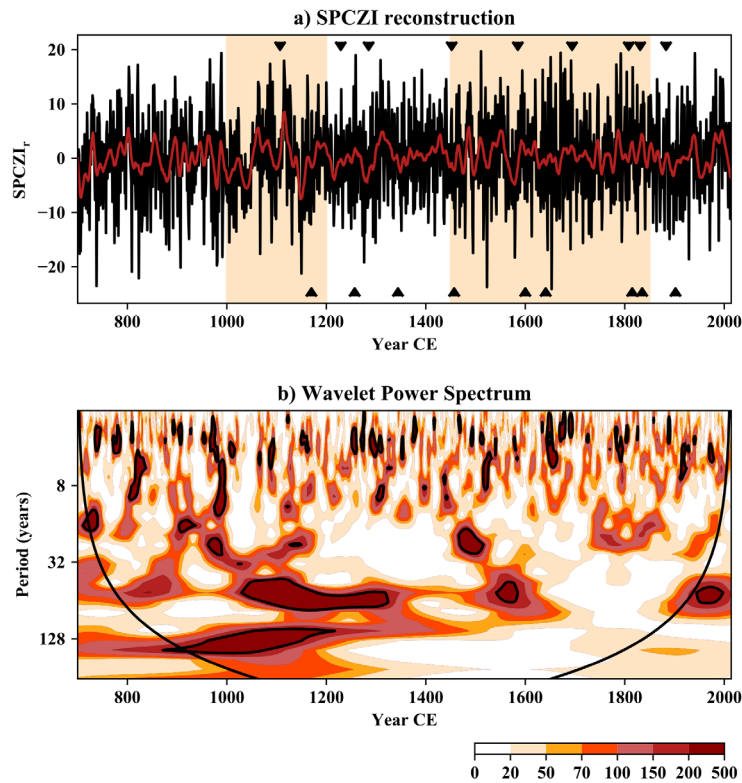


Figure 2-3 (a) SPCZI_r from 700 to 1998 CE. The red line shows the smoothed reconstruction using a 13-year Gaussian low pass filter, bands indicate the approximate timing of the MCA and LIA and triangles represent the timing of large volcanic eruptions; (b) wavelet spectrum of the SPCZI reconstruction (Torrence & Compo, 1998). Black contours indicate power above the 95% confidence interval when using an AR(1) red noise model.

By contrast, the LIA (~1450 to 1850 CE; Ahmed et al., 2013; Grove, 1988), a period of relatively cool temperatures and glacial advance in the Northern Hemisphere, is not discernible in the SPCZI reconstruction. The LIA is sometimes considered to be a Northern Hemisphere-only phenomenon due to the difficulty in identifying its effects in Southern Hemisphere climate proxies and large differences in timing and magnitude observed between regions (Chambers et al., 2014; Jones et al., 2009; Putnam et al., 2012). Cooling is commonly attributed to the combined effects of increased volcanic forcing and decreased solar sunspot activity, particularly during the Maunder Minimum (Ahmed et al., 2013; Jones et al., 2009; Miller et al., 2012). To explore the possible role of these proposed drivers, we investigate whether volcanic or solar forcing contribute to variability in the SPCZ reconstruction.

2.5.1 Response to Volcanic and Solar Forcing

Large volcanic eruptions can eject sufficient gases, aerosols, and particles into the stratosphere to reduce solar insolation, cooling the Earth's surface (Robock, 2000). Past studies have linked changes in major circulation patterns, including the phase of ENSO, to tropical volcanism (Adams et al., 2003; Christiansen, 2008; Emile-Geay et al., 2008; McGregor & Timmermann, 2011; Miao et al., 2018). While most studies based on observations and proxy data find an increased likelihood of an El Niño event following a large volcanic eruption, modelling studies are yet to reach a consensus on the mechanisms behind the linkage (Khodri et al., 2017). If the SPCZ_r results are consistent with previously observed paleoclimate “volcano-El Niño” linkages, a positive (eastward shifted) SPCZ_r would follow a large eruption. We tested this hypothesis using superposed epoch analysis (SEA), a composite analysis technique extensively used to identify the impacts of external perturbations on climate (e.g., Adams et al., 2003; D'Arrigo et al., 2009; Dätwyler et al., 2019; Handler, 1984; F. Liu et al., 2016; Meehl & Arblaster, 2009), following the “double-bootstrap” methodology of Rao et al. (2019), which addresses many of the criticisms of SEA as a statistical tool (Adams et al., 2003; Haurwitz & Brier, 1981). Large tropical volcanic eruption key years since 700 CE were identified from the eVolv2k volcanic stratospheric sulphur injection (VSSI) database, with selection criterion VSSI > 10 Tg [S] (Toohey & Sigl, 2017).

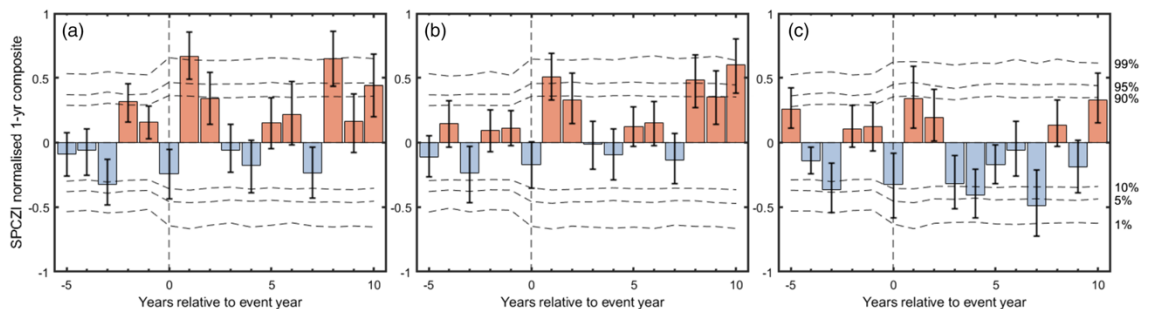


Figure 2-4 Normalised SPCZIr SEA results for large tropical volcanic eruptions since 700 CE. Results are shown for the reconstruction presented in this paper (a), and for SPCZIr based on the subset of tree rings from the Northern Hemisphere (b) and Southern Hemisphere (c). The vertical bars show the 5th to 95th percentiles of the SPCZIr response based on 1,000 unique draws of key years, while the dashed horizontal lines indicate the threshold for epochal anomalies to be statistically significant using random bootstrapping. Positive values indicate an eastward-shifted SPCZ.

Of the 20 large volcanic events identified during the reconstruction period, El Chicon in 1982 and Pinatubo in 1991 postdate the start of a known El Niño event and were therefore excluded from analysis. The mean SEA result of the remaining 18 eruptions shows a significant (99%) tendency toward an eastward shifted SPCZ_r the year following an eruption (Figure 2-4a). The 5th–95th percentile result, which represents variability in the response to volcanic events based on 1000 unique draws of key years, is also significant ($P < 0.05$) at $t + 1$ years. SPCZ_r rebounds to a westward shifted SPCZ_r 3–5 years post event, consistent with the findings of Adams et al. (2003),

with the significant eastward shift in the SPCZ 8 years post event likely representing the return of the system to its irregularly periodic state.

While volcanic signals in tree-ring proxy data sets from the Northern Hemisphere have been extensively studied (e.g., D'Arrigo et al., 2009, 2013; Mann et al., 2012; Scuderi, 1990), Southern Hemisphere data sets have not been widely investigated (Palmer & Ogden, 1992). We tested whether a similar volcanic impact could be identified in both the Northern and Southern Hemisphere tree rings by reconstructing SPCZI using proxies from a single hemisphere. Figure 2-4b shows that the Northern Hemisphere chronologies drive most, but not all, of the volcanic signal in the combined reconstruction at $t + 1$ years. While the volcanic impact at $t + 1$ years is not significant in the Southern Hemisphere-only reconstruction, the combined reconstruction responds more strongly and consistently to volcanic events than the Northern Hemisphere-only reconstruction.

The location, seasonality, and distribution of volcanic aerosols in relation to the location and growing season of the Southern Hemisphere chronologies contributes to the minimal response seen in year $t + 1$ (Adams et al., 2003; Zanchettin et al., 2019). Additionally, regional and species variations in volcanic response (see Appendix A) mute the Southern Hemisphere signal. Conversely, the Southern Hemisphere-only reconstruction shows a stronger ($P < 0.1$) shift toward a La Niña-like SPCZ _{τ} 3–5 years after a volcanic event, likely due to the tree ring wet bias, where a stronger signal is recorded in a wet year, which occurs when the SPCZ is westward of its mean position for the Southern Hemisphere and hence toward the location of the sampled trees. Figure 2-4 demonstrates that the trans-Pacific network of tree rings underpinning the reconstruction produces a more robust and less biased reconstruction than can be produced from either the ANZDA or MXDA chronologies alone.

Variations in solar intensity have also been proposed as a cause of decadal-scale variability in the SPCZ region (Meehl et al., 2008; Meehl & Arblaster, 2009; van Loon et al., 2007). We find no consistent response to variation in total solar irradiance associated with the ~11-year Schwabe sunspot cycle. Analysis using SEA (see Appendix A) suggests no response to the Schwabe cycle in either the Northern Hemisphere or Southern Hemisphere tree-ring chronologies, and we conclude that the 11-year periodicity identified by wavelet and multitaper spectrum analysis is not linked to the solar cycle, but rather to internal variability in the ocean-atmosphere system. Reduced sunspot activity associated with the Maunder Minimum (1645–1715 CE) is not distinguishable in the reconstruction, although a strong multiyear La Niña-like event did occur from 1667–1670 CE. The lack of solar fingerprinting on the SPCZ and the short-term impact of large volcanic events might explain why LIA cooling is not discernible in the SPCZI _{τ} .

2.5.2 Paleoclimate Implications

If the reconstruction accurately captures movements of the SPCZ in pre-instrumental times, the eastward shift identified during the MCA period could have important implications for our understanding of colonization processes in East Polynesia. While the drivers of Polynesian migration are not known (Goodwin et al., 2014), paleoclimate evidence suggests that changing hydroclimatic conditions and prolonged drought may have instigated eastward exploration (Sear et al., 2020). A recently published synthesis of high precision radiocarbon samples from the region has narrowed the phases of colonization down to two periods, the earliest representing colonization of the Society Islands from Samoa during ~1025–1120 CE, followed by migration to the outer islands from ~1190–1290 (Wilmshurst et al., 2011). The “ENSO hypothesis” of maritime migration between the Pacific Islands proposes that periods of increased frequency of strong El Niño events and consequently reduced strength in the easterly trade winds in the central Pacific provided windows of opportunity for eastward migration without the need for windward sailing technology (Anderson et al., 2006). For the early migration window this hypothesis is strongly supported by the SPCZI_r, which suggests climatic conditions during the MCA would have contributed to prolonged drought in West Polynesia and may have eased eastward travel. The wind field reconstruction of Goodwin et al. (2014) also supports this hypothesis, identifying two multidecadal intervals with persistent westerly wind anomalies during this period. The later migration window is characterised by periods with both an eastward and westward shifted SPCZ_r, with no significant difference from the long-term average (two-sided Student's *t* test).

2.6 Conclusions

We present a robust 1300-year reconstruction of precipitation variability in the SPCZ region which explains 58% of the variance in the November–April instrumental SPCZI data and provides context to the instrumental period. During the MCA (1,000–1,400 CE), the main axis of convergence in the SPCZ was to the east of the current position, suggesting a period of sustained dry conditions in the Southwest Pacific. The distinct SPCZ behaviour during the MCA, when the climate was warmer on average than during the instrumental period, can be used to assess general circulation model projections for Pacific Island communities and the wider region. Discrepancies between the SPCZI reconstruction and proxy records from the eastern Pacific during the MCA highlight the complexity of interpolating regional climate patterns and trends from local records, and the need for additional high-resolution proxy records from the Southern Hemisphere.

2.7 Acknowledgments

The November–April average SPCZI is available in Appendix A of Salinger et al. (2014). Kind thanks to S. McGree and J. Salinger for providing the extended SPCZI data set. We also wish to thank Scott Power and two anonymous reviewers for their helpful comments

that have greatly improved the paper. PAH is supported by an Australian Government Research Training Scholarship and the UNSW Scientia PhD Scholarship Scheme. Further support provided by the ARC Centre of Excellence in Australian Biodiversity and Heritage (CE170100015) and the Lamont-Doherty Earth Observatory contribution number 8439.

2.8 Conflict of Interest

The authors declare that they have no competing financial interests.

2.9 Data Availability Statement

All tree-ring chronologies included in the reconstruction and the output SPCZIr presented in this paper are publicly available from the NOAA/World Data Service for Paleoclimatology archives (<https://www.ncdc.noaa.gov>). The 20th Century Reanalysis V3 data were provided by the NOAA/OAR/ESRL PSD, Boulder, Colorado, United States, from their website (<https://www.esrl.noaa.gov/psd/>).

Chapter 3 Towards a drought atlas for the South Pacific

3.1 Abstract

Understanding drought occurrence and trends across the South Pacific islands is limited by the paucity of long meteorological records. The South Pacific Drought Atlas (SPaDA), a new paleoclimatic reconstruction of South Pacific hydroclimate based on tree-ring chronologies, is presented to partially fill this gap. The SPaDA is based on a trans-Pacific network of tree rings, made possible by the teleconnections between the El Niño-Southern Oscillation (ENSO), the major driver of inter-annual precipitation and drought in the Pacific, and four dendrochronological regions. Instrumental-period ENSO events and four historical droughts are accurately reproduced by the SPaDA demonstrating its strong reconstruction ability back to the 1780s. A random forest classifier, a supervised machine learning algorithm, was used to identify modes of ENSO variability in the pre-instrumental reconstruction period, providing a multi-centennial context for their occurrence. The Chapter concludes with several suggestions to improve future iterations of the SPaDA and produce robust, long term drought reconstructions for the South Pacific islands.

3.2 Introduction

Small Pacific Islands are particularly susceptible to droughts which compromise water availability, food security, public health, and economic activity (Annamalai et al., 2015; Barkey & Bailey, 2017). In the South Pacific, the spatial distribution of precipitation – and precipitation deficits – is strongly controlled by the position and movement of two large bands of low atmospheric pressure, the Intertropical Convergence Zone (ITCZ) and the South Pacific Convergence Zone (SPCZ), see Figure 1-1. Shifts in the mean position of these convergence zones, modulated by interannual fluctuations in the El Niño-Southern Oscillation (ENSO) and longer-term variability from the Interdecadal Pacific Oscillation (the IPO) (Power et al., 1999), strongly influence moisture availability across the region (Ludert et al., 2018; McGree et al., 2016).

Generally, an equatorward movement of the convergence zones during El Niño events and positive phases of the IPO results in dry conditions in the southwestern Pacific. Conversely, during La Niña events and negative IPO phases, the SPCZ and ITCZ move away from the equator, making drought conditions more likely for those South Pacific islands lying at the northeast end of the region (van der Wiel et al. 2016; Werner et al. 2017). During extreme events, the impacts across the region (and globally) can be substantial. During extreme El Niño events, the SPCZ can shift by up to ten degrees of latitude toward the equator, achieving a near-zonal (west-east) orientation and merging with the ITCZ (Cai et al., 2012). The strong El Niño of 2015/16 was

experienced across a large swathe of the Pacific Ocean from New Caledonia to Kiribati, by below-average rainfall, with 2.7 million Papua New Guineans impacted through drought and forest fires, and Palau declaring a State of Emergency (FAO 2016). This extreme El Niño was one of the three strongest events since 1950 (Santoso et al., 2017) and its impacts reached beyond the Pacific basin, extending across the planet (Rifai et al., 2019). Climate models suggest both the frequency and intensity of ENSO events have increased since the pre-industrial age and will continue to increase (Power et al., 2017). Extreme El Niño events are also projected to occur more frequently in a warmer world (Cai et al., 2014, 2012). However, our understanding of extreme El Niño events and how and why they differ from other El Niño events, is limited by their infrequency; with only three events having occurred during the satellite era, in 1982/1983, 1997/1998, and 2015/16 (Santoso et al., 2017).

During extreme El Niño events, the maximum sea surface temperature (SST) anomaly is situated in the eastern equatorial Pacific, which weakens the east-west SST gradients. This strengthens the ITCZ in the eastern equatorial Pacific region and allows the SPCZ to swing upwards towards the Equator (Cai et al., 2015). As a result of the extreme shift in position and changes in intensity of the ITCZ and SPCZ, extreme El Niño events cause a unique pattern of precipitation anomalies across the Pacific Islands. Intense rainfall occurs in the otherwise dry and cold eastern equatorial Pacific Ocean (Santoso et al., 2017) and some countries, such as Nauru, experience rainfall anomalies the opposite way to other El Niño events (i.e., decreased rather than increased precipitation; Murphy et al., 2014). This distinct precipitation pattern provides a potential way to identify the occurrence of extreme events in the past – through patterns of anomalous precipitation, or drought. Characterising extreme events through spatial patterns of drought is not only physically meaningful but has an additional benefit in placing the focus on the impacts these events have on small Pacific Island nations.

Climate records for the Pacific region are quite sparse. For many Pacific Islands robust records are only available from the 1950s (Lorrey et al., 2012). Documentary data has greatly enhanced our understanding of drought occurrence prior to instrumental records in many parts of world and is the best source for information on the effects of drought on societies (Brázdil et al., 2018). Despite significant research efforts, documentary climate information for the Pacific Islands is limited. D'Aubert and Nunn (2012) have collated the most extensive record of historical drought in the Pacific, covering the period 1722-1987. However, it is not a complete record, as drought information is difficult to identify in historical records. Records are also unevenly distributed over the different island groups and through time, which makes it particularly hard to identify spatial drought patterns which might indicate a zonal event (D'Aubert & Nunn, 2012).

Another data source capable of providing spatially resolved drought records at high temporal resolution are tree-ring chronologies (Brázdil et al., 2018). Moisture-sensitive tree stands can provide excellent records of unusually dry or wet years. There is a long history of utilising tree rings to develop records of growing season drought in many parts the world. The compilation of such records to cover a spatial area are normally referred to as ‘drought atlases’ (Cook, Anchukaitis, et al., 2010; Cook & Jacoby, 1977; Cook et al., 1999, 2015; Morales et al., 2020; J. G. Palmer et al., 2015; Stahle et al., 2016). A lack of island-based tree-ring proxies has precluded the development of a drought atlas for the Pacific region to date. However, as shown in Chapter 2, remote tree-ring chronologies can be used successfully in reconstructions of Pacific climate variables. The SPCZ reconstruction relied on tree-ring chronologies from Central America and Australasia – regions with strong teleconnections to the Pacific. Chapter 2 demonstrates that robust reconstructions can be developed even in the absence of local proxies.

This Chapter explores whether remote tree rings from ENSO-sensitive regions can be used not only to reconstruct a point index, like the SPCZ, but also to develop a drought atlas for South Pacific islands (the SPaDA). In developing the atlas, the methods used in Chapter 2 are modified to address the scarcity of data in the Pacific. The Chapter then investigates whether the spatial pattern of drought in the atlas, in conjunction with documentary evidence, can be used to identify zonal El Niño events and provide multi-centennial context for their occurrence.

3.3 Data and methods

3.3.1 Climate data

Previous drought atlases have targeted the Palmer Drought Severity Index (PDSI; W. C. Palmer, 1965) for which global gridded datasets are available. Gridded self-calibrating PDSI data are available over much of the South Pacific (Van Der Schrier et al., 2013). However, due to a lack of meteorological data, calculation of the evapotranspiration component relies on default parameters for most islands. This negatively influences tree-ring reconstructions based on this data, as shown in Figure B-1 and Figure B-2 for the island of Rapa Nui.

Like PDSI, the Standardized Precipitation Evapotranspiration Index (SPEI; Vicente-Serrano et al., 2010) is a water balance-based drought index, but is computationally much simpler, resolving some of the data issues of PDSI in the South Pacific. It has the additional advantage of being a multi-scalar index, which increases its suitability for regions with strong wet/dry seasonality. Indices which integrate over periods with different precipitation incidences, like PDSI, will be biased by the wet season and may not be able to identify seasonal droughts in wet/dry climates (Romero et al., 2020). SPEI has been successfully used as the calibration target for tree-ring drought reconstructions in extra-tropical climate regions (Seftigen et al., 2015; Tejedor et al.,

2017). Here, we present the results of a six-month SPEI reconstruction for the southwest Pacific wet season (i.e., November-April).

To calculate SPEI, monthly values of precipitation minus potential evapotranspiration are calculated and summed over the timescale of interest. SPEI is then obtained by fitting a log-logistic probability distribution function to the series and transforming it to a standardised normal distribution with reference to a baseline period (refer to Beguería et al., 2014; Vicente-Serrano et al., 2010 for details). The potential evapotranspiration component of the SPEI was calculated according to the method of Thornthwaite (1948), which only requires monthly precipitation and temperature. More complex methods for estimating evapotranspiration are not suitable for a South Pacific-wide study as most stations do not have sufficient data for additional meteorological parameters. The Thornthwaite method therefore provide a consistent approach for the entire region.

Monthly precipitation and temperature data for Pacific Island meteorological stations was sourced from the Climatic Research Unit (University of East Anglia) and Met Office CRU TS version 4.04 database. Data for islands not included in the CRU TS v4.04 database (Willis Is., Norfolk Is., Raoul Is., Pitcairn Is., and Nauru) was sourced from the relevant meteorological agencies. A long baseline period (30 to >50 years) that captures natural variability is required to calculate SPEI (Vicente-Serrano et al., 2010). Data availability for Pacific Islands varies through time, with the number of stations increasing across the region rapidly following World War Two but decreasing after 1990 (Figure 3-1).

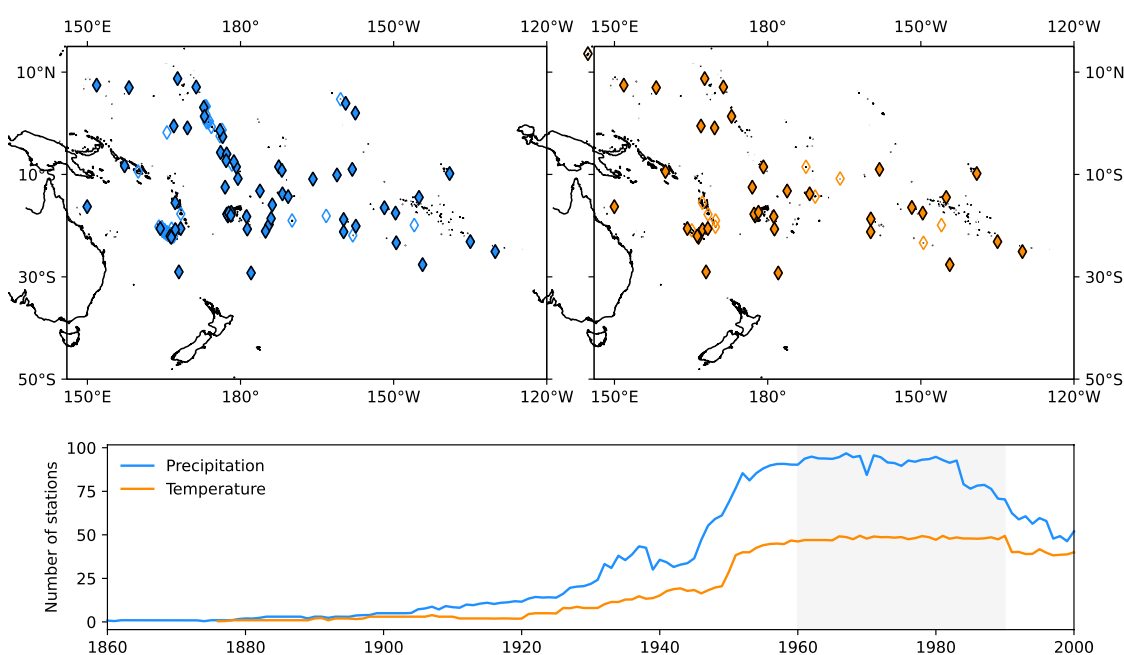


Figure 3-1 Location of precipitation (top left) and temperature stations (top right) with data available during the baseline period 1960-1990. Filled diamonds indicate stations with less than 10% of

monthly values missing over the baseline period. The total number of stations with data over time is also shown in bottom panel, with the baseline period indicated by the grey bar.

The period 1960-1990 was selected for the baseline to maximise both the number of individual stations with data and the geographical coverage of those stations. Rather than computing SPEI directly from gauge data, the grid points associated with the gauge stations were extracted from the CRU TS v4.04 gridded precipitation and temperature datasets. Using the gridded data takes advantage of the CRU TS v4.04 methodology (see Harris et al., 2020) to fill data gaps, allowing the analysis to be extended to island groups that would otherwise have insufficient data over the baseline period.

Tree-ring chronologies were selected from locations bordering the South Pacific with strong ENSO teleconnections. Chronologies previously used in the development of the Monsoon Asia Drought Atlas (MADA; Cook et al., 2010), Eastern Australia and New Zealand Drought Atlas (ANZDA; Palmer et al., 2015), Mexican Drought Atlas (MXDA; Stahle et al., 2016), and South American Drought Atlas (SADA; Morales et al., 2020) were downloaded from the International Tree-Ring Data Bank (ITRDB). The raw wood properties were standardised (i.e., detrended and transformed into dimensionless growth indices) using methods which preserve medium-term (multi-decadal) variability, including the ‘signal free’ method (Wilson et al., 2019).

3.3.2 Reconstruction method

Consistent with other regional drought atlases, SPEI was reconstructed using point-by-point regression (PPR; Cook et al., 2010, 1999, 2007), a nested, principal components-based regression method. Using this method, regressive models are sequentially applied to the principal components of the tree ring chronologies during a common calibration period between the predictors (tree rings) and the predictands (SPEI data points). Only tree-ring chronologies beginning at or before 1700 CE with a significant relationship ($p \leq 0.1$; Spearman, Pearson, and robust Pearson) with the target SPEI were included in the potential predictor pool (Figure 3-2). Each successive group of chronologies (nest) includes fewer chronologies but extends further back in time and is individually calibrated and verified against the instrumental target. We excluded any nest (and preceding nests) with a correlation of less than 0.4 with the most recent, best replicated nest. The variance of the final reconstruction was stabilised using a 300-year spline to correct variance effects related to decreasing sample size back in time (Esper et al., 2002; Frank et al., 2006; Osborn et al., 1997).

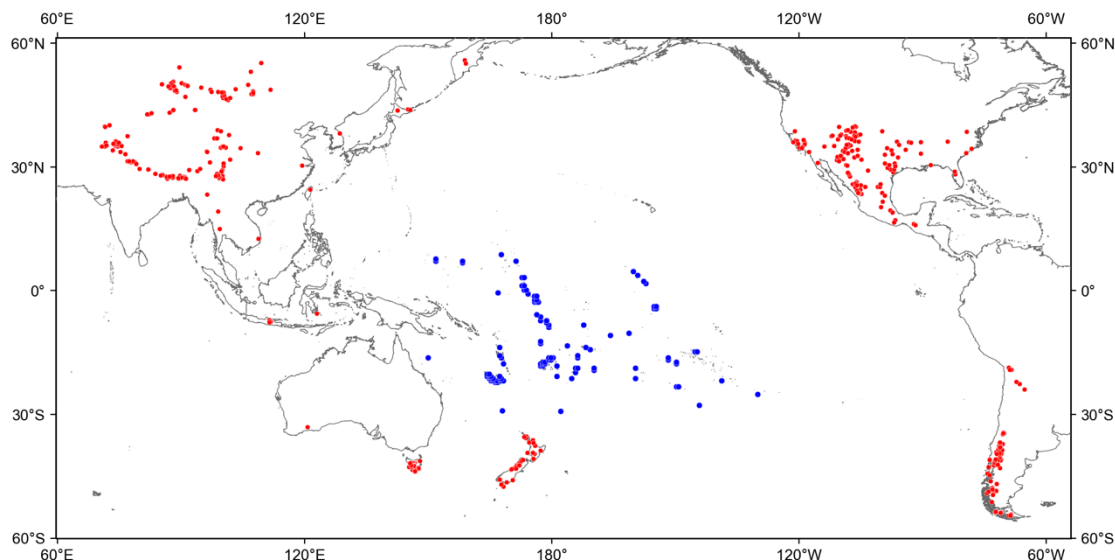


Figure 3-2 Locations of all tree-ring chronologies included in the initial predictor pool (red) and the CRU grid point reconstruction targets (blue). Five grid points were calculated from instrumental data not included in the CRU gridded products.

In contrast to previous studies, a consistent calibration interval was not used for all SPEI data points. The last year of the calibration period was limited to 1998 which is the end date of many of the tree-ring chronologies. Based on data availability, the initial calibration year was then selected on an island group basis to maximise the calibration interval length. Between 38 - 57 years were used for calibration (Table 3-1). The calibration interval for the island groups is too short to undertake split-period calibration and verification, which is the standard for dendrochronological reconstructions (see Chapter 2, Section 2.4.3). To address this issue, the reconstructions were primarily validated using a leave-one-out cross-validation procedure (Morales et al., 2020), using the cross-validation reduction of error (CVRE; Meko, 1997) as the primary validation statistic. A reconstruction point was considered valid with $CVRE > 0.2$. The CVRE is a relatively easy calibration target to pass and the selection of predictors using correlation to the instrumental data may lead to inflation of this statistic. Therefore, for individual stations with a sufficiently long data record, independent verification was undertaken and the more stringent verification statistics, reduction of error (VRE) and coefficient of efficiency (VCE), were also calculated.

Table 3-1 Calibration and verification intervals for each island/island group. Refer to Figure 3-6 for a spatial reference of island/island group names.

Island/ island group	No. CRU points	Calibration interval	Calibration years	Verification points	Verification interval	Verification years
Cook Islands	4	1943-1995	52	3	1931-1942	11
Federated States of Micronesia	4	1950-1998	48			
Fiji	16	1947-1998	51	2	1927-1947	20

French Polynesia	10	1953-1998	45	1	1920-1952	32
Kiribati	22	1948-1990	42	2	1908-1938	30
Marshall Islands	2	1951-1998	47			
Nauru	1	1952-1998	46			
New Caledonia	19	1953-1998	45	1	1902-1952	50
Niue	2	1941-1996	55			
Norfolk Island	1	1941-1998	57			
Pitcairn Island	1	1956-1998	42			
Raoul Island	1	1941-1998	57			
Samoa	2	1959-1998	39	1	1916-1956	40
Tokelau	1	1951-1995	44			
Tonga	6	1948-1998	50	1	1931-1941	10
Tuvalu	7	1948-1996	48	1	1932-1947	15
Vanuatu	4	1960-1998	38			
Willis Island	1	1950-1998	48			
Wallis and Futuna	1	1949-1998	49			

The reconstruction methodology is based on the implicit assumption that the teleconnections between the climates of the South Pacific and the locations of the tree-ring predictors are stationary in time. The assumption of stationarity is particular problematic for reconstructions calibrated to short datasets (Gallant et al., 2013), where it is likely that the instrumental data does not account for the full range of natural variability. The impact of the calibration interval on the robustness of the drought reconstructions was tested using two stations with data stretching back to the 1890s: Tahiti, French Polynesia, and Apia, Samoa (Figure 3-3). Reconstructions were developed on calibration periods ranging between 40 and 80 years, using all available periods of each length. For example, 21 reconstructions for Tahiti were calibrated using 40 years of continuous data between 1938 and 1998.

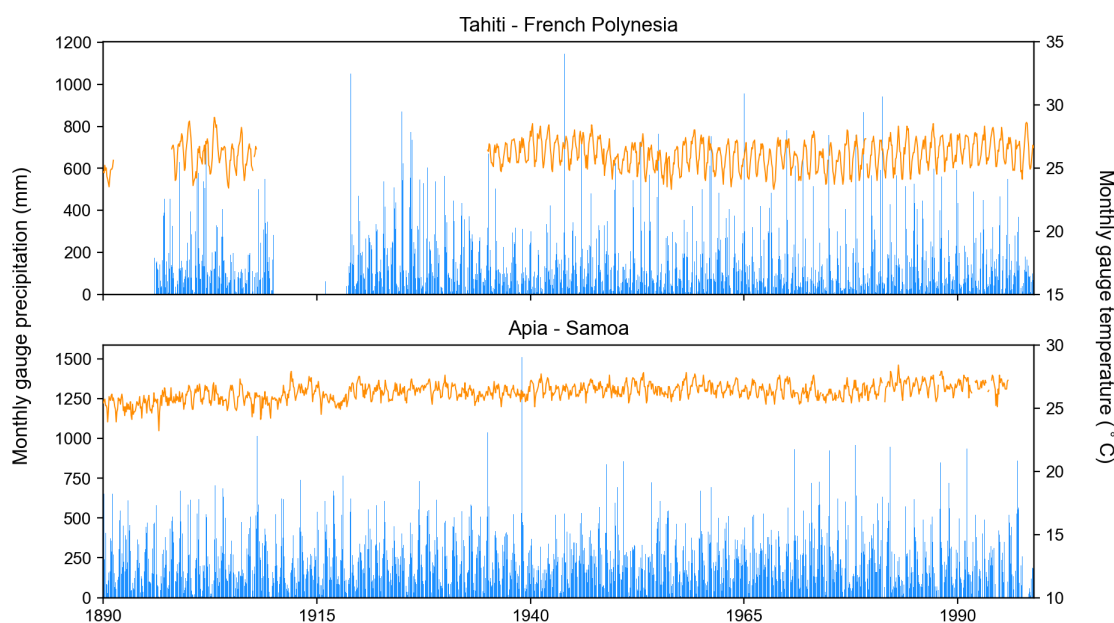


Figure 3-3 Precipitation (blue) and temperature (orange) data availability for two gauges with long records.

3.3.3 Identifying ENSO-related droughts

A Random Forest Classifier (RFC; Breiman, 2001) was used to identify ENSO phases based on spatial patterns of drought in the SPaDA. An RFC is an ensemble machine learning algorithm which calculates multiple decision trees from bootstrap samples of the dataset, with the final classification prediction taken as the most commonly selected across the ensemble. The training dataset was reconstructed SPEI at each grid point from 1875-1998, with years classified as La Niña, neutral, El Niño or extreme/Zonal El Niño based on instrumental data and known events. Recorded ENSO events since 1900 were taken from the Australian Bureau of Meteorology listing (<http://www.bom.gov.au/>) and from 1876-1900 from the compilation of Meyers et al. (2007). Zonal El Niño events were identified as 1972/73, 1982/83, 1991/92, and 1997/98 based on the characterisation of Santoso et al. (2017) and Vincent et al. (2011) for events since 1950. While the 1991/92 El Niño exhibited a zonal SPCZ in the satellite data, in terms of sea surface temperature (SST) and precipitation anomalies it is not considered extreme (Santoso et al., 2017; Vincent et al., 2011). The average December-February (DJF) Niño3.4 index calculated from HadISST sea surface temperatures during these four event years was +1.98 °C. Two other years, 1877/78 and 1888/89, significantly exceeded this value and were also included in the zonal El Niño list. The El Niño event in 1940/41 has a DJF Niño3.4 index of +1.903 °C and thus could also be classified as an extreme event based on this metric. The base classification model was trained on all seven ‘zonal’ events, with the sensitivity of the model results to the selection of training events tested using a leave-one-out procedure, in which one zonal event was reclassified as El Niño in each iteration and the classification model re-run.

As so few extreme El Niño events occur during the instrumental period, the classification problem is highly imbalanced. Conventional RFC seeks to minimise the overall error rate, and therefore performance is typically poor for very rare cases in imbalanced datasets. Random under-sampling was therefore employed as a standard modification to adapt RFC to the imbalanced classification (Chen et al., 2004). Random under-sampling down-samples the majority cases (i.e., La Niña, neutral, and El Niño events) to provide a more balanced dataset for training on rare cases (zonal El Niño events). However, down sampling the majority cases for this dataset would result in a very small training sample. To rectify this, 300 maximum entropy bootstrap replications (Vinod & López-de-Lacalle, 2009) of reconstructed SPEI were applied at each grid point to provide additional data samples, increasing the dataset to 300 x 124 classified ENSO events for training and validation. A 50:50 train/test split was employed, with model performance assessed using the metrics of precision, recall, and F1 score, which assess the ability of the model to correctly classify ENSO phases (true positives) without falsely identifying ENSO events (false positives).

To verify the classification results, the RFC model classification was compared to other paleoclimate reconstructions of ENSO. As all reconstructions contain large uncertainties, multiple proxy comparisons are made to develop the best possible picture of the climate conditions in each year. The reconstruction of Li et al., (2013) was based on more than 2,000 tree rings from a similar geographical range as this study. The multi-proxy ENSO reconstructions of Gergis & Fowler (2009) and McGregor et al. (2010) include coral proxies from the tropical Pacific, and tree rings and ice cores from regions with strong teleconnections to the Pacific. The coral-based El Niño reconstruction of Freund et al. (2019), which additionally classifies El Niño events as either eastern Pacific (canonical) events or central Pacific (El Niño Modoki) events, is the fourth proxy comparison. Most of the coral proxies used in Freund et al. (2019) were collected from the Pacific rather than teleconnected regions. Each of these reconstructions uses a different suite of proxy records and different reconstruction methods. However, only the drought atlas and the reconstruction of Freund et al (2019) are truly independent from one another, as there is some overlap in the proxies used amongst the other reconstruction pairs.

3.4 Results

3.4.1 Model calibration and validation

The fraction of variance explained in the calibration period (CRSQ) is above 29% for all grid points, above 50% for 94 grid points (90%), and above 70% for 45 grid points (43%). The reconstruction explains the most variance in SPEI for the Kiribati Line Islands, Tonga, and Vanuatu, and the least variance in SPEI for Norfolk Island, the Cook Islands, and Tuvalu (refer to Figure 3-6 for a spatial reference of island/island group names). Figure 3-4 shows that all grid points pass the CVRE threshold of 0.2 during the calibration period, with values very similar, but slightly lower than CRSQ for all grid points. Using the CVRE threshold, the reconstruction can extend back to 1410 CE for all grid points.

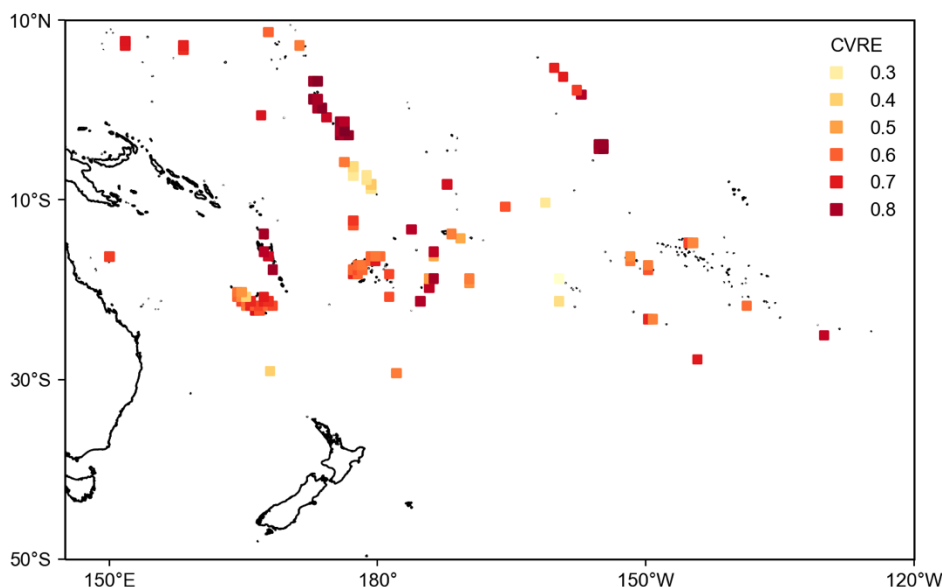


Figure 3-4 Calibration period leave-one-out cross-validation reduction of error (CVRE) for each reconstructed grid point for the best-replicated nest.

Verification statistics for individual island grid points with suitable long-term records show that the model has some reconstruction skill at 11 of the 12 locations (Table 3-2), as indicated by VRE and VCE values greater than 0 in the last, best replicated nest. Moving back in time, the reconstruction is considered valid for all nests with VRE and VCE greater than 0. The valid reconstruction period varies considerably between the verification points, with the first year of validity ranging between 350 – 1640 CE. This raises the question about the selection of a common period over which to analyse the reconstruction. All reconstructed grid points are analysed over the interval 1640-1998 CE, but it should be noted that reconstruction uncertainty is spatially variable and increases back in time.

Verification statistics for the reconstructions of Apia, Samoa and Tahiti, French Polynesia with varying calibration period lengths are shown in Table 3-3. Calibration and verification statistics for Apia remain strong for all models with calibration periods ranging from 40 to 80 years. However, the models for Tahiti calibrated on 40 years of data only pass the verification tests in 3/21 iterations, despite very high CRSQ values for all iterations. This suggests overfitting due to the short calibration period. The grid point reconstruction for Tahiti used in the SPaDA (Table 3-1) has a 45-year calibration period. This model barely passes verification, indicating that it is only slightly more informative than the mean of the calibration period in predicting the verification period values. Increasing the length of the calibration period to 60 years results in a well-verified model for Tahiti.

Table 3-2 Verification statistics for selected island grid points based on long instrumental records. Year refers to the earliest year of reconstruction validity using a cut-off of VRE and VCE > 0.

Island group	Gauge	Calibration interval	Verification interval	VRE	VCE	Year (CE)
Cook Islands	Aitutaki	1943-1995	1931-1942	0.01	-0.85	-
	Puka Puka			0.29	0.05	1640
	Rarotonga			0.37	0.31	410
Samoa	Apia	1959-1998	1916-1956	0.19	0.16	1390
Fiji	Suva	1947-1998	1927-1947	0.40	0.39	350
	Rotuma	1947-1998	1927-1947	0.19	0.19	1510
French Polynesia	Tahiti	1953-1998	1920-1952	0.08	0.03	1640
Kiribati - Line Islands	Washington Is.	1948-1990	1908-1938	0.50	0.49	480
	Fanning Is.			0.50	0.50	800
New Caledonia	Noumea	1953-1998	1902-1952	0.35	0.34	1100
Tonga	Vavua	1948-1998	1931-1941	0.21	0.15	350
Tuvalu	Funafuti	1948-1996	1932-1947	0.14	0.14	1550
Niue	Alofi	1941-1996	1907-1940	0.31	0.28	480

Table 3-3 Calibration and verification statistics for Apia and Tahiti for reconstructions models using different calibration period lengths. The mean and standard deviation are provided for each statistic across all iterations of a calibration period length.

Calibration interval	Calibration years	Verification interval	No. iter	CRSQ	CVRE	VRE	VCE
Apia							
1958-1998	40	1893-1917	41	0.72 ± 0.06	0.68 ± 0.06	0.24 ± 0.06	0.22 ± 0.07
1938-1998	60	"	21	0.58 ± 0.05	0.55 ± 0.06	0.21 ± 0.04	0.2 ± 0.04
1918-1998	80	"	1	0.564	0.539	0.177	0.172
Tahiti							
1958-1998	40	1897-1907	21	0.75 ± 0.14	0.72 ± 0.16	-0.19 ± 0.21	-0.35 ± 0.28
1938-1998	60	"	1	0.693	0.615	0.234	0.191

3.4.2 Selected tree ring proxies and teleconnections to the Pacific

A total of 598 tree-ring chronologies contribute to one or more of the SPaDA grid point reconstructions. Figure 3-5 shows the distribution of these chronologies, with colours representing the number of individual grid points to which the chronology contributed. Approximately 20% of chronologies contribute to fewer than five grid point reconstructions. For some of these chronologies, the relationships to island climate appears to have a geographical explanation, for example, chronologies in the MXDA which are correlated only with the Line Islands. However, other relationships suggest some spurious correlations have been included in the selection of predictors. Future iterations of the SPaDA may benefit from using a more stringent selection criteria to screen out spurious correlations when calibration periods are short. Conversely, around 7% of the chronologies contributed to over 50% of the grid point reconstructions. These chronologies come from all the predictor regions except for the ANZDA,

possibly because ENSO teleconnections are stronger in the Equatorial regions compared to the temperate zones like New Zealand, where many of the ANZDA tree-ring chronologies are located (refer to Figure 1-2 and Figure 1-3).

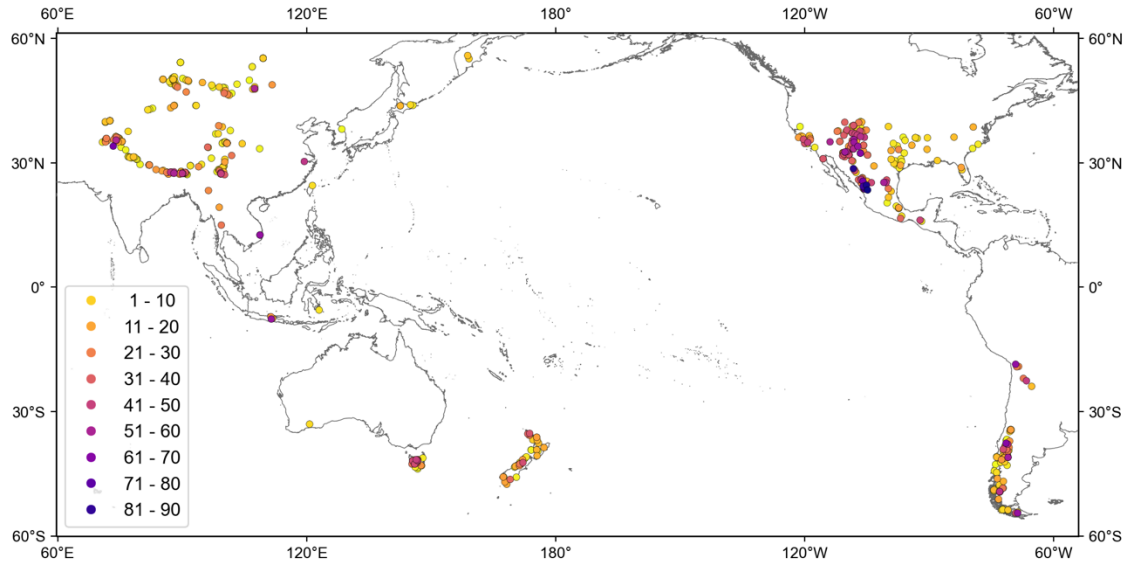


Figure 3-5 Number of reconstructed grid points to which each tree-ring chronology contributes.

Figure 3-6 shows the proportional weighting of chronologies from each of the predictor regions to the reconstructions – summed for all grid points in an island group. Here, the weighting is the sum of the absolute regression beta weights for each chronology, which represents the contribution of that chronology to the regression equation. The same figure shows that chronologies from the MADA region dominate most reconstructions across the SPaDA domain. However, as MADA chronologies are the largest proportion of the total predictor pool (39%), this may be more representative of chronology numbers than the strength of the teleconnection. There is no clear spatial pattern in the distribution of weightings, i.e., the contribution of each predictor region does not appear to fade with distance, indicating the influence of large-scale climate patterns in common to each of the regions.

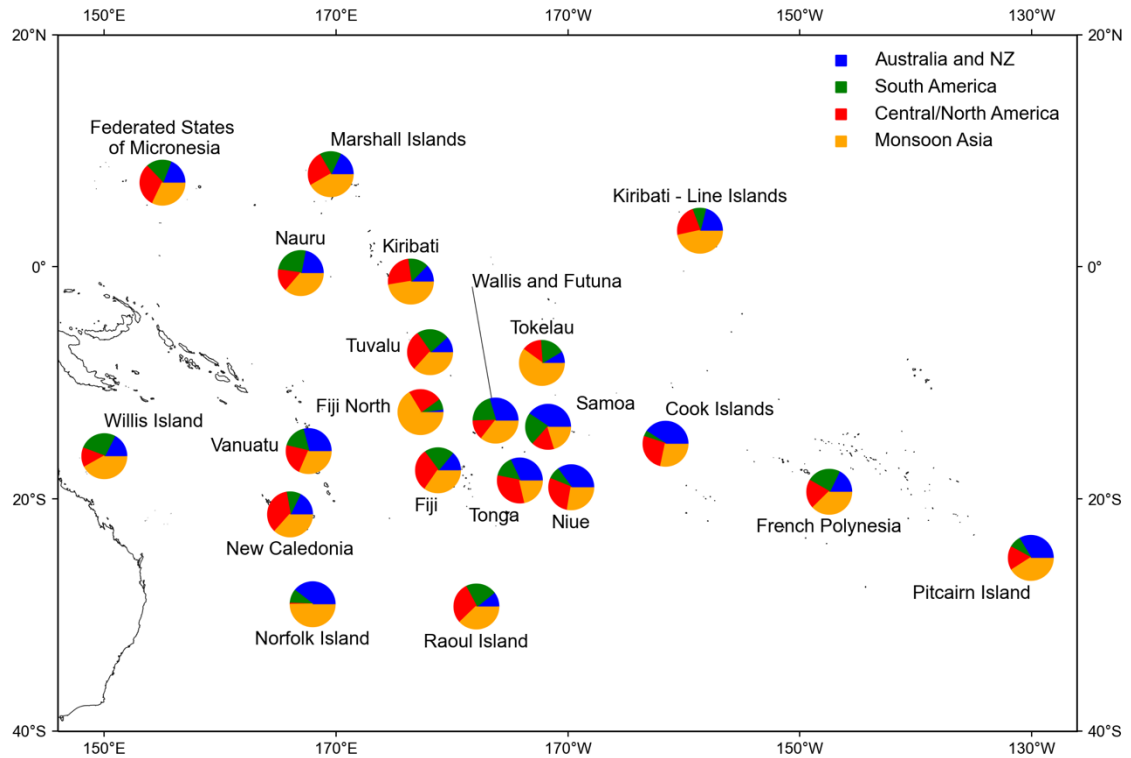


Figure 3-6 Proportional weighting of chronologies from each of the four regions (ANZDA – Australia and New Zealand, SADA – South America, MXDA – Central and North America, and MADA – Monsoon Asia) to the reconstruction by island group. The weighting for each island/island group is defined as the sum of the absolute value of beta weights of all chronologies from a region.

3.4.3 Drought anomalies during instrumental ENSO events

The ability of the SPaDA to reconstruct the Pacific Island drought response to warm and cold ENSO events was investigated using composite analysis. Figure 3-7 shows the average anomalies in the instrumental and reconstructed SPEI during the El Niño events that occurred during the data period – 12 for instrumental SPEI (1950-2018), and 20 for reconstructed SPEI (1875-1998). The SPEI for two years falling within the calibration (i.e., overlapping) period, in which the SPCZ took a zonal orientation, is also compared.

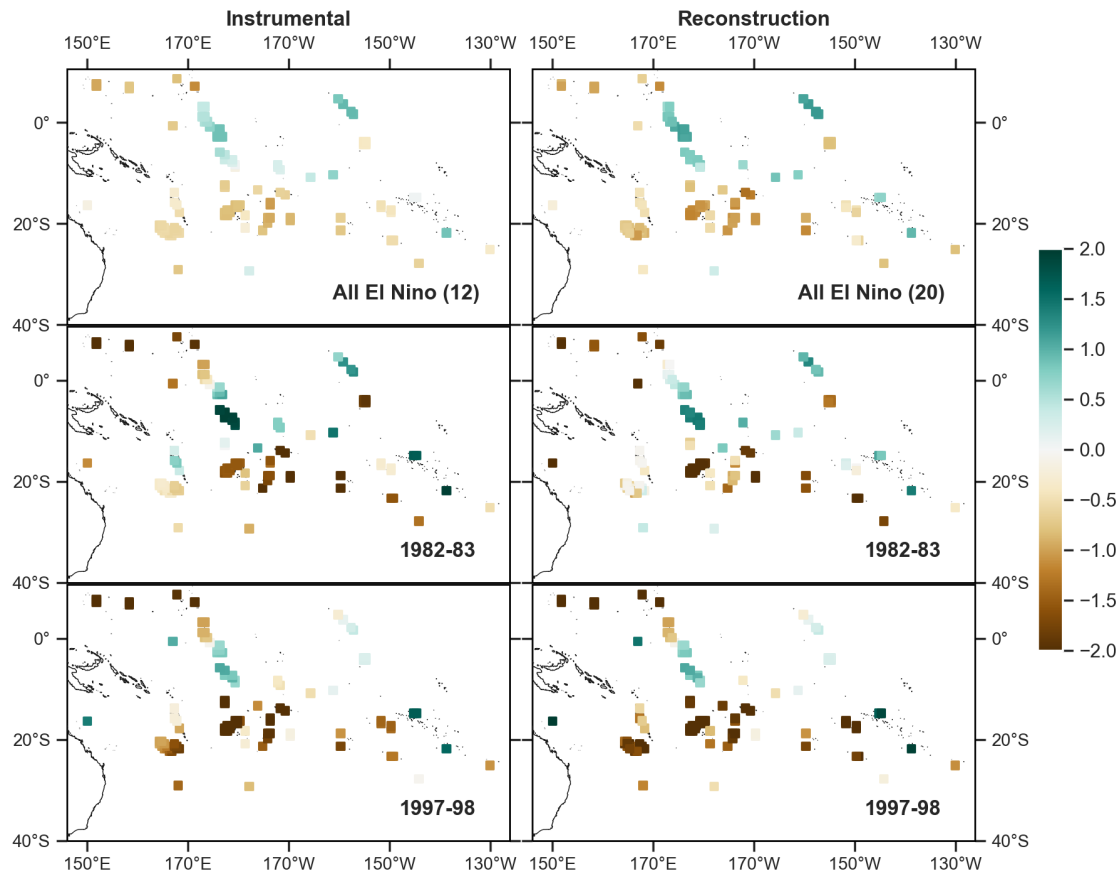


Figure 3-7 Instrumental (left) versus reconstructed (right) November-April SPEI during El Niño events during the data period (1950-2018 for instrumental, 1875-1998 for reconstruction). The average of all El Niño events is shown in the top row, and individual El Niño years in which the SPCZ took a zonal orientation are shown in the remaining two rows.

Similarly, Figure 3-8 compares instrumental and reconstructed SPEI during the La Niña events that occurred during the data period – 22 for instrumental SPEI and 34 for reconstructed SPEI, as well as the SPEI during two calibration period years in which the SST anomalies suggest an extreme event occurred. Reconstructed drought conditions in the SPaDA compare favourably with instrumental SPEI during both warm and cold ENSO events. Both the magnitude and spatial pattern of SPEI anomalies are consistent between the instrumental and reconstructed data in the ‘all event’ composites. The SPaDA also shows a good ability to replicate the selected calibration period extreme events, although SPEI anomalies are somewhat underestimated for the strong La Niña in 1989/90.

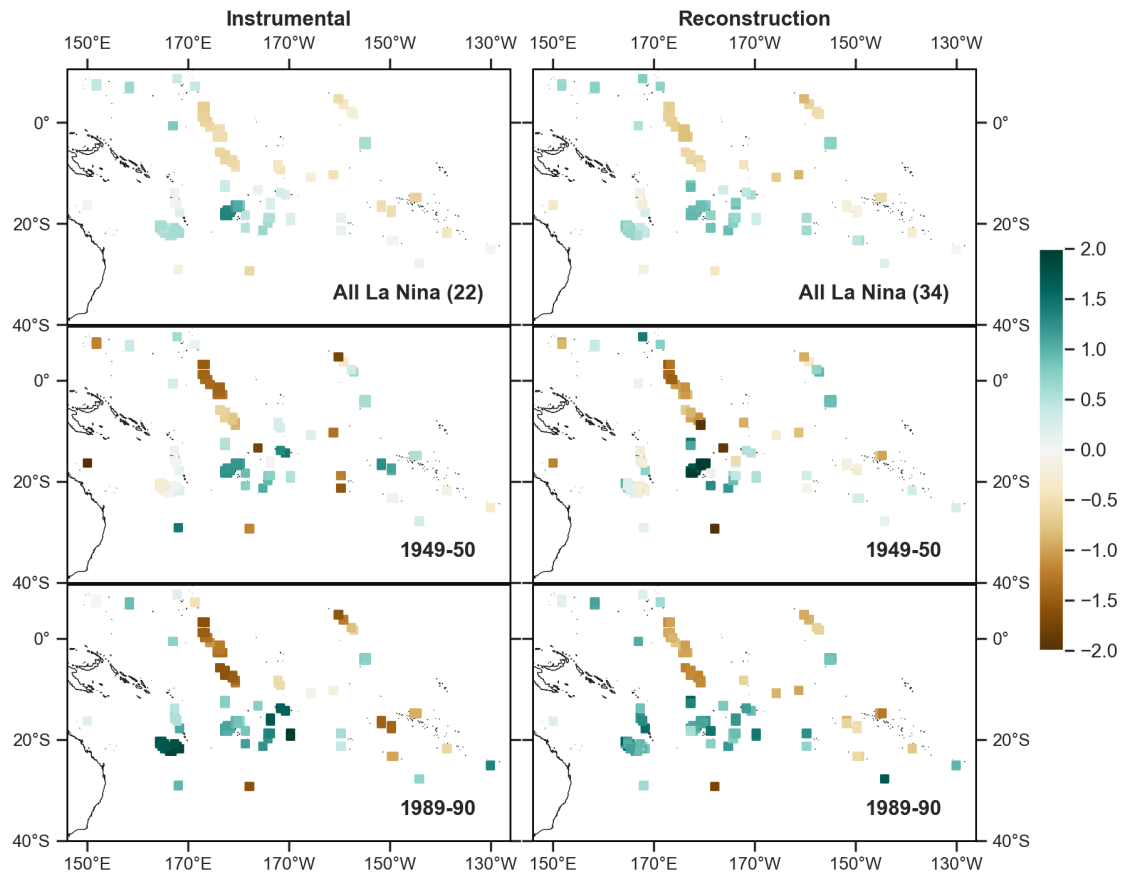


Figure 3-8 Instrumental (left) versus reconstructed (right) November-April SPEI during La Niña events during the data period (1950-2018 for instrumental, 1875-1998 for reconstruction). The average of all La Niña events is shown in the top row, and individual strong La Niña years are shown in the remaining two rows.

The stability of the relationship between soil moisture in the SPaDA and SSTs is tested by calculating the 50-year running Pearson correlation between the first principal component (PC1) of the reconstruction and the Niño-34 index, and spatial correlations between SPEI and Niño-34 for overlapping 50-year periods (Figure 3-9). This is important because changes in the SPaDA-SST relationship could be an indicator of non-stationary teleconnections between the Pacific and the predictor regions, which would affect any conclusions drawn from the SPaDA results. The correlation between PC1, which explains 53% of variance in the data, and Niño-34 over the 1875 – 1998 CE period is -0.78 ($p < 0.0001$).

Figure 3-9 shows that the relationship is stationary as indicated by correlations remaining within the 95% confidence interval calculated from 1000 synthetic reconstructions with the same statistical characteristics as the SPaDA (Gallant et al., 2013). However, the spatial maps show that the relationship with Niño-34 is not stable for all grid points, with some grid points (e.g., Northern Vanuatu) only showing significant correlations during some periods. This is most likely due to poor reconstruction validity at these grid points rather than a true change in the strength of the relationship.

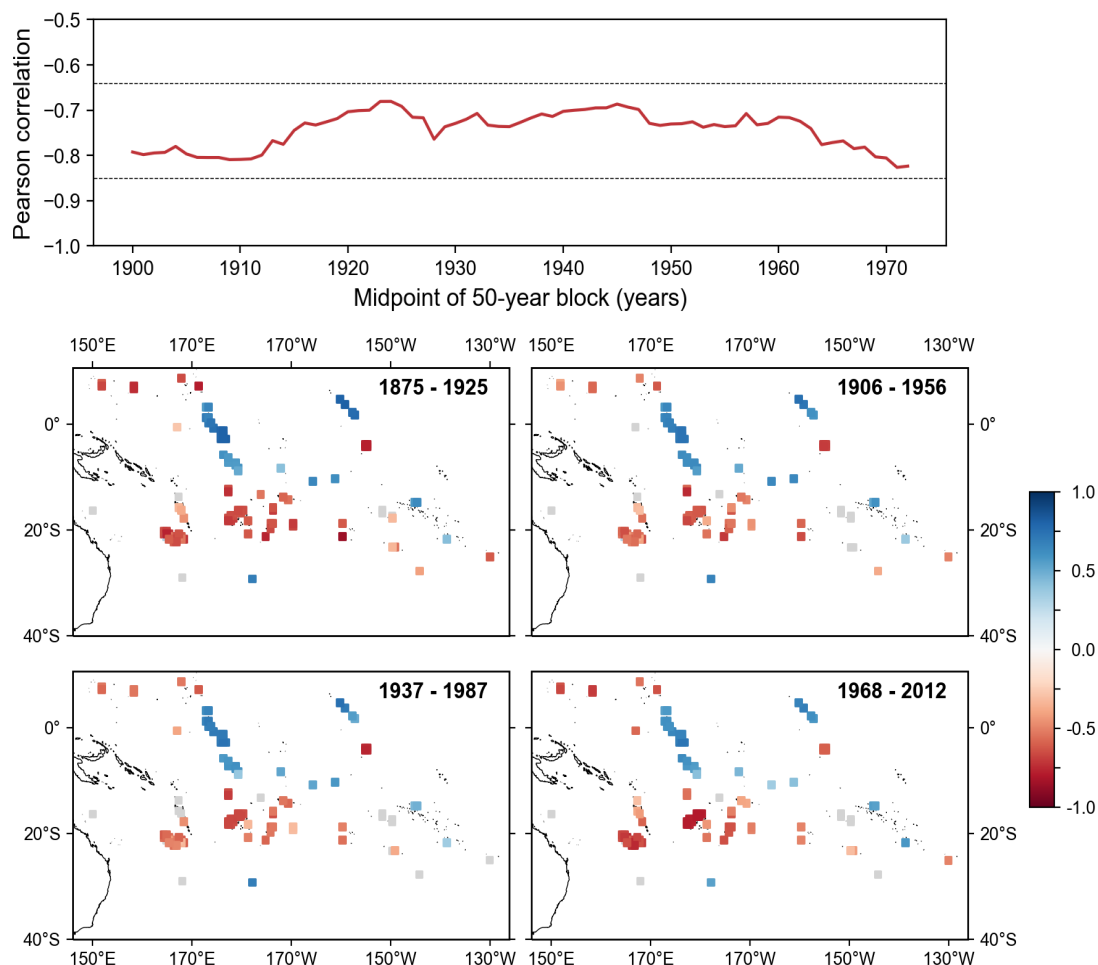


Figure 3-9 (Top) 50-year running Pearson correlation between the first principal component of reconstructed SPEI and the instrumental Niño-34 index with 95% confidence interval calculated from synthetic data. **(Bottom)** Spatial correlation between SPEI and Niño-34 for overlapping 50-year periods. Correlations not significant at $p < 0.05$ are greyed out.

3.4.4 Drought anomalies during significant historical drought events

In the absence of an independent validation period for most SPaDA grid points, the reconstructions can be verified by comparing the SPaDA to documentary and paleoclimate evidence for significant historical droughts events. Figure 3-10 shows reconstructed SPEI for four historical drought events, three centred on the southwest Pacific, and one centred on the eastern and equatorial Pacific. The ‘Year of Hunger’, was a series of droughts and unseasonable frosts which occurred over 1785-1787 in Mexico, resulting in famine and the estimated deaths of 300,000 people (Therrell, 2005). Tree-ring reconstructions have shown that the pattern of drought in central America was consistent with influence of La Niña (Therrell, 2005). The SPaDA SPEI anomalies show dry conditions over the eastern and equatorial Pacific, and wet conditions in the southwest Pacific, and north of the equator, consistent with La Niña conditions during this period. However, as many of the same tree rings used in Therrell (2005) are also incorporated into the SPaDA, the evidence for this drought event is not entirely independent.

Historical records (Russell, 1877) describe a severe drought experienced by European colonialists within two years of arriving in Sydney, Australia. Tree-ring reconstructions indicate that drought conditions were experienced across eastern Australia from 1791-1795, with the most extreme soil moisture deficits occurring in the summer of 1791/92 (Palmer et al., 2015). Simultaneously, drought and famine were occurring over much of India and the Caribbean (Grove, 2007). Paleoclimate records suggest the Settlement Drought was associated with an unusually strong El Niño (Gergis & Fowler, 2009). No documentary evidence is available to confirm whether this event also caused anomalous rainfall over the Pacific Islands (D'Aubert & Nunn, 2012); however, SPEI anomalies during 1791/92 are amongst the highest during the reconstruction period. Based on the SPaDA reconstruction, extreme drought should have occurred over much of the Southwest Pacific, with extreme wet conditions across the Equatorial Pacific (Figure 3-10b).

Stalagmite isotopes from Espiritu Santo, Vanuatu indicate an unusually dry year in 1866 ± 3 years (Partin et al., 2013). A drought occurring around 1866 or 1867 was also recorded in the dairy of John G. Paton, who was a missionary on Aniwa, 500 km to the south (Paton, 1893). Orissa (now Odisha) in the Bengal region of India experienced a devastating famine in 1866 after a weak monsoon the proceeding summer caused the rice harvest to fail. It is estimated that a million people died in Orissa alone. The SPaDA shows localised drought conditions in southern Vanuatu, New Caledonia, and parts of Fiji during 1865/66.

The Great Drought (1876-1878) was a concurrent period of multiyear droughts across Monsoon Asia, Brazil, Africa, and the Pacific. Widespread crop failures resulted in the 'Global Famine', with estimated fatalities exceeding 50 million people (Singh et al., 2018). In New Caledonia, a disastrous drought at the end of 1877 exacerbated tensions between the Melanesian Kanak peoples and the French colonial regime, with thousands of Kanak casualties (Davis, 2002). The yam crop in Fiji and taro crop in Vanuatu – both staples – failed due to lack of rainfall. In contrast, torrential rain damaged native crops on Kiribati leading to starvation deaths on the Gilbert Group islands (D'Aubert & Nunn, 2012). The Great Drought is attributed to an El Niño of extreme strength and duration occurring in 1877/78 with impacts more severe and widespread than the extreme El Niño events of 1982/83 and 1997/98 (Singh et al., 2018). Figure 3-10d shows average reconstructed SPEI from 1876 to 1878. The SPaDA shows anomalously dry conditions over much of the southwest Pacific, with extreme drought occurring in Niue and Wallis and Futuna. However, unusual wet conditions are only seen in parts of French Polynesia.

The selected historical cases demonstrate that the SPaDA provides reliable spatiotemporal information on drought events outside of the instrumental period. The identification of droughts in the SPaDA for which significant documentary or other non-tree ring evidence is available (i.e., the Settlement Drought, the Great Drought) greatly increases the confidence in the results. It is

also promising that the SPaDA can capture localised drought events, which may be related to climate patterns other than strong El Niño/La Niña which drive regional events. Verification against independent records shows that the SPaDA has the potential to contribute to our knowledge of climate extremes in the Pacific at least back until the 1780s.

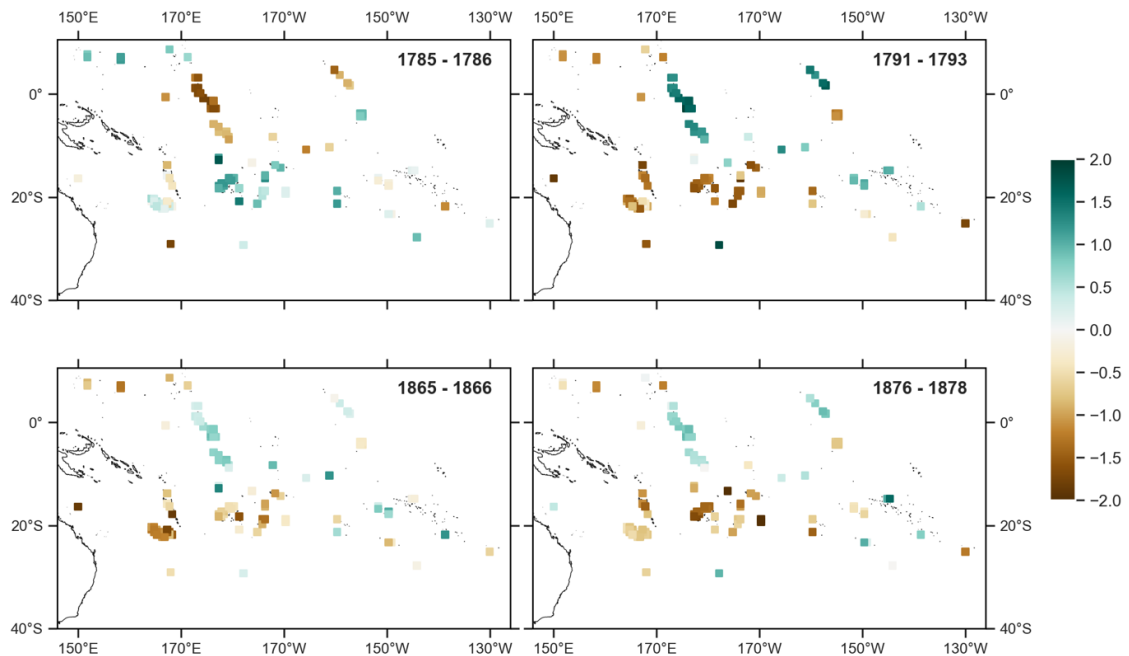


Figure 3-10 November-April SPEI during known historical droughts: the Mexican Year of Hunger (1785-86), the Australian Settlement Drought (1791-93), the Vanuatu drought (1865-66), and the Great Drought (1876-78).

3.4.5 Characteristics of the reconstruction

There is considerable year-to-year variability in the estimates of the wet/dry conditions across the SPaDA domain (Figure 3-11). The spatial pattern of alternating wet/dry conditions between the western and eastern Pacific Island is also clearly visible, in that a large proportion of grid points are severely dry ($\text{SPEI} < -1$) and severely wet ($\text{SPEI} > 1$) in the same year. Wavelet spectra of the first two (unrotated) principal components are shown in Figure 3-12 below. The wavelet spectra for PC1, which explains 53% of variance, shows power concentrated in the ENSO band (2-8 years). Multi-taper method spectral analysis (MTM; Mann & Lees, 1996) indicates that the peak at 3-4 years is significant at the 99% level. The second PC (PC2), which explains 7.5% of variance, also shows significant high-frequency variability at ~ 3 years, but additionally shows periods with significant power in the decadal to multi-decadal frequency range, with MTM analysis identifying significant peaks at ~ 24 years (99% level) and ~ 70 years (95% level). The IPO influences drought in the Pacific Islands through shifting the mean position of the SPCZ (McGree et al., 2016) thus variability on multi-decadal timescales is expected in the reconstruction.

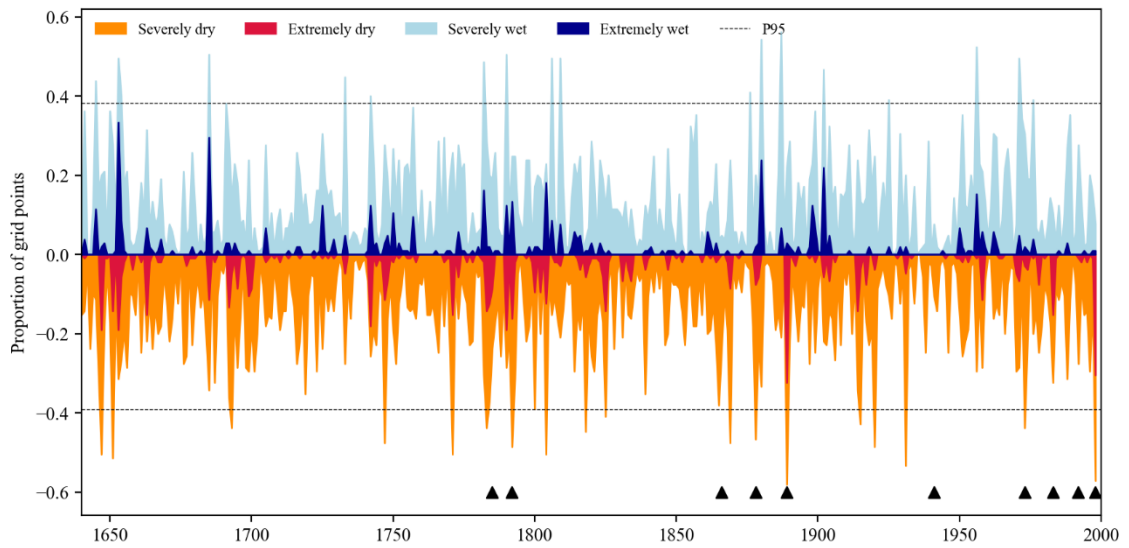


Figure 3-11 Percentage of area under severely dry ($\text{SPEI} < -1$, orange) and extremely dry ($\text{SPEI} < -2$, red) conditions, and for severely wet ($\text{SPEI} > 2$, light blue) and extremely wet ($\text{SPEI} > 4$, blue) conditions over the whole SPaDA domain. The dashed lines indicate 95% percentiles of the distribution. The black triangles indicate the occurrence of the four historical drought years and the seven ‘zonal’ El Niño years (1877/78 is common to both groups of events). Only years 1940/41 and 1991/92 do not have a substantial proportion of extremely wet/extremely dry grid points.

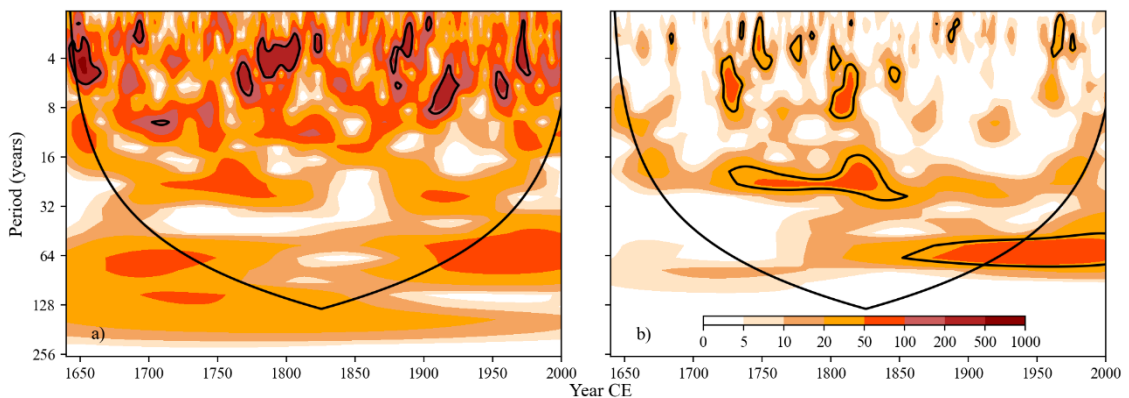


Figure 3-12 Wavelet spectra of the first two (unrotated) principal components of the SPEI reconstruction (Torrence & Compo, 1998) a) PC1, and b) PC2. Black contours indicate power above the 95% confidence interval when using an AR(1) red noise model.

3.4.6 Performance of the Random Forest classifier (RFC)

Figure 3-7 and Figure 3-8 show that the SPaDA reliably captures spatial patterns of drought in response to ENSO events over the entire instrumental period (1875–2012). Therefore, the RFC trained on the SPaDA grid points is expected to contain useful information about the occurrence of ENSO events over the reconstruction period. Table 3-4 shows the testing results for the model, which measures how well the model identified instrumental ENSO events for the 50% of data retained for training. The model performs extremely well during the testing period. Precision is lowest for the neutral class, and recall lowest for the El Niño class, which reflects the misattribution of some El Niño events as neutral. Importantly, the model distinguishes between El Niño and zonal El Niño events in most instances. However, as the maximum entropy bootstrap replications used as training/testing years are not truly independent from one another, the model

performance is likely overstated, and further work is required to accurately quantify the classifier performance.

Table 3-4 Testing results for the Balanced Random Forest classifier

Category	Precision	Recall	F1-score
La Niña	0.99	0.95	0.97
Neutral	0.95	0.99	0.97
El Niño	1.00	0.92	0.96
Zonal	1.00	0.97	0.98
Weighted average	0.97	0.97	0.97

3.4.7 Identification of extreme events

Based on the RFC classification, composite SPEI for all years from 1640-1874 CE for each ENSO category are shown in Figure 3-13. The spatial patterns and magnitude of the SPEI anomalies are consistent with the results during the instrumental period for La Niña and El Niño events. The percentage years in each category also matches well with the percentages during the instrumental period: 57% of years are classified as neutral compared to 53% in the instrumental period, and 26%, 12% and 4% classified as La Niña, El Niño and zonal compared to 29%, 13% and 5% during the instrumental period. The composite for the 10 years identified as zonal events shows the same spatial pattern as the El Niño composite but with much larger SPEI anomalies. Averaged across the SPaDA domain, grid point anomalies are 1.7 times larger during zonal years compared to other El Niño years. The hypothesis underlying this study was that for some islands, atypical patterns of precipitation occurring during zonal events would allow them to be identified via RFC. Atypical rainfall during zonal events occurs due to the extreme shift and change in intensity of the SPEI (Murphy et al., 2014). For most countries, this means more extreme precipitation anomalies than other El Niño years, but for some particular cases, namely Nauru and Tarawa (Kiribati), precipitation anomalies of the opposite sign to other El Niño years can be observed (Murphy et al., 2014). These atypical patterns are not seen in the zonal composite in Figure 3-13.

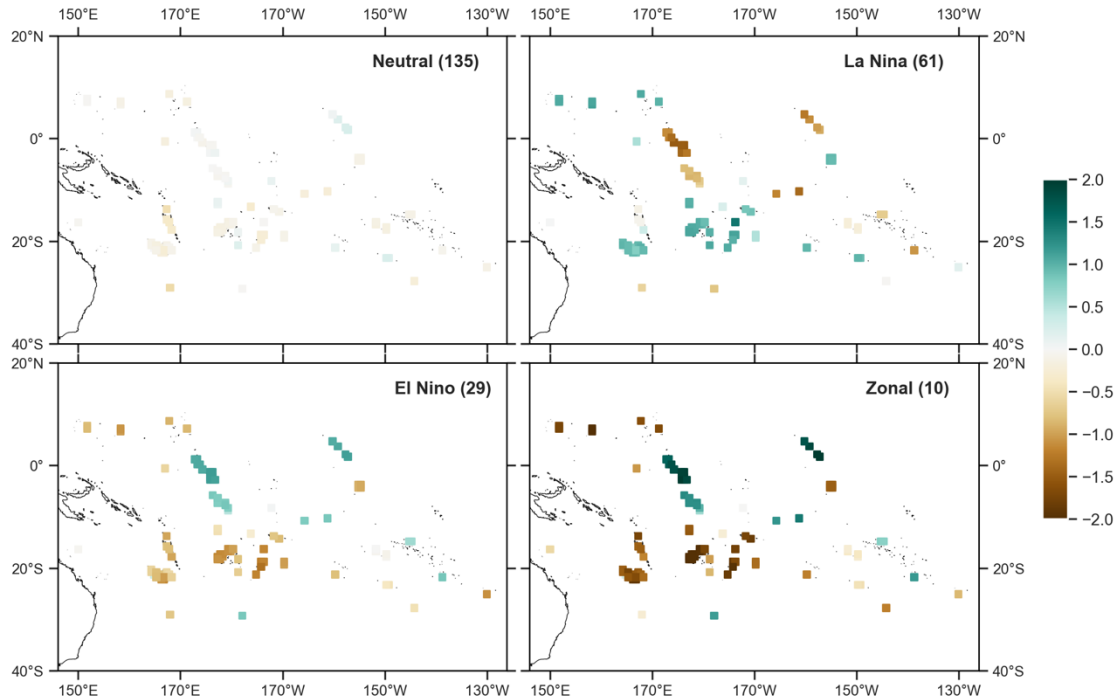


Figure 3-13 Summary of results of the Random Forest classification for pre-instrumental years 1640 – 1874 CE. November-April SPEI during years classified as neutral (135 years), La Niña (61 years), El Niño (29 years), and Zonal (10 years).

For reference, Figure 3-14 shows instrumental SPEI for four gauges identified in Murphy et al. (2014) as displaying atypical precipitation anomalies during extreme El Niño events. Funafuti and Majuro are both examples of islands with more extreme precipitation anomalies during zonal events, Tarawa and Nauru are examples of ‘sign switching’ precipitation anomalies. For all four grid points, the stars indicate years with a zonal El Niño event in which instrumental SPEI identifies atypical conditions. Only at Majuro do all three calibration-period zonal events (1982/83, 1991/92 and 1997/98) show atypical conditions. At Tarawa, 1982/83, and 1997/98 are atypical but 1991/92 is not, and for Funafuti and Nauru only one year is atypical (1982/83 and 1997/98 respectively). Even during the instrumental period, the characteristics of each event are quite different. Figure 3-15 shows reconstructed SPEI for the same four grid points during the 10 years identified as zonal by the RFC. At Majuro and Funafuti, 4 and 6 out of the 10 years respectively show atypical SPEI similar to the instrumental period. For Nauru only one year shows the atypical drought pattern, and no years are atypical for Tarawa. The SPaDA is better able to represent those grid points with extreme anomalies during zonal years than grid points demonstrating ‘sign switching’, which explains why extreme anomalies, but not atypical spatial patterns are observed in the zonal composite in Figure 3-13.

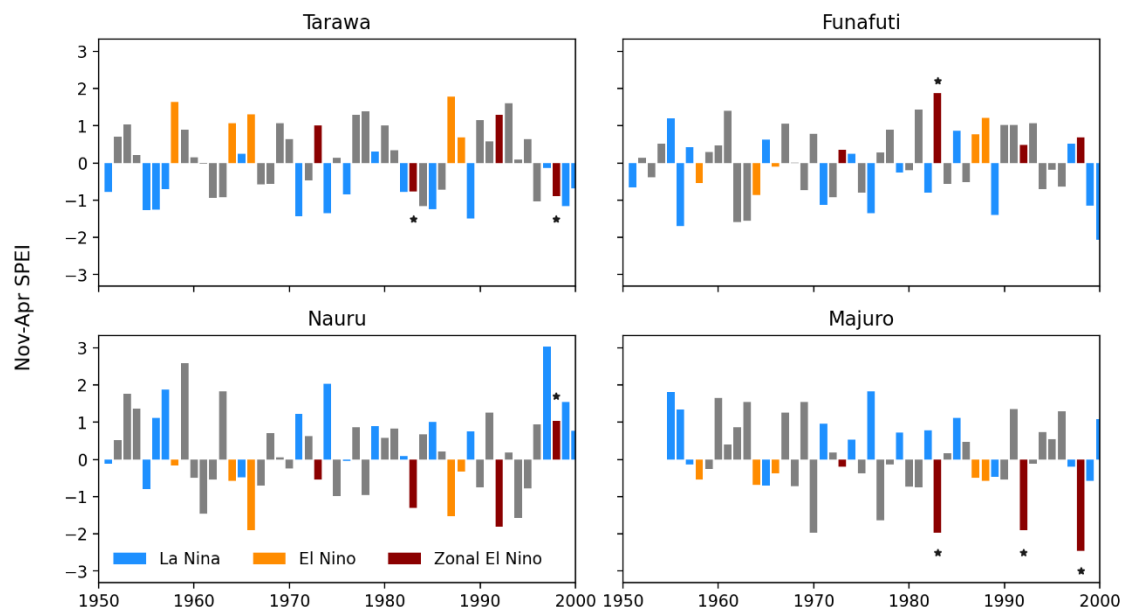


Figure 3-14 Instrumental November-April SPEI during neutral, La Niña, and El Niño years for gauges with anomalous precipitation regimes during zonal El Niño events. Starred years indicate the zonal events demonstrating anomalous SPEI during the data period. Nauru is calculated from precipitation and temperature data with the other gauges taken as the nearest CRU grid point.

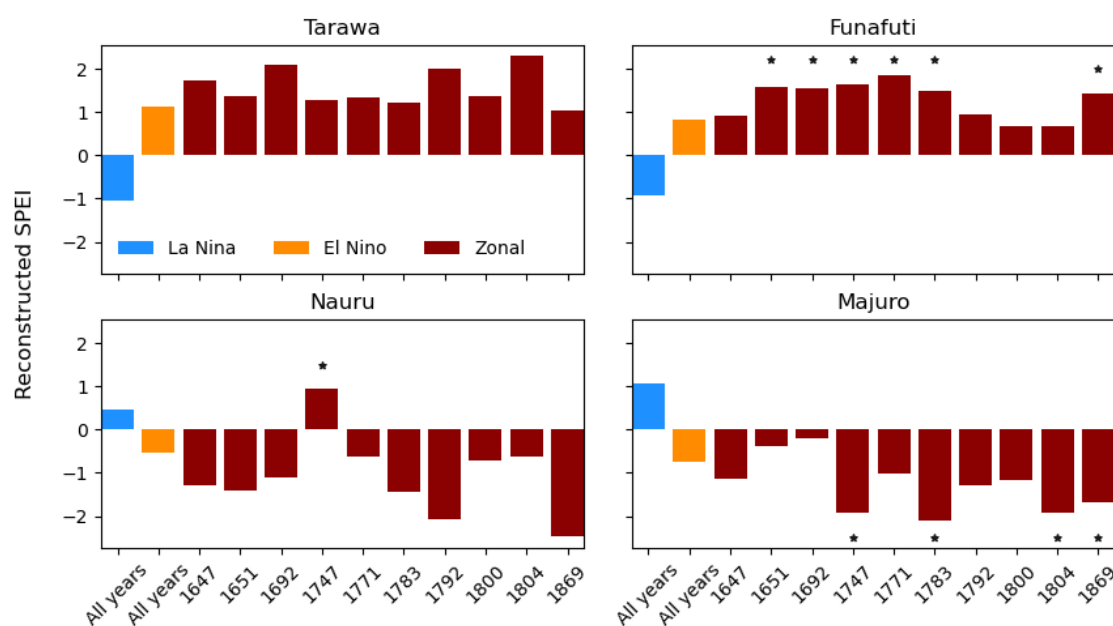


Figure 3-15 Average reconstructed November-April SPEI during years classified as La Niña, and El Niño by the random forest model, with SPEI during the 13 zonal events plotted individually. Starred years indicate the zonal events demonstrating anomalous SPEI matching the gauge behaviour during the instrumental period.

Table 3-5 lists the 10 events classified as zonal El Niño events. The column ‘probability’ shows the proportion of the 300 maximum entropy bootstrap (MEboot) replications for which the event was classified as zonal. The probability, therefore, is an estimate of the uncertainty around the classification as a zonal event internal to the Random Forest model. The leave-one-out hit rate indicates the number of leave-one-out model iterations in which the event was classified as zonal

and is an indicator of the sensitivity of the RFC to the training data classification. In general, low probability events have lower hit rates, indicating high sensitivity to event selection and only two events (1783 and 1869) were consistently selected in all iterations. Years with atypical grid point anomalies (starred years in Figure 3-15) show very high probabilities, indicating that the anomalous SPEI was consistent across the MEboot replications and consistently identified as zonal by the RFC.

Table 3-5 Probability of a zonal El Niño event according to Random Forest classification of MEboot replications of reconstructed drought.

Year	Probability	Leave-one-out hit rate
1647	0.59	6/8
1651	0.84	6/8
1692	0.66	5/8
1747	0.84	5/8
1771	0.86	6/8
1783*	1.00	8/8
1792	0.51	3/8
1800	0.49	4/8
1804	0.98	7/8
1869*	0.89	8/8

*Starred years are insensitive to the choice of zonal events used in training the Random Forest Model, that is, are classified as zonal events in every leave-one-out iteration.

3.4.8 Comparison to other reconstructions

The tree-ring ENSO reconstruction of Li et al. (2013) and multiproxy ENSO reconstruction of McGregor et al. (2010) are annual reconstructions and can be compared directly to PC1 of the SPaDA, which shows predominantly ENSO-frequency variability (Figure 3-12). Figure 3-16 shows the running Pearson correlation between the SPaDA PC1 and the two reconstructions over the common reconstruction interval. There is a high degree of fidelity between the results of this study and both the reconstructions. The correlation is slightly stronger between PC1 and the Li et al. reconstruction, which is unsurprising as they are based on similar predictor sets. Nevertheless, the strength and stability of the correlations is quite remarkable considering the SPaDA is a spatially resolved SPEI reconstruction and the other studies reconstructed ENSO directly.

Figure 3-17 compares the event based multiproxy reconstruction of Gergis and Fowler (2009) and coral reconstruction of Freund et al. (2019) with SPaDA drought years classified as either El Niño or zonal El Niño by the RFC prior to the instrumental period. Most zonal years were identified as strong or very strong El Niño events in the multi-proxy reconstruction. There is also substantial overlap in years identified as El Niño events by the RFC with the Gergis and Fowler event list, although the RFC model has not identified many of the events classified as weak or medium El Niño by Gergis and Fowler. This is very likely due to a difference in the criteria used to discriminate between El Niño and neutral events. In comparison, there is low correspondence

between the SPaDA event list and the coral reconstruction of Freund et al. (2019). The RFC classified 39 years as El Niño or zonal El Niño and 45 El Niño events were identified by Freund et al. There are 11 overlapping events between the reconstructions, which is fewer than would be expected by chance ($p = 0.15$, binomial test).

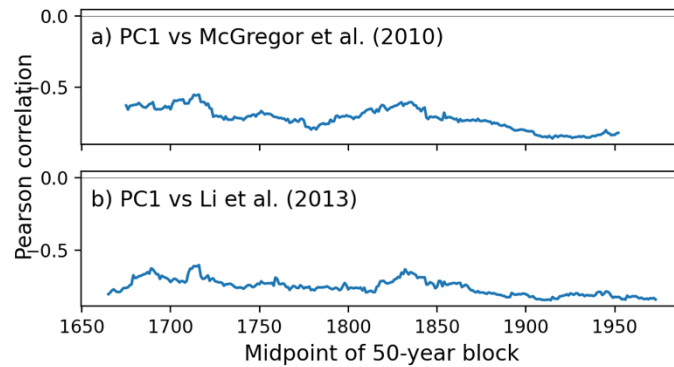


Figure 3-16 50-year running Pearson correlation between the SPaDA PC1 and the ENSO reconstructions of a) McGregor et al. (2010) over 1650-1977 CE and b) Li et al. (2013) over the period 1640-1998 CE. All correlations are significant ($p \ll 0.01$).

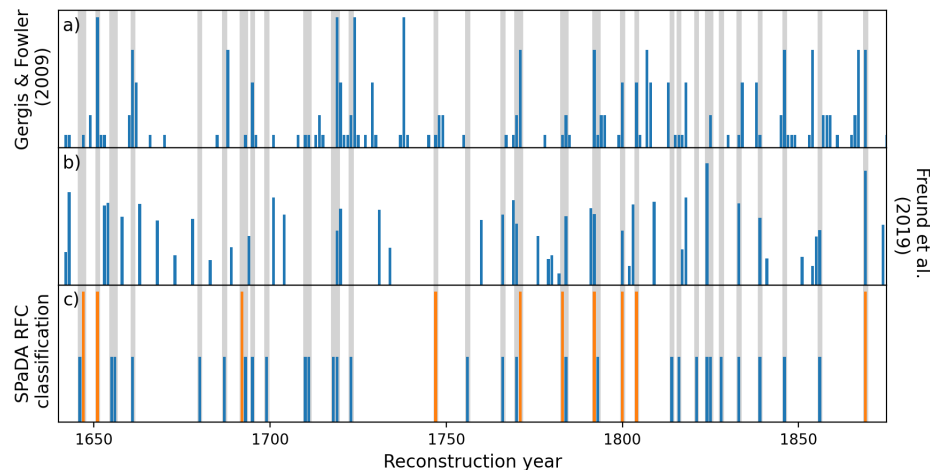


Figure 3-17 Event-based comparison between the published reconstructions of a) Gergis and Fowler (2009) and b) Freund et al. (2019) with c) events identified by the RFC model as El Niño (blue) and zonal El Niño (orange) for the period 1640-1875 CE. The calendar year events of Gergis and Fowler (2009) have been shifted forwards by one year for consistency with the other reconstructions. While Freund et al. (2019) report event amplitude, Gergis and Fowler presented a qualitative ENSO strength index. For plotting purposes weak, medium, strong, very strong, and extreme events have been given amplitudes of 0.1, 0.25, 0.5, 0.75, and 1. Events identified in the SPaDA have similarly been given an amplitude of 0.5 (El Niño) or 1 (zonal El Niño).

3.5 Wider Considerations

The primary aim of this Chapter was to explore whether remote tree rings from ENSO-sensitive regions can be used to develop a spatially resolved drought atlas for the South Pacific. A secondary aim was to investigate whether the spatial patterns of drought in the SPaDA could be used to identify extreme or zonal El Niño events thus providing multi-centennial identification of their occurrence. Underpinning both these aims was the intention to provide long-term information on drought in the Pacific Islands that can be used to better understand hydrological

risks. Considerable progress towards calibrating and verifying the SPaDA has been made in this Chapter. For example, the SPaDA is able to replicate documented droughts linked to ENSO events and compares well to previously published ENSO reconstructions. Similar to the findings of Chapter 2, this Chapter shows that when applied in a network, remote tree-ring proxies have considerable reconstruction ability for the South Pacific. There were two major challenges in developing the SPaDA, both relating to the instrumental dataset: 1) The lack of independent verification data; and 2) the short calibration period. Neither of these challenges was able to be satisfactorily overcome in this work, reducing confidence in the results of the SPaDA, particularly for the period prior to 1780 CE. The following sections discuss some of the necessary considerations for future development of the SPaDA.

3.5.1 The need for independent verification

Data availability was a major limitation in developing the SPaDA and has resulted in several changes to the established methodology for producing reconstructions from tree rings. A major consequence of the short instrumental data is the lack of an independent verification period for most grid points. Although using CVRE as the primary verification metric has precedence in the development of drought atlases (Morales et al., 2020), CVRE is a measure of the variance explained during the calibration period and not a true verification statistic. Verification data is only available for a very small number of the SPaDA grid points (Table 3-1), and thus, the majority of the SPaDA domain remains statistically unverified. In the absence of verification data, evidence for reconstruction skill in the SPaDA is demonstrated in two ways. First, the SPaDA accurately captures high-frequency Pacific SST dynamics over the entire instrumental data period (Figure 3-9), providing evidence of spatial and temporal reliability back to 1875. The SPaDA was then qualitatively compared to reports of unusual hydroclimatic variability from historical climate records, which is a standard verification procedure even for tree-ring reconstructions that have independent verification periods. The ability of the SPaDA to represent the four historical droughts (Figure 3-10) does improve confidence in the results, however, much of the information we have on the timing and magnitude of these droughts were derived from tree rings, are and not completely independent of the SPaDA estimates. A lack of documentary evidence also means there is no historical event verification for the first 140 years of the reconstruction.

The final verification was undertaken by comparing the results of the SPaDA and the Random Forest classifier to other ENSO reconstructions. There is excellent agreement between PC1 of the SPaDA and the two annually resolved ENSO reconstructions (Figure 3-16) which improves confidence in the results. There is also good agreement between the RFC classification results and the event-based multiproxy ENSO reconstruction, although the RFC identified far fewer El Niño events than were identified by Gergis and Fowler (2009) which suggests a mismatch in the criteria used to define an El Niño. However, there is very little fidelity between the RFC

classification and the coral-only reconstruction of Freund et al. (2019) (Figure 3-17). This is problematic because only the coral-based reconstruction is truly independent of the SPaDA results. The fidelity between the other three reconstructions is increased by shared tree-ring predictors.

Many paleo reconstructions of ENSO have been developed (e.g., Cobb et al., 2003; D'Arrigo et al., 2005; Emile-Geay et al., 2013; Khider et al., 2011; Li et al., 2013; Wilson et al., 2009; Zhu et al., 2022), but in many cases there is little correspondence between them outside of the data period (Yun & Timmermann, 2019). The choice of proxy type/s and locations impact the divergence between reconstructions much more than the choice of reconstruction method (Wilson et al., 2009). Tree-rings are incorporated into many reconstructions due to a lack of proxy data from within the Niño-3.4 region. However, using data from teleconnected regions necessarily assumes stationarity and cannot provide independent verification for the ENSO impacts on megadroughts discussed in many drought atlases (Emile-Geay et al., 2013). While coral proxies are located close to the geographical centre of ENSO action, they have several disadvantages including short length, discontinuities, and dating errors (DeLong et al., 2013; Zhu et al., 2022). Dating errors of even one year degrade correlations and make it impossible to compare event years between reconstructions, and the probability of such errors in coral records increases back in time (Wilson et al., 2009). In addition, the current coral network is dominated by records from the western and central equatorial Pacific which have been shown to capture La Niña events more faithfully than El Niño events (Zhu et al., 2022).

To further demonstrate the difficulty in comparing tree-ring and coral based reconstructions, Figure 3-18 plots the running correlation between PC1 of the SPaDA and two new ENSO reconstructions (Zhu et al., 2022), one based only on coral records (Zhu_c2022) and one incorporating both corals and tree rings (Zhu_ctr2022). These reconstructions were both developed using paleo data assimilation methods and calibrated using the same data and calibration interval. As Figure 3-18a shows, PC1 of the SPaDA and the multiproxy Zhu_ctr2022 reconstruction are highly correlated over the entire common reconstruction interval (1640-1998), with similar correlation strength as the previous comparisons in Figure 3-16. In contrast, PC1 and Zhu_c2022 are only significantly correlated over the period from ~1850 CE (Figure 3-18b). Despite the overlap in coral proxies used, and the consistent methods and calibration, Zhu_ctr2022 and Zhu_c2022 also lose fidelity prior to 1850, with non-significant correlations during much of the first half of the common reconstruction interval (Figure 3-18c).

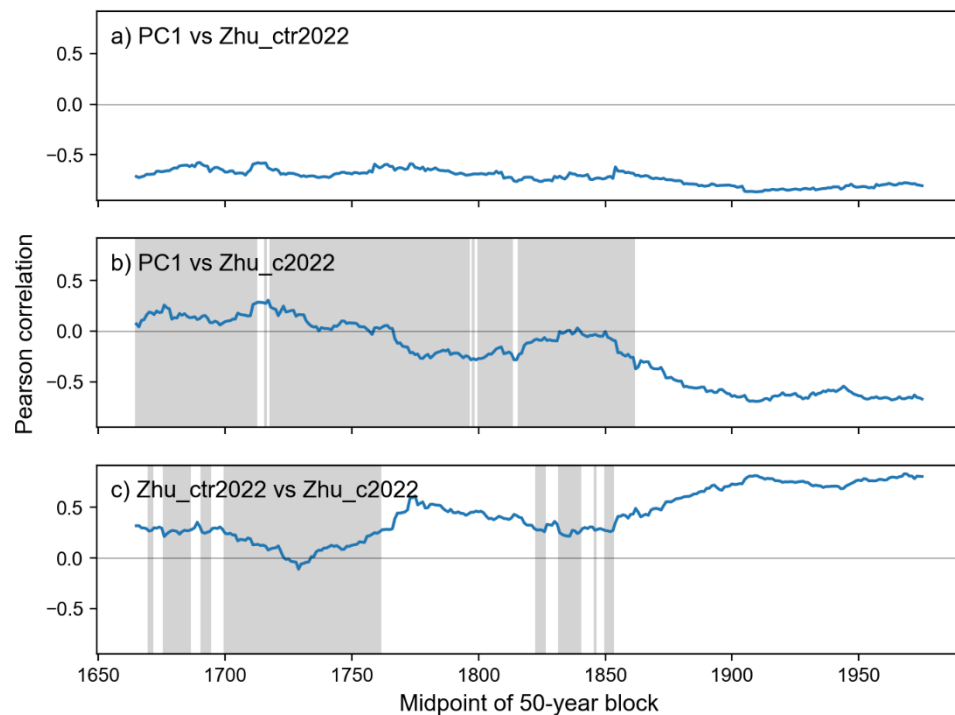


Figure 3-18 50-year running Pearson correlation between the SPaDA PC1 and the ENSO reconstructions of Zhu et al., (2022): a) PC1 vs the multiproxy coral and tree-ring reconstruction, b) PC1 vs the coral only reconstruction, and c) the Zhu et al. reconstructions compared directly. Grey bars indicate periods where correlations are not significant ($p > 0.05$).

Therefore, the lack of fidelity between the SPaDA and the coral reconstruction of Freund et al. (2019) does not necessarily invalidate the SPaDA results. Nor do potential dating errors negate the usefulness of the coral reconstructions in Freund et al., which are used to investigate the changing frequency of El Niño events over time. Errors in the chronology of a few years are negligible to frequency calculations over centuries. However, this does mean that the SPaDA is still without independent statistical verification during the instrumental period for most of the spatial domain, and without documentary or truly independent paleo verification for most of the reconstruction length. Without this verification and considering the limitations of the calibration period discussed above, the SPaDA results prior to ~1780 should be used with caution.

3.5.2 Length of the calibration period

Capturing low-frequency climate variability is important to accurately represent past extreme events in the SPaDA. The underestimation of low-frequency variability is a common problem in paleo-reconstructions (Christiansen & Ljungqvist, 2017). Predictor selection almost always includes screening predictors against instrumental data; but, due to the data length, screening is largely restricted to high-frequency variability (Christiansen & Ljungqvist, 2017). Linear regression models calibrated to short instrumental data periods are therefore optimised to the calibration period frequencies (years to decades) and can underestimate low-frequency information (Osborn & Briffa, 2004).

If the relationship between the predictor and the predictand are frequency-dependant, only the calibration period frequencies will be accurately captured in the reconstruction (Christiansen & Ljungqvist, 2017). Thus, Franke et al. (2013) showed that tree-ring reconstructions can systematically overestimate low-frequency variability (i.e., redden the reconstruction) due to bias in the spectral frequency of the tree-ring proxies compared to the instrumental data being propagating through to the reconstructions. The pseudoproxy experiments of Smerdon et al. (2016) demonstrated that regression techniques themselves can both increase and decrease the ratio of low-to-high spectral frequency, independent of spectral biases in the proxies. They found complex and spatially variable changes to reconstruction spectral variance in their pseudoproxy climate field reconstructions.

Additionally, Yun & Timmermann (2019) found that selection of the calibration period (i.e., length independent) has a large effect on multidecadal to centennial-scale climate variability in their pseudoproxy reconstructions of ENSO. They concluded that low-frequency variability has a stronger dependency on the selected calibration period due to the role of external forcing, which explains why there was calibration period-independent fidelity in the internally forced ENSO band, but a lack of fidelity in the low-frequency band in their reconstructions.

These studies show that regression techniques used for paleo-reconstructions can change the spectral characteristics of the reconstructed variable with respect to the data used for calibration. Both the length of the calibration period in relation to the main frequencies of Pacific climate variability, and the period used for calibration, play important roles in the spectral variance of the final reconstruction. These studies used calibration periods ranging from 80-150 years. Most grid points in the SPaDA have a very short calibration period, which may further contribute to spectral bias in the low-frequency range. Figure 3-12 demonstrates that low-frequency variability at interdecadal and longer frequencies is present in PC2 of the SPaDA. Note that the separation of modes of variability by frequency is a common artifact in principal component analysis, and, with appropriate rotation of the EOFs, a method used to distinguish between ENSO and lower-frequency climate modes without filtering (Chen & Wallace, 2016; Chen et al., 2017).

Whether low-frequency information in the SPaDA is underestimated, however, is almost impossible to quantify because of the same data limitations that prevent the use of a longer calibration period. The impact of the calibration period length on the spectra of reconstructions for Apia, Samoa, was tested using the multi-taper method. Figure 3-19 shows timeseries of the proportional band-power in the decadal (10-20 year) and multidecadal (> 20 year) frequency bands in 50-year moving windows, for all reconstructions calibrated using 40 and 60 years of data (Table 3-3). While the reconstructions agree on the periods of higher or lower band-variance, there is a large spread in the proportion of total power represented by the decadal and multidecadal

band, and the divergence between the reconstructions increases moving further back in time. Pearson correlations between the reconstructions also vary widely, between 0.38 - 0.97 for the 40-year calibration periods and 0.57 – 0.93 for the 60-year calibration periods. The strength of the correlation is not closely related to the overlap in the calibration period datasets, indicating that the reconstructions are sensitive to the characteristics of the calibration period, particularly when only 40 years are used. This analysis was not repeated for the Tahiti variable calibration period reconstructions as almost none passed the verification tests.

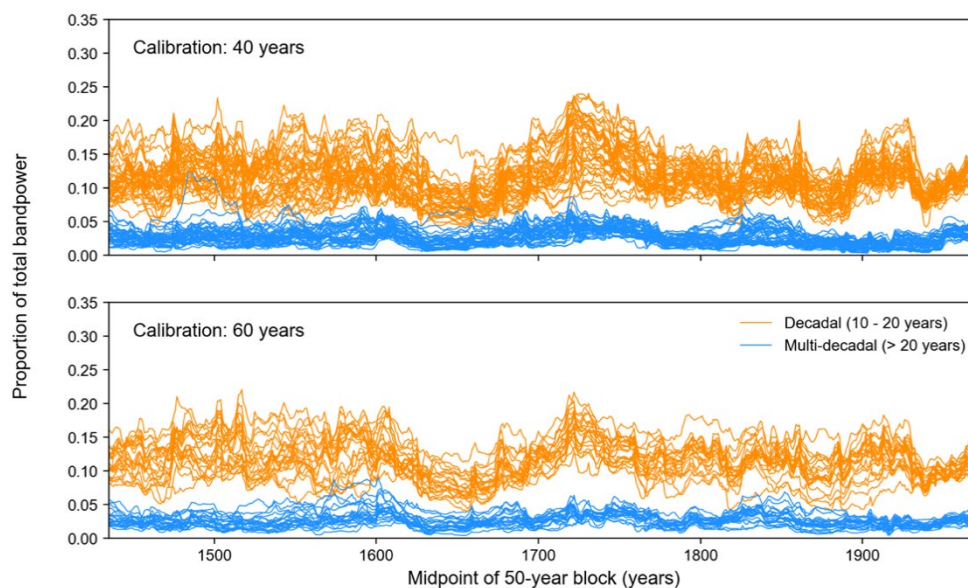


Figure 3-19 Power in the decadal (10-20 years, orange) and multidecadal (> 20 years, blue) frequency bands as a proportion of total power in 50-year moving windows for all reconstructions of Apia, Samoa calibrated using 40 or 60 years of instrumental data.

The implication, if low-frequency variability in the SPaDA is underestimated, is that the results will underestimate the true range of climate variability over the reconstruction interval. The RFC could reasonably be expected to have underestimated the occurrence of extreme or zonal El Niño events in the past. The wider implication of the short calibration period is that there is less certainty in the reconstruction results than there would be if a longer calibration period was used, even for grid points with independent verification periods.

3.5.3 Assumptions of stationarity

As mentioned above, the major criticism of using tree-ring reconstructions to discuss ENSO dynamics is the likelihood that teleconnections are not stationarity over centuries. However, the purpose of using a circum-Pacific network of tree rings in the SPaDA is to reduce the influence of non-stationarities between the Pacific and any single region on the reconstruction. Both temporal instabilities in ENSO-precipitation relationships, and the effects of non-linear ENSO teleconnections (e.g., regions where the precipitation response to one phase of ENSO is stronger than the other), should be reduced using the SPaDA predictor network. Using pseudoproxy

experiments, Batehup et al. (2015) demonstrated that choosing proxies from multiple teleconnected regions minimises the effects of non-stationarities on reconstruction skill. Further evidence that non-stationarities are unlikely to have affected the SPaDA is provided by the stability of the correlation between the SPaDA PC1 and the multiproxy reconstruction of Zhu et al. (2022) (Zhu_ctr2022; Figure 3-18a). The Zhu_ctr2022 reconstruction incorporates the MADA, North American drought atlas, New Zealand North Island kauri composite and a tree-ring composite from Altiplano, South America, as well as coral proxies. The SPaDA incorporates the MADA, MXDA, and the full ANZDA and SADA domains. If regional non-stationarities were affecting either reconstruction, periods of low fidelity should be apparent in the running correlation. While the SPaDA is likely robust to instability in ENSO teleconnections, until a long, continuous, error-free proxy from a centre of ENSO action is developed, the potential effects of non-stationarity on the SPaDA reconstruction cannot be fully assessed.

3.6 Conclusions

Recent research has made considerable progress on understanding recent trends in and causes of meteorological drought in the South Pacific (e.g., McGree et al., 2016). However, due to data limitations, the quantification and attribution of historical drought trends and variability is still lacking (Iese et al., 2021). The severe impacts droughts can have on small Pacific Islands, and uncertainty around future drought trends, means this is an important research gap. If a well verified SPaDA can be developed, it has the potential to substantially contribute to the understanding of past droughts in the South Pacific. In addition to resolving some of the limitations addressed in the previous section, future work could focus on reconstructing SPEI for both the wet and dry seasons to improve the understanding of the seasonal behaviour of droughts over the South Pacific.

The use of the RFC to identify extreme events shows great promise. The RFC result composites in Figure 3-13 demonstrate that the trained classifier can identify La Niña and El Niño events faithfully throughout the reconstruction interval. Anomalous patterns of precipitation do not consistently identify zonal events, as was hypothesised at the start of this study, which is due to the large differences in drought conditions in the instrumental data used to train the model, rather than the performance of the RFC itself. The ability of the RFC to provide the probability associated with a classification in addition to classifying each year is very useful. This method has the potential to explore the different impacts ENSO events have on Pacific Island drought.

What else is needed to develop a drought atlas for the South Pacific? Updated tree-ring chronologies would allow SPEI data after 1998 to be used for calibration, potentially allowing more grid points to be independently verified. New calibration methods could also be explored, such as moving-block calibration and verification (see Chapter 5, Appendix D), although the

results for Apia and Tahiti show that 40 years of data is the minimum period needed for calibration. Further efforts to recover documentary evidence of climate from the Pacific Islands would provide additional data for verifying the SPaDA results independent of proxies. Critically, more research effort is needed to develop new proxies from the centres of ENSO action – be they marine proxies or terrestrial proxies from the Pacific Islands.

Chapter 4 Do Southern Hemisphere tree rings record past volcanic events? A case study from New Zealand

The content in this chapter has been reproduced (with reformatting) from the following journal paper:

Higgins, P. A., Palmer, J. G., Turney, C. S. M., Andersen, M. S., & Johnson, F. (2022). Do Southern Hemisphere tree rings record past volcanic events? A case study from New Zealand. *Climate of the Past*, 18(5), 1169–1188. <https://cp.copernicus.org/articles/18/1169/2022/>

4.1 Abstract

Much of our knowledge about the impacts of volcanic eruptions on climate comes from proxy records. However, little is known about their impact on the low to mid-latitudes of the Southern Hemisphere. Using superposed epoch analysis, we investigated whether volcanic signals could be identified in annual tree-ring series from eight New Zealand dendrochronological species. We found that most species are reliable recorders of volcanic cooling and that the magnitude and persistence of the post-event response can be broadly linked to plant life history traits. Across species, site-based factors, particularly altitude and exposure to prevailing conditions, are more important determinants of the strength of the volcanic response than species. We then investigated whether chronology selection impacts the magnitude of post-volcanic cooling in tree-ring-based temperature reconstructions by developing two new multispecies reconstructions of New Zealand summer (December–February) temperature with one reconstruction from the pool of all available chronologies, and the other from a selected subset shown to be sensitive to volcanic eruptions. Both reconstructions record temperature anomalies that are remarkably consistent with studies based on instrumental temperature and the ensemble mean response of climate models, demonstrating that New Zealand ring widths are reliable indicators of regional volcanic climate response. However, we also found that volcanic response can be complex, with positive, negative, and neutral responses identified – sometimes within the same species group. Species-wide composites thus tend to underestimate the volcanic response. This has important implications for the development of future tree-ring and multi-proxy temperature reconstructions from the Southern Hemisphere.

4.2 Introduction

Emissions from large volcanic eruptions are a key source of temperature and hydroclimate variability on interannual to decadal timescales (Iles et al., 2013; Robock, 2005; Sigl et al., 2015). As few large volcanic eruptions have occurred during the instrumental era, much of our knowledge about volcanic impacts on climate, particularly regional and global temperature,

comes from proxy records spanning centuries to millennia (D'Arrigo et al., 2013; Tejedor et al., 2021; Wilson et al., 2016). These records are predominantly high-altitude or high-latitude tree-ring proxies from the Northern Hemisphere (e.g., Briffa et al., 1998; D'Arrigo et al., 2009; Pieper et al., 2014). In comparison, there are very few proxy-based characterisations of the temperature response to volcanic events from the Southern Hemisphere (Neukom et al., 2014; Tejedor et al., 2021). The limited number of studies considering Southern Hemisphere tree-ring proxies have generally not found significant impacts following what are considered “large” volcanic eruptions (Allen et al., 2018; Cook et al., 1992; Krakauer & Randerson, 2003; Palmer & Ogden, 1992). Two eruptions (Santa Maria in 1902 CE and Agung in 1963 CE) have been identified in tree-ring sites spanning South America, but the impacts of other eruptions on growth have proved less conclusive (Villalba & Boninsegna, 1992).

Discovering whether the hemispheres have contrasting sensitivities to volcanic eruptions is vital to understanding future climate projections (Neukom et al., 2014). The muted volcanic impact in Southern Hemisphere proxy reconstructions could be due to a maritime dampening effect on post-eruption cooling and/or the distribution of landmasses toward the Equator (Allen et al., 2018; Krakauer & Randerson, 2003; Raible et al., 2016). Such explanations suggest that the magnitude of Southern Hemisphere cooling is too small to be reliably recorded in tree-ring archives. However, climate models show a clear Southern Hemisphere volcanic signal via reduced mean surface air temperatures (Neukom et al., 2014, 2018). There are several potential explanations for the discrepancy between proxy reconstructions and climate models in the Southern Hemisphere. These include the underestimation of the moderating effects of the ocean on post-eruption cooling in climate models, changes to the hydrological cycle in response to volcanic cooling, uncertainties in volcanic forcing data, and/or proxy noise and spatial distribution (Neukom et al., 2018; Zhu et al., 2020).

The question remains as to whether Southern Hemisphere proxies – specifically tree rings – do record volcanic events. To our knowledge, no studies have explored the factors which influence whether (or not) volcanic signals can be identified using tree-ring data from the Southern Hemisphere. Tree growth depends on a range of environmental and biological factors, and thus careful site and tree selection is necessary to ensure that a specific influence of interest can be studied (Norton & Ogden, 1987). Northern Hemisphere tree-ring studies are predominantly from high latitudes or mid-latitude alpine treeline sites where tree growth is temperature limited (Scuderi, 1990). Around 80% of chronologies from such sites show significant growth reductions following large eruptions due to unusually low growing-season temperatures (Krakauer & Randerson, 2003). For high-latitude sites, decreased light availability after eruptions also contributes to the strong growth reduction (Tingley et al., 2014). Tree-ring studies from Northern Hemisphere mid-latitude lowland sites have shown that volcanic response is less clear, as

temperate-zone trees are less temperature-limited and have more complex relationships with multiple climate variables (Pieper et al., 2014; Wilson et al., 2016).

Exploring possible responses to volcanic eruptions, Pieper et al. (2014) proposed three modes for tree growth in temperate regions: (1) growth reduction due to decreased growing-season temperature, resulting in narrow rings, (2) neutral or no response if the climate sensitivity to volcanic eruptions is insufficient to influence tree growth, and (3) enhanced growth due to an increase in the diffuse light fraction and reduced water stress, resulting in wide rings. Temperate-zone trees from the Southern Hemisphere are also likely to display similar mixed volcanic signals, depending on their relative sensitivity mode and the magnitude of the regional cooling effect. Understanding these factors will help elucidate the proxy archive contribution to the Southern Hemisphere model–data discrepancy. This knowledge will benefit future studies of hemispheric temperatures and help identify which species and/or regions should be prioritised for future proxy development.

Our goal in this study is to assess whether Southern Hemisphere tree rings record past volcanic events using a multispecies network of high-quality, replicated tree-ring chronologies from New Zealand. This country is a long, narrow, archipelagic landscape stretching from 34 to 47 °S. Climatically, the northern part protrudes into the warm sub-tropical ridge, whereas the southern end is embedded in the cool southwesterlies (Salinger, 1980). The North Island and South Island axial ranges, which rise to 3764 m, are a significant barrier to east–west airflow, leading to strong regionalisation of precipitation anomalies (Salinger, 1980). Land clearing has resulted in the loss of forests from most low-land areas and nearly all of the eastern drylands. The most common remaining forest types are wet conifer–broadleaved forests and montane to alpine forests dominated by southern beech (Nothofagaceae) (McGlone et al., 2017).

Tree-ring chronologies have been developed from locations widely distributed throughout New Zealand. Since the initial dendrochronological studies undertaken by LaMarche et al. (1979), records have been generated from nine endemic species, of which seven are conifers and two are Nothofagaceae (Table 4-1). Five main species have been used to develop multi-centennial tree-ring chronologies: kauri (*Agathis australis*), pink pine (*Halocarpus biformis*), silver pine (*Manoao colensoi*), cedar (*Libocedrus bidwillii*), and silver beech (*Lophozonia menziesii*). Most chronologies are primarily sensitive to austral summer temperatures, with temperature reconstructions developed from beech (Norton et al., 1989), silver pine (Cook et al., 2002), cedar (Palmer & Xiong, 2004), pink pine (Duncan et al., 2010), and multi-species networks (Salinger et al., 1994). Thus, New Zealand, with its wide latitudinal and altitudinal range, regionalised climate zones, and wide distribution of tree-ring chronologies from multiple species – including some instances of multiple species from the same site – is ideal for studying tree-ring sensitivities

to past volcanic events. Using the New Zealand dendrochronological dataset, we aim to answer the following specific questions.

1. Can we identify volcanic signals in high-quality tree-ring series from the Southern Hemisphere?
2. Are there differences in the expression of volcanic signals amongst the species?
3. Does chronology selection impact the magnitude of post-volcanic cooling in tree-ring-based temperature reconstructions?

4.3 Data and methods

4.3.1 Tree-ring chronologies

The New Zealand tree-ring chronologies analysed in this study were collated to develop the Eastern Australia and New Zealand Drought Atlas (Palmer et al., 2015; Figure 4-1). Palmer et al. (2015) identified chronologies from the International Tree Ring Data Bank and personal collections, screened the tree-ring measurements for dating problems using the software program COFECHA (Holmes., 1983), and developed site “master” chronologies from the raw ring widths using the “signal-free” method of standardisation (Melvin & Briffa, 2008). The metadata for all New Zealand chronologies are provided in Table C-1 in Appendix C. As only a single chronology has been developed from mountain toatoa (*Phyllocladus alpinus*), it was excluded from the study, leaving a pool of 96 chronologies from eight dendrochronological species for volcanic response analysis.

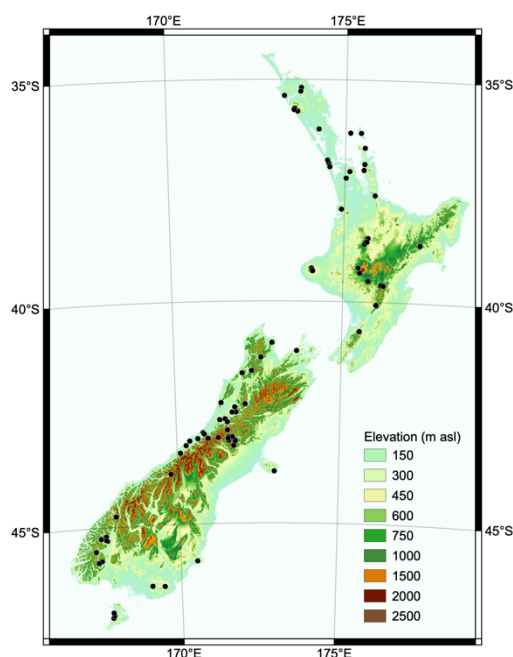


Figure 4-1 Distribution of tree-ring chronologies in New Zealand. Elevation data sourced from the LINZ Data Service and licensed for reuse under CC BY 4.0.

Table 4-1 Distribution, reported climate sensitivities, and key references for New Zealand dendrochronological species.

Code	Species	Common name	No. chronologies	Ring width (mm/y)	Persistence (GINI ²)	Distribution	Reported climate sensitivity	Temperature sensitivity ³	Chronology development
AGAU	<i>Agathis australis</i>	Kauri	17 (9*) ¹	1.66 ± 0.59	0.106	North Island, north of 38°S; predominantly lowland forests, can be > 500 m	ENSO; inverse relationship to current year temperature and precipitation.	Inverse relationship to current summer temperatures.	(Boswijk et al., 2006; Buckley et al., 2000; Fowler et al., 2008; LaMarche et al., 1979; Ogden & Ahmed, 1989; Palmer et al., 2006)
HABI	<i>Halocarpus biformis</i>	Pink pine	20 (19*)	0.44 ± 0.1	0.074	Low altitude to sub-alpine; central North Island to Stewart Island	Frost tolerant; sensitive to year-round temperatures	Current growing season (P); prior summer (S).	(D'Arrigo et al., 1996; Fenwick, 2003; Xiong et al., 1998)
LACO	<i>Manoao colensoi</i> (formerly <i>Lagerostrobus colensoi</i>)	Silver pine	6 (4)	0.56 ± 0.20	0.065	Low-elevation forests of the South Island west coast and some North Island locations.	Summer temperatures	Inverse relationship to prior autumn (P); Current summer/autumn (S).	(Cook et al., 2002; D'Arrigo et al., 1998)
LIBI	<i>Libocedrus bidwillii</i>	New Zealand cedar	26 (21)	0.7 ± 0.17	0.091	Widely distributed over North and South Islands south of 38°S; 200 to 1200 m above sea level	Summer temperatures, precipitation	Inverse relationship to prior summer (P); Current summer (S).	(LaMarche et al., 1979; Xiong & Palmer, 2000)
NOME	<i>Lophozonia menziesii</i> (formerly <i>Nothofagus menziesii</i>)	Silver beech	7 (1)	1.14 ± 0.24	0.136	Montane and subalpine forests, common in the South Island	Summer temperatures	Inverse relationship to prior summer/ autumn (P); Current summer (S).	(Norton, 1983b, 1984)
NOSO	<i>Fuscopora cliffortioides</i> (formerly <i>Nothofagus solandri</i> var. <i>cliffortioides</i>)	Mountain beech	11 (4)	0.92 ± 0.23	0.136	Closed forests of the central North Island and the eastern South Island, valley floor to ~1300 m	Summer temperatures	Inverse relationship to prior summer/ autumn (P); Mixed current summer signal (S).	(Norton, 1983a, 1984)
PHAL	<i>Phyllocladus alpinus</i>	Mountain toatoa	1	0.59 ± 0.22	0.065	Throughout New Zealand, lowland to subalpine forests	N/A	N/A	(LaMarche et al., 1979)
PHGL	<i>Phyllocladus totoa</i> (formerly <i>P. glaucus</i>)	Toatoa	4	0.63	0.129	North Island, montane forest between 850 and 1000 m	Summer temperatures, precipitation, pressure anomalies	Inverse relationship to prior summer/ autumn.	(Dunwiddie, 1979; LaMarche et al., 1979; Palmer, 1989; Salinger et al., 1994)
PHTR	<i>Phyllocladus trichomanoides</i>	Tanekaha	5	1.04	0.118	Lowland forest up to 800 m above sea level, north of 42°S	Summer temperatures, precipitation, pressure anomalies	Inverse relationship to prior summer/ autumn.	(Dunwiddie, 1979; LaMarche et al., 1979; Palmer, 1989; Palmer & Ogden, 1992; Salinger et al., 1994)

¹ Number in brackets indicate the number of chronologies extending to 1990 available for the temperature reconstructions. *Includes published master chronology.

² GINI coefficient – an all-lag measure of diversity in tree-ring records (Biondi & Qeadan, 2008)

³ Summary of sensitivity to New Zealand average temperatures, calculated for this study (see also Figure C-1 to Figure C-6). Where significant relationships to both prior and current season temperatures exist, P indicates the primary (dominant) sensitivity and S indicates the secondary sensitivity.

Table 4-1 summarises the distribution, average climate responses, and main wood properties (average annual ring growth and temporal correlation or persistence) of the species, as described by the studies documenting the development of the chronologies. In addition, the response of each species to average New Zealand monthly temperatures, calculated for this study, is also summarised. All species show significant ($p < 0.05$) relationships with average New Zealand temperatures (Mullan, 2012; Salinger, 1981) during individual months of the current growing season, except toatoa (Table 4-1, Figure C-1 to Figure C-6 in the Appendix C). Tree growth is only weakly correlated with average monthly temperatures, with $|r| < 0.3$ for most chronologies. Pink pine shows stronger correlations with summer temperatures, with r values of 0.4–0.6. Pine pink is also significantly correlated to temperatures over the entire growing season, whereas the other species are seasonally restricted with significant correlations to peak summer temperatures only. Most species are positively correlated to current season temperatures, with wider ring widths associated with warm years; however, kauri and beech show an inverse relationship to temperature, with warm temperatures restricting growth. Cedar, silver pine, mountain beech, and both *Phyllocladus* species show stronger sensitivities to prior than current season temperatures (Figure C-1 to Figure C-6).

4.3.2 Selection of volcanic events

Event selection is a significant source of uncertainty in tree-ring studies of volcanic cooling. The choice of volcanic events can greatly influence the magnitude of average regional cooling identified (Esper et al., 2013; Wilson et al., 2016). In addition, for many events that occurred before instrumental records, the timing, location, and size of eruptions are uncertain (Garrison et al., 2018; Timmreck et al., 2021). For this analysis, we are interested in those events which would likely have reduced growing-season temperatures over New Zealand and thus be identifiable as ring-width anomalies. Therefore, we selected events using a regional volcanic dimming threshold rather than an eruption magnitude. Prior to the instrumental era, we picked events from the Greenland and Antarctic ice core sulfate aerosol analysis of Toohey and Sigl (2017) based on peak stratospheric atmospheric aerosol depth (SAOD). We averaged SAOD, modelled using the Easy Volcanic Aerosol module (Toohey et al., 2016), over the latitudinal range of New Zealand (30 to 50 °S). The SAOD magnitude corresponding to a substantial temperature response is unknown before analysis. However, selecting a magnitude post-analysis based on the observed response risks biasing the results (Haurwitz & Brier, 1981). Therefore, the following two different SAOD thresholds were used: $SAOD > 0.08$, which resulted in 10 eruptions for analysis between 1400 and 1900 CE, and $SAOD > 0.04$, resulting in 18 eruptions for the same period (Figure 4-2). Between 1900 and 1990 CE, we selected the three largest tropical eruptions, which have been shown to have significant impacts on instrumental temperatures in New Zealand (Salinger, 1998). At each methodological step, the analysis was carried out using both the 13 (10 pre-1900 CE

events plus 3 post-1900CE) and 21 (18 pre-1900CE events plus 3 post-1900 CE) event lists separately. Full details of all selected eruptions are provided in Table C-2 in Appendix C.

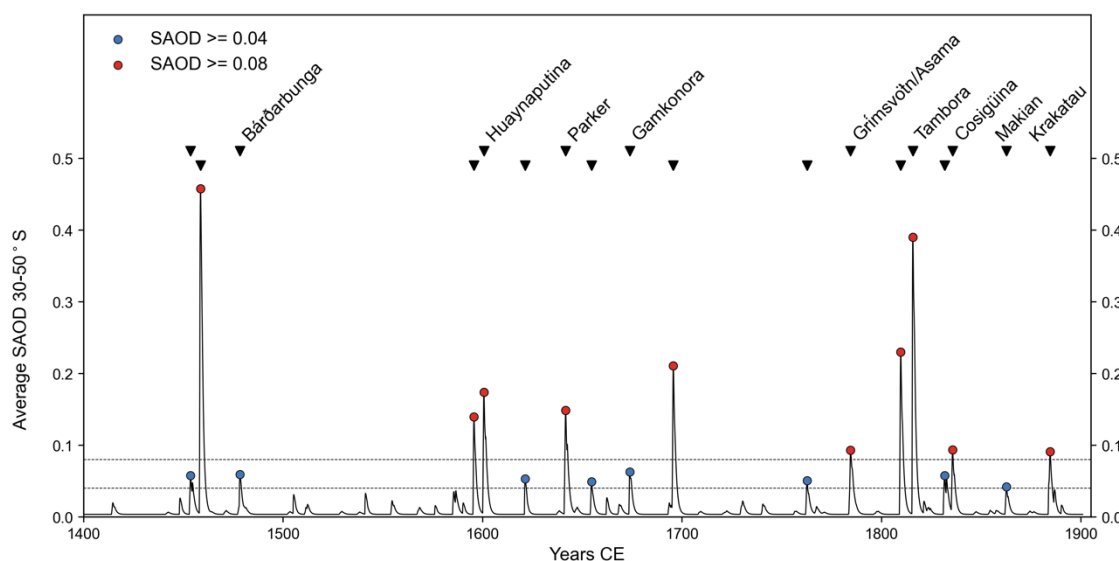


Figure 4-2 Selection of volcanic events based on thresholds of peak modelled stratospheric atmospheric optical depth (Toohey and Sigl, 2017), averaged over 30–50 °S, greater than 0.04 (blue) and 0.08 (red). Known eruptions are labelled.

4.3.3 Superposed epoch analysis

We tested whether a volcanic signal can be identified in New Zealand tree-ring chronologies using superposed epoch analysis (SEA; Haurwitz and Brier, 1981), a statistical technique widely used to determine the impacts of volcanic eruptions on climate (Adams et al., 2003; Rao et al., 2019; Salinger, 1998; Scuderi, 1990; Tejedor et al., 2021). The composite response of individual chronologies to the 13 largest eruptions and the 21 full eruption list between 1400 and 1990 CE was studied 0–5 years post-event, with anomalies calculated by subtracting the average of the nearest 5-year background period undisturbed by volcanic forcing (Table C-2; Büntgen et al., 2020). Species-level responses were then tested using a composite chronology produced by simple averaging of annual values across sites (Cook & Kairiukstis, 1990). Volcanic responses were categorised as positive or negative if the anomalies exceeded the 5th or 95th percentile response of 10 000 random samples of years undisturbed by volcanic forcing or neutral if they fell between these bounds.

4.3.4 Temperature reconstructions

To investigate the influence of chronology selection on the identification of volcanic signals in temperature reconstructions, we report two new reconstructions of New Zealand summer temperatures (December–February). We used the New Zealand average “seven-station” monthly instrumental temperature series (Mullan, 2012; Salinger, 1981), obtained from the New Zealand National Institute of Water and Atmospheric Research (NIWA), to examine the temperature response of the chronologies. Correlations were calculated between autoregressively modelled

chronologies and monthly climate data, with each month treated as a separate time series. A 20-month window was selected for correlation analysis, extending from October of the previous growing season to May at the end of the current austral growing season. Two growing seasons were included as significant prior season climate sensitivities have been reported for some species.

Based on the response analysis, December–February (DJF) was selected as the seasonal target, as this window captures the strongest correlations across all species (Table 4-1). To ensure sufficient overlap between the chronologies and the temperature dataset for calibration and verification, only chronologies extending to or beyond 1990 CE were retained for the reconstructions. As many sites have not been updated since they were originally sampled in the 1970s and 1980s, only 58 of the 96 chronologies were retained. The first reconstruction (NZall) included the full suite of available chronologies extending to 1990 CE, while the second (NZsel) was limited to those chronologies that showed a significant volcanic signal using SEA. In each case, only those chronologies significantly ($p < 0.1$) correlated to average DJF temperatures over the period 1911–1990 CE were used. The tree-ring series were also tested as potential predictors with a lag of 1 year with respect to the temperature data, as prior climate often has a lingering influence on current year’s tree growth (Fritts, 1976; Table 4-1). Average DJF temperatures were reconstructed using nested principal component linear regression (Cook et al., 1999, 2007, 2010). A 50:50 split calibration–validation scheme was used in which the model was initially calibrated on the first half of the data (1911–1950 CE) and validated on the second half (1951–1990 CE); following this, the model was re-estimated with the calibration and validation periods reversed. Once the split models were verified based on the verification period reduction of error (VRE) and verification period coefficient of efficiency (VCE; Cook and Kairiukstis, 1990) metrics, the entire data period was used to produce the final reconstructions (Briffa et al., 1990).

The volcanic response in tree-ring reconstructions of temperature was also tested using SEA and the two sets of volcanic eruption years. Further, variation in the temperature response to different volcanic events was estimated by calculating the 90th percentile bootstrap confidence interval from 1000 replicates drawn without replacement from the event list (Rao et al., 2019). In each iteration, approximately two-thirds (9 of 13 or 15 of 21) of the volcanic events were selected. The confidence interval provides some indication of how eruptions of different sizes, locations, and seasonality may impact the SEA results. To further assess how event selection may have affected the SEA results, the analysis was repeated using volcanic events selected from the ice core analysis of Crowley & Unterman (2013), using a Southern Hemisphere-wide average threshold of SAOD > 0.08 and SAOD > 0.04 rather than a regional threshold (Table C-3).

We compared the volcanic response seen in our multi-species reconstructions to the ensemble mean DJF response of seven climate models from the Coupled Model Intercomparison Project 5 (CMIP5) suite with Last Millennium (past1000, 850–1850 CE) simulations. The CMIP5 models were forced with either the Gao et al. (2008) or Crowley and Unterman (2013) volcanic forcing series (see Table C-4). Data from the historical simulations were appended to extend the dataset from 1850 to 2005 CE.

4.4 Results

4.4.1 Overall species volcanic responses

The results of the superposed epoch analysis for the 13 largest volcanic eruptions between 1400 and 1990 CE are shown in Figure 4-3. Two composite responses are shown for each species: the response averaged across all sites (“all chronology composite”) and the response calculated only from the site chronologies that individually showed a significant (either positive or negative) response to volcanic eruptions (“sensitive chronology composite”). Analysis was repeated for the full set of 21 eruptions with SAOD > 0.04, with similar (but weaker) results for most species, suggesting that not all events had a measurable climatic impact over New Zealand (Figure C-7).

The species-wide response to volcanic events varied widely between New Zealand dendrochronological species. Three out of eight species, i.e., silver pine, mountain beech, and tanekaha, recorded a composite neutral response. Tanekaha is only weakly correlated to New Zealand average temperatures (Figure C-6b), which may explain its subdued response. However, compared to other species, mountain beech and silver pine both show relatively strong temperature sensitivities (Figure C-1a and Figure C-4). As many mountain beech chronologies extend only to the mid-1700s, the species composites were tested against a smaller subset of volcanic events, which may contribute to this result.

Of the remaining five species, one recorded a positive response, while four recorded a negative response. Kauri (Figure 4-3a) was the only species to show a composite positive response to volcanic events, maximal in year $t + 1$. Kauri showed a consistent response across sites, with all except two chronologies showing a positive anomaly following an event, although only 8 of the 17 positive responses were significant at $p < 0.05$. The sensitive chronology composite recorded a very strong $t + 1$ response, indicating that at these eight sites, kauri receives a significant growth benefit from the climatic changes following a volcanic eruption. This response is coherent with the predominant kauri temperature sensitivity, which is an inverse response to current summer temperatures (Figure 4-3). However, as most kauri chronologies are only weakly correlated to monthly temperatures, the strong volcanic response suggests climatic changes other than temperature also contribute to the post-event growth benefit.

Pink pine, cedar, silver beech, and toatoa show lagged negative responses to volcanic events, with peak negative anomalies recorded in years $t+2$ or $t+3$ (Figure 4-3b, c, e, and g). The pink pine response is consistent across sites. All except one pink pine chronology recorded a negative response in $t+2$, which was significant for most of the chronologies (14/21; $p < 0.05$). This response is coherent with the pink pine's broad sensitivity to temperatures over the current growing season (Figure C-2), i.e., cooler spring–summer–autumn temperatures suppress growth across most pink pine sites. Similarly, the negative silver beech response is coherent with its current season temperature sensitivity (Figure C-1b), although neither the temperature correlation nor the volcanic response is particularly strong. All four toatoa chronologies recorded a significant negative response in $t+3$. However, as toatoa shows only weak lagged correlation with monthly temperatures (Figure C-6a), the link between temperature sensitivity and volcanic response is not easily elucidated. In contrast, cedar does not show a consistent species-wide response. Both significant negative and positive responses were recorded in 13 of the 26 chronologies, with the rest showing a neutral response. This is despite a largely consistent within-species temperature sensitivity, which is an inverse response to prior season temperatures (Figure C-5).

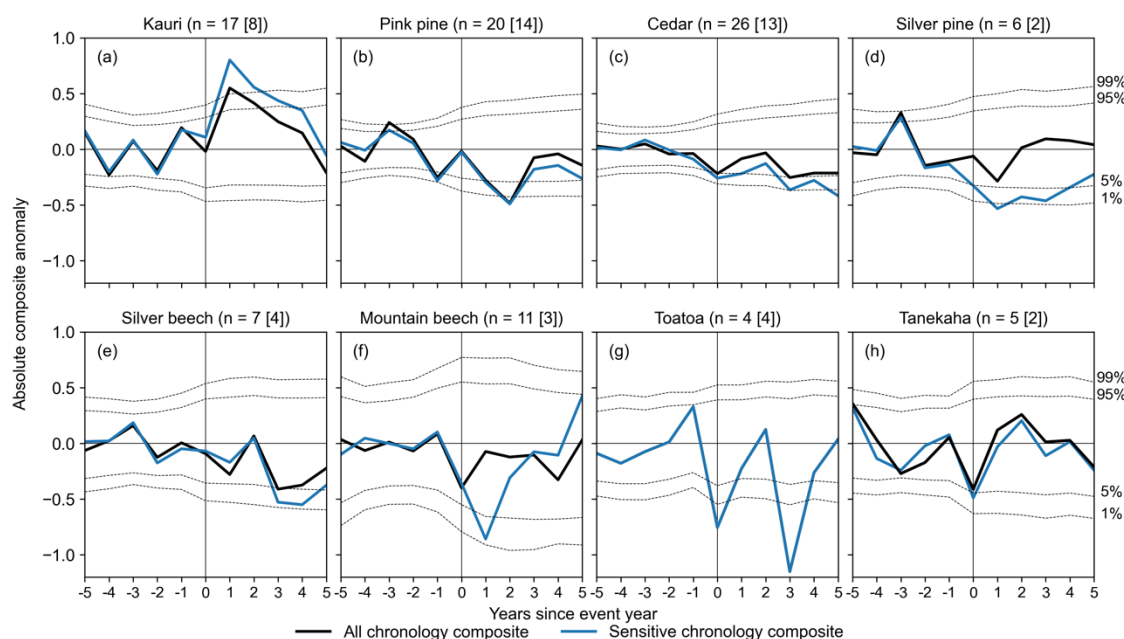


Figure 4-3 Mean chronology departures 5 years before and 5 years after the 13 largest eruption years (year 0), separated by tree species. The chronologies contributing to the species-wide composite are shown in black, with the number of chronologies indicated in parentheses. The sensitive chronology composite is shown in blue and the number of contributing chronologies is shown in brackets. Significance bands (dotted grey lines) are the 1st, 5th, 95th, and 99th percentile of 10 000 random samples of non-event years from the species-wide composite.

4.4.2 Within-species variability in volcanic response

The overall muted species response of cedar masks very different individual chronology responses. Cedar ring-width series respond differently to volcanic events depending on their location, with both very negative and very positive responses recorded. The other species do not

show similar variation. The cedar chronologies have the widest geographical distribution of any species, and thus geographical factors may influence the variability in response. We used k-means clustering via principal component analysis (Ding & He, 2004) to investigate whether within-species variation could be explained by obvious factors like regional climate or elevation. Principal component analysis (PCA) was applied to the longest common time interval of the chronologies (1732–1976 CE), and the first four principal components were retained.

Five chronology groups were identified via clustering (Figure 4-4a), broadly corresponding to differences in region and altitude. North Island chronologies were distributed in two groups. All chronologies are from montane to subalpine areas above 800 m, with groups differentiated between coastal (G1) and inland (G2) locations. A single chronology from the north of the South Island was included in G2. Chronologies from the western coast of the South Island were also distributed in two groups, differentiating between lowland (G3) and montane (G4) forest. The final grouping (G5) includes three chronologies from the dry eastern lowlands. Strong – but opposing – volcanic responses are identified via clustering. Significant lagged post-eruption growth reduction is identified in groups G1 and G2 from montane to subalpine sites from the North Island, including Takapari (Figure C-8c), and the southernmost grouping, G5. Group three (G3), which includes lowland chronologies from the north-western coast of the South Island, including Ahaura and Flagstaff Creek (Figure C-8d and e), receives a growth benefit in the two years following an eruption similar to that observed in North Island kauri. In cedar, we observed all three of the proposed temperate-zone tree responses to volcanic events – positive, negative, and neutral growth – all within a single species, highlighting the importance of site-based factors in determining tree response in temperate zones.

4.4.3 Calibration and validation of the temperature reconstructions

The peak summer period was selected as the seasonal reconstruction target, as the largest number of chronologies across species showed significant correlations with temperatures between December and February (Table 4-1). Selecting only those chronologies correlated at $p < 0.1$ with average DJF temperatures resulted in a predictor pool of 45 chronologies for reconstruction NZall, of which 25 showed significant volcanic impacts and were used to produce the reconstruction NZsens.

Both New Zealand DJF average temperature reconstructions are shown in Figure 4-5 alongside their instrumental fit over the 1911–1990 CE calibration period. There is good agreement between the reconstructions, with a Pearson r of 0.81 over the entire reconstruction period and 0.9 after 1750 CE. The initial, best-replicated nests, which cover the period 1790–1990 CE, account for 67.5% and 58.2% of instrumental temperature variability for the NZall and NZsens reconstructions, respectively. The minimum amount of variance explained over all nests is 44.1%

for NZall and 34.3% for NZsens. The full calibration and validation statistics are provided in Figure C-9 and Figure C-10. For both reconstructions, VRE values are positive over all nests from 1413 to 1990 CE; however, VCE values are only positive after 1520 CE in the NZsens reconstruction when calibrated to the early window (1911–1950 CE). The declining instrumental data quality in the early period and the relatively few predictors retained for NZsens, are likely responsible for the negative values.

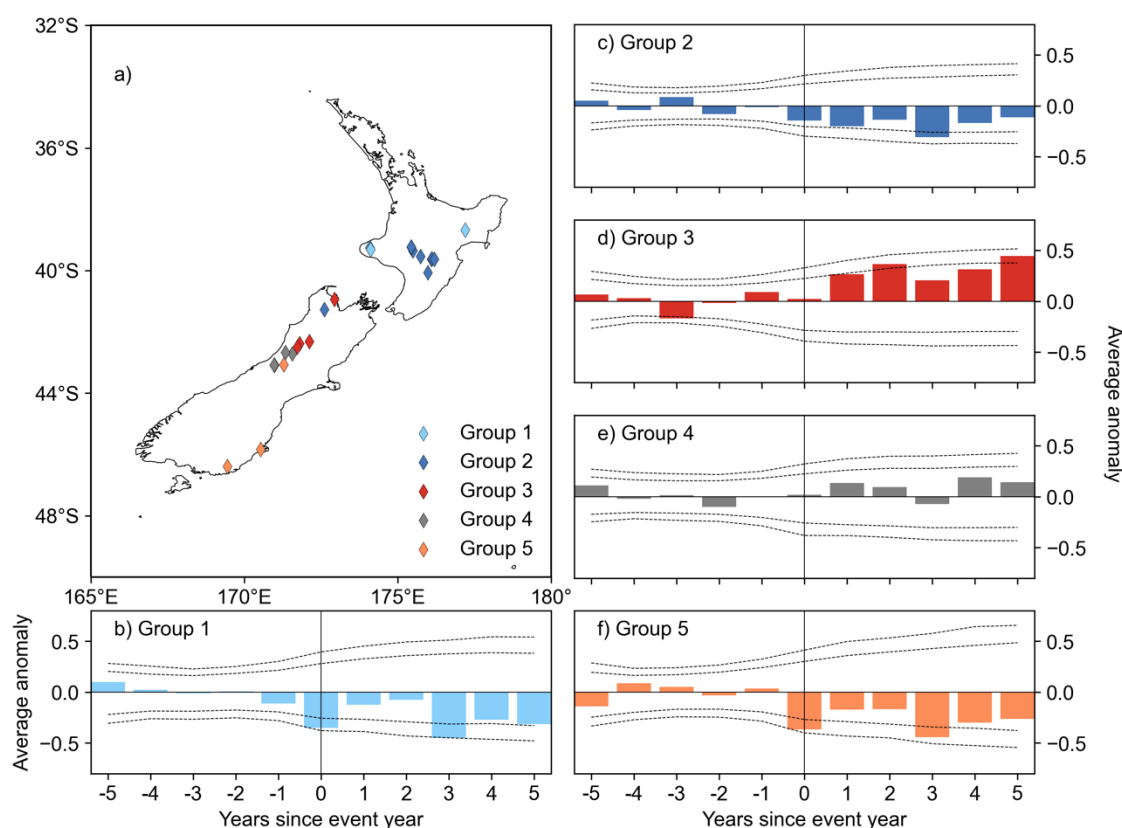


Figure 4-4 a) Results of k-means clustering of New Zealand cedar chronologies. b–f) Mean chronology departures 5 years before and after eruption years (year 0), separated by cluster, and the 95th and 99th significance levels calculated by generating 10 000 random samples of non-event years from the group composite. The map in a) was made with Natural Earth free vector map data, which are available at <http://naturalearthdata.com> (last access: 17 November 2021).

Increasing temperatures are observable in both reconstructions from around 1950 CE, matching the trend in instrumental temperatures. Prior to the instrumental period, temperatures were higher than average for a sustained period during the 16th century and for a shorter period in the early 18th century. Periods of cooler-than-average temperatures have also occurred, starting at ~ 1470, 1630, and 1860 CE. The reconstructions are consistent with previously published temperature reconstructions from New Zealand (Cook et al., 2002; Duncan et al., 2010; Palmer & Xiong, 2004) despite differences in the climate targets (seasons and locations), reconstruction methodologies, and large differences in the number and geographical distribution of chronologies used in their development (Figure C-11 and Table C-5).

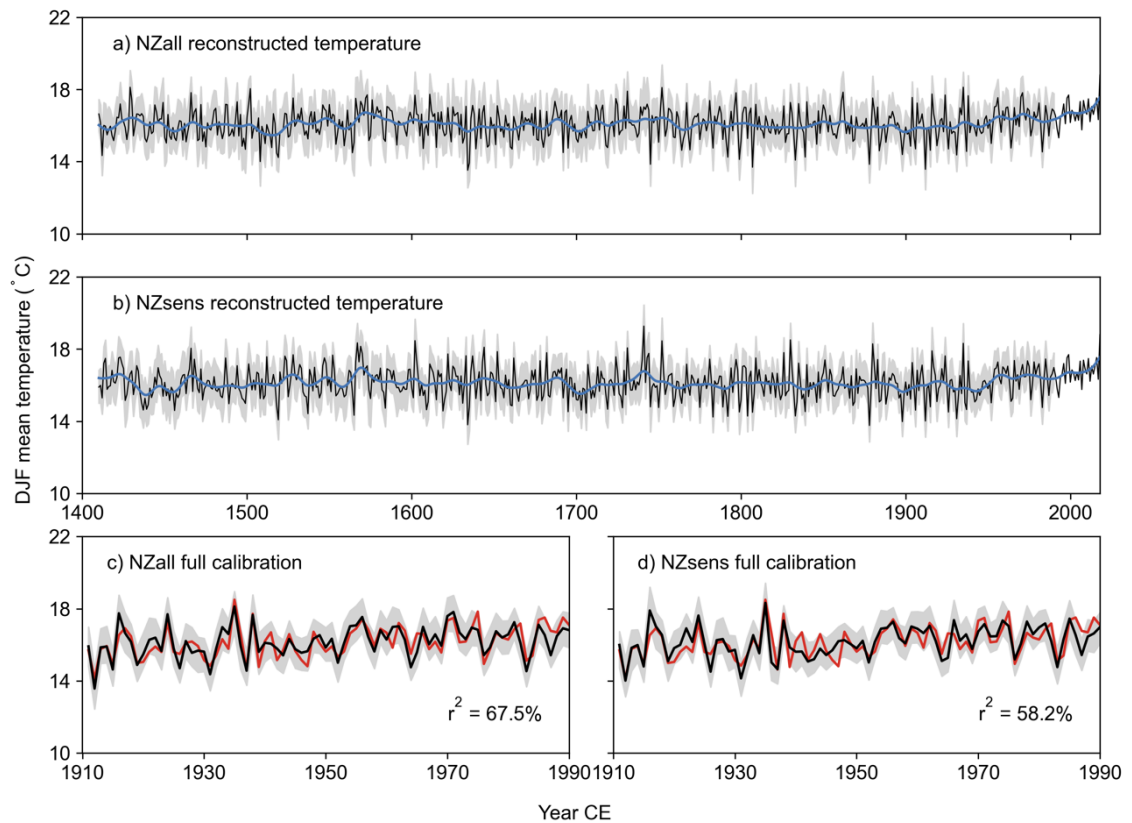


Figure 4-5 New Zealand average DJF temperature reconstructions. Unfiltered (black) and filtered (20-year spline; blue) mean DJF reconstruction with 90% uncertainty interval (grey) between 1400 and 2018 CE for a) NZall and b) NZsens. Reconstruction fit to instrumental temperature (red) over the full calibration period 1911–1990 CE for c) NZall and d) NZsens. The 90% uncertainty interval was calculated from 300 maximum entropy bootstrap replications.

4.4.4 Volcanic signals in the temperature reconstructions

Figure 4-6 shows the results of the SEA analysis for the two New Zealand temperature reconstructions, for both sets of volcanic events, compared to the volcanic response of an ensemble of seven CMIP5 model outputs for the New Zealand region. For the 21 events with $SAOD > 0.04$, results are remarkably similar between the temperature reconstructions and the model ensemble. Both the timing and magnitude of the post-event anomaly, which is only significant in year $t + 1$, are consistent across the models and reconstructions, as is the timing of the post-event recovery, which occurs in year $t + 2$. The response to the subset of the 13 largest events shows larger year $t + 1$ temperature anomalies for both the climate models and the reconstructions, with the greatest increase in response magnitude displayed by the model ensemble. Year $t + 1$ anomalies are ~ 0.1 °C larger for NZall, ~ 0.2 °C larger for NZsens, and ~ 0.4 °C larger for the model ensemble than the 21-event anomalies. However, the mean model ensemble lies within the 90% uncertainty range of both reconstructions, indicating that the difference in magnitude between models and reconstructions is not significant for either the restricted 13-event set or the full 21-event set. The difference in post-event recovery is significant, with temperatures recovering by year $t + 2$ in the reconstructions and modelled temperature

anomalies persisting in year $t + 2$. This is the opposite result to many tree-ring-based temperature reconstructions from the Northern Hemisphere, which show lagged persistence compared to climate models due to biological effects in the ring-width series (see Sect. 4.4).

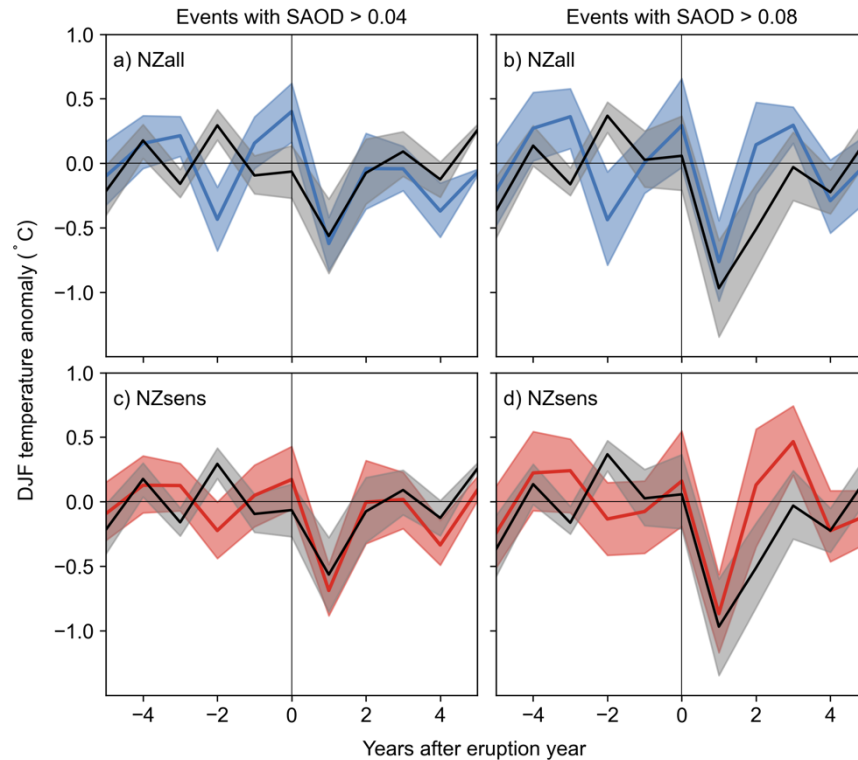


Figure 4-6 Mean anomalies 5 years before and after 21 eruption years with $\text{SAOD} > 0.04$ a, c) and 13 eruption years with $\text{SAOD} > 0.08$ b, d) for both the NZall (blue) and NZsens (red) reconstructions. The mean response from an ensemble of seven climate models to the same set of events is shown in black. The 90th percentile bootstrap confidence intervals were constructed from 1000 replicates of either 15 or 9 event years at random.

The difference between the NZall and NZsens reconstruction response is minor for both subsets of volcanic events. The anomaly recorded by NZsens is $0.07\text{ }^{\circ}\text{C}$ larger than NZall for the 21-event series and $0.1\text{ }^{\circ}\text{C}$ larger for the 13-event series. The small difference between the reconstructions can be explained by the weightings applied to the chronologies in each reconstruction, with both reconstructions heavily weighted towards the same subset of chronologies. Four of the eight highest-weighted chronologies underpinning NZall are sensitive to volcanic events, and three of these are within the top four highest-weighted chronologies underpinning NZsens (Figure 4-7). Thus, limiting NZsens to only sensitive chronologies had less impact on post-eruption temperature anomalies than was expected.

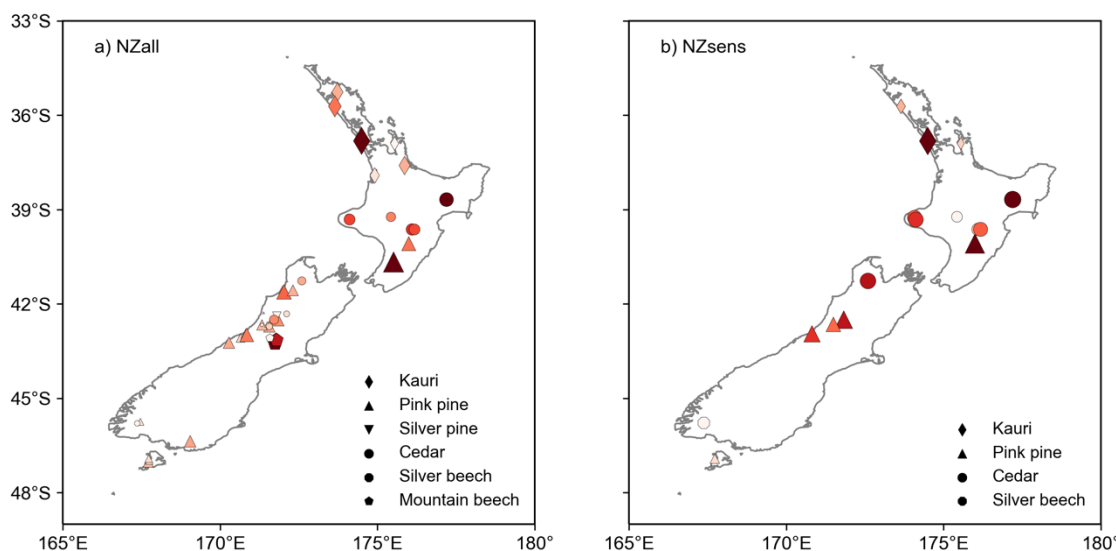


Figure 4-7 Distribution of tree rings used in a) the NZall temperature reconstruction and b) the NZsens temperature reconstruction. Larger, darker red markers represent chronologies with greater relative weighting in the multiple regression. Made with Natural Earth free vector map data available at <http://naturalearthdata.com> (last access: 17 November 2021).

4.5 Discussion

4.5.1 Volcanic responses recorded by New Zealand trees

Previous studies have not identified significant volcanic responses in Southern Hemisphere tree rings (Krakauer and Randerson, 2003; Palmer and Ogden, 1992) or in the temperature reconstructions based on them (Allen et al., 2018; Cook et al., 1992). In contrast to previous studies, we found that volcanic events can be clearly identified in New Zealand ring widths, although some species are stronger recorders of volcanic signals than others. Unlike Northern Hemisphere high-latitude and treeline sites, which tend to show a consistent reduction in growth due to volcanic cooling and reductions in light availability, no consistent response was identified across New Zealand conifer and Nothofagaceae species. Predominantly negative (pink pine, cedar, toatoa, silver beech), positive (kauri), and neutral (mountain beech, tanekaha, silver pine) responses were recorded. As most New Zealand chronology sites have been sampled from localised areas of residual forest that are restricted compared to their natural distributional range, it is difficult to distinguish between species-related sensitivities to volcanic eruptions and regional climate factors that may control the response. In reality, it is the combination of biological characteristics, including intrinsic species sensitivity, regional climate, and site-specific factors (e.g., soils, exposure to prevailing conditions), which determine the observed volcanic response. While necessarily simplified, here we discuss some possible explanatory factors for the species-wide responses.

The species-level results in Figure 4-3 and Figure C-7 clearly show two response types following volcanic events: a rapid but short-lived response and a delayed response that begins in year $t + 2$ or $t + 3$ but then persists over several years. The first response, demonstrated by mountain beech

and kauri, we label here the “fast responder”, and the second, shown by pink pine, silver pine, cedar, and silver beech, we label the “stress tolerator” (after Grime, 1979). Many New Zealand conifers appear as typical stress-tolerator species, which have adapted to growing in highly stressful conditions. As a group, they are longer-lived, slower-growing, taller, and markedly frost-tolerant species compared to endemic angiosperms and are tolerant of poor soils (e.g., low nutrients and often poor drainage). Silver beech is highly frost and exposure resistant, shade tolerant, and grows on extreme exposure sites (Manson, 1974; Stewart, 2002). Several species, including pink pine and silver pine, show an affinity for leached, low-nutrient, and waterlogged soils (McGlone et al., 2017). The stress tolerators are characterised by narrow average ring widths and high biological persistence (temporal autocorrelation) arising from carbohydrate storage or leaf retention (see Table 4-1). Therefore, stress tolerators are slow to respond to changes in conditions, such as volcanic cooling. The stress-tolerator response resembles the response of high-latitude Northern Hemisphere trees, although arctic trees display even greater lagged persistence, with suppressed growth for up to 10 years following volcanic events (Krakauer and Randerson, 2003).

In contrast, the fast responders both respond and recover more quickly from a detrimental change in conditions (e.g., mountain beech) or can rapidly capitalise on beneficial conditions (e.g., kauri). These are relatively fast-growing species, indicated by wider average ring widths than the stress tolerators, and they have lower persistence (Table 4-1). Mountain beech is shade intolerant but has several responses to abnormally cold temperatures, including rapid shoot growth and temporarily halting bud formation, which allows it to rebound quickly after a poor summer (Wardle, 1970). Kauri could be considered a stress tolerator due to its affinity for poor soils, occurrence on ridges and slopes, and drought tolerance (McGlone et al., 2017); however, relative to other New Zealand conifers in this study, it is a fast responder.

In contrast to the subdued, persistent decrease in growth shown by the stress tolerator species, the initial decline in toatoa ring width in year $t + 0$, subsequent extreme decline in year $t + 3$, and recovery by year $t + 4$ closely resembles the boom–bust behaviour of the fast responders, but with several years’ lag. The dominant climate response of toatoa is a weak negative correlation to prior growing-season temperatures (Figure C-6a) but a strong positive correlation to summer temperatures two growing seasons prior. This results in a quasi-biennial pattern of wide and narrow rings, which has also been observed in other species of *Phyllocladus*. This pattern may be related to a climate-triggered flowering cycle (Allen, 1998; Ogden & Dunwiddie, 1982), foliage production followed by cladode senescence, or a mast seeding event, which can be triggered by multiple cool summers in New Zealand Podocarpaceae (Norton & Kelly, 1988). All three potential explanations suggest toatoa channel resources to reproduction at the expense of cambial growth (Harper, 1977) following a climate trigger after volcanic events – perhaps increased

humidity and reduced summer water stress at low-elevation North Island sites or an increase in photosynthesis due to a greater fraction of diffuse radiation. More research on the ecology and life history of toatoa is needed to confirm these possible mechanisms.

We compared the response at six sites which each have chronologies from two different species (Figure C-8), providing the unique opportunity to compare species differences in volcanic sensitivity directly whilst controlling for most other factors. The three species that are co-located and thus available for site-based comparison (cedar–pink pine and cedar–silver pine) all showed stress-tolerator responses to volcanic eruptions. Pink pine and cedar often grow together in mixed stands. Both species are sensitive to temperature, although pink pine has a maximum correlation to late summer temperature, whereas cedar responds to conditions in the winter prior to the growing season and in spring (Fenwick, 2003). A significant difference in the response between species was observed only at one of three sites. Comparison over additional sites is therefore required to determine whether the difference in seasonal temperature response may result in a difference in the sensitivity of pink pine and cedar to climate disturbance following eruptions. Differences between the cedar and silver pine responses were observed at two of the three sites, with cedar showing greater sensitivity to volcanic eruptions. Silver pine is primarily found in the moist, temperate, low-elevation forests of the western coast of the South Island. It is a shade-tolerant species that grows in highly competitive closed-canopy forests on infertile, poorly drained or waterlogged soils (Cook et al., 2002; Wardle, 1977). It is an exceptionally slow-growing species and shows little year-to-year variability in ring width (Table 4-1). Thus, it is unsurprising that volcanic effects were more readily identified in cedar at the Ahaura and Flagstaff Creek sites (Figure C-8).

4.5.2 A kauri growth benefit

An interesting result of this study is the strong positive species-wide response of North Island kauri to volcanic events (Figure 4-3a) despite the weak correlation of the chronologies to monthly temperatures (Figure C-3). Over 70% of the kauri chronologies recorded a small but significant increase in ring width in the year following a large eruption ($SAOD > 0.04$), indicating a growth benefit from volcanism. Previous studies of kauri climate response function have shown that growth is not primarily related to temperature but is enhanced during cool, dry years, with the strongest (negative) correlation to austral spring temperatures (Buckley et al., 2000; Ogden & Ahmed, 1989). Ring growth is thus enhanced during El Niño events, which result in cool, dry spring conditions in northern New Zealand, and kauri has been successfully used as a proxy for the El Niño–Southern Oscillation (ENSO; Fowler et al., 2008). The mechanism behind this relationship remains largely unclear, although it has been proposed that reduced cloud cover during El Niño events may benefit kauri growth via increased insolation (Fowler et al., 2000). The opposite conditions follow a volcanic eruption, with reduced direct insolation and increased

diffuse insolation due to scattering by volcanic aerosols (Gu et al., 2003). The commonality between the two sets of events is cooler-than-average spring and summer temperatures.

This suggests that kauri may capitalise on a decrease in summer evapotranspiration during both El Niño events and following significant eruptions. Maximum kauri growth occurs during spring, with large declines in growth rate over the peak summer months when evapotranspiration exceeds precipitation in the northern North Island (Fowler et al., 2005). Dendrometer band studies suggest that reduced spring and summer moisture stress may delay the cessation of growth, resulting in wider annual rings (Palmer and Ogden, 1983). No summer cessation of growth was observed by Palmer and Ogden (1983) at the highest-altitude site, Mt Moehau (1MOE, Table C-1). This site receives moisture from condensation and fog drip, as well as rainfall, reducing the summer precipitation deficit. Plausibly, the increase in diffuse radiation and resulting enhanced photosynthesis (Gu et al., 2003; Robock, 2005) may also contribute to post-event kauri growth. However, tree growth is generally more constrained by the environment than photosynthesis (Fatichi et al., 2019; Zweifel et al., 2021), and thus increased photosynthesis may not necessarily translate into growth (i.e., a wider ring) in the presence of another limiting factor, such as the summer moisture deficit. Additional research is needed to understand the relative importance of temperature, light availability, humidity, and soil moisture to sub-annual growth in kauri.

Many observational and modelling studies propose a link between large tropical volcanic eruptions and sea surface temperature variability in the tropical Pacific, with El Niño-like conditions more likely in the year following a significant event (Adams et al., 2003; Christiansen, 2008; Emile-Geay et al., 2008; Khodri et al., 2017; McGregor et al., 2010; Miao et al., 2018), although this link is not always identifiable in the paleoclimate data (Dee et al., 2020). The three eruptions included in this analysis since 1900 CE co-occurred with an El Niño event, and the 1982/83 CE El Niño is one of the largest on record (Santoso et al., 2017). While we do not wish to debate the eruption–ENSO response as part of this study, these potential interactions complicate our analysis of the volcanic signal in kauri.

In an attempt to distinguish between the effects of El Niño events and volcanic eruptions on kauri growth, we repeated the SEA analysis, removing the three volcanic eruptions since 1900 CE. A smaller composite ring-width anomaly was recorded without the three events, but the response remained significant in year $t + 1$ (Figure C-13). To test the potential follow-through impact of the kauri response to El Niño events on the temperature reconstructions, we removed the ENSO component via linear regression of the Southern Oscillation Index on the reconstructed temperature series. There is a negligible difference between the original and ENSO-adjusted temperature reconstructions for all volcanic events between 1880 and 1990 CE, except for the response to El Chichón in 1982 CE, which is much larger in the unadjusted reconstruction (Figure

C-14). Based on currently available data, we cannot confidently discount that the kauri growth benefit identified in year $t + 1$ may be a secondary response to changes in tropical Pacific sea surface temperatures following a large eruption. However, this is unlikely to have a large impact on the post-event anomalies identified in the temperature reconstructions.

4.5.3 Site-related volcanic responses

Differences in volcanic response between sites are observed for all species, largely between sites with significant decreases in growth and sites with neutral responses (Figure 4-3 and Figure C-7). More temperature-limited sites, such as sites at higher elevation and lower latitude, are expected to be more sensitive to volcanic cooling and thus experience the most reduction in growth. Broadly in line with this expectation, chronologies that are highly correlated to monthly temperatures show greater sensitivity to volcanic eruptions (Figure C-15). However, there are many exceptions, both for temperature-sensitive sites with a neutral volcanic response and sites that are only weakly correlated to temperature but that are markedly affected by the climatic changes following volcanic eruptions. Thus, volcanic response cannot be simply interpreted as a response to cooler-than-average temperatures.

Based on the variability in volcanic response observed in cedar (Figure C-8) it is evident that site-related factors can have a substantial impact on the volcanic response within a species group. This finding was further explored using k-means clustering of the widely distributed cedar chronologies (Figure 4-4). Altitude and latitude are expected to be important explanatory factors for cedar tree growth, as together they represent the relative importance of temperature and water stress at a site. Temperature-limited high-altitude cedar sites at or near the treeline in the North Island ranges show a significant decline in tree growth following eruptions, as did coastal sites at higher latitudes ($\sim 46^\circ\text{S}$). We observed a significant increase in cedar growth at low-elevation sites on the northern South Island (Group 3) in response to volcanic cooling, which we interpret as a reduction in summer evaporative demand. Low-elevation trees are more likely to experience summer water stress than their high-elevation counterparts due to higher average temperatures if precipitation rates are similar. In contrast to the significant positive correlation of treeline cedar sites to average summer temperatures (Figure C-5), the Group 3 chronologies display a negative correlation to summer temperatures (not significant at $p < 0.05$) indicating that soil moisture may be a limiting factor at these sites. Thus, we find that both high- and low-elevation cedar stands can reliably record volcanic signals, provided that the sites experience sufficient temperature or moisture stress. Sites that are neither strongly temperature nor water limited (Group 4; Figure 4-4) show a neutral response to volcanic eruptions. A limitation of this analysis is that we have not considered potential spatial differences in the regional pattern of cooling or changes in regional atmospheric circulation patterns (Salinger, 1998), which could also impact the results for species with a wide distributional range (e.g., cedar).

Tree growth of species at different sites is limited by a variety of environmental factors, of which temperature and soil moisture are only two (Fritts, 1976). For many New Zealand species, little is known about what types of sites might accentuate these factors and thereby enhance the climatic sensitivity in the tree-ring series (Dunwiddie, 1979). Although the overall Group 2 cedar response was significant, not all high-altitude sites recorded a volcanic signal. Considering the location, aspect, forest characteristics, and soil type at individual cedar sites, we find that exposure to prevailing conditions is the key explanatory variable for the within-species response for sites near the altitudinal limit. Sites that record a significant growth response have high exposure to prevailing winds and are more sensitive to abnormally low growing-season temperatures. In contrast, chronologies from sites characterised by undulating ridgelines and more continuous forest showed a neutral growth response. Sites experiencing mesic conditions and closed-canopy forests tend to show lower sensitivity to adverse environmental conditions, such as low temperatures (Phipps, 1982). Closed-canopy forests are also more likely to be sensitive to increases in the fraction of diffuse radiation driving photosynthesis (Gu et al., 2003; Tingley et al., 2014), and thus the increase in diffuse radiation fraction may compensate for the decrease in temperature to a greater extent compared to sites with more open canopies.

North Island kauri is another species for which exposure appears to be a determining factor in the chronology response to eruptions. For kauri, sites with a strong positive response to volcanic eruptions are coastal sites exposed to prevailing wind conditions or sites limited by poor underlying sediment substrates (e.g., 1TRO, 1KAW; Table C-1). In comparison, sites that showed little volcanic response were those on the leeward side of the coastal range, which are buffered by inland microclimate effects (e.g., 1PBL, 1PKF; Table C-1). These sites likely experience less water stress during the summer; therefore, we expect that they receive less benefit from reduced evaporative demand related to volcanic

cooling, resulting in a neutral response. The importance of aspect to climate sensitivity – particularly when windward sites are exposed to prevailing winds – has been highlighted in many previous studies (e.g., Dang et al., 2007; Rozas et al., 2013). For New Zealand, a thorough exploration of the importance of site-based parameters other than elevation and latitude (e.g., aspect, exposure, soil type) to volcanic sensitivity is limited because these parameters have not been recorded for many sites.

4.5.4 Implications for temperature reconstructions

We expected to find a substantially greater volcanic response in NZsens (i.e., limited to only those chronologies with an individual significant volcanic response) compared to NZall. However, while NZsens shows a larger post-volcanic temperature response, the difference between the two reconstructions is not significant Figure 4-6 As shown in Figure 4-7, both reconstructions are

heavily weighted towards the same subset of chronologies. Since, sites with higher sensitivity (correlation) to temperature in general show higher volcanic response (Figure C-15), limiting NZsens to only sensitive chronologies has only a small impact on post-eruption temperatures. Another factor leading to the minimal difference between the reconstructions is that many volcanically sensitive chronologies, particularly kauri, were cored before 1990 CE and therefore not included in either temperature reconstruction. These sites should be updated with priority for future studies of volcanic impact in the Southern Hemisphere. In developing NZsens, we used a “volcanic sensitivity” threshold based on the SEA result significance ($p < 0.05$). By doing so, we reduced the size of the predictor pool, which reduced the strength of the reconstruction, particularly over the initial 100 years, when there were relatively few predictors (Figure C-10a).

When testing the reconstructions using the event list from Toohey and Sigl (2017) (Figure 4-6), we concluded that losing reconstruction strength outweighs the small increase in volcanic sensitivity in NZsens and that it is not beneficial to restrict the predictor pool. However, when we then repeated the SEA analysis using the event list derived from Crowley and Unterman (2013), the mean response of NZall to the largest subset of 12 events with SAOD > 0.08 (Table C-3; Figure C-12c) was not significant ($p > 0.05$). The benefit of the restricted predictor set in strengthening the volcanic signal in NZsens is highlighted when using this event list. It is important to note that the mean NZall response to the full set of Crowley and Unterman (2013) events with Southern Hemisphere-average SAOD > 0.04 is significant (Figure C-12a), which suggests that some eruptions classified as SAOD > 0.08 in Table C-3 were not climatically effective over New Zealand. Potential reasons for the differences between the two volcanic datasets, which may have impacted the findings here, are discussed Sigl et al. (2014) and Toohey and Sigl (2017).

Figure C-12c indicates that the SEA compositing procedure can fail when using a small number of events if the volcanic signal is small compared to other sources of interannual variability, especially when not all events have a climate impact. This is one potential reason that this study has identified significant volcanic signals in Southern Hemisphere tree rings when previous studies did not. Before Gao et al. (2008), no comprehensive reconstruction of global aerosol loading was available. Uncertainty in eruption dates and sizes likely contributed to the lack of volcanic signal identified in studies undertaken prior to the release of the “Gao” dataset (e.g., Cook et al., 2002; Villalba & Boninsegna, 1992). Revisiting the data from other major Southern Hemisphere dendrochronology regions (e.g., Tasmania, South America) is therefore an important aspect for future research.

Previous studies that narrowly focused on the impacts of the 1815 CE eruption of Tambora on New Zealand tree rings (Norton, 1992; Palmer & Ogden, 1992) also presented inconclusive

results. The authors of these studies were seeking synchronous growth reductions across species, whereas our analysis, with the benefit of much more data, shows responses vary widely between species. Because of this variation in response, studies that rely on compositing across species and regions (e.g., Krakauer and Randerson, 2003) are also likely to underestimate the true volcanic response in Southern Hemisphere tree rings.

In this study we also compared reconstructed temperature anomalies with anomalies from climate models over the New Zealand region for DJF – peak growing season in the Southern Hemisphere. We found no difference between the magnitude of the year $t + 1$ anomaly for either the 13- or 21-event composites, with the difference between the reconstructed and modelled anomalies $< 0.12\text{ }^{\circ}\text{C}$ for both sets of events. Recent work investigating the reasons for differences between climate model and proxy reconstructions of post-event temperature anomalies in the Northern Hemisphere (Zhu et al., 2020) found that these differences can be minimised by focusing on the growing season rather than annual temperatures, undertaking regional rather than hemispheric analysis, and resolving biological persistence. By focusing on regional DJF temperatures, we resolved two of these issues. A criticism of temperature reconstructions based solely on ring widths is that biological persistence in treeline conifers decreases the abruptness and magnitude of volcanic cooling. In the Northern Hemisphere, more emphasis is now being placed on maximum latewood density (MXD) or mixed MXD and ring widths for investigations of volcanic cooling (Wilson et al., 2016; Zhu et al., 2020). For this study, we focused only on ring widths, as few investigations of alternative wood properties have been undertaken in New Zealand (Blake et al., 2020; Xiong et al., 1998).

Unlike some Northern Hemisphere studies, our ring-width temperature reconstructions show no increased persistence in temperature anomalies following eruptive events compared to the climate model ensemble (Figure 4-6). Ring widths from New Zealand conifers therefore appear suitable for volcanic investigations. Northern Hemisphere high-altitude and high-latitude trees predominantly used to determine the temperature impacts of volcanic eruptions contain higher biological persistence than the chronologies we used in our temperature reconstructions, influencing their post-eruption response. For example, the average first-order autocorrelation of our predictor chronologies is 0.53 (range 0.15–0.87; SD 0.15) compared to Arctic sites with an average of 0.62 (range 0.15–0.93; SD 0.13; Cropper and Fritts, 1981). Nevertheless, several New Zealand species do show a lagged volcanic response (Figure 4-3 and Figure C-7) that is not present in the final temperature reconstructions. Methodological decisions play an important role in the persistence of tree-ring-based temperature reconstructions (Büntgen et al., 2021). In our reconstructions, pre-whitening of both the tree-ring predictors and the temperature data, including significant lagged predictors, and the selection of predictors from multiple species all contribute to the responses we identified.

4.6 Conclusions

Very few studies have considered whether volcanic signals are identifiable in tree-ring chronologies from the Southern Hemisphere. We investigated whether volcanic events could be identified in New Zealand tree rings using data from eight dendrochronological species. In doing so, we set out to answer the following three questions. First, can volcanic signals be identified in the Southern Hemisphere? Second, are there species-level differences in volcanic signal strength? Finally, does chronology selection impact the magnitude of post-volcanic cooling in temperature reconstructions from tree rings?

In answering the first two questions, we found that New Zealand dendrochronological species are reliable recorders of volcanic cooling, but that response varies across species. The magnitude and persistence of the species-wide volcanic response can be broadly linked to plant life history traits. The larger magnitude and more immediate responses are recorded by the “fast-responder” species, such as mountain beech and kauri, and more delayed but persistent responses are recorded by the “stress-tolerator” species, such as silver pine. In general, volcanic events can be more readily observed in the ring widths of fast-responder species, which should be prioritised for future regional or hemispheric studies. Unfortunately, the paucity of information on the ecology of many New Zealand species limits our understanding of how species allocate resources to processes other than cambial growth in response to short-term changes in climatic conditions.

The volcanic response of New Zealand trees is complex, with positive, negative, and neutral responses identified sometimes within the same species group. For subalpine sites, this finding is not dissimilar to previous studies of temperate-zone Northern Hemisphere species. We found that site-related factors have greater control over displayed volcanic responses than species and presented a suite of plausible, testable hypotheses explaining the results. The altitude of the site with respect to the species altitudinal limit and exposure to prevailing conditions are factors thought to determine whether a tree-ring volcanic response could be identified. In some cases, sites near the lower altitudinal limit of the species were also strong responders, suggesting a reduction in summer moisture stress could also be an important factor in post-volcanic growth. Our results indicate that studies intending to utilise tree rings to investigate regional volcanic cooling should carefully consider the characteristics of the sample site. While valid for all dendrochronological studies, it is particularly important for identifying volcanic signals, as we find that the range of temperature-sensitive sites is greater than the range of volcanically sensitive sites.

In answer to the last question, we developed two new reconstructions of New Zealand summer temperature to investigate whether chronology selection impacted the magnitude of post-volcanic cooling. There was little difference in the post-event anomalies, suggesting that limiting the

predictor pool for volcanic sensitivity is unnecessary when targeting average growing-season temperatures in New Zealand. Both reconstructions showed temperature anomalies remarkably consistent with studies based on instrumental temperature and the ensemble mean response of CMIP5 climate models. Based on these results, New Zealand ring widths are reliable indicators of regional volcanic climate response.

More broadly, the findings of this study have important implications for the development of future tree-ring or multiproxy hemispheric temperature reconstructions from the Southern Hemisphere, which often incorporate species-specific “master” chronologies (i.e., composite chronologies developed from across many sites) into their predictor pool. As shown in this study, the compositing process can result in reduced volcanic signals when more than one type of response (i.e., positive, negative, or neutral) is recorded by a single species. However, as most New Zealand species-level composites show significant volcanic responses, temperature reconstructions based on composite chronologies should also show the influence of volcanic eruptions.

4.6.1 Data availability

All data and software used in this study are publicly available. The New Zealand “seven-station” temperature series was downloaded from NIWA at <https://niwa.co.nz/seven-stations> (last access: 4 July 2021; NIWA Research, 2021). The Southern Oscillation Index time series was sourced from <https://climatedataguide.ucar.edu/climate-data/southern-oscillation-indices-signal-noise-and-tahitidarwin-slp-soi> (last access: 7 August 2021; Trenberth and National Center for Atmospheric Research Staff, 1984). The raw tree-ring width series can be downloaded from the International Tree Ring Data Bank at <https://www.ncei.noaa.gov/products/paleoclimatology/tree-ring> (last access: 13 March 2021; NCEI, 2022). Superposed epoch analysis was undertaken using R code published on Mendeley Datasets with <https://doi.org/10.17632/8p7y29hz5h.1> (Rao et al., 2019). The two new temperature reconstruction series can be accessed through the NOAA/World Data Service for Paleoclimatology archives (<https://www.ncdc.noaa.gov> (last access: 6 February 2022; NOAA, 2022).

4.6.2 Supplement

The supplement related to this article is available online at: <https://doi.org/10.5194/cp-18-1-2022-supplement>.

4.6.3 Author contributions

PAH and JGP conceptualised this study, JGP curated the data, and PAH undertook the analysis. PAH wrote the manuscript with contributions from all authors.

4.6.4 Competing interests

The contact author has declared that neither they nor their co-authors have any competing interests.

4.6.5 Disclaimer

Publisher's note: Copernicus Publications remains neutral with regard to jurisdictional claims in published maps and institutional affiliations.

4.6.6 Special issue statement

This article is part of the special issue “Interdisciplinary studies of volcanic impacts on climate and society”. It is not associated with a conference.

4.6.7 Acknowledgements

We acknowledge the World Climate research Programme's Working Group on Coupled Modelling, which is responsible for CMIP, and we thank the climate modelling groups (listed in

Table C-4 of this paper) for producing their model output and making it available. The authors thank Kathy Allen, Michael Sigl, and the two anonymous reviewers for their helpful comments that greatly improved this paper.

4.6.8 Financial support

Philippa A. Higgins is supported by an Australian Government Research Training Scholarship and the UNSW Scientia PhD Scholarship Scheme. Fiona Johnson is supported by the UNSW Scientia Program. Further support was provided by the ARC Centre of Excellence in Australian Biodiversity and Heritage (grant no. CE170100015).

4.6.9 Review statement

This paper was edited by Michael Sigl and reviewed by two anonymous referees.

Chapter 5 Unprecedented High Northern Australian Streamflow Linked to an Intensification of the Indo-Australian Monsoon

The content in this chapter has been reproduced (with reformatting) from the following journal paper:

Higgins, P. A., Palmer, J. G., Rao, M. P., Andersen, M. S., Turney, C. S. M., & Johnson, F. (2022). Unprecedented high Northern Australian streamflow linked to an intensification of the Indo-Australian monsoon. *Water Resources Research*, 58, e2021WR030881. <https://doi.org/10.1029/2021WR030881>

5.1 Abstract

Streamflow in Australia's northern rivers has been steadily increasing since the 1970s, most likely due to increased intensity in the Indo-Australian monsoon. However, because of limited data availability, it is hard to assess this recent trend and therefore contextualise potential future climatic changes. In this study, we used a network of 63 precipitation-sensitive tree-ring chronologies from the Indo-Australian and Asian monsoon regions to reconstruct streamflow in the Daly catchment in the Northern Territory of Australia from 1413 to 2005 CE. We used a novel wavelet-based method to transform the variance structure of the tree-ring chronologies to better match the hydroclimate prior to reconstruction with a hierarchical Bayesian regression model. Our streamflow reconstruction accounts for 72%–78% of the variance in the instrumental period and closely matches both historical flood events and independent proxy records, increasing confidence in its validity. We find that while streamflow has been increasing since the 1800s, the most recent 40-year period is unprecedented in the last ~600 years. Comparison to an independent coral-based streamflow record shows regional coherency in this trend. Extreme high flows were found to be linked to La Niña events, but we found no significant relationship between streamflow and El Niño events, or streamflow and other regional climatic drivers. More work is therefore needed to understand the drivers of the recent streamflow increase, but, regardless of the cause, water managers should be aware of the paleoclimatic context before making decisions on water allocations.

5.2 Plain Language Summary

Large-scale agricultural development has been proposed for the Daly catchment in the Northern Territory of Australia. Since the start of record keeping in the Daly catchment in the 1970s, streamflow has been steadily increasing, most likely due to increases in Australian monsoon rainfall. However, because of the limited amount of data, it is hard to assess whether this recent increase in streamflow is unusual, part of a longer trend, or a natural cycle in monsoon rainfall. In this study, we used rainfall-sensitive tree growth and a statistical model to reconstruct Daly River streamflow over the past 592 years. Our streamflow reconstruction closely matches known

past flood events, increasing confidence in its validity. We find that streamflow has increased since the 1800s but that the most recent 40-year period is unprecedented in the last 600 years. More work is needed to understand the drivers of this increased streamflow but regardless of the cause, water managers should be aware of the Daly River's history before making decisions on allocating water to agriculture or other large users.

5.3 Introduction

Water resources in the large floodplains of monsoonal north Australia are determined by the onset, duration, and intensity of the Indo-Australian summer monsoon (IASM). Importantly, recharge to aquifers contributing critical dry season discharge to groundwater fed springs and rivers is also linked to the intensity of monsoon rainfall (McCallum et al., 2010; Singh et al., 2019). Endemic flora and fauna, and the cultural values of Indigenous peoples, are dependent on the wet/dry seasonality in flows (CSIRO, 2009; Russell-Smith et al., 1997). The IASM is closely tied to the El Niño–Southern Oscillation (ENSO). Both climatic phenomena, the IASM and ENSO, exhibit substantial inter-annual and decadal variability (Smith et al., 2008; Suppiah, 1992). This variability can cause both droughts and floods, with severe impacts on the lives and livelihoods of people living in the region.

Since 1950, monsoonal Australia has experienced an increase in summer rainfall (Taschetto & England, 2009), and annual streamflow (Zhang et al., 2016), thought to be a result of changes in the IASM. Historical meteorological records from ship logs show that this recent trend is part of a longer-term intensification of the IASM, occurring at least since the early 1800s (Gallego et al., 2017). Despite this intensification, rainfall variability remains high; consecutive years of monsoon failure occurred during the 2018–19 and 2019–20 wet seasons, resulting in very low river levels and water restrictions over much of Australia's north (BOM, 2019, 2020a).

It is highly uncertain whether the recent trend in rainfall will continue. Projections of future monsoon rainfall are challenging because of the strong climate coupling between the land, atmosphere, and oceans. Climate models predict a future thermodynamic increase in mean monsoonal rainfall (Christensen et al., 2013), however, there are large inter-model uncertainties, most notably for the IASM (Brown et al., 2017). The ensemble mean of the Climate Model Intercomparison Project Phase 5 projects an increase in IASM rainfall variability at daily to decadal timescales (Brown et al., 2017). Increased variability has important implications for the management of water resources, as existing infrastructure, management plans, and entitlements may be inadequate for future changes (De Loe & Kreutzwiser, 2000), particularly in regions like monsoonal Australia where water storage potential is limited (CSIRO, 2009).

Palaeohydrological reconstructions are useful tools for supporting water resource management and planning under uncertainty (Allen et al., 2015; Rice et al., 2009). There has been a recent

interest in palaeohydrological reconstructions for monsoon rivers (e.g., Nguyen et al., 2020 and references therein) due to the inability of short instrumental records to fully characterise hydroclimatic variability, and uncertainty around future changes in streamflow and flood frequency (Rao et al., 2020). Long reconstructed records can increase our understanding of variability in monsoon streamflow and floodplain dynamics, as well as their relationship with major drivers of climate variability such as ENSO. However, very few streamflow reconstructions are available for the IASM region (see D'Arrigo et al., 2011; Verdon-Kidd et al., 2017) in part due to the limited availability of high-resolution (sub-annual to annual) precipitation and streamflow proxies across the region (Allen et al., 2015; D'Arrigo et al., 2008). There is an urgent need for multi-centennial reconstructions of streamflow variability in monsoonal Australia to reduce the uncertainty over the impact of future climate change and increasing resource demands.

The Daly River, a monsoonal river system in the northwest of the Northern Territory, is one of the northern Australia's largest rivers and one of the few with perennial flows (Morrison, 1970). Annual streamflow is highly dominated by monsoon rainfall, with dry season flows, fed by groundwater discharge, accounting for less than 10% of total annual flow. Reliable stream gauging stations and monitoring bores for the Daly River system are sparse. Very limited data exists prior to the mid-1970s and there is low confidence in dry season flow records for many gauges. The paucity of data greatly inhibits the potential to assess the linkages between the hydrological regime, resource availability and dependent ecosystems (CSIRO, 2009). Declining rainfall trends in southern Australia and the perception of abundant land and water resources in the monsoon tropics have recently renewed interest in agricultural development in northern Australia and the Daly region (Petheram et al., 2008; Yeates et al., 2013). With limited storage potential in seasonally dynamic aquifers, increased dry season agricultural demand is likely to change surface and groundwater regimes with consequences for the environment (CSIRO, 2009). Extending short hydrological records is essential for improving the assessment and management of water resources in the Daly catchment and the IASM region more broadly.

Here we present a paleohydrologic reconstruction of Daly River streamflow that extends available instrumental observations by more than five centuries and discuss its linkages with both changes in the IASM and Pacific atmosphere-ocean climate variability. Our Daly River streamflow reconstruction was developed using a tree-ring network from across the IASM region and remote sites with strong teleconnections to the IASM. We demonstrate the benefits of a new method for paleohydrologic reconstruction, in which a wavelet-based variance transform maximises the ability of the tree-ring predictors to characterise the hydroclimate, resulting in a streamflow reconstruction that better matches the instrumental data. We then compare our record to other observational and proxy records for the region, specifically low-resolution sediment cores from the Daly River and a coral-based river reconstruction from subtropical eastern Australia,

demonstrating that recent increases in streamflow are regionally coherent and unprecedented in the reconstruction interval.

5.4 Study area and data availability

5.4.1 The Daly catchment

The 320-km Daly River flows from the foothills of Arnhem Land to discharge into the Timor Sea in the northwest, with a catchment area of approximately 53,000 km² (Figure 5-1). Important tributaries of the Daly River include the Katherine, which contributes around 40% of the total flow in the system, and the Flora, Edith and Douglas rivers, all of which have high conservation and tourism value (CSIRO, 2009).

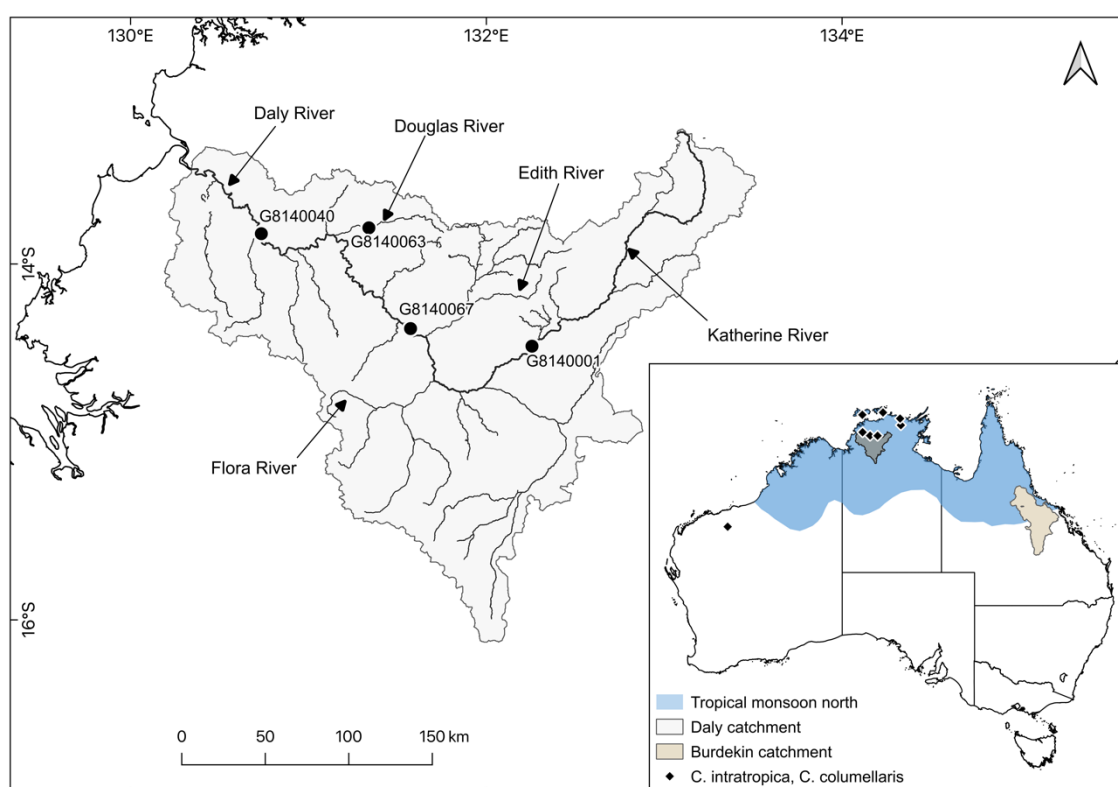


Figure 5-1 The Daly catchment showing the location of the four selected stream gauges (blue triangles with gauge numbers). The inset map shows the location of the Daly catchment (grey) and Burdekin catchment (beige) within the Australian tropical monsoon region (light blue), and the locations of *Callitris intratropica* and *C. columellaris* tree-ring chronologies within and proximal to the monsoon region (black diamonds). The approximate southern monsoon region boundary was adapted from the Australian Bureau of Meteorology climate classification.

The Daly region receives an average of 1020 mm of rainfall annually of which more than 95% falls in the November to April wet season. Annual potential evapotranspiration is 1940 mm/year; thus the region is water limited (CSIRO, 2009). There is a steadily increasing trend in total annual rainfall (significant at $p < 0.001$; Mann-Kendall test) throughout the historical period (Figure 5-2a). and consequently, evapotranspiration is also increasing due to increased catchment water availability (Wasko et al., 2021). Annual streamflow is closely linked to wet season rainfall, with an average of 94% of runoff occurring during wet season months. Peak discharge occurs during

January, February, and March (Figure 5-2b). Dry season baseflow in the perennial reaches of the Katherine and Daly rivers is the result of discharge from the region's two major karstic aquifers, the Tindall Limestone and the Oolloo Dolostone (CSIRO, 2009). Variations in dry season baseflow are due to higher or lower aquifer levels in the preceding wet season (CSIRO, 2009).

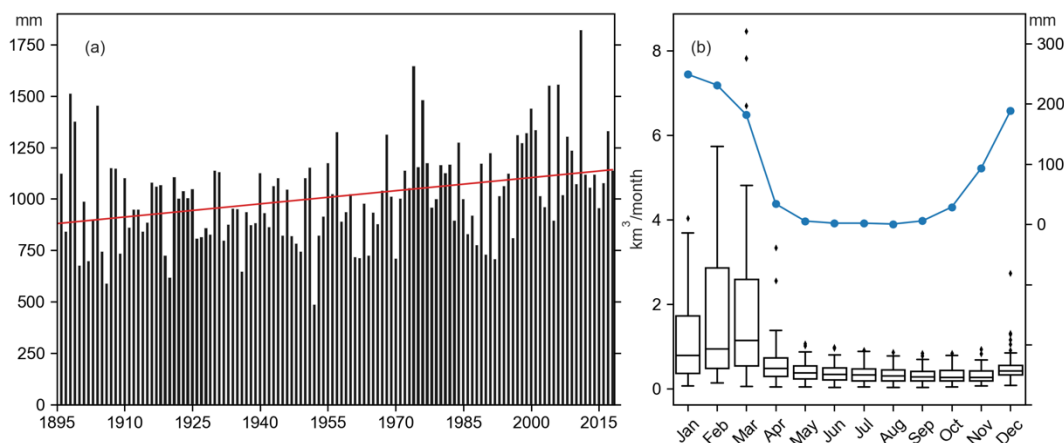


Figure 5-2 (a) Catchment average annual water year (September–August) rainfall (mm) from 1896 to 2018, with the long-term trend shown in red; (b) Boxplots showing monthly discharge (km³/month, left axis) for the instrumental period (1961–2018) at gauge G8140040, Daly River at Mount Nancarrow, with catchment average monthly rainfall (mm, right axis) plotted in blue.

5.4.2 Hydrological data

Daily streamflow data (ML/day) for gauges in the Daly River catchment were downloaded from the Northern Territory Government Water Data Portal at <https://water.nt.gov.au/>. Gauges on perennial rivers with at least 40 years of data before 2005 (the last year for many tree-ring chronologies) were selected. Suitable gauges were identified on the Douglas River downstream of the Old Douglas Homestead, the Katherine River at Railway Bridge, and the Daly River upstream of Dorisvale Crossing (Figure 5-1). For the Daly River at Mount Nancarrow, the gauge nearest to the catchment outlet, the time series was extended from 1961 to 1971 using data from nearby gauges and a regression model (see Appendix D).

Years with more than 15% of daily values missing during the peak discharge period (January–March), were excluded from analysis (Table 5-1). For other years, gap-filled daily streamflow data was downloaded from the Australian Bureau of Meteorology (BOM) Hydrologic Reference Stations database (<http://www.bom.gov.au/water/hrs/index.shtml>). Annual streamflow (km³) was then calculated for the Northern Territory water year of September to August (CSIRO, 2009). Streamflow between the four gauges is highly correlated (Pearson $r = 0.78 - 0.97$; Figure D-2). Including all four gauges in the reconstruction model meant that 1962 was the only year without any streamflow data (i.e., missing data from all four gauges).

Table 5-1 Selected streamflow gauges in the Daly catchment.

Gauge number	River	Gauge location	Catchment area (km ²)	Average flow (km ³ /year)	Data period	Missing years (before 2005)
G8140040	Daly	Mount Nancar	47,652	8.55	1961-2018	1962, 1966, 1977, 1978, 1985
G8140067	Daly	Upstream Dorisvale Crossing	33,227	5.79	1966-2018	1968, 1975, 1980, 1989, 1991, 2000
G8140063	Douglas	Old Douglas Homestead	831	0.25	1959-2018	1962, 1968, 1969, 1971, 1976, 1977, 1993, 2002
G8140001	Katherine	Railway Bridge	8,357	2.34	1963-2018	1971, 1975

Daly catchment-average water year rainfall was calculated from monthly gridded data from the Queensland Government SILO Climate Database (<https://www.data.qld.gov.au/dataset/silo-climate-database>). Daily rainfall for the town of Katherine was downloaded for the BOM gauges 014902 and 014903 from their website at <http://www.bom.gov.au/climate/data/>. Years missing more than 15% of daily rainfall values were excluded from the analysis. The Global Precipitation Climatology Project (GPCP; Adler et al., 2003) monthly gridded rainfall from 1979-2020, used to calculate the correlation between Daly catchment and regional rainfall, and the Extended Reconstructed Sea Surface Temperature (ERSST) v5 dataset, were both obtained from the NOAA/OAR/ESRL PSL website at <https://psl.noaa.gov/>.

5.4.3 Historical flood records

The largest settlement in the Daly catchment is the town of Katherine on the Katherine River, also the location of gauge G8140001. Three significant flood events, in 1998, 2006, and 2011, have occurred since streamflow was reliably recorded at Katherine. However only the 1998 event falls within the reconstruction period. Pre-instrumental data sources, predominantly newspaper articles, provide a record of major flood events since the permanent European occupation of the region began in 1872. Large floods at Katherine occurred in December 1897 (reconstruction year 1898), 1914, 1931, 1940, and 1957 (Water Studies Pty Ltd., 2000).

5.4.4 Tree-ring proxy records

Very few tree-ring chronologies exist for the tropics, including northern Australia, due to the difficulty in finding tropical tree species with annual growth rings (Rozendaal & Zuidema, 2011). However, recent efforts have identified the dendrochronological potential of both *Callitris intratropica* and *C. columellaris* (cypress pine) species (Allen et al., 2019, 2020; Baker et al., 2008; O'Donnell et al., 2015). While these species have great potential to inform understanding of the hydroclimate of monsoonal Australia (Allen et al., 2020; D'Arrigo et al., 2008), the chronologies developed to date are short, with the majority ~100-250 years in length. Longer reconstructions can be developed by utilizing remote tree-ring proxies (Allen et al., 2015) from

regions with strong teleconnections to monsoonal Australia. For the initial predictor pool, we downloaded all publicly available tree-ring chronologies from Australia, New Zealand and Monsoonal Asia located between 70°E, 40°N and 180°E, 47°S (Figure D-4) from the International Tree Ring Databank (ITRDB). The wood property series from each site were converted to chronologies by the process of standardization (i.e., detrended and transformed into dimensionless growth indices). The process aims to remove growth trends thought to be largely unrelated to climate using the ‘signal free’ (Melvin & Briffa, 2008) and ‘Regional Curve Standardization’ (Briffa et al., 1992) methods of tree-ring standardization.

5.5 Methods

Figure 5-3 provides a schematic overview of the methods used to reconstruct Daly catchment streamflow. The methods are described briefly below and in further detail in Appendix D.

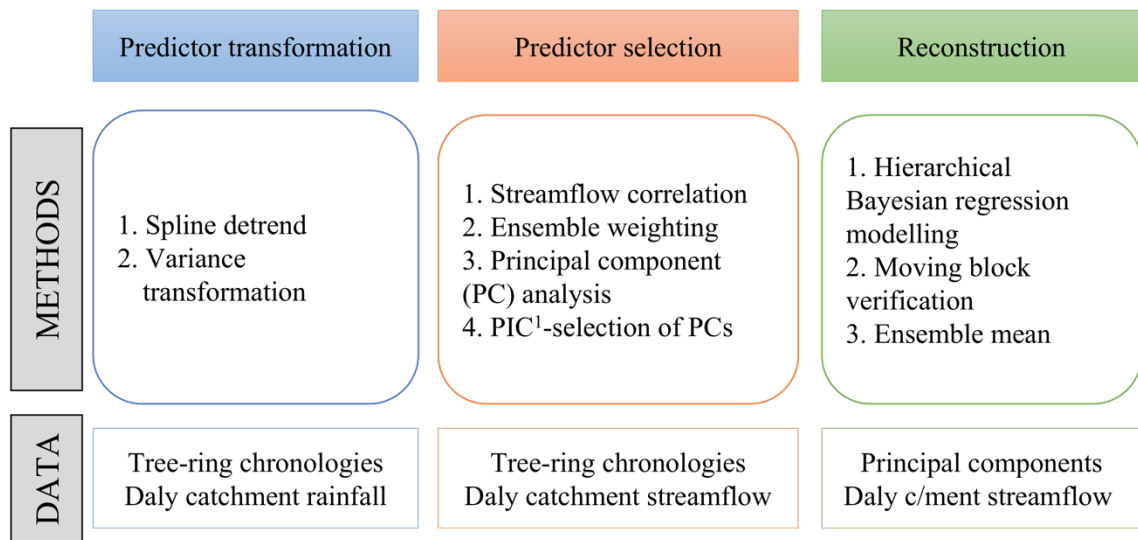


Figure 5-3 Schematic overview of the reconstruction methodology. ¹Partial information correlation.

5.5.1 Streamflow reconstruction

Tree rings are useful predictors of streamflow because both tree growth and variations in streamflow are controlled by soil moisture, which is influenced by rainfall and evapotranspiration (Meko et al., 1995). However, tree rings provide only indirect information about climate variations. In addition, factors including local proxy noise, seasonal sensitivities, and standardization methods result in biases in the high- to low-frequency spectrum of proxy records compared to the instrumental datasets they are attempting to reconstruct (Franke et al., 2013). Spectral biases are likely to be compounded when using remote tree-ring chronologies in reconstructions as only a portion of the climatic information contained in the proxy - related to the teleconnection - is relevant to the reconstruction.

To address these issues, after selecting the tree-ring chronology predictor pool, we applied a novel method for paleohydrologic reconstruction, in which a unique wavelet-based variance transform

(Jiang et al., 2021, 2020) was used to modify the spectral characteristics of each tree-ring chronology to better match Daly catchment average annual rainfall (see Appendix D). A nested hierarchical Bayesian regression model with partial pooling (Devineni et al., 2013; Rao et al., 2018), which is suitable for our short data records with missing years, was then used to produce the streamflow reconstruction from the transformed chronologies. The partial pooling framework combines the regression strength of the model across the four gauges, which can result in lower uncertainty in estimated parameters and reconstructed discharge, as well as improved final model skill (see Appendix D). We used a moving block calibration-verification scheme (Nguyen et al., 2020) in which 7-year, overlapping periods of the instrumental record were successively withheld to independently test the modelling (see Appendix D).

To evaluate the reconstruction, we used standard verification tests in dendrochronology: the calibration period coefficient of multiple determination (CRSQ or R^2), the validation period reduction of error (VRE), and the validation period coefficient of efficiency (VCE) (Cook & Kairiukstis, 1990). The VCE is equivalent to the Nash-Sutcliffe efficiency test (Nash & Sutcliffe, 1970) and is the most stringent verification criteria. The Bayesian R^2 , a data-based estimate of the proportion of the variance explained for new data, and the Sign Test, which calculates the number of years that the reconstruction correctly (+) or incorrectly (-) tracks the sign of observations during the calibration period (Cook & Kairiukstis, 1990), were also used in verifying the model.

5.5.2 Historical flood events

To further verify our results, the ability of the streamflow reconstruction to identify historical flood events recorded at the Katherine township was assessed via superposed epoch analysis (SEA), a compositing technique that tests the probability of an association between high flows and flood years occurring by chance (Haurwitz & Brier, 1981; Rao et al., 2019). To apply SEA to flood identification in our reconstruction, the six historical flood events which occurred during the reconstruction interval were used as key event years for SEA. A composite matrix was created by selecting reconstructed streamflow at Katherine (G8140001) from ten years prior to five years following each event. Streamflow was normalised to the ten years before an event to remove noise unrelated to the event signal, then averaged across all events to determine the composite signal (see Appendix D). The significance of the flood event-streamflow relationship was tested by comparing the key event composite to that generated from 10,000 draws of six years at random without replacement ('pseudo-flood years') from the reconstruction between 1888 (first event year - 10) and 2005 CE.

5.5.3 Extreme event analysis and climate forcing

Extreme dry/wet events were classified as those exceeding below the 5th and above the 95th percentiles of flows, respectively, during the reconstruction period (1413-2005 CE). Changes in

the frequency of extreme events were estimated using a nonparametric Gaussian kernel function (Mudelsee et al., 2004) with bandwidth selected via the method of Sheather & Jones (1991) and 95% confidence intervals estimated based on 1,000 bootstrap simulations. Trends in the recurrence rate of extreme events were tested against the null hypothesis of constant recurrence rate using the Cox-Lewis statistic (Cox & Lewis, 1966):

$$U = \frac{\sum_{j=1}^m (T_{event}(j) / m) - [T(1) + T(n)] / 2}{[T(n) - T(1)] \times (12m)^{-1/2}}$$

which is a standard normal distribution under the null hypothesis (Mudelsee et al., 2003), where $T(1)$, $T(n)$ are the first and last years of the observation interval, and m is the number of extreme events.

Bootstrapping was used to assess whether extreme events are significantly associated with different ENSO phases (Allen et al., 2020). The occurrences of El Niño/La Niña events since 1875 were determined based on December-February (DJF) Niño3.4 sea surface temperature (SST) anomalies above/below 0.5 °C and referenced against the events listed on the Australian Bureau of Meteorology website (www.bom.gov.au). Bootstrap replicates were drawn with replacement from the SST data to match the same number of years as the wet and dry extremes. The co-occurrence of extremes and ENSO phases was considered significant if the number of actual events lay outside the 95% bias-corrected and accelerated (BCA) bootstrap confidence interval (Efron, 1987) of the distribution based on 30,000 bootstrap replicates. The number of bootstrap replicates was increased from 1,000 until the confidence interval remained unchanged.

5.6 Results and Discussion

5.6.1 Tree-ring predictor selection

Figure 5-4 shows the correlations between Daly catchment average rainfall and rainfall from regions with strong teleconnections to the IASM, during both the dry and wet (monsoon) seasons. Daly catchment rainfall is significantly correlated to rainfall in south-eastern Australia during the May-September dry season when Indian Ocean sea surface temperatures affect Australian rainfall (McBride & Nicholls, 1983; Risbey et al., 2009). Conversely, Daly catchment rainfall is significantly anti-correlated to the Asia Summer Monsoon during the November-April wet season, reflecting coherence between the regional monsoons (Wang et al., 2014). Correlations between Indonesian and northern Australian rainfall are significant throughout the year but are stronger during the dry season.

Figure 5-4 also shows the locations of the 63 tree-ring chronologies with significant correlation to Daly catchment streamflow retained for the final model (see Table D-1 for details). Nearly 70% of the retained predictors are from regions impacted by monsoon rainfall. Five chronologies

are within the IASM region, of which three are proximal to the Daly catchment (within 20 km, see Figure 5-1). A further 36 are within the Asian Summer Monsoon region, and the remaining 22 from subtropical to temperate Australia, and New Zealand.

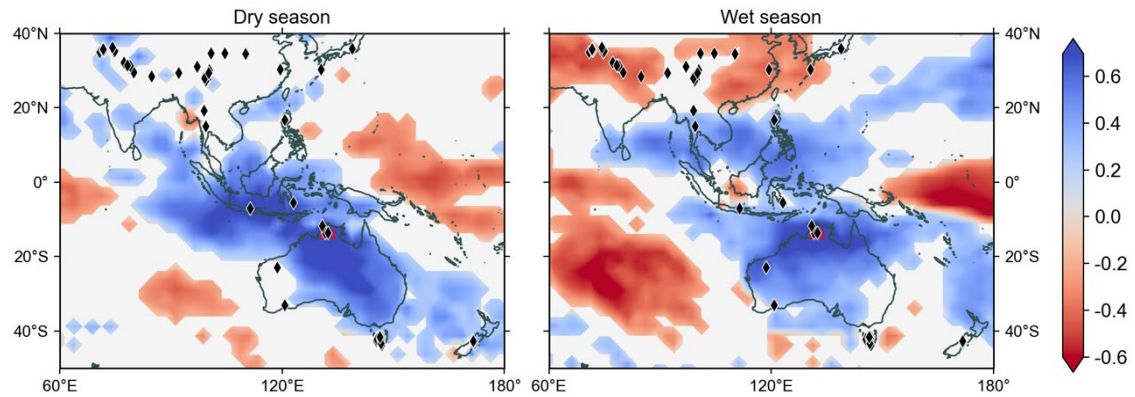


Figure 5-4 Left: Spatial Pearson correlation fields comparing average Daly catchment (red square) GPCP rainfall and GPCP rainfall over Australia, the South-east Asian Monsoon and Asian Monsoon regions during the northern Australia dry season (May–Sept) between 1979 and 2020. Right: Same figure for the northern Australia wet season (Nov–Apr). Correlations not significant at $p < 0.1$ are greyed out. Black diamonds represent the location of the 63 tree-ring chronologies with a significant correlation to at least three of four Daly catchment streamflow gauges after variance transformation.

Absolute Pearson correlations between streamflow and significant tree-ring predictors vary from $r = 0.28$ to 0.61 with a median value of $r = 0.42$. This is a substantial increase in correlation compared to the pre-transform predictors, which varies from $r = 0.0$ to 0.51 with a median value of $r = 0.21$. Transforming the spectral variance of the tree-ring chronologies is therefore shown to strengthen their correlation to Daly catchment streamflow.

5.6.2 Streamflow reconstruction

The final nested reconstruction based on the variance transformed tree-ring chronologies spans 1413 to 2018 CE, with instrumental data appended after 2005. Figure 5-5a compares observations with reconstructed streamflow at the most downstream gauge, G8140040 at Mount Nancar, using the tree-ring data for the best replicated (1898–2005) nest. Results for the other three gauges are shown in Figure D-9. This reconstruction accounts for 72–78% of the variance in streamflow observations at each gauge over the calibration period from 1959 to 2005. Table 5-2 shows the calibration-validation statistics used to evaluate the validity and stability of the nested models for the best-replicated nest, and median statistics of all nests between 1413 and 2005 CE. Timeseries results for all nests are provided in Figure D-10.

Table 5-2 Calibration and verification statistics for the best-replicated nest (1895-2005) and median values for the whole reconstruction interval (1413-2005) for the four Daly catchment gauges.

Gauge number	Initial nest (1895-2005)					Median values (1413-2005)			
	R ²	Bayes R ²	VRE	VCE	Sign Test (<i>p</i>)*	R ²	Bayes R ²	VRE	VCE
G8140040	0.78	0.62	0.60	0.36	27+8- (0.002)	0.68	0.58	0.61	0.36
G8140067	0.78	0.65	0.59	0.34	23+4- (<0.001)	0.69	0.58	0.61	0.40
G8140063	0.78	0.64	0.69	0.50	27+5- (<0.001)	0.70	0.59	0.66	0.37
G8140001	0.72	0.60	0.56	0.26	28+6- (<0.001)	0.67	0.57	0.57	0.26

**n* is less than the number of calibration years due to data gaps.

The calibration and verification statistics demonstrate that the reconstruction is reliable, despite the relatively short calibration period. Despite the decreasing number of tree-ring predictors moving back in time, the statistical results remain strong for the earliest part of the record, with the least replicated nest accounting for 59-62% of the calibration period variance. Uncertainty intervals (Figure D-9) show that the 5th percentile VRE and VCE values are above zero throughout the reconstruction period, indicating that the reconstruction contains meaningful information over its entire length (Cook & Kairiukstis, 1990). In addition, the significant ($p < 0.01$) Sign Test results are a good indication that the tree-ring chronologies are accurately tracking the direction of year-on-year variability in streamflow during the calibration period.

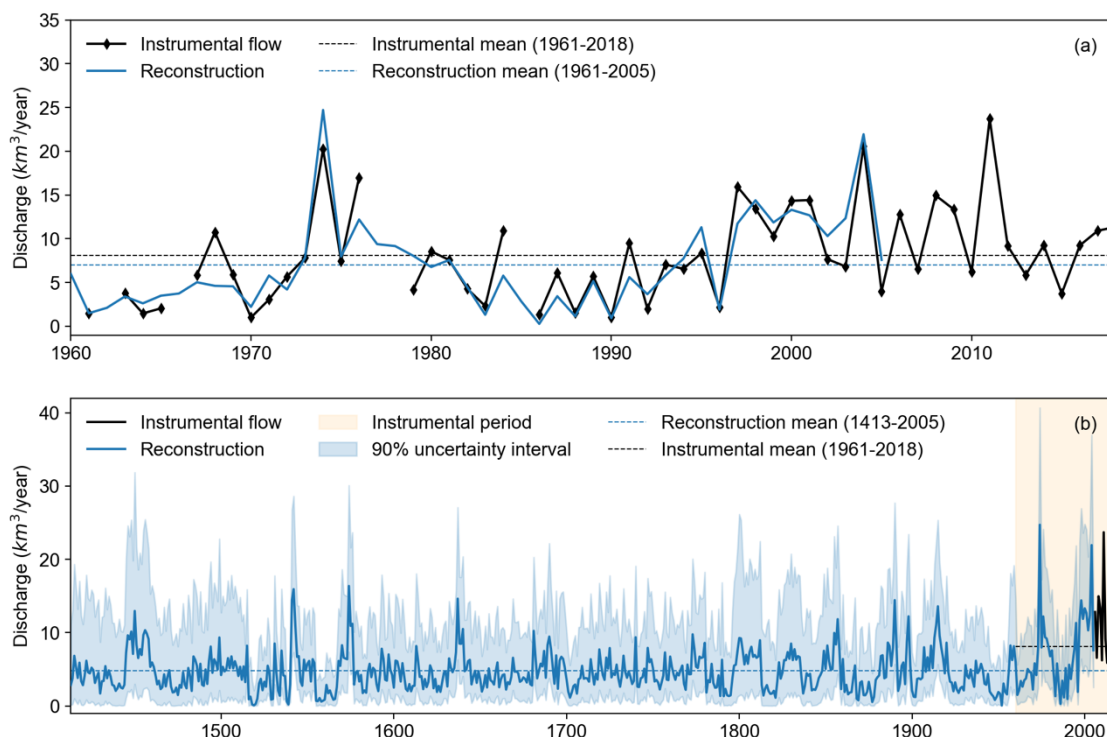


Figure 5-5 (a) Instrumental (black) versus reconstructed (blue) streamflow in km³/year for Daly River gauge G8140040 over the instrumental period 1961-2018. (b) Reconstructed flow at G8140040 from 1413 to 2005 CE with the 90% confidence interval for the reconstruction shown in light blue.

The full reconstruction for G8140040 is shown in Figure 5-5b; results are similar for the other gauges (not shown). The reconstruction shows that streamflow during the instrumental period represents a period of unusually high flow that is unprecedented in the preceding five centuries.

The 57-year gauge instrumental period from 1961 to 2018 has mean streamflow of 7.79 km³/year, which is significantly higher ($p < 0.001$, two-sided Student's t-test) than the pre-instrumental mean of 4.60 km³/year, and any period of equivalent length in the reconstruction. Similarly, the gauge calibration period from 1961 to 2005, which has mean streamflow of 6.99 km³/year, exceeds any previous 44-year period, but the difference is not significant for periods between 1873-1922 CE. These results are consistent with an intensification of IASM rainfall starting in the early to mid-1800s.

5.6.3 Historical comparisons

The largest recorded flood event at Katherine occurred in 1998 after ex-Tropical Cyclone Les brought 400-500 mm of rain within three days (Skertchly & Skertchly, 1999). The rainfall characteristics of other major historical flood events are similar, with several hundred millimetres of rain falling within a few days (Water Studies Pty Ltd., 2000). There is a moderately strong and significant positive correlation ($r = 0.60$; $p < 0.001$) between the annual maximum five-day rainfall, which represents the approximate length of rainfall events resulting in historical floods, and total water year rainfall at Katherine (Figure 5-6). In most cases, major floods occurred during very wet years, with total rainfall in the top ~11% of the record. The exceptions are 1914 and 1931, which were average rainfall years. These results are indicative only as extreme rainfall events, especially those related to cyclonic rainfall, are not evenly distributed over the catchment, and there is a paucity of rainfall gauges in the early part of the record.

The significant positive relationship between high-intensity events which may cause flooding and total annual rainfall suggests flood years should be identifiable by higher-than-average reconstructed Katherine River streamflow. We tested the probability of random association between flood years and high streamflow at gauge G814001 using superposed epoch analysis. We found that mean reconstructed flows across these six years are significantly higher ($p < 0.01$) than would be expected by chance (Figure 5-6). The ability of the reconstruction to identify pre-calibration historical flood events increases confidence in the reconstruction model outside of the instrumental period.

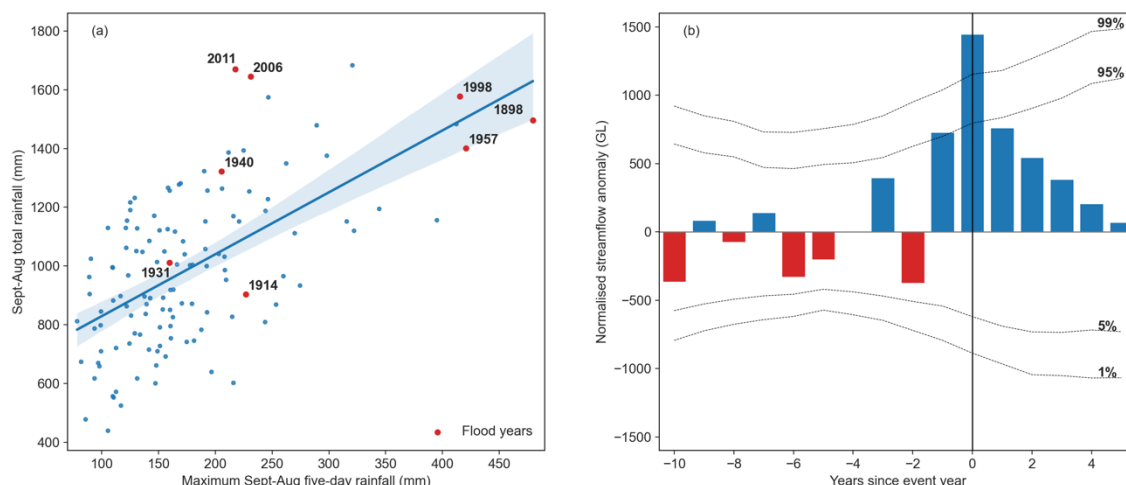


Figure 5-6 (a) Relationship between maximum five-day rainfall and total annual (September–August) rainfall at Katherine for all years on record (blue) and historical flood years (red). The blue line shows the significant positive trend ($r = 0.60$; $p < 0.001$) between the variables within the 95% confidence interval. (b) Superposed epoch analysis showing that Katherine River streamflow is significantly ($p < 0.01$) higher than expected by chance during historical flood years.

5.6.4 Extreme events

Surface warming of the equatorial Pacific associated with El Niño events drives an intensification of the Walker circulation, resulting in decreased average deep convection over Australia (Holland, 1988; McBride & Nicholls, 1983). The reverse occurs during La Niña events, with weakening of the Walker Circulation and increased convection. However, this relationship is not symmetric, with La Niña events generally more highly correlated with rainfall over Australia than El Niño events (Power et al., 2006; Risbey et al., 2009). Teleconnections between ENSO phases and Australian rainfall also vary with the phases of the Interdecadal Pacific Oscillation, with warm (positive) phases decreasing the strength and spatial coherence of ENSO-rainfall relationships (Power et al., 1999). Recent research (Allen et al., 2020) has shown that precipitation at the end of the wet season (March–May) in monsoonal Australia is asymmetrically linked to ENSO, with increasingly extreme wet events associated with increasingly cooler SSTs, but less clear relationships between dry extremes and El Niño phases.

We tested the relationship between annual Daly River streamflow extremes and Pacific SSTs by comparing the number of high and low streamflow events that co-occurred with a known ENSO event. Figure 5-7 shows that extreme high streamflow events, defined as exceeding the 95th percentile of reconstructed flow, are significantly linked to Pacific SST anomalies, as demonstrated by the significant co-occurrence with La Niña events. Conversely, low flow events, defined as below the 5th percentile of reconstructed flow, were found to significantly *not* co-occur with La Niña events. El Niño events were not found to be significantly related to either high or low flow extremes, with the number of co-occurring events very similar to the mean of the bootstrap distribution. Not all El Niño events are associated with weak IASM rainfall. While lower-than-average monsoon rainfall occurs during canonical El Niño events, there is little

change in total rainfall during El Niño Modoki events, which result in a shorter but more intense monsoon (Taschetto et al., 2010). We tested the relationships between El Niño events and Daly River low flow extremes for canonical El Niño and El Niño Modoki events separately, but again the results were not significant (Figure D-11).

These findings are consistent with the relationship between cool Pacific SSTs and rainfall over Australia in observations, and are similar to the findings of Allen et al. (2020), despite the differences in the study period. Figure 5-7, panels e and f, shows the composite December-January SSTs over the 9 extreme low and 15 extreme high flow years. High streamflow years are associated with warmer-than-average SSTs off the coast of Australia which lead to greater convection and monsoon rainfall, whereas low flow extremes are associated with cool SST anomalies and suppressed convection (BOM, 2012). The mechanisms behind the asymmetrical relationship between ENSO and northern Australian rainfall and streamflow is an area of active research, with the interaction between ENSO and other modes of variability a likely cause (Cai & van Rensch, 2013; Heidemann et al., 2021; Power et al., 2006).

While high total annual streamflow is more likely to occur during a La Niña than El Niño phase, the rainfall events that cause significant flooding at Katherine cannot be linked to ENSO phasing based on the available data. While the flooding at Katherine during 2011 was associated with a strong La Niña that also caused extensive flooding in Eastern Australia, other major historical floods at Katherine have occurred during years with average Pacific SSTs and El Niño years. As most of the region's rain falls as intense, intermittent, tropical showers, monsoon troughs, or ex-tropical cyclone lows, rain events during average years are sufficient to cause local flooding. Tropical cyclones in the instrumental record are ~20% more likely to occur in northern Australia during La Niña years (Kuleshov et al., 2009), but ENSO phases do not significantly impact the occurrence of monsoon bursts which are more likely to occur during active phases of the Madden-Julian Oscillation (Berry & Reeder, 2016). Rainfall event timing linked to antecedent conditions is also a factor, with heavy rainfalls occurring later in the wet season when the subsurface is saturated more likely to result in extreme discharge than equivalent events earlier in the season (Chappell & Bardsley, 1985).

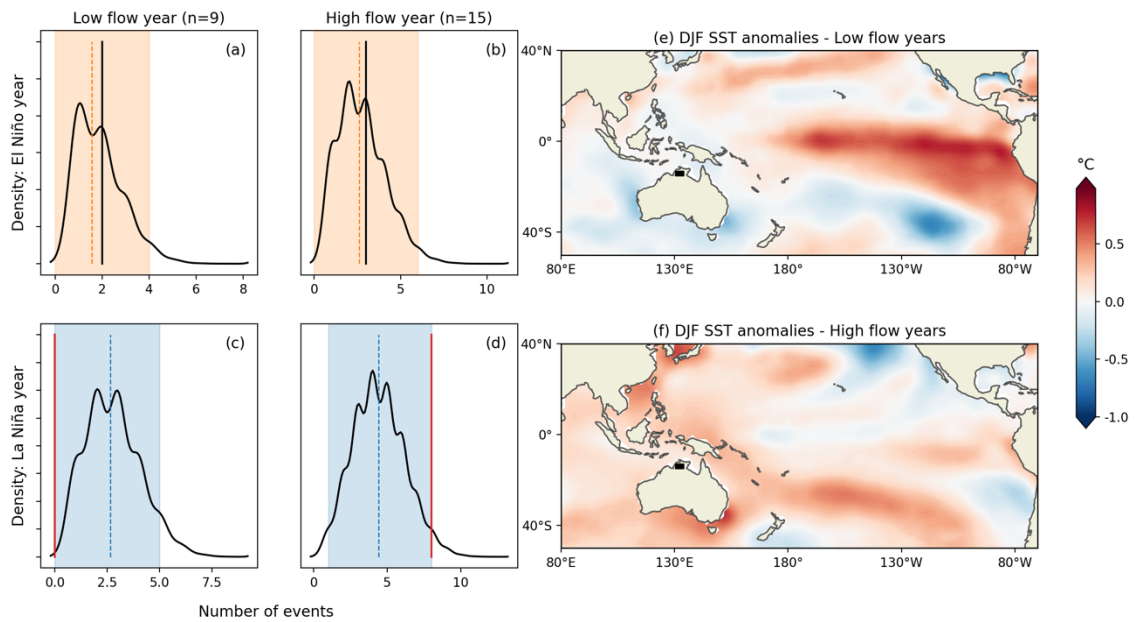


Figure 5-7 Kernel density estimate plots of 30,000 bootstrapped replications of instrumental Niño3.4 DJF SST anomalies from 1875-2005 showing the co-occurrence of extremes in the reconstructed streamflow and El Niño (a, b) and La Niña (c, d) events. The number of extreme low and high flow events in the reconstruction associated with each ENSO phase is shown in black and compared to the bootstrap mean (dashed lines); significant values lying outside the 95% bias-corrected bootstrap confidence interval are shown in red. The average December to January (DJF) SST anomalies during low flow years (e) and high flow years (f) are also shown, with the approximate location of the Daly catchment indicated by the black square.

Indian Ocean SSTs also affect northern Australian rainfall, with positive phases of the Indian Ocean Dipole (IOD) linked to decreased winter-spring rainfall. The influence of the IOD begins in May-June, and peaks in September-October, diminishing rapidly at the start of the monsoon. Therefore, the IOD has very little impact on the peak of the monsoon (Jourdain et al., 2013; Taschetto et al., 2010), and, as expected, we found no relationship between the IOD and Daly River annual average or extreme streamflow. An IASM-region streamflow reconstruction for the Citarum Basin in Java, Indonesia, which specifically targets spring (Sept-Nov) streamflow, has shown an increase in the frequency of low streamflow events accompanying the increase in the frequency and magnitude of positive IOD events since the 1960s (D'Arrigo et al., 2011). This illustrates the importance of the seasonality of reconstructions when considering the impacts of different climate drivers on extreme events in the IASM region.

Changes in the frequency of extreme low and high streamflow events in the Daly catchment were investigated using a Gaussian kernel technique. Results for the Katherine River and Daly River gauge G8140040 are shown in Figure 5-8a, b and remaining gauges in Figure D-12. Persistent weak monsoons have been proposed as the cause of the 16th-century megadrought (1560-1587 CE) in monsoon Asia (Cook et al., 2010b). We also see a peak in the occurrence of low flow events in the mid-16th century, noting that the Daly River reconstruction is not independent of the drought reconstruction of Cook et al. (2010).

The mid-1600s to early 1800s shows low reconstruction variance and a low frequency of both low and high streamflow events. Paleoclimate studies suggest two potential mechanisms that could explain this result. The low variance period broadly coincides with the Little Ice Age (LIA), a period of lower-than-average temperatures in the Northern Hemisphere, believed to result from both low solar activity (Maunder and Dalton grand solar minima) and high volcanic activity (Grove, 1988). Climate proxy reconstructions and modelling suggest a contraction of the seasonal latitudinal migration of the Intertropical Convergence Zone (ITCZ) during the LIA, with modest rainfall reductions over monsoonal Australia, centered on the 1600-1700 CE period (Denniston et al., 2016; Yan et al., 2015). Proxy reconstructions of ENSO by D'Arrigo et al. (2005) and McGregor et al. (2010) have also identified a period of low ENSO amplitude over the 17th and 18th centuries, although their findings disagree with other studies (Cobb et al., 2003). Either smaller north-south movements of the ITCZ or lower ENSO amplitude could plausibly result in lower monsoon streamflow variability during the LIA.

Figure 5-8 shows that the occurrence of high flow events has increased markedly over the last ~100 years. A significant ($p < 0.001$) increasing trend in 95th and 90th percentile flows at Daly River gauge G8140040 was identified over the period 1800 to 2018 CE using the Cox-Lewis test against the null hypothesis of a constant occurrence rate. Noting that the Daly catchment gauge reconstructions are not independent, trends in both 95th and 90th percentile flows at Katherine River gauge G8140001 were also significant over this interval ($p < 0.01$; $p = 0.05$, respectively), although the increase in high flows began slightly earlier at ~1770 CE. The results did not change if either the reconstruction end date of 2005 or the observation end date of 2018 were used, and increasing trends calculated over the entire reconstruction interval from 1413 CE were also significant for both gauges.

A sand splay deposit taken at the Nancar Hideout on the lower Daly River, close to the location of streamflow gauge G8140040, shows that low rates of deposition occurred from ~1420 to ~1760 CE, indicating a dry period, followed by an increase in deposition and streamflow in the period from ~1760 to 2005 CE (Wasson et al., 2010). Flood frequency derived from the sediment cores has risen steadily over the last ~160 years, with a doubling in the last ~60 years (Wasson et al., 2010). Noting the dating uncertainties (± 10 -60 years), this record is highly consistent with our tree ring-based reconstruction, providing independent verification of the recent trend in extreme streamflow.

5.6.5 Regional coherency

To test whether recent increases in monsoon streamflow are regionally coherent or unique to the Daly catchment, we compared our terrestrial proxy reconstruction to a coral luminescence-based reconstruction of the Burdekin River from 1648–2011 (Lough et al., 2015). The Burdekin River,

located in the dry tropics of Northeast Queensland (Figure 5-1), also experiences wet season rainfall related to the IASM. Lough et al. (2015) found an increase in the magnitude and frequency of high flow events from the mid-1900s compared to the preceding century in their Burdekin streamflow reconstruction.

We assessed changes in Burdekin River streamflow using the same methods described above for the Daly catchment (Figure 5-8c), extending the reconstruction from 2011 to 2018 using instrumental data. As for the Daly catchment, trends in both 95th and 90th percentile Burdekin River flows increased significantly over the reconstruction interval from 1800 to 2018 CE ($p < 0.05$), with trends also significant since the beginning of the reconstruction period at 1648 CE ($p < 0.05$).

Both catchment and rainfall changes may have contributed to the increasing streamflow trends. Agricultural development in the Burdekin Catchment since the settlement period (1851-1900) has likely contributed to higher discharge through vegetation cover and soil compaction changes to rainfall-runoff ratios (Lough et al., 2015). However, there are currently low levels of development and intensive agriculture in the Daly, with less than 10% of land under intensive use (Álvarez-Romero et al., 2016). Land surface changes, therefore, are unlikely to have had a significant contribution to the observed increase in streamflow in the Daly River or the coherent trend between the catchments.

Recent increasing trends in northern Australia summer rainfall are well documented. The increasing trend has been observed using rainfall data from 1900 onward, but may have begun in the early 1800s (Gallego et al., 2017). The trend has intensified since the 1950s (Nicholls, 2004; Rotstayn et al., 2007; Suppiah, 1992; Taschetto & England, 2009), which matches the observed changes in the frequency of extreme events in the Daly and Burdekin catchments. Most of the increasing rainfall trend can be explained by an increase in the frequency of multi-day rainfall events during active monsoon phases, rather than changes in the intensity of individual rainfall events (Clark et al., 2018; Dey et al., 2020). This implies that the weather systems causing heavy rainfall patterns are developing more often (Clark et al., 2018).

The mechanisms behind increasing monsoon rainfall are still unclear. Recent changes in ENSO are not a contributing factor as the increased frequency of El Niño events in the late 20th Century should result in fewer wet years and fewer high annual streamflow events (Shi et al., 2008). Nor does the trend follow the thermodynamic increase in rainfall event intensity expected with climate change (Berry et al., 2011; Clark et al., 2018; Smith et al., 2008). Rotstayn et al. (2007) showed that increased concentrations of anthropogenic aerosols can drive temperature and pressure-induced changes in monsoonal winds and increased precipitation in climate modelling, but these findings were later disputed (Shi et al., 2008). Changes in regional sea surface temperatures (Shi

et al., 2008), land-ocean temperature differences (Wardle & Smith, 2004), and timing of the monsoon onset (Taschetto & England, 2009), are also proposed mechanisms. It follows that the causes of the recent increasing trend in Daly and Burdekin annual streamflow totals are currently unknown, and further research effort is required.

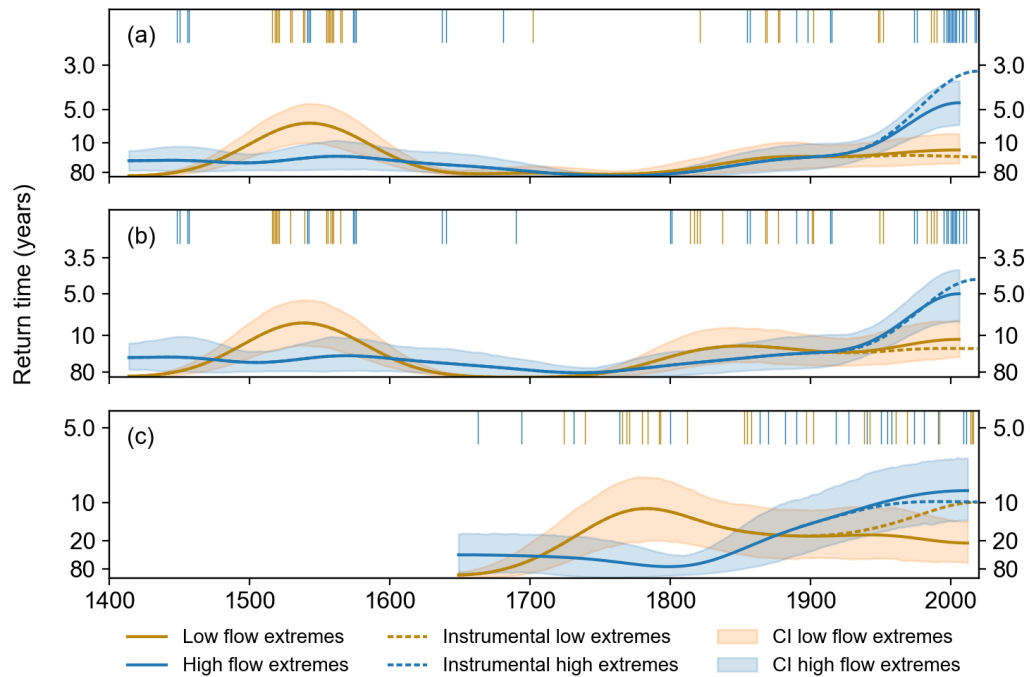


Figure 5-8 Extreme high flow/low flow event years and the time-varying frequency of the occurrence of these events between 1413 and 2018 for the a) Daly River at G8140040 and b) Katherine River at G8140001. A kernel smoothing method was used with a bandwidth of 38 years (solid lines), with dashed lines showing the adjusted frequency curve if instrumental data is appended to the reconstruction after 2005. In c) the frequency of extremes between 1648 and 2018 for the Burdekin River coral reconstruction of Lough (2015) is plotted with a bandwidth of 38 years, with instrumental data appended to the reconstruction after 2011. The shaded areas (blue and orange) represent the 95% confidence intervals based on 1,000 bootstrap simulations.

5.7 Conclusions

A long-term perspective on past northern Australian streamflow variability is provided by our tree-ring reconstruction for the Daly catchment, one of the few high-resolution streamflow proxy reconstructions for the IASM region. Despite the relatively short length of the instrumental records used for calibration and verification, little decrease in model statistics was observed moving back in time, indicating that the reconstruction provides useful information throughout the reconstruction period. Our Daly catchment reconstruction extends the record by more than five centuries. The length and robustness of the reconstruction, ability to identify historical flood events and coherence with other proxy reconstructions demonstrate the utility of the variance transform methodology to isolate streamflow signals from noisy tree-ring proxies, particularly when proxies far from the reconstruction target location are used. This method can be applied to reconstructions from other catchments in regions with few local proxies.

The reconstruction shows that high annual streamflow in the Daly catchment is associated with La Niña events, but low streamflow is not associated with El Niño events, confirming previous findings that IASM rainfall responds asymmetrically to ENSO. More generally, warm (cool) SST anomalies near the Australian coastline are associated with high (low) annual streamflow due to enhanced (suppressed) convection.

The recent magnitude and frequency of high streamflow events is unmatched over the past five centuries, regionally coherent, and closely follows observed trends in summer monsoon rainfall. The mechanisms behind the increasing trend in monsoon rainfall, and thus streamflow, are currently unknown. Increasing annual streamflow cannot be directly interpreted as a trend in flood hazard, because the increased frequency of rainfall events rather than increased event intensity lies behind this trend. The short duration high-intensity rainfall events that cause flooding at Katherine can occur in otherwise dry years, and antecedent catchment conditions and tropical cyclone events also contribute to flood occurrence.

Although it is unclear how average IASM rainfall will change with continued global warming, rainfall variability will likely increase. The consecutive failure of two monsoon seasons in 2019 and 2020 demonstrate that despite robust and regionally coherent trends in high streamflow, multi-year dry events still occur. Increased variability could have serious implications for water resources in the Daly catchment, as ecological and social functions rely on dry season baseflow from aquifers recharged during the previous summer's monsoon. Our reconstruction shows that current resource allocations in the Daly have been set during a period of unprecedented high river and aquifer levels which should be carefully considered by water managers when deciding on sustainable future allocations.

5.8 Conflict of Interest

The authors declare no conflicts of interest relevant to this study.

5.9 Data Availability Statement

All tree-ring chronologies included in the modelling are publicly available from the NOAA/World Data Service for Paleoclimatology archives at <https://www.ncdc.noaa.gov>. The code underpinning this paper is available on request from the corresponding author.

5.10 Acknowledgments

The authors acknowledge the efforts of all the dendrochronologists who have contributed tree-ring chronologies to the ITRDB, allowing for studies such as this one to be undertaken. Our thanks also to Ze Jiang for his helpful discussions on methodology and to Hung Nguyen and two anonymous reviewers, whose comments have improved this manuscript. PAH is supported by an Australian Government Research Training Scholarship and the UNSW Scientia PhD Scholarship Scheme. MPR is supported by a NOAA Climate and Global Change Fellowship under UCAR

CPAESS award #NA18NWS4620043B. FJ is supported by the UNSW Scientia Program. Further support provided by the ARC Centre of Excellence in Australian Biodiversity and Heritage (CE170100015). Open access publishing facilitated by University of New South Wales, as part of the Wiley-University of New South Wales agreement via the Council of Australian University Librarians.

Chapter 6 Combining paleoclimate data and future climate projections to predict hydrological drought risk

6.1 Abstract

Climate change is projected to cause more frequent and severe hydrological droughts. Understanding future drought risk is critical to support good water management decision-making. Combining paleo-streamflow reconstructions with climate model outputs allows us to compare past variability to future projections and produce better estimates the potential risk of future droughts. Here, we present a technique for developing both streamflow reconstructions and future projections, based on gridded estimates of the Palmer drought severity index, using the Murray-Darling Basin (MDB) as a case study. To verify the method, the reconstruction is compared to a reconstruction developed using the more traditional, tree-ring method. The future projections are compared to an existing ensemble of downscaled and bias-corrected climate model outputs for the MDB. The gridded method is shown to be suitable for the MDB and could be extended to any other region globally with a similar existing dataset. To show how water managers could utilise the reconstructions, we fit joint probability models to characteristics of drought events and analyse the likelihood that the most severe historical drought events, the Millennium Drought (~1997-2010) and the Recent Drought (2017-2019) could be exceeded in the future. The future projections show that droughts as or more severe (longer duration and/or greater magnitude) than the Millennium Drought are likely to occur in future and should be considered in future scenario planning.

6.2 Introduction

While droughts are a natural and recurring feature of the Australian hydroclimate (Kiem et al., 2016), the severity of the recent droughts, particularly in eastern Australia, is increasingly attributed to anthropogenic climate change. Research has shown that rising temperatures and associated changes in atmospheric circulation contribute to streamflow deficits observed during periods of low precipitation (Cai & Cowan, 2008; Nguyen et al., 2021; Ummenhofer et al., 2009). Climate change is also predicted to contribute to more frequent and severe droughts (Burke, 2011; Cook et al., 2014; Satoh et al., 2022; Sheffield et al., 2012), with cascading environmental and socio-economic impacts for affecting communities. While much progress has been made towards understanding the causes and impacts of drought in Australian catchments (e.g., Ummenhofer et al., 2009; Allen et al., 2020; King et al., 2020; Nicholls, 2004), there are still research gaps. Information contained in paleoclimate records shows that the instrumental data does not account for the full range of natural climate variability in Australia (see Chapter 5, and Flack et al., 2020; Gallant & Gergis, 2011; Ho et al., 2015b; Kiem et al., 2020; Palmer et al., 2015; Verdon & Franks, 2007). Thus, drought risk estimates based only on the instrumental period are likely to

underestimate the actual risks considering natural variability and climate change (Kiem et al., 2020).

Two key research needs have been identified, firstly improving records of pre-instrumental drought characteristics using paleo records and secondly, identifying methods for translating paleoclimate drought information into useful future scenarios for water management (Kiem et al., 2016). Paleoclimate data provides a good understanding of the baseline hydroclimate variability over long timescales which can be used to improve drought risk estimates. However, to understand the impact of climate change on drought, projections of future trends in climate obtained from General Circulation Models (GCMs) are also required (Armstrong et al., 2020; Kiem & Verdon-Kidd, 2011). The combination of paleoclimate reconstructions with climate model outputs allows us to compare past variability to future projections and better estimate the potential risk of future droughts exceeding those in the instrumental period (Cook et al., 2015; Hessel et al., 2018).

Despite the promises of these research advances, there are multiple technical challenges. Firstly, producing paleo-reconstructions for Australia, and secondly, combining paleo-reconstructions with climate model projections. There is a dearth of suitable paleoclimate proxies (i.e., annually, or seasonally resolved, and precisely dated) over much of mainland Australia. Hydroclimate reconstructions must therefore primarily rely on remote proxies (see Chapter 5 and publications including Gallant and Gergis, 2011; McGowan et al., 2009; Ho et al., 2015). Once a reconstruction has been developed, a method for reconciling the paleoclimate data with future projections must be identified. Armstrong et al. (2020) applied the ‘change factor’ approach to simulate future rainfall scenarios compared to a paleo-reconstruction of rainfall in the Lockyer Valley (Vance et al., 2015). Cook et al. (2016) derived the Palmer Drought Severity Index (PDSI) from an ensemble of climate model outputs which could then be directly compared to PDSI reconstructions from eastern Australia (Palmer et al., 2015). GCMs do not simulate streamflow sufficiently well for outputs to be used directly (Kundzewicz et al., 2018), thus, additional steps are required to post-process model outputs. Ideally, regionally downscaled and bias corrected model outputs would be routed through a catchment model. However, downscaling GCMs is computationally and resource intensive, as is building and calibrating a large catchment model. Such a workflow is prohibitive in many circumstances, particularly for large-scale studies over multiple catchments.

There is a need for regionally specific hydrological projections which quantify the impacts of both natural climate variability and anthropogenic change, and their associated uncertainties, to support water management decision-making (Kiem & Verdon-Kidd, 2011) that can be developed in a timely manner. In this Chapter, we present a method using existing PDSI spatial-field data

that can be directly applied to derive continuous past and future streamflow projections. The Murray-Darling Basin (MDB) in eastern Australia is used as a case study; however, the method as described could be applied to catchments across Australia or any other region in the world with a similar dataset. This Chapter presents three related pieces of work.

- 1) Reconstructions of past streamflow using PDSI fields that are then verified against reconstructions developed using the more traditional, tree-ring chronology method.
- 2) Projections of future streamflow using PDSI fields that are then verified against runoff from existing downscaled and bias corrected model outputs for the MDB.
- 3) Analysis of the occurrence and characteristics of droughts in the past and future gridded streamflow reconstructions demonstrating the benefits of reconstructions to understanding future drought risk.

6.3 Past and future streamflow reconstructions from gridded PDSI

The Palmer Drought Severity Index (PDSI) is a widely used regional drought index that incorporates temperature, precipitation, and soil moisture storage into a single measure of drought severity (Palmer, 1965). Tree-ring ‘drought atlases’ are gridded reconstructions of PDSI derived from networks of tree rings. Drought atlases have been used to investigate various scientific questions, mostly related to the causes, frequency, and recurrence interval of severe, prolonged droughts over the Common Era (Cook et al., 2007, 2010b, 2016). Drought atlases have also been shown to be practical proxies for streamflow reconstruction (Coulthard et al., 2016; Ho et al., 2016, 2017; Nguyen et al., 2020). The theoretical basis for drought atlas streamflow reconstruction is that PDSI is a measure of soil moisture, which is directly related to streamflow (Nguyen et al., 2020), as both components of the hydrologic cycle depend on the same set of climate variables including precipitation, temperature, and evaporation (Ho et al., 2016). The practical basis for drought atlas streamflow reconstruction is that as both streamflow and PDSI can be reconstructed from tree rings, it should be possible to build a model that directly relates streamflow to PDSI derived from tree rings (Coulthard et al., 2016; Ho et al., 2016).

There are several benefits to using drought atlases for streamflow reconstruction: atlas outputs remove the need for standardisation of tree-ring chronologies and nested reconstructions; they are more spatially uniform, making them applicable for large-scale studies (Nguyen et al., 2020); and they may filter non-climatic noise compared to using tree rings directly (Ho et al., 2016). Nevertheless, drought atlases should be used cautiously, as they contain non-stationary uncertainties which increase back in time due to decreased sample depth (the number of tree-ring chronologies available for reconstruction) (Nguyen et al., 2020). The impact of underlying

drought atlas reconstruction uncertainties on the derived streamflow reconstruction uncertainty is difficult to quantify.

Here, the motivation for using drought atlases to reconstruct streamflow is that gridded PDSI products are available for both past (drought atlas) and the future - derived from climate models (Cook et al., 2014). Thus, if a suitable model for streamflow can be developed from gridded PDSI during the instrumental period, this provides the opportunity also to project future streamflow trajectories based on modelled PDSI projections. The Murray-Darling Basin was selected as a case study for continuous PDSI-based past and future streamflow reconstructions to help place recent severe droughts in the context of past natural variability and expected future changes due to anthropogenic climate change. However, as climate model PDSI outputs are available over all inhabited continents, and drought atlases have been developed for much of the Americas, Europe, continental Asia, and Australasia, the method described here could be used to produce past and future streamflow for catchments in any of these regions.

6.4 Case study catchment: the Murray-Darling Basin

The Murray-Darling Basin (MDB) produces around 50% of Australia's irrigated agriculture and is often termed Australia's 'food bowl' (Alston & Whittenbury, 2013). At ~2700 km, the Darling River is the longest in Australia (Bowling and Baker, 1996), and its drainage basin and tributaries form the upper half of the MDB (Figure 6-1a). The Darling flows from the tropical/subtropical highlands in Queensland to the arid/semi-arid interior of western New South Wales (Meredith et al., 2009). The Murray River and its tributaries form the southern portion of the basin (Figure 6-1a), flowing for almost 2500 km across the heavily populated states of New South Wales, Victoria, and South Australia.

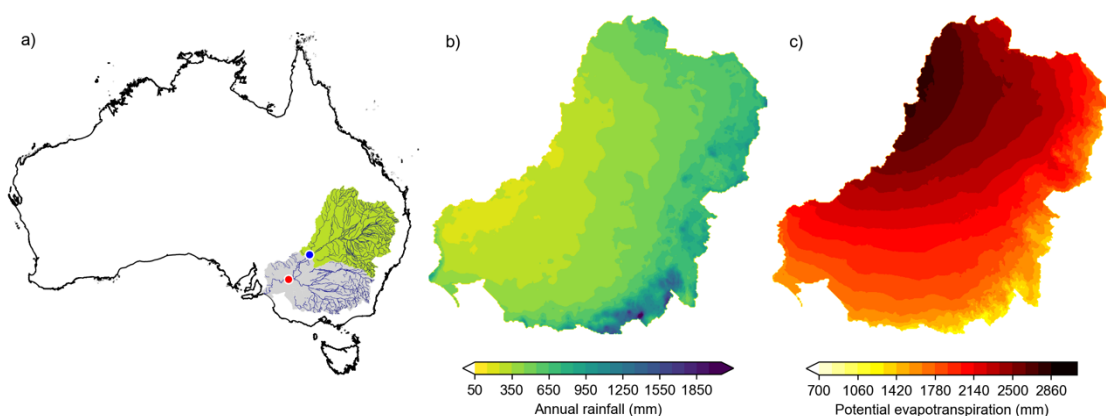


Figure 6-1 a) Location of the study sites, the Darling River at Wilcannia (blue dot), located in the upper Murray-Darling Basin (green), and the Murray River at Lock-7 (red dot), located in the lower Murray-Darling Basin (grey); Historical (1961-1990 CE) average annual rainfall (mm; b) and Morton point potential evapotranspiration (mm; c) over the MDB. Data from the SILO gridded database (QLD Government, last accessed 14/7/2022).

The MDB is predominantly semi-arid, with potential evapotranspiration rates far exceeding annual rainfall over much of the catchment (Figure 6-1b, c). The region is characterised by extreme climatic variability, and flow is highly right-skewed, with a large proportion of average flows occurring in very wet years and during major floods (Thoms and Sheldon, 2000). The basin faces environmental pressures from over-extraction and climate change, which both reduce water availability in the river system (Meredith et al., 2009).

Flow in the Darling River largely reflects the rainfall pattern for the northern part of the Murray-Darling region. Flow is approximately bimodal (Figure 6-2), with the highest streamflow in the late summer–early autumn (February–March) following the summer rainfall period and a second peak in the late winter–early spring (August–October) following the winter rainfall. Most of the rain in the upper basin stems from tropical systems or from interactions between tropical and extra-tropical systems and is thus more prevalent during the warmer months (Gallant et al., 2012). During the Australian monsoon season (November–April), strong cold fronts can penetrate the sub-tropics, triggering thunderstorms and very heavy, localised rainfall (Gallant et al., 2012). Tropical cyclones moving inland from the coast can also contribute to heavy summer rainfall. Winter rainfall results from meridional troughs extending through eastern Australia's subtropics. The convergence associated with these troughs accounts for around 25–40% of annual rainfall in the northern MDB (Wright, 1997).

In contrast, most rainfall in the southern MDB results from extra-tropical weather systems, such as cold fronts, low-pressure cut-off systems and cloud bands, and mostly occurs from May–October (Gallant et al., 2012; Wright, 1997). The highest rainfall occurs over the Great Dividing Range range, which forms the eastern border of the basin, with orographic uplift as the primary mechanism (Gallant et al., 2012). Cut-off low-pressure systems contribute between 25% and 50% of rainfall across the lower MDB and are responsible for over 80% of the rainfall that occurs on heavy rain days during the cool months (Wright, 1997).

On interannual scales, major climate drivers also affect MDB rainfall and streamflow. The El-Niño Southern Oscillation (ENSO) is a significant driver of rainfall variability across the MDB and has a magnified impact on streamflow variability (Chiew & McMahon, 2003). Winter, spring and summer MDB rainfall variations are most strongly associated with ENSO events, but the relationship between rainfall anomalies and the strength of ENSO events is not linear (Gallant et al., 2012; King et al., 2013). Some of the inter-annual variability in winter/spring rainfall in the MDB can also be attributed to the Indian Ocean Dipole (IOD; Gallant et al., 2012; Verdon and Franks, 2005), which has stronger influences over the southern basin. Increasing research effort is being placed on the interactions between these climate drivers, particularly when it comes to the causes of severe and prolonged droughts in the MDB (Gallant et al., 2012; King et al., 2020;

Ummenhofer et al., 2009), along with the influence of multi-decadal climate variability (Verdon-Kidd et al., 2014). Precipitation anomalies are enhanced over the MDB La Niña/negative IOD and El Niño/positive IOD periods co-occur (Cleverly et al., 2016; Holgate et al., 2022), and major droughts have been linked to the absence of the ENSO and IOD phases that bring drought-breaking rains, rather than to below-average precipitation (King et al., 2020).

While a recurring feature of the basin's climate, drought in the MDB has severe consequences, decreasing water security, increasing food and cotton prices, and causing environmental harm. During the instrumental period, three protracted droughts and several droughts of shorter duration have occurred. The 'Federation drought' (~1895–1902), 'World War II drought' (~1937–1945) and the 'Millennium drought' (~1997–2009) all differed in their severity and spatial extent and were affected by different combinations of climate drivers (Kiem et al., 2016). While of shorter duration, the most recent drought (2017–2019) has been the most severe for the upper basin, with very low flows and extreme heat leading to catastrophic environmental consequences in the lower Darling (Vertessy et al., 2019). The 2017–19 drought coincided with a positive IOD mode and a central Pacific El Niño (Nguyen et al., 2021). Rainfall for the northern MBD was 43% below the 1961–1990 average over 2017–2019, and 52% below average over 2018–2019 (BOM, 2020b). Both these rainfall anomalies are record lows for the instrumental period, breaking the previous records set during the Federation Drought in 1900–1902. Conditions were very dry but less extreme in the southern MDB (BOM, 2020b).

During the Millennium drought, the longest recorded instrumental drought in the MDB, the reverse situation occurred, with the southern basin experiencing extreme rainfall deficits and more modest deficits experienced in the northern basin (BOM, 2020c). The Millennium Drought was exceptional for both its length and effect on water resources. The only severely dry years over large parts of the MDB were 2002 and 2006, however, long periods without major wet episodes prevented water storage from recovering. The drought resulted in much more significant declines in the runoff than expected from the rainfall deficits (Saft et al., 2015) and low streamflow persisted over parts of the basin long after high rainfall ended the meteorological drought in 2010 (Peterson et al., 2021). The Millennium and the Recent droughts are the focus of the drought analysis in Section 6.5.2.

6.4.1 Streamflow data

The diversion, storage, and extraction of water from the Murray River system have resulted in a very different hydrological regime compared to pre-development conditions, with large reductions in Murray flow and the reversal of the natural flow seasonality in some reaches (Leblanc et al., 2012). While water management measures have had comparatively less impact on flows in the Darling, dams, weirs, and irrigation diversions have also affected natural flows

(Thoms & Sheldon, 2000). Tree-ring streamflow reconstructions build on the correlation between tree growth and discharge, and cannot be directly developed for heavily managed catchments (Galelli et al., 2021). Therefore, for this work, we use the ‘predevelopment flow’, which is modelled discharge in the absence of water management measures by the Murray-Darling Basin Authority (MDBA; datarequests@mdba.gov.au). Streamflow is modelled for two gauges, the Darling River at Wilcannia, representing flow at the mouth of the upper MDB, and the Murray River upstream of lock number 7 (hereafter, Lock-7) representing flow in the lower MDB (Figure 6-1a). Modelled streamflow data is also available for a much longer period (1896 – 2019) than gauge data which has only been reliably measured since the 1970s.

Figure 6-2 compares the naturalised (modelled pre-development) streamflow to measured gauge data at Wilcannia (a, b) over the common period. Figure 6-2a shows that while naturalised streamflow is higher than gauged streamflow at Wilcannia in most years due to water extractions, there is little difference in inter-annual variability between the series. Figure 6-2b shows similar monthly patterns in Darling streamflow between the two series, although the seasonality is muted in the gauge data due to extractions and managed releases. Volumetric data is not available for Lock-7 and water levels have only been measured since 2007, so a similar comparison is not possible for Murray streamflow.

Figure 6-2c and d show the high variability and right-skewness of streamflow based on the entire timeseries of monthly naturalised streamflow for the Darling at Wilcannia and Murray at Lock-7, respectively. The approximately bimodal nature of streamflow in the Darling and strong seasonality in the Murray can be observed in the monthly boxplots.

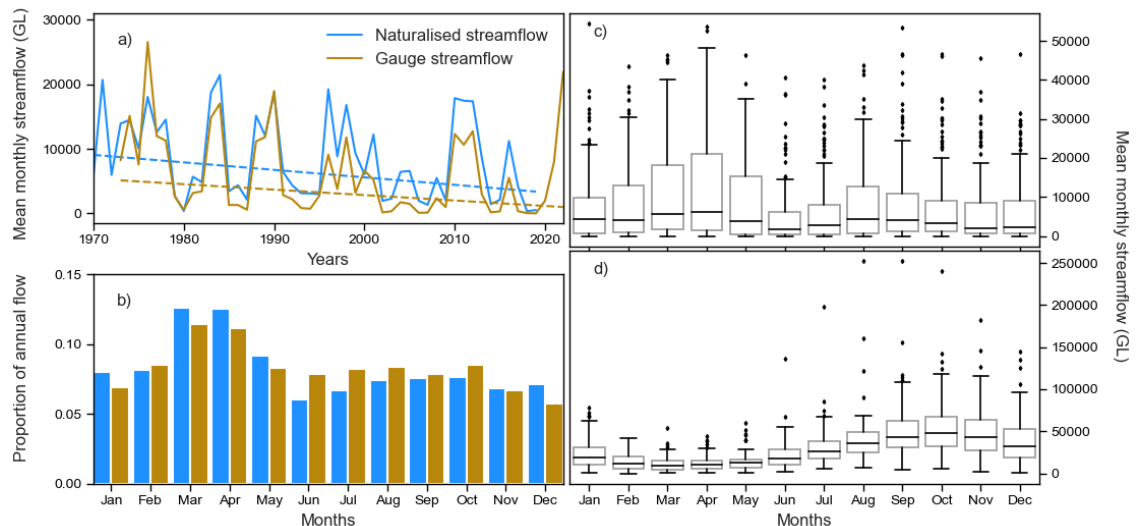


Figure 6-2 a) Time series of naturalised average monthly streamflow (blue) compared to gauged average monthly streamflow (brown) in the Darling River at Wilcannia (1970-2022). Decreasing trends (dashed lines) in both gauge (1973-2022) and naturalised (1970-2019) streamflow are significant (Mann-Kendall trend test, $p < 0.05$); b) Comparison of the proportion of annual streamflow occurring in each month at Wilcannia, for the naturalised (blue) and gauged (brown) streamflow; c) Average monthly naturalised streamflow in the Darling River at Wilcannia; d)

Average monthly naturalised streamflow in the Murray River at Lock-7. Data from the Murray-Darling Basin Authority (2020).

Both the naturalised and gauged annual streamflow series at Wilcannia show significant declining trends from the 1970s to the current year (Mann-Kendall trend test, $p < 0.05$), despite very high streamflow in 2021 and the first half of 2022 in the gauge data. Similarly, there has been a significant declining trend from the 1970s in the naturalised Murray River streamflow at Lock-7 (Mann-Kendall trend test, $p < 0.01$). Declining streamflow trends have been observed at gauges in undisturbed catchments across the MDB over the last 50 years, with steeper declines in the lower basin compared to the upper basin (BOM, 2020c). Streamflow declines are predominantly observed in the winter (JJA) and spring (SON), with no trends apparent during autumn (MAM; (BOM, 2020c).

6.5 Streamflow reconstruction and projection

6.5.1 Streamflow reconstructions

The paleoclimate proxy data for the Darling River streamflow reconstruction were the gridded, tree-ring-based drought reconstructions contained in the Eastern Australia and New Zealand Drought Atlas (ANZDA; Palmer et al., 2015), the Mexican Drought Atlas (MXDA; Stahle et al., 2016), the Monsoon Asia Drought Atlas (MADA; Cook et al., 2010), and the South American Drought Atlas (SADA; Morales et al., 2020). Published streamflow reconstructions based on drought atlases have been developed using a range of methods, including a generalised linear model with regularised canonical correlation analysis (Ho et al., 2016, 2017) and a linear dynamical system model based on principal components (Nguyen et al., 2020). Both these methods share similarities with the principal components of point-by-point regression (PPR; Cook et al., 1999, 2007, 2010) previously described in Chapters 2 and 3.

Here, PPR is used to produce the streamflow reconstruction from gridded PDSI. Streamflow was first power transformed using the exponent that best reduced skewness in the data ($p = 0.3$ for the Darling and $p = 0.2$ for the Murray). Before selecting predictor grid points, each atlas was reprojected to a 2° grid using bilinear interpolation of spherical coordinates with the python package ‘xesmf’. Interpolation retains variance compared to spatial averaging of grid points. A stringent predictor cut-off ($p \leq 0.05$) was used due to the large number of grid points (> 900) and due to the high spatial correlation in the gridded PDSI compared to the tree rings, which results from the filtering and smoothing of the data during the drought atlas reconstruction. The power-transformed streamflow data and the tree-ring chronologies were autoregressively pre-whitened before modelling. Predictor selection, calibration and verification of the model were undertaken on the transformed, autoregressively modelled data, with the final reconstruction reddened and transformed back into data units.

None of the tree rings used to underpin the ANZDA are located within the MDB. Nevertheless, the ANZDA appears to capture drought signals localised to the upper and lower basin (Cook et al., 2016), as well as drought signals related to large-scale climate drivers. The inclusion of the MADA, MXDA, and SADA domains in the reconstruction solely relies on teleconnections (i.e., large-scale climate drivers) between these regions and the upper and lower MDB. All four drought atlases have identified a link between ENSO phases and drought. Drought in the MADA has further been linked to phases of the IOD (Ummenhofer et al., 2013), and the SADA additionally displays a signal related to the Southern Annular Mode (SAM; Morales et al., 2020). The benefit of using predictors from teleconnected regions when few or no local paleoclimate predictors are available has been previously established in Chapters 2, 3, and 5.

Previous gridded streamflow reconstructions have incorporated grid points from a single drought atlas, from the same region as the catchment (Ho et al., 2016, 2017; Nguyen et al., 2020). To test the assumption that grid points from drought atlases from teleconnected regions can also be reliably used to reconstruct MBD streamflow, a second reconstruction was developed for comparison, using tree-rings directly. All publicly available tree-ring chronologies underpinning the four drought atlases from the International Tree Ring Databank (ITRDB) were downloaded for the initial predictor pool. The wood property series from each site were converted to chronologies by the process of standardization (i.e., detrended and transformed into dimensionless growth indices). The process aims to remove growth trends thought to be largely unrelated to climate using the “signal free” (Melvin and Briffa, 2008) and “Regional Curve Standardization” (Briffa et al., 1992) methods of tree-ring standardization. Pre-selection of tree-ring predictors considered only those chronologies with a significant relationship ($p \leq 0.1$) to average naturalised streamflow. The final predictor pool was determined via a backwards stepwise regression approach (Miller, 2019; Woodhouse et al., 2006).

6.5.2 Calibration and verification

The last year of the calibration period was limited to 2000 for both reconstructions as this is the final year of many of the tree-ring chronologies and the last reconstruction year of the SADA. As is standard procedure in dendrochronological reconstructions, a 50/50 split calibration and verification regime was used, with models first calibrated to the first half of the data (e.g., 1897-1948) and validated on the second half (e.g., 1949-2000), then the periods reversed. If both split periods pass the verification tests, the model is considered to suitably predict unseen data and therefore appropriate for reconstruction purposes. Once verified both ways, a final model is then fit to the entire instrumental period (Briffa et al., 1990). Standard verification tests applied to split period models are the calibration period coefficient of multiple determination (CRSQ or R^2), the validation period reduction of error (VRE), and the validation period coefficient of efficiency (VCE; Cook & Kairiukstis, 1990).

VRE is a measure of the performance of a model relative to the mean of the calibration period where:

$$VRE = 1 - \left[\frac{\sum (X_i - \hat{X}_i)^2}{\sum (X_i - \bar{X}_c)^2} \right]$$

X_i and \hat{X}_i refer to the observed and simulated value at i , and \bar{X}_c is the mean value over the calibration period. VRE ranges from $-\infty$ to $+1.0$, with $VRE > 0$ indicating that the model is more successful at predicting verification data than the calibration mean. Similarly, VCE compares the model fit to the verification period mean \bar{X}_v :

$$VCE = 1 - \left[\frac{\sum (X_i - \hat{X}_i)^2}{\sum (X_i - \bar{X}_v)^2} \right]$$

Again, $VCE > 0$ indicates some model skill over the mean of the verification period. Unless $\bar{X}_c = \bar{X}_v$, VCE will always be less than VRE by a factor related to the difference in the calibration and validation period means.

6.5.3 Future streamflow projections from modelled PDSI

To investigate climate change impacts on streamflow, we produced a forwards streamflow projection using PDSI calculated from CMIP5 model projections of the 21st century (Cook et al., 2014, 2016). Cook et al., (2014) calculated PDSI from GCMs. Model PDSI calculations use Penman-Monteith potential evapotranspiration and are thus consistent with the PDSI reconstruction target used to develop the four drought atlases. The projections cover the time interval 1901–2099 at a monthly resolution, using the historical (1850–2005) and RCP 8.5 (2006–2099; business-as-usual, high greenhouse gas emissions) forcing scenarios. The ensemble includes projections from 14 models for a total of 30 individual simulations (Table E-1). It may be beneficial to exclude models that perform poorly in terms of simulating important processes for the MBD, for example, the ENSO-rainfall relationship over Australia in spring (Moise et al., 2015). However, as the method also relies on modelled PDSI from regions outside of Australia, it was decided to retain these three models (MIROC-ESM-Chem, MIROC-ESM, and GISS-E2-R).

Climate models are not temporally consistent with instrumental data over their ‘historical’ period. Thus, it is not possible to create a regression model for streamflow using the modelled PDSI during the calibration period. To ensure continuity between the reconstruction and future projections, PDSI outputs from each of the CMIP5 models were reprojected to a 2° grid, and the model grid points corresponding to the selected drought atlases predictors were extracted. Model PDSI was averaged over either DJF or JJA, consistent with the reconstruction target (growing season) of each drought atlas. Over the common historical period (1900–2000), the GCM PDSI grid points were scaled to have the same mean and variance as the corresponding drought atlas grid points. Drought atlas data from 1897–2000 was then pre-appended to the modelled grid points

from 2001-2099 and the PPR algorithm was run as a forward projection. Using the same historical data (drought atlas grid points) with the same PPR parameterisation used to produce the reconstructions ensures that very similar weightings were applied to each grid point over all projected models and reconstructions, allowing the projections to be appended to the streamflow reconstruction to produce a continuous time series from 1500-2099.

6.5.4 Future streamflow projections from downscaled runoff estimates

To verify that gridded PDSI outputs from global climate models are suitable for projecting streamflow, the PDSI-based projections were compared to streamflow projections from the Australian Water Outlook (AWO; Azarnivand et al., 2022). The AWO projections are derived from four CMIP5 climate models (Table E-2), chosen from amongst the subset of models which best represent Australian climate conditions, and covering the range of projected changes in precipitation and temperature. These models have been subjected to one dynamical downscaling and three statistical bias correction methods. Here, only the model output bias corrected using the Multivariate Recursive Nested Bias Correction (MRNBC) method are used for comparison to the PDSI projections. The MRNBC method incorporates the interaction among variables across daily, monthly, and annual timescales to better represent low-frequency variability (Johnson & Sharma, 2012; Mehrotra & Sharma, 2016). Projections of the landscape water balance components were generated from the bias-corrected CMIP5 model outputs using the Australian Water Resource Assessment Landscape model v6 (AWRA-L; Frost and Wright, 2018).

The 5-km resolution gridded AWRA-L projected runoff was used to derive potential future Darling and Murray streamflow. Over the historical period (1961-2019), modelled streamflow at Wilcannia and Lock-7 lags the AWRA-L runoff by two months over most catchment grid cells (Figure E-1 and Figure E-2). Averaging runoff over the entire upper or lower MDB with a two-month lag was shown to suitably approximate streamflow over the historical period (Figure E-3; Pearson $r = 0.88$ for the Darling and $r = 0.92$ for the Murray). Therefore, projections of future streamflow were also generated by averaging AWO estimated runoff at a two-month lag and converting from millimetres to streamflow units using the entire catchment area.

6.5.5 Analysis of drought risk

Before undertaking analysis, the model simulations over the historical period (PDSI and AWO) were rescaled to the mean of the 1961-2019 instrumental period to allow for comparison between future and instrumental period droughts. Scaling was undertaken by applying the percentage change from the modelled 1961-2019 baseline in each projection year to the instrumental 1961-2019 baseline. The streamflow reconstructions were not rescaled as they were already scaled to instrumental data during the calibration period (1897-2000) and have instrumental data appended from 2001-2019.

To examine how instrumental droughts compare to the streamflow reconstructions, droughts were ranked by separately assigning a rank score to each episode by duration, magnitude (cumulative streamflow anomaly), and peak value (maximum streamflow anomaly), with increasing ranks for increasing parameter values. Each of the three rank scores was then summed to obtain the final score, where a higher score represents a stronger drought episode (Biondi et al., 2005). Drought events were defined as one or more consecutive years with streamflow below a reference level. Following Biondi et al. (2005), the power-transformed streamflow was converted to standard deviation units (SDUt), and thus the reference level is 0, which represents the long-term mean. Figure 6-3 provides a stylised graphical representation of the three drought variables – duration, magnitude, and peak. Analyses of all three variables are sensitive to the selection of the reference level, and thus what constitutes a drought (Hessl et al., 2018). Therefore, the start and end of drought episodes identified in this analysis do not necessarily correspond to the accepted beginning and end of historical drought periods, which were defined based on other metrics. Nevertheless, selecting a constant threshold allows drought events to be assessed relative to one another.

In addition to comparing events by rank, it is useful for extreme event risk assessment to calculate exceedance probabilities (the likelihood that droughts of a particular strength will be exceeded in future), or alternatively, the return period of these events. The various drought elements (duration, magnitude, and peak) have different distributions and are typically correlated, necessitating a joint probability approach (Hessl et al., 2018). The joint distribution of drought duration and magnitude can be represented by a bivariate distribution with geometric marginals for duration and exponential marginals for drought magnitude (Biondi et al., 2005). The joint distribution of drought duration and peak can be represented by a bivariate distribution with geometric marginals for duration and truncated logistic marginals for the event peak (Biondi et al., 2008). Details on the mathematical properties and derivation of these two joint distribution models can be found in Kozubowski and Panorska (2005, 2008) and their application to streamflow reconstructions is described in Biondi et al. (2005, 2008). Once the fitted model parameters are calculated, the bivariate models can be used to calculate the chance of occurrence of a drought of both longer duration and higher magnitude or peak than a given drought. The return period of that drought can then be approximated as the inverse of its exceedance probability (Kim et al., 2003).

To assess how drought risk may change in the future, for each of the 30 streamflow projections joint probability models of duration/magnitude and duration/peak were fit to the entire streamflow timeseries (1500-2099 CE) with SDUt calculated from the historical mean (1500-2019 CE). The fitted parameters were then used to calculate the change in likelihood of known historical droughts given the potential future streamflow projections.

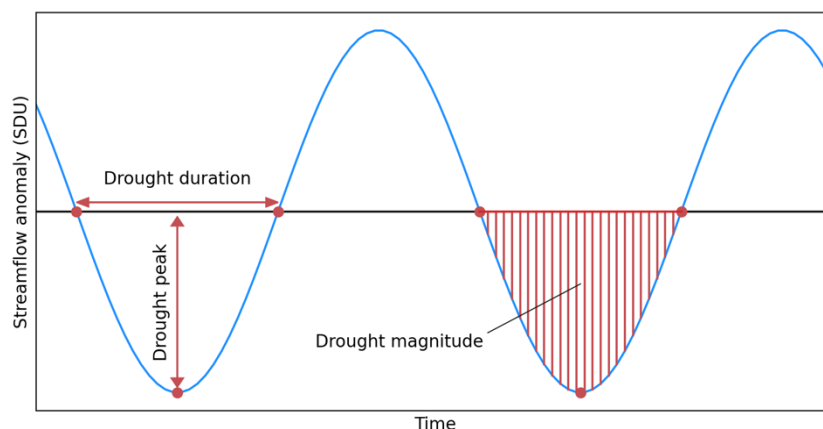


Figure 6-3 Stylised plot of streamflow anomalies (standard deviation units) in blue showing how drought duration, magnitude, and peak are defined for each drought event.

6.6 Results

6.6.1 Continuous past and future streamflow reconstructions

6.6.1.1 Seasonality in the drought atlases

All four drought atlases target peak growing season (summer) drought in their respective hemispheres; thus, the ANZDA and SADA target DJF and the MADA and MXDA target JJA. The focus on the summer window for drought-atlas reconstructions highlights droughts are most likely to adversely affect plant growth (Cook et al., 2010a). However, the seasonal signature contained in the atlases is broader than just the target season (Palmer et al., 2015). The PDSI integrates soil moisture anomalies over several months and thus may contain a signal from precipitation in previous seasons. Similarly, annual ring widths, with which the atlases are constructed, likely also include temperature and precipitation signals from growing-season months outside of the target window (St. George et al., 2010).

To investigate the seasonal signals contained in each atlas, and thus which season might be an appropriate reconstruction target for MDB streamflow, we calculated bootstrapped Pearson correlations between seasonal averaged power-transformed Darling and Murray streamflow and the first four principal components (PCs) of each drought atlas at lags of t_0 (concurrent year) and $t+1$ (streamflow lags climate by one year). The first four PCs explain ~70% of the variance in the ANZDA and MXDA, but much lower variance in the SADA (54%) and MADA (36%). For the Darling at Wilcannia (Figure 6-4), the best-correlated drought atlas is the ANZDA as expected, with strong correlations in the austral spring (SON), summer (DJF), and autumn (MAM). The SADA also shows significant but weaker correlations in austral spring and summer, with a winter (JJA) signal also present. The Northern Hemisphere drought atlas seasonal correlations are less clear. The MXDA shows weak correlations to Darling streamflow throughout the year, with the strongest correlations in austral spring and summer. In comparison, the MADA is not well

correlated to Darling streamflow, possibly because the first three PCs capture relatively little variance in PDSI.

Streamflow lags precipitation by approximately two months in the Darling catchment. The seasonal correlations in Figure 6-4 are well-aligned with the seasonality of the common large-scale climate drivers which act over austral winter-spring-summer in the upper MDB (Section 6.3). Based on the seasonal correlations, and the seasonality of these large-scale climate modes, July – December (July-Dec) streamflow was selected as the reconstruction target. The second half of the year corresponds to the smaller of the two peaks in streamflow, accounting for around 40% of annual flow, and matches the seasons for which significant declining trends in streamflow have been observed for the upper MDB (winter-spring). Longer periods, such as the calendar or water year were also tested, however models generally performed less well when calibrated to the late summer peak in streamflow. Summer rainfall in the northern MDB predominantly results from high-intensity, short-duration tropical disturbances (Gallant et al., 2012), which is less well captured by tree rings.

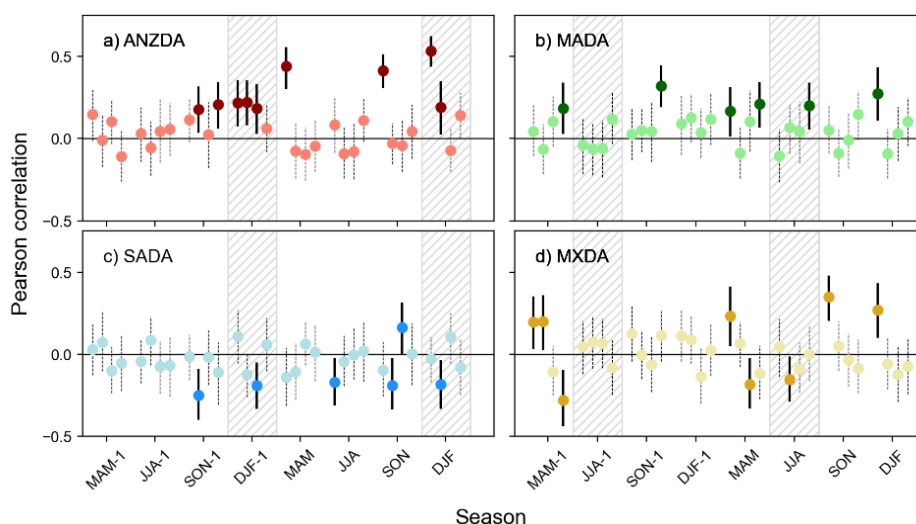


Figure 6-4 Correlation between seasonally averaged, transformed Darling River streamflow and the first four principal components of the four drought atlases a) ANZDA, b) MADA, c) SADA, and d) MXDA. Significant correlations based on 1000 bootstrap replications are shown in bold circles/lines, correlations not significant ($p > 0.05$) by light circles/dashed lines. The hatched periods correspond to the seasonal reconstruction targets of each drought atlas (a, c – DJF; b, d – JJA).

Figure 6-5 shows the same correlation analysis for the Murray River at Lock-7. Apart from the SADA, which appears to be a poor predictor of Murray streamflow, the atlases have predictive strength throughout the year. The first principal component of the ANZDA is particularly well correlated to all seasons of Murray streamflow. For this reason, the water year (June-May) was selected as the reconstruction target. While choosing a single target across both basins would be simpler, selecting separate periods maximises the reconstruction skill and reduces the uncertainty in each reconstruction.

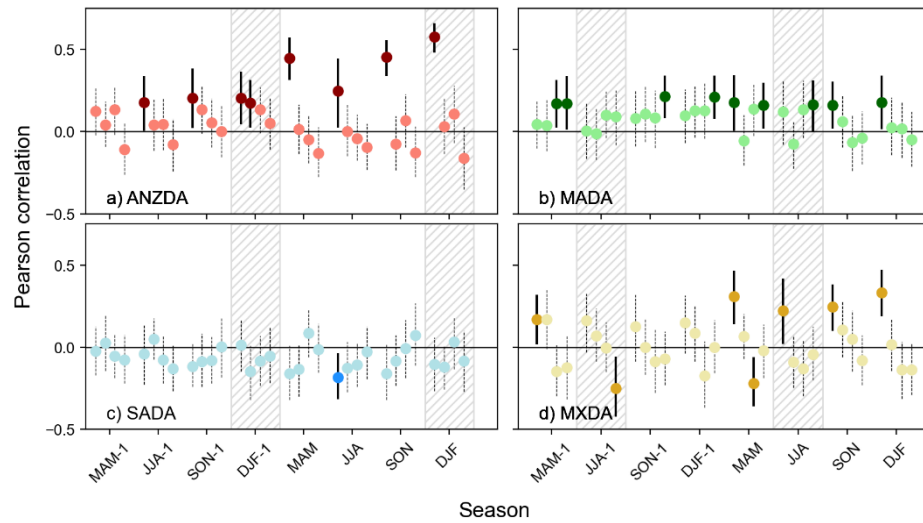


Figure 6-5 Correlation between seasonally averaged, transformed Murray River streamflow and the first four principal components of the four drought atlases a) ANZDA, b) MADA, c) SADA, and d) MXDA. Significant correlations based on 1000 bootstrap replications are shown in bold circles/lines, correlations not significant ($p > 0.05$) by light circles/dashed lines. The hatched periods correspond to the seasonal reconstruction targets of each drought atlas (a, c – DJF; b, d – JJA).

The grid point predictors selected from each drought atlas are based on their correlation with power-transformed July-Dec Darling streamflow and water year Murray streamflow significant at $p < 0.05$ (Figure 6-6). The grid points selected for the Murray at $t=0$ and the Darling at a lag of 1 year (Figure 6-6a, d) are virtually identical. As the Murray water year falls over two years, this is consistent with the strong correlations between the drought atlases and current year winter-spring-summer streamflow in both the upper and lower MDB (i.e., 2001 in the Darling reconstruction corresponds to ANZDA reconstruction year 2002 and water year 2002 in the Murray reconstruction). Most of the ANZDA domain (mainland Australia and Indonesia) is positively correlated with Darling streamflow, with stronger correlations over the Darling catchment than the rest of Australia, as expected.

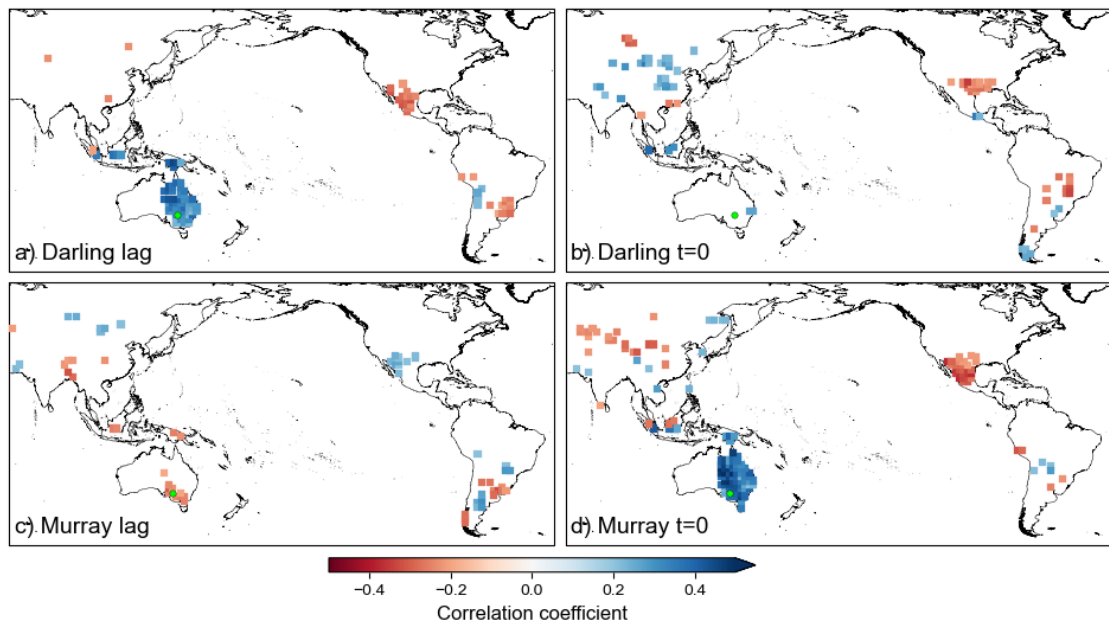


Figure 6-6 Drought atlas grid points selected as predictors for the gridded reconstruction based on a) significant ($p < 0.05$) correlation with transformed Darling July-Dec streamflow at Wilcannia and b) significant ($p < 0.05$) correlation with transformed water year Murray streamflow at Lock-7.

Correlations between the Murray and ANZDA are even stronger than the Darling and ANZDA, likely because the longer seasonal window captures significant variability in ANZDA PDSI over the late summer/autumn. Streamflow is also negatively correlated to most of the MXDA domain, but positively correlated to grid points over southern Mexico (Oaxaca). This pattern matches the inverse drought signal between north and central Mexico and southern Mexico during ENSO phases (Stahle et al., 2016). Correlations are weak over most of the SADA domain, with a stronger relationship to grid points over the La Plata Basin, a region without local tree-ring chronologies (Morales et al., 2020). It is possible that this region, which is far from the Andes and not affected by orographic precipitation, may better represent variability related to large-scale climate drivers concerning both the MDB and South America. The positive and negative correlations with the grid points selected from the MADA are also plausible when the impact of ENSO and the IOD on drought in monsoon Asia are considered. Drought is spatially variable over monsoon Asia with the Himalayas and the Tien Shan mountains affecting regional patterns (Ummenhofer et al., 2013). The selected grid points appear to represent genuine teleconnections between the upper and lower MDB and the drought atlases.

6.6.1.2 Reconstruction calibration and verification

Darling July-December streamflow could be successfully reconstructed using both the tree-ring predictors directly and the gridded PDSI. Figure 6-7 compares the two final reconstructions over the entire calibration period (1987-2000). Both reconstructions show good statistical skill based on the split period calibration and validation. The reconstruction based directly on tree-ring chronologies (Figure 6-7a) accounts for ~70% of the variance in naturalised streamflow over the

calibration period, with the whole reconstruction period covering 1600 – 2000 CE, which is the period over which both the early-period calibration and late-period calibration show positive verification statistics (VRE and VCE > 0; Figure E-4). In comparison, the reconstruction based on gridded drought atlas outputs (Figure 6-7b) accounts for ~60% of the variance in naturalised streamflow and covers the period 1500 – 2000 CE, the common period of the four drought atlases. The decrease in variance explained in the gridded reconstruction is largely due to reduced ability to capture the extreme values during the 1950s compared to the tree-ring reconstruction. The reconstruction shows little skill (RE > 0, VCE = 0) prior to 1500 CE when there is no contribution from the ANZDA grid points. As the gridded reconstruction is not nested over the skilful period, there is only a single set of verification statistics.

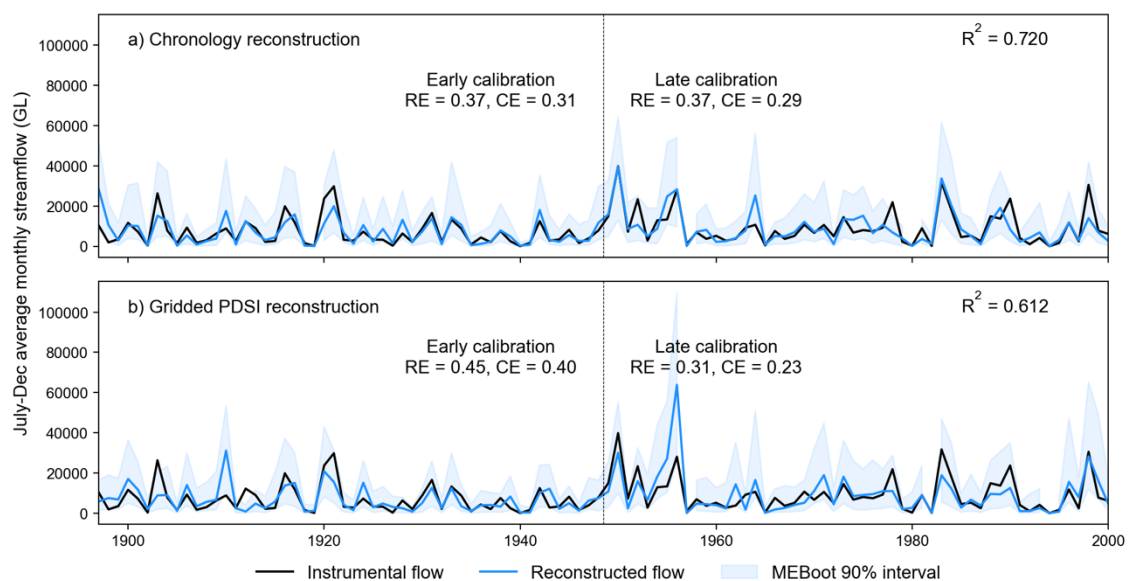


Figure 6-7 Reconstructed (blue) versus instrumental (black) Darling July-Dec naturalised streamflow over the full calibration period (1897-2000) for a) the reconstruction based on tree-ring chronologies and b) the reconstruction based on gridded drought atlas outputs. The uncertainty interval (light blue shading) is based on 300 maximum entropy bootstrap replications.

Figure 6-8 compares the tree-ring chronology and gridded reconstructions of Murray water year streamflow over the full calibration period (1987-2000). The reconstruction statistics are very similar, with both reconstructions accounting for approximately 60% of the instrumental variance. The tree-ring reconstruction covers the period 1440 – 2000 CE (Figure E-4), and as for the Darling, the gridded reconstruction shows little skill prior to 1500 CE.

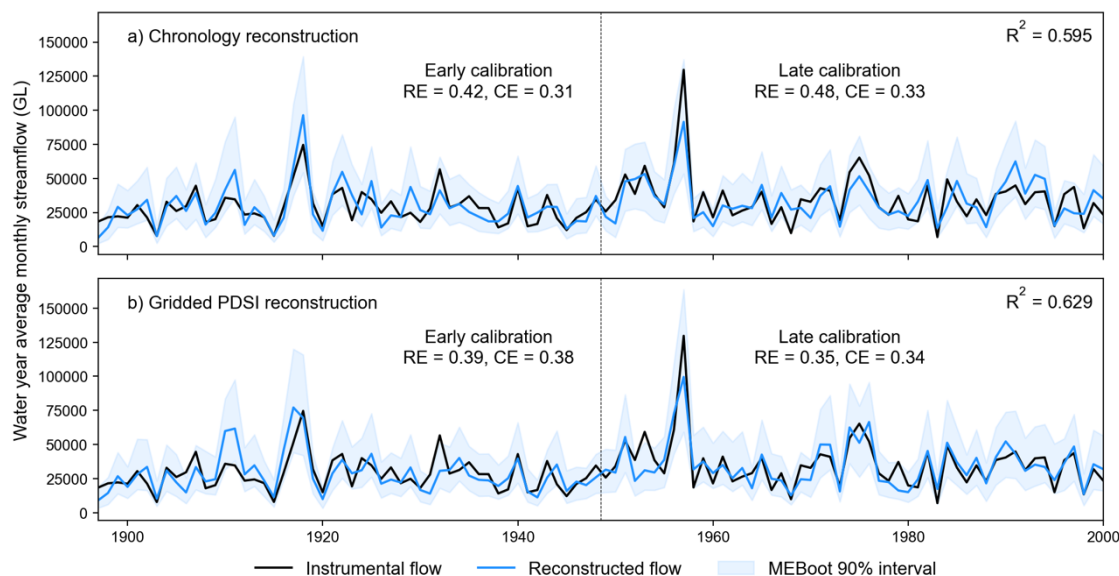


Figure 6-8 Reconstructed (blue) versus instrumental (black) Murray water year naturalised streamflow over the full calibration period (1897-2000) for a) the reconstruction based on tree-ring chronologies and b) the reconstruction based on gridded drought atlas outputs. The uncertainty interval (light blue shading) is based on 300 maximum entropy bootstrap replications.

Both Murray reconstructions underestimate the most extreme flood peak in the instrumental data (the water year 1956/57). In 1956, an exceptional flood event occurred in the Murray Basin, far exceeding the next highest streamflow year on record (1917, 80% smaller than 1956). This event resulted from consecutive months of above-average rainfall, with the highest totals falling in March due to Tropical Cyclone Agnes (Callaghan, 2019). Wet catchment conditions contributed to the extreme flooding, as the rainfall followed widespread flooding in the previous year (Callaghan, 2019). It has long been recognised that tree-ring widths are less able to capture extreme wet events than droughts (Fritts, 1976; Meko & Woodhouse, 2011; Wise & Dannenberg, 2019). Partly, this is a saturation problem; once the soil moisture store is filled, water is no longer the limiting factor to growth. Additionally, much of the precipitation during extreme events results in runoff rather than percolation to the root zone (Fritts, 1976). The 1956 event is so large that none of the standard streamflow transformations (power weighting, log-transform, Box-Cox transform) could successfully normalise the water year time series (Figure E-5). In contrast, the gridded model for the Darling substantially overestimates the flood peak in 1955, which again indicates poor capture of extreme high flow years during the instrumental period.

To test whether the gridded models perform poorly for extreme streamflow values in general, a residuals plot for the Darling and Murray gridded reconstructions are shown in (Figure 6-9). The error estimation is undertaken on the power-transformed streamflow values used for model calibration. Figure 6-9 shows that neither gridded model has residuals biased towards the high or low-flow extremes. Except for 1955 in the Darling reconstruction, the highest instrumental streamflow values are not within the top 10% of underpredicted or overpredicted years. Similarly,

only one of the five lowest streamflow values in the Darling and Murray reconstructions falls within the top 10% of overpredicted years. Nevertheless, the inability to capture the magnitude of extreme flood events during the instrumental period suggests events occurring in the pre-instrumental period may also be poorly captured. Additional work is needed to improve the reconstruction of extremely high flow events in the MDB.

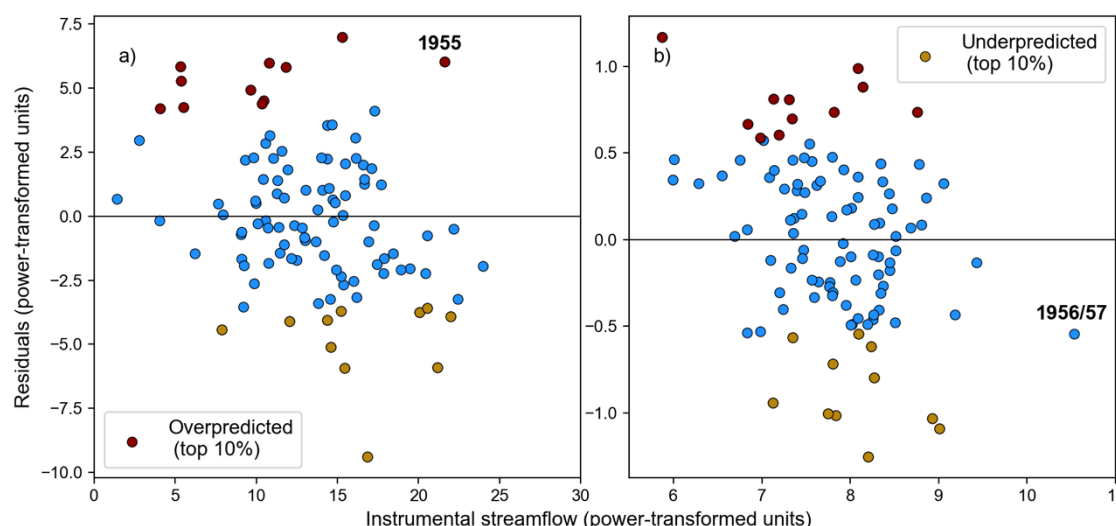


Figure 6-9 Residuals for the full calibration period (1897-2000) for a) the reconstruction of July-Dec Darling streamflow based on gridded drought atlas outputs and b) the reconstruction of water year Murray streamflow based on gridded drought atlas outputs. The top 10% of overpredicted values are shown in red, the top 10% of underpredicted values are shown in brown, and the remaining 80% of values are shown in blue.

Despite the over/underestimation of the peak values in 1955 and 1956/57, the lack of bias in the residuals and the positive verification statistics suggest the gridded reconstructions have suitable reconstruction ability and can be used for further analysis. The tree-ring and gridded reconstructions for each river are significantly correlated over the entire 500-year reconstruction interval (Pearson $r = 0.47$ for the Darling and $r = 0.59$ for the Murray), and while correlations decrease outside of the calibration period, they otherwise remain stable (Figure E-6). The gridded PDSI from the drought atlases shows similar variance explained for MDB streamflow to the underlying tree-ring chronologies, confirming that grid-based reconstructions are appropriate for Australian catchments. However, the decline in the performance of the chronology reconstruction of the Darling River before 1600 CE suggests the first 100 years of the grid-based reconstruction should be interpreted with caution.

6.6.1.3 Comparison of the streamflow projection methods

The performance of the gridded PDSI streamflow projection methodology was assessed by comparing the 30 gridded projections to the four bias-corrected model projections from the Australian Water Outlook (Figure 6-10). The AWO projections have already been extensively evaluated for their performance in simulating key aspects of the MDB climate over the historical

period (E. Vogel, personal communication, 11 July 2022) and are considered plausible future scenarios for the region. Figure 6-10 shows that the mean, median, and range of annual streamflow between 2020-2099 in the gridded projections are similar to the characteristics of the AWO projections, although many of the gridded projections for the Darling River show higher streamflow variance than the AWO projections. As expected from the larger model ensemble, the gridded projections represent a broader range of future scenarios.

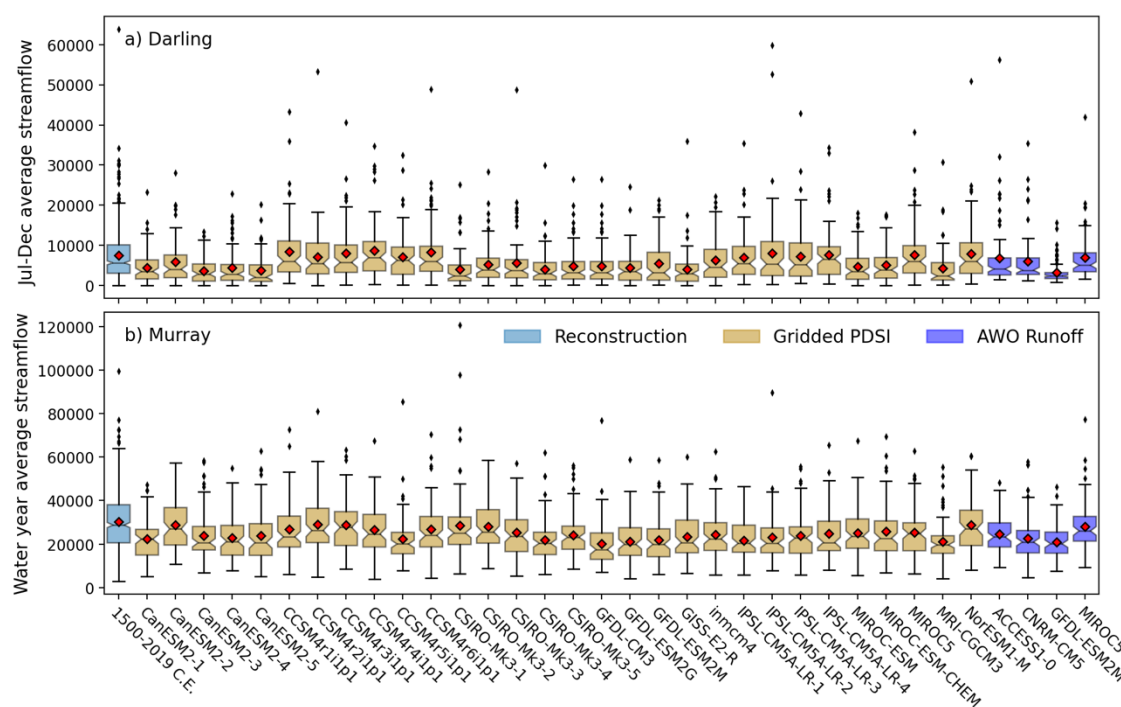


Figure 6-10 Boxplots of a) July-Dec streamflow at Wilcannia and b) Water year streamflow at Lock-7 in the reconstruction period (1500-2019 CE; light blue) and each year from 2020-2099. The 30 projections based on gridded PDSI (brown) are compared to the four simulations from the AWO bias-corrected model outputs (purple), with the mean of each simulation shown as a red diamond.

Figure 6-11 shows the average percentage change in streamflow over the 2020-2099 CE projections compared to the 1961-2019 CE historical period used for scaling for the 30 gridded and four AWO projections. Most models predict lower streamflow in future compared to the baseline period across the MDB. Future streamflow is more uncertain for the Darling than the Murray, as models predict a larger range of possible future conditions (-47 to +29% deviation from the baseline for the Darling and -28 to +4% deviation from the baseline for the Murray). The range of changes predicted by the gridded projections is very similar to the range predicted by the smaller AWO ensemble (-52 to +3% deviation from the baseline for the Darling and -25 to +0.3% deviation from the baseline for the Murray). The models downscaled and bias corrected in the AWO were selected to cover the range of plausible future scenarios. The gridded PDSI projection method provides a good estimation of future streamflow when compared to the best available estimates. As the gridded projections have been shown to be suitable for Australian

catchments, all remaining results are based only on the gridded results, with the final streamflow time series covering the period 1500-2099 CE.

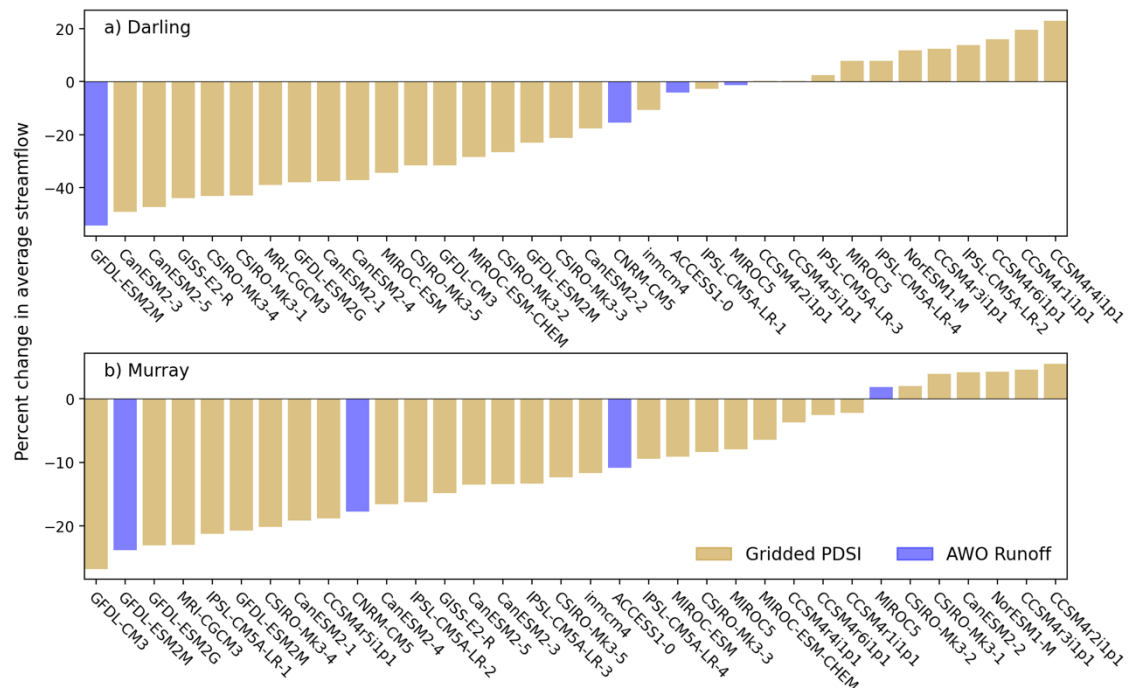


Figure 6-11 The average percent change in streamflow over 2020-2099 in the projections compared to the 1961-2019 instrumental period used for scaling for a) projected July-Dec streamflow at Wilcannia and b) projected water year streamflow at Lock-7. Projections based on gridded PDSI are shown in brown and derived from the AWO bias-corrected model outputs in purple.

6.6.1.4 Streamflow from 1500-2099 CE

For both the Darling and Murray reconstructions, the average streamflow over the entire reconstruction interval (1500-2019 CE) is not statistically different from the average streamflow during the 1897-2019 CE instrumental period (Darling: 7650 vs 7580 GL; Murray: 30800 vs 29500 GL). Neither gauge shows any significant trend in streamflow over the reconstruction interval. Concurrent dry epochs in the upper and lower MBD before the instrumental period occurred in the early 1500s, through most of the 1600s, and from ~1820-1850 CE. These match periods of aridity identified in previous paleoclimate studies (Cook et al., 2016; Ho et al., 2015a). Wet epochs are less coherent between the two halves of the basin. The highest streamflow anomalies in the Darling River reconstruction occur from ~1560-1580 CE, whereas high streamflow during the 1950s is unmatched in the Murray River reconstruction. The flood of 1956 remains an anomaly compared to the entire reconstruction period, with no similar magnitude event identified in the Murray reconstruction. However, as previously discussed, extreme wet years are likely underestimated, and thus it is difficult to assess how anomalous this event was.

The complete 1500-2099 CE July-December streamflow simulation for the Darling River at Wilcannia is shown in Figure 6-12. The multi-model ensemble interquartile range (IQR—25th to 75th percentile of projected streamflow) of the 30 gridded projections shows a decreasing trend

from 2020 to ~2040. From 2040 to the end of the century the range of future projections widens, with the 25th percentile result showing a continuing declining trend, but the 95th percentile result showing an increasing trend. The trend in the median of the model ensemble is not significant (Mann-Kendall trend test, $p > 0.05$), but average future streamflow in the Darling is likely to be lower than the average of the past 500 years (Students t-test, $p < 0.01$). The full 1500-2099 CE water year streamflow simulation for the Murray River at Lock-7 is shown in Figure 6-13. The multi-model ensemble interquartile range of the 30 gridded projections shows a decreasing trend in streamflow from 2020 to the end of the century, although the trend in the 75th percentile result is not significant (Mann-Kendall trend test, $p > 0.05$). The projections indicate that declines in streamflow observed in the Murray over the last 50 years of instrumental data are likely to continue.

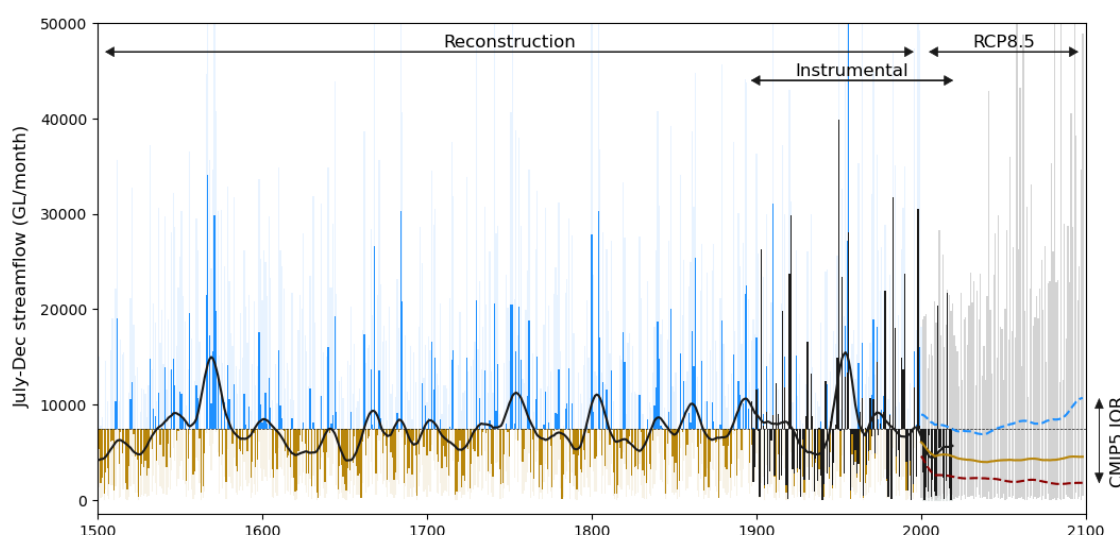


Figure 6-12 Reconstructed Darling River July-Dec streamflow for each year between 1500 and 2000 CE as a departure from the ‘historical’ period mean (1500-2019 CE; blue and brown bars, with 90% confidence interval as light shaded bars), along with the 30-year low-pass filtered reconstruction (black) highlighting multi-decadal variability. The instrumental Darling dry season streamflow between 1897 and 2019 CE is shown as black bars. Projected streamflow modelled using PDSI derived from the multi-model CMIP5 RCP8.5 ensemble (Table E-1) during the ‘future’ (2001–2099 CE) simulation period of these runs is shown as the grey lines. The 30-year low-pass filtered projected streamflow is shown as bold brown (median), dashed red (25th percentile), and dashed blue lines (75th percentile).

Compared to the reconstructions, flow duration curves calculated from the full model ensemble (Figure E-7) also indicate future drying in both rivers, with a decrease in the Q50 (the flow exceeded 50% of the time) by -26% in the Darling and -23% in the Murray. For the dry extremes (Q95 flow), the decline in the Darling is much greater than in the Murray, at -56% and -23% respectively. The wet extremes (Q5 flow) also show a decrease in the full ensemble compared to the past 500 years, by 13% in both rivers. There is, however, no decrease in the most extreme flood years.

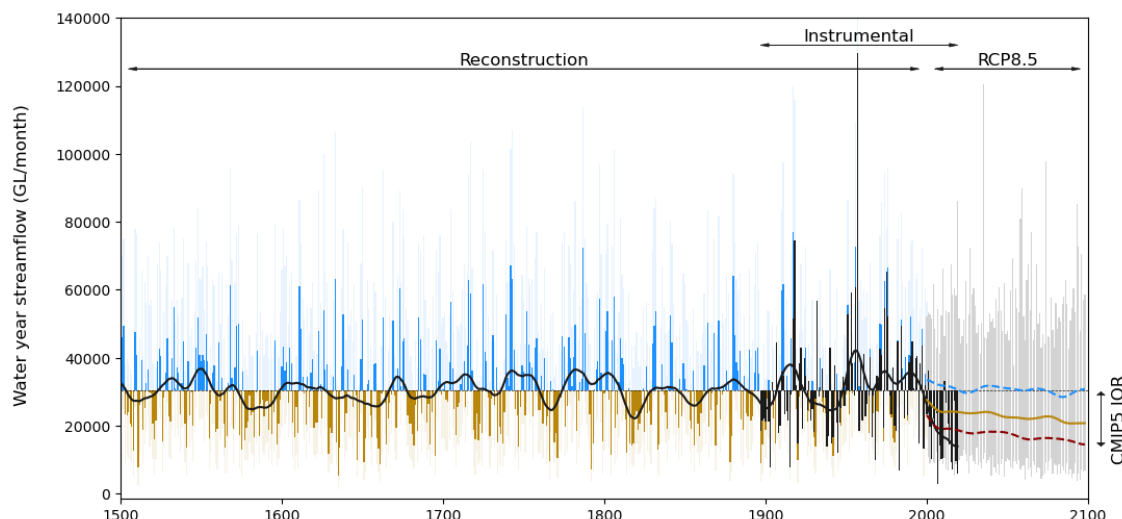


Figure 6-13 Reconstructed Murray River water year streamflow for each year between 1500 and 2000 CE as a departure from the ‘historical’ period mean (1500–2019 CE; blue and brown bars, with 90% confidence interval as lightly shaded bars), along with the 30-year low-pass filtered reconstruction (black) highlighting multi-decadal variability. The instrumental Murray streamflow between 1897 and 2019 CE is shown as black bars. Projected streamflow modelled using PDSI derived from the multi-model CMIP5 RCP8.5 ensemble (Table E-1) during the ‘future’ (2001–2099 CE) simulation period of these runs is shown as the grey lines. The 30-year low-pass filtered projected streamflow is shown as bold brown (median), dashed red (25th percentile), and dashed blue lines (75th percentile).

6.6.2 Analysis of past and future drought occurrence

6.6.2.1 Droughts over the past 500 years

The reconstructed streamflow series were analysed in terms of drought duration, peak, and magnitude. On average, the 104 dry episodes in the Murray reconstruction had a marginally longer duration (mean of 2.5 years and range from 1 to 10 years) than the 108 episodes in the Darling reconstruction (mean of 2.4 years and range from 1 to 9 years). Nearly half (46%) of the dry events in the Darling reconstruction are single-year events, compared to 35% for the Murray.

The ten strongest drought events in the Darling and Murray reconstructions, based on the combined ranking of the three drought parameters are listed in Table 6-1. Millennium, recent, and Federation droughts are the three highest ranked droughts in the Murray reconstruction, suggesting that the instrumental period has been exceptional for both dry and wet extremes. Another well-documented historic drought, the Settlement Drought of the late 1700s, is also ranked in the top ten Murray River droughts.

Table 6-1 List of the ten “strongest” drought episodes in the Darling River and Murray River reconstructions over the period 1500–2019 CE. Bold events are coherent in both the upper and lower MDB. The final rank score was derived from the sum of the individual rank scores for duration, peak, and magnitude (not shown) thus ties are possible. The higher the score, the stronger the event.

Darling River at Wilcannia						Murray River upstream of Lock-7					
Start year	End year	Duration (years)	Peak (SDU)	Magnitude (SDU)	Rank score	Start year	End year	Duration (years)	Peak (SDU)	Magnitude (SDU)	Rank score
1991	1995	5	3.06	8.42	313	2002	2010	9	3.67	13.17	311

2000	2004	5	3.03	6.77	310	2012	2019	8	2.77	11.66	307
1523	1531	9	2.14	6.09	308	1897	1901	5	2.14	4.49	289
1501	1507	7	1.78	6.18	301	1634	1636	3	2.91	5.67	282
1957	1961	5	2.69	4.37	298	1816	1823	8	1.38	6.65	278
2011	2015	5	2.49	4.42	298	1503	1508	6	1.57	4.22	276
1813	1818	6	1.76	5.73	296	1659	1661	3	2.21	4.81	275
1965	1969	5	2.34	4.61	296	1678	1684	7	1.38	5.22	272
1646	1653	8	1.45	6.94	296	1791	1793	3	2.47	4.18	272
2006	2009	4	2.11	6.50	288	1966	1970	5	1.59	2.95	262

Similarly, the highest ranked droughts for the Darling occurred during the instrumental period, but the early 1500s shows more sustained low streamflow anomalies. The Millennium drought is listed in the top ten droughts for the Darling reconstruction; however, it is not a contiguous period. Here we can see the effect of the choice of threshold on drought identification. Because streamflow in 2005 was not below the long-term average in the Darling, the Millennium drought appears as two dry periods, 2000-2004 (rank 2) and 2006-2009 (rank 10). This is a potential weakness of the methodology for defining drought periods, as a single wet year is unlikely to be sufficient to return a catchment to pre-drought conditions, but it terminates the drought run in this analysis. Despite its exceptional peak streamflow anomaly, the recent drought is only the 18th ranked event in the Darling reconstruction, due to its short duration (2017-2018 in this analysis). Based on precipitation anomalies, the recent drought continued through 2019 (BOM, 2020b), however, it is only identified as a two-year drought in the runs analysis as naturalised streamflow data is not available for all of 2019.

Bivariate models for drought duration/magnitude and drought duration/peak were fit to each streamflow reconstruction to assess the exceedance probabilities for the strongest drought episodes. Figure E-8 and Figure E-9 show that the marginal distributions are good approximations for drought characteristics in the Darling and Murray rivers. The goodness-of-fit of the joint probability models was tested by considering the fit of the model parameters to the conditional distributions of magnitude or peak for droughts of a given duration. Figure E-10 and Figure E-11 show that the magnitude of droughts with a duration of 1-3 years (the durations where there are a reasonable number of samples) can be approximated by a gamma distribution with the shape and scale parameters estimated by fitting the model to the entire time series. Similarly, the conditional distributions of peak streamflow anomaly for droughts with a duration of 1-3 years are suitably approximated by the modelled cumulative distribution function (Figure E-10 and Figure E-11). The goodness-of-fit of the models can also be explored by comparing sample and theoretical correlation coefficients between drought durations/magnitudes and durations/peaks. For the entire Darling River time series (1500-2019 CE), drought duration and magnitude have a correlation of 0.80 with a calculated model correlation of 0.77, and duration and drought peak have a correlation of 0.54 with a calculated model correlation of 0.42. The models show a similarly good fit for the Murray River time series, with sample correlation between drought

duration and magnitude of 0.80 and a calculated model correlation of 0.77, and sample correlation between duration and drought peak of 0.48 with a calculated model correlation of 0.41. The sample and model correlations are quite close, especially for duration and magnitude.

The 30 highest ranked droughts that occurred over the entire reconstruction period (1500-2019) in the Darling and Murray rivers are plotted against selected quantiles derived from the fitted conditional probability of drought magnitude and peak given droughts of durations between 1 and 14 years (Figure 6-14 and Figure 6-15, respectively). For both the Darling and the Murray, droughts of longer duration than the instrumental period droughts have occurred, with the 1500s appearing as a particularly dry period. However, in terms of drought magnitude, the droughts of the instrumental period are unmatched in both the upper and lower basin. This suggests a role of increasing temperature on the severity of recent droughts in eastern Australia.

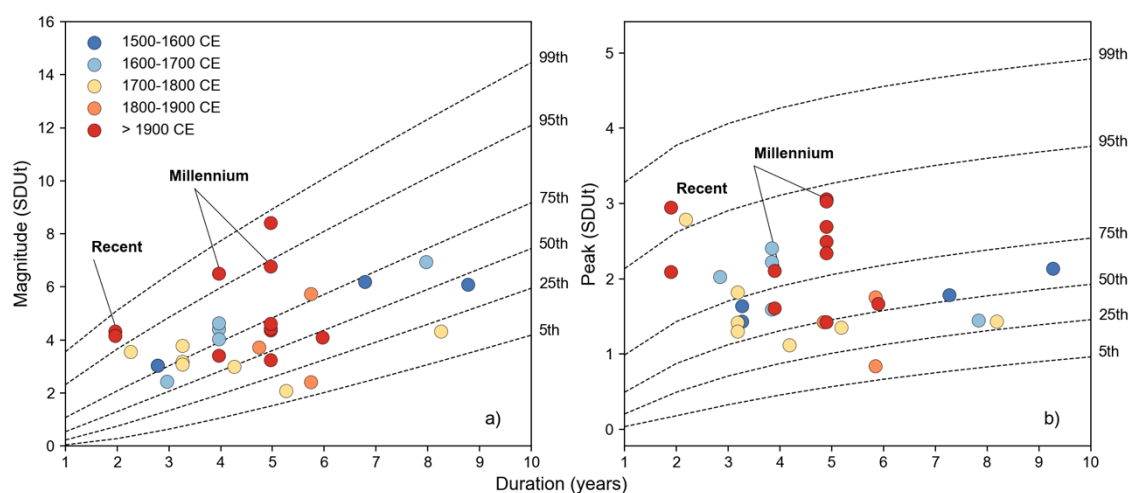


Figure 6-14 The top 30 ranked droughts during the historical period (1500-2019 CE) for the Darling River at Wilcannia compared to selected quantiles of the conditional distribution for a) drought duration and magnitude and b) drought duration and peak. The colours indicate the century when the drought began, and points are jittered for display purposes.

Both the Millennium and recent droughts exceed the 95th percentile for the conditional distribution of magnitude given duration in the upper and lower MDB (Figure 6-14a, Figure 6-15a). The likelihood that a drought of nine years would have exceeded the magnitude of the Millennium drought in the Murray River is 1.4%, and the possibility that a drought of eight years would have exceeded the Murray streamflow anomaly from 2012-2019 is 2.6%. For the Darling, the chance that a drought of four years would have exceeded the magnitude of the worst period of the Millennium drought (2006-2009) is 3.4%, and the chance of a more substantial two-year drought than 2017-2018 is 2.6%.

Now considering the peak streamflow anomaly (Figure 6-14b, Figure 6-15b), only the recent drought in the Darling River exceeds the 95th percentile of the conditional distribution, with a likelihood of exceedance of 3.2%. The peak of the recent drought in the Murray and the

Millennium drought in both basins are less severe, with an exceedance probability of greater than 5%, given their durations.

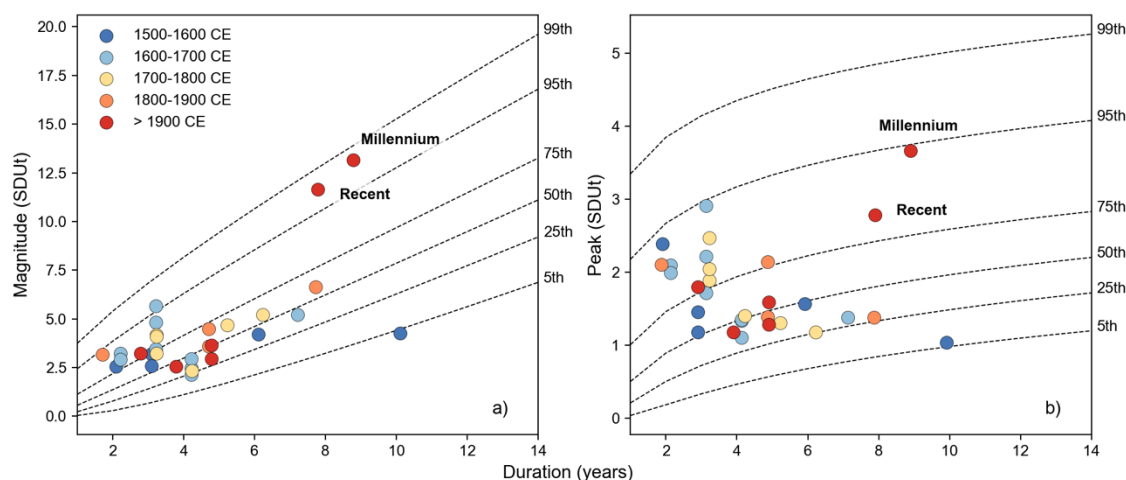


Figure 6-15 The top 30 ranked droughts during the historical period (1500-2019 CE) at Murray River Lock-7 compared to selected quantiles of the conditional distribution for a) drought duration and magnitude and b) drought duration and peak. The colours indicate the century when the drought began, and points are jittered for display purposes.

Because joint probability models were fit to the drought characteristics, it is also possible to calculate joint exceedance probabilities. For example, the likelihood that a drought lasted longer than nine years with a magnitude more significant than the Millennium drought in the Murray basin is 0.11%. A drought longer than eight years with a magnitude greater than the recent drought is twice as likely to have occurred, at 0.23%. This represents a return period of around 430 years for the recent drought and over 900 years for the Millennium drought. In comparison, while still severe, the recent drought in the Darling is less extreme; the chance that a drought of two years would have had a peak streamflow anomaly greater than the recent drought is 2.4%, and the chance that a drought would have lasted longer than two years and had a greater magnitude than the recent drought is 17.4%.

6.6.2.2 Future drought risk

To investigate how drought risk might change in future, the joint probability analysis was repeated 30 times, with a time series comprised of the reconstruction (1500-2019) and one of the gridded projections (2020-2099). Figure 6-16 and Figure 6-17 show how the calculated quantiles derived from the conditional probability of drought magnitude and peak for a given duration could change based on the revised parameters for each series. Against these quantile ranges, the top 30 droughts from the historical period (plotted in blue) are compared to the single highest ranked future drought from each simulation (plotted in red).

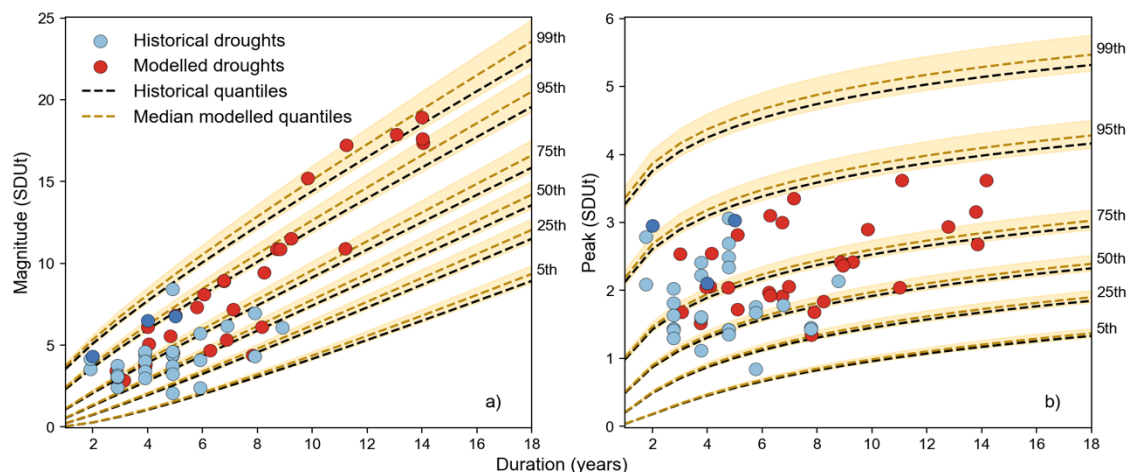


Figure 6-16 The top 30 ranked droughts during the historical period (1500-2019 CE; blue) compared to the highest ranked drought for each streamflow projection (2020-2099 CE; red) for the Darling River at Wilcannia for a) drought duration and magnitude and b) drought duration and peak. The dark blue dots indicate the Millennium and recent droughts. The dashed black lines represent selected quantiles of the conditional distribution based on historical data, the dashed brown lines represent the median quantiles for the conditional distribution of historical and projected streamflow for each of the 30 gridded PDSI projections, and the yellow bands represent the full range of projected quantiles from the gridded projections. Points are jittered for display purposes and may appear in slightly different locations to the points in Figure 6-14.

For both the Darling and Murray Rivers, Figure 6-16 and Figure 6-17 show an increase in the severity of future droughts, with droughts of much longer duration and higher magnitude projected. Future predictions of drought peak given duration are less exceptional, with much longer durations but only a small increase in peak streamflow anomaly for the Darling. No future model projects a single-year low flow period that matches the Murray's extremely low flow seen in 2006/2007 (water year streamflow of ~2900 GL compared to the instrumental average of ~30800 GL). It is important to note that drought peak is naturally bounded, as streamflow cannot go below zero. While the same constraint theoretically exists for drought magnitude, there are no instances of multiple years with no or exceptionally low streamflow in either the reconstructions or projections.

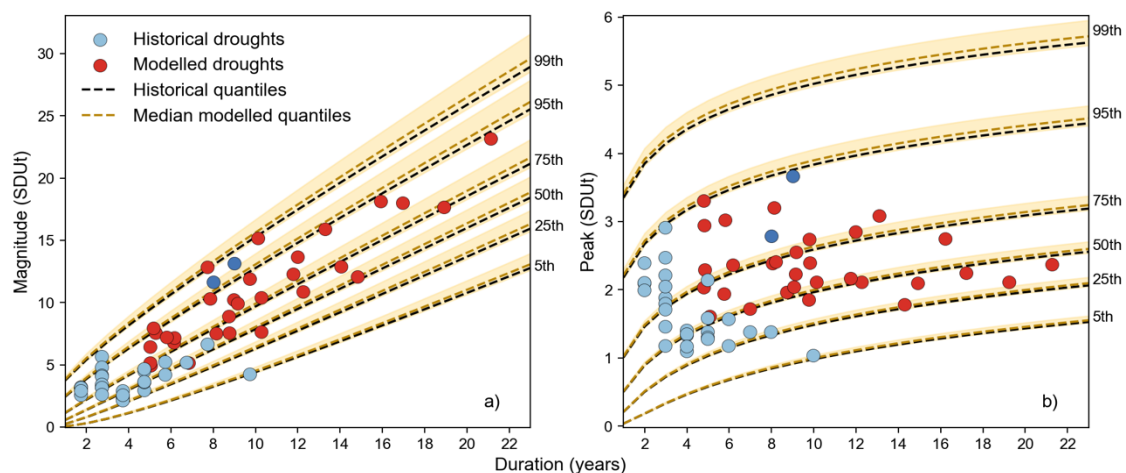


Figure 6-17 The top 30 ranked droughts during the historical period (1500-2019 CE; blue) compared to the highest ranked drought for each streamflow projection (2020-2099 CE; red) for the Murray River at Lock-7 for a) drought duration and magnitude and b) drought duration and peak. The dark blue dots indicate the Millennium and recent droughts. The dashed black lines represent selected quantiles of the conditional distribution based on historical data, the dashed brown lines represent the median quantiles for the conditional distribution of historical and projected streamflow for each of the 30 gridded PDSI projections, and the yellow bands represent the full range of projected quantiles from the gridded projections. Points are jittered for display purposes and may appear in slightly different locations to the points in Figure 6-15.

It is also possible to calculate the change in the likelihood that droughts of the same strength as the Millennium or recent droughts will be exceeded in future. In the Murray, the chance of a nine-year drought exceeding the magnitude of the Millennium drought increases from 1.3% to 1.7% under the median future projection (dashed brown line in Figure 6-17a), and more than doubles under the driest future projection reaching 3%. The chance of an eight-year drought exceeding the magnitude of the recent drought also increases substantially, from 2.6% to 3.7% and 5% under the median and driest future scenarios respectively. The joint probability that a drought will be longer than nine years and more severe than the Millennium drought increases to 0.36% under the worst-case scenario. While the likelihood is still minimal, this represents a decrease in the return period from 900 years to 280 years. Similarly, the return period of a longer and more extreme drought than the recent drought decreases from 430 years to only 150 years under the driest future scenario.

In the Darling, the chance of a two-year drought having a higher peak streamflow anomaly than 2017-2018 increases from 2.4% based only on historical data to 3.5% under the median future scenario and 4.5% under the driest future scenario. The chance that such a drought would have a higher peak value and last longer than two years increases from 17% to 21% and 23% under these scenarios. The joint probabilities are so high because the chance of a drought lasting longer than two years is very high (41%).

6.7 Discussion

6.7.1 Implications for water management

Water managers need information on plausible future trends in streamflow and the likely occurrence of hydrological extremes for resource planning and to feed into the design of adaptation and mitigation measures. A thorough understanding of natural variability is required to fully understand the future risk of extreme events, like droughts. Due to the limitations of the instrumental record, paleoclimate data is used to provide a much longer time series to evaluate recent extremes against previous centuries. In this Chapter, a direct method is introduced for developing continuous past and future streamflow reconstructions, building on prior studies which demonstrated the utility of gridded drought atlases for streamflow reconstruction (Coulthard et al., 2016; Ho et al., 2016, 2017; Nguyen et al., 2020). Applied to two time series of naturalised streamflow from the Murray-Darling Basin, the results of this Chapter show that

streamflow reconstructions from 1500-2000 CE developed from gridded PDSI have similar reconstruction strength to the more traditional chronology-based method and account for a similar proportion of instrumental variance. In addition, streamflow projections developed from PDSI derived from climate models display similar streamflow characteristics over the 2020-2099 CE period as the best available estimates from bias-corrected and downscaled climate model outputs. Through these comparisons, the gridded method is suitable for producing continuous past and future streamflow series for eastern Australia. As the method used to develop streamflow projections is not subject to the computational constraints as downscaling climate models, a larger ensemble of model outputs, and thus potential future conditions could be explored.

The streamflow time series indicate drier future conditions in the MDB compared to streamflow over the last 500 years. The median projection shows a continuous decline in streamflow for the Murray River to the end of the century. There is broad agreement across the projections, with declines also predicted by the 25th and 75th percentile results. This is consistent with projected decreases in winter rainfall in southeast Australia, which contributes a large proportion of water year streamflow in the lower basin (Moise et al., 2015; Timbal et al., 2015). For the Darling, the median projection stabilises after an initial decline in streamflow, albeit below the mean of the last 500 years. Toward the end of the century the projections diverge, with an increasing trend in the 75th percentile result and a decreasing trend in the 25th percentile result. There is large uncertainty in the climate model rainfall projections, with models disagreeing on the direction of rainfall change (Kirono et al., 2020; Moise et al., 2015). Although there is higher certainty in the trend in winter/spring rainfall which predominantly contributes to July-Dec streamflow compared to summer rainfall (Ekström et al., 2015), uncertainty in projected rainfall is mainly responsible for the uncertainty in the streamflow projections.

In addition to long-term trends in streamflow, the likelihood of extreme events is important for future water management planning. For water supply planning, duration and magnitude are the most important features of drought episodes (Biondi et al., 2005; Biondi & Meko, 2019). The Millennium Drought is a good example; despite relatively modest precipitation deficits in most individual years, the length of the drought and its magnitude (cumulative deficit) resulted in substantial economic and ecological impacts in the Murray catchment. Because severe multi-year droughts are rare and have different spatial and temporal characteristics (Kiem et al., 2016), their effects are difficult to predict and manage. Events that are much more severe than preceding events almost always result in larger impacts (Kreibich et al., 2022). This is because infrastructure and non-structural drought risk measures are generally implemented after a severe event and not proactively. A tendency to place a large subjective probability on extreme events can result in the failure of these risk management strategies for future, unprecedented events (Kreibich et al., 2022; Van Dijk et al., 2013).

Therefore, numerical probability statements about drought occurrence can be used to inform science-based management and policy decisions (Biondi et al., 2005). The benefit of continuous past and future streamflow reconstructions for risk management is that they can provide a more accurate estimation of the baseline likelihood of extremes with which to compare to (internally consistent) future projections. For example, we can say that more prolonged droughts than the Millennium drought have almost certainly occurred in the Murray in the past, but that the likelihood that longer droughts had a higher magnitude than the Millennium drought is very small (0.11%). This is clearly more informative than ‘worst on record’. The likelihood that a drought as severe as the Millennium drought will be exceeded in future is also beneficial when designing adaptation measures. Droughts longer than the Millennium drought are not unlikely considering the range of future projections; with nearly half (14/30) of the models predicting droughts of more than nine years. While the likelihood of a drought both longer and with greater magnitude than the Millennium drought remains small under the range of projections (0.36% under the worst-case projection), it is certainly a scenario worth considering in long-term planning considering the potential consequences.

Paleo-reconstructions are often criticised for their failure to agree and thus considered too uncertain for use in water management planning. Published estimates of the return period for the Millennium drought in the MDB have ranged from 300 years, based only on instrumental data (Potter et al., 2010), up to ~1500 years, based on a multiproxy paleo-streamflow reconstruction from 1783-1988 (Gallant & Gergis, 2011; Gergis et al., 2012). The estimate here, of more than 900 years, is in good agreement with the results of Gallant and Gergis (2011), considering the baseline is much longer, from 1500-2000 CE. Estimates of the severity of historical droughts will always differ depending on the length of the record used for comparison, as well as other factors such as proxy selection, calibration period, reconstruction method etc. The longer the record, the more likely there will have been an event approaching or exceeding the most extreme event in the instrumental period. Outside the instrumental period, the 1500s emerges as the driest period in the gridded MDB reconstructions. Other, longer paleoclimate records indicate that the 1100s were even drier in eastern Australia (Flack et al., 2020). Thus, if it was possible to extend the streamflow reconstructions back to this period, estimates of likelihood could be different.

Valid conclusions can be drawn from comparing estimates from different reconstructions, even if they don’t precisely agree. For example, the two paleo-streamflow reconstructions of the Murray River agree that using only instrumental data results in an estimate of the return period that is too low. This should not be interpreted as the paleo-record indicating a lower likelihood of exceedance compared to the instrumental data. Rather, it illustrates that when a greater range of natural variability is considered, the Millennium drought still emerges as an extreme event,

pointing towards the role of increasing air temperatures in amplifying the impact of below-average precipitation in recent droughts.

Water storages are more resilient to short droughts with high peak streamflow anomaly but small cumulative deficits. However, for the environment, such droughts can be catastrophic. The 2017-2019 drought was unprecedented in the northern MBD, with the highest temperatures and the lowest three-year precipitation totals on record (BOM, 2020b). The Darling ceased to flow at Wilcannia over the second half of 2018. The loss of flow and extremely high temperatures caused an ecological shock resulting in the estimated deaths of hundreds of thousands to over a million fish in Menindee Lakes, downstream of Wilcannia (Vertessy et al., 2019). In-stream infrastructure that prevents fish movement during low flow events, and over-extraction of water from the river, place the lower Darling at a high risk of fish deaths during severe droughts (Vertessy et al., 2019).

The results of the joint probability modelling of drought duration and peak for the Darling River should be interpreted with this context in mind. Based on natural variability over the past 500 years, the likelihood that a two-year drought would have a peak streamflow anomaly greater than the recent drought is 2.4%, increasing to 4.5% under the driest future scenario, a return period of 22 years. It is, therefore, very likely that the low streamflow conditions that resulted in the environmental catastrophe of December 2018-January 2019 in the Darling have occurred in the past and will occur with greater frequency in the future. The chance that a future drought will last longer than two years with a peak greater than the recent drought is extremely high because drought events are projected to increase in length.

Drought is a natural hazard, not a disaster in and of itself. Understanding the likelihood of drought occurrence in future is only one element needed for a comprehensive understanding of future drought risk. The consequences of droughts for people and the environment also depend on the economic, environmental, and social vulnerabilities of different regions and sectors and the ability of water resource systems to respond during drought events (Prosser et al., 2021). The impact of past drought events with similar peak anomalies was probably much smaller in the absence of extreme temperatures and the management infrastructure which contributed to the catastrophe. Whether future events will have similar impacts will depend on the management decisions that are made in the short term to mitigate this risk. Protecting native fishes from future fish kill events requires sufficient environmental flows to ensure connectivity with weir pools, providing refugia for species during severe drought events (Vertessy et al., 2019). Future streamflow scenarios like the ones presented in this Chapter can be used to test the suitability of different planning alternatives in maintaining flows during droughts.

A key challenge for action on future projections is the uncertainty reflected in the large range of potential outcomes. Clear presentation and communication of drought projections and their uncertainty can help overcome this challenge (Kirono et al., 2020). Figure 6-16 and Figure 6-17 present a very clear and alarming future for the Darling and Murray rivers whilst incorporating the uncertainty of the model ensemble. It is hoped that communication tools like these figures can help push back on the view that if water management can be shown to be effective across instrumental hydrological variability, then it should be effective in the future (Prosser et al., 2021).

6.7.2 Expanding gridded projections to a more extensive study and other future work

Drought atlases have been previously shown to be suitable for streamflow reconstructions in the United States and across monsoon Asia. In this Chapter, we demonstrate that they are also suitable for reconstructing streamflow in eastern Australia. Once a model relating PDSI grid points to streamflow has been developed and verified, it can also be applied to produce future streamflow projections for any catchment. However, there are technical challenges to upscaling the method compared to reconstructing a single catchment. The first challenge is to automate the selection of the reconstruction season. In their regional studies of the United States and Monsoon Asia, Ho et al. (2017) and Nguyen et al. (2020) both averaged streamflow annually, over the water year and the calendar year, respectively. A large proportion of the gauges reconstructed by Ho et al. (2017) were not validated. Poorly performing models were spatially aggregated, suggesting that drivers of water year streamflow in some parts of the United States are not well captured by the gridded PDSI reconstruction used in that study. For large-scale studies, it would be preferable to specifically target the reconstruction season to the season over which variability in streamflow is captured by the drought atlas/es, as done here for the Darling (July-Dec) and Murray (water year). As illustrated by these two rivers, this would not necessarily be the same season over the entire reconstruction domain. One simple method would be to cluster streamflow gauges into climate zones and determine the appropriate season for each zone. For Australia, climate regions are well defined and likely to be an appropriate reconstruction target (e.g., Freund et al., 2017). For other regions, hierarchical clustering of streamflow stations could be employed.

The number of grid points posed a significant challenge for using the point-to-point (PPR) algorithm, which has limitations on the number of predictor inputs. In this study, PPR was used for consistency with the tree-ring based reconstruction. However, there are many other suitable methods for reconstruction based on similar workflows, i.e., reducing the number of predictors through PCA and then developing a regression model that relates the predictors to streamflow, that could be employed instead. One such method is described in Chapter 5, and Ho et al. (2017) and Nguyen et al. (2020) describe two others. These methods can be set up to run in projection as well as reconstruction mode (i.e., both forwards and backwards) which would simplify the method used to produce projections from the PPR algorithm in this work.

Finally, streamflow gauge records are commonly much shorter than the modelled naturalised streamflow available for the Darling at Wilcannia and Murray at Lock-7. In many cases, streamflow records are too short for split period validation. Thus, another suitable validation scheme (e.g., moving block validation, see Chapter 5) would need to be employed. One benefit to using drought atlases for reconstruction is that instrumental data is generally appended to the end of the reconstruction extending the reconstruction period beyond the end date of many tree-ring chronologies (this was not the case for the SADA; hence the end date at the year 2000). Thus, the period available for calibration is extended relative to the tree-ring predictors used in the atlas production. None of these challenges poses many limitations to scaling up the method for a regional study. Solutions to all points raised are already available and can be implemented relatively simply.

The streamflow reconstructions produced to date (Gallant & Gergis, 2011; McGowan et al., 2009) have relied on proxies remote from the MDB and thus necessarily assume stationarity. This is also an assumption underpinning the reconstructions presented in this Chapter. However, as previously discussed in Chapter 3, utilizing a network of tree-ring chronologies from multiple teleconnected regions minimises the effects of non-stationarities on the reconstruction (Batehup et al., 2015). Nevertheless, efforts should continue to develop high-resolution local proxies to further strengthen streamflow reconstructions. The reconstructions cannot explain about 40% of Darling and Murray streamflow variance, and this percentage could be reduced by adding local predictors from key parts of the catchment. Identifying proxies capable of recording summer precipitation signals from the upper MDB (e.g., proxies that capture short-duration, heavy rainfalls, such as isotopes) may allow the full water year to be captured in the Darling River reconstruction. The importance of heavy rains for breaking drought events in the MDB also points to the need to better capture high flow extremes in the reconstructions. Information on the maximum interval between drought-relieving rain events could be critical to refining the risk of multi-year droughts.

The gridded projections in this Chapter were based on the CMIP5 model outputs. Early studies based on the CMIP6 suite of models find that future drought changes are larger and more consistent in CMIP6 compared to CMIP5 (Ukkola et al., 2020). Thus, it may be worthwhile update the gridded projections using the CMIP6 model suite. Nevertheless, both CMIP5 and CMIP6 models tend to underestimate rainfall persistence, or the occurrence of sustained rainfall anomalies, which results in a tendency to underestimate drought duration and magnitude relative to instrumental data (Rocheta et al., 2014; Ukkola et al., 2020). The MRNBC bias correction method applied to the AWO model ensemble adjusts the model outputs to better represent persistence (Johnson & Sharma, 2012). No adjustment has been made to account/correct for persistence in the gridded PDSI model outputs. Further work is therefore needed to validate the

representation of drought characteristics in the gridded projections relative to the AWO ensemble to determine whether an adjustment for persistence is required.

6.8 Conclusions

Regionally specific hydrological projections which quantify the impacts of both natural climate variability and anthropogenic change are needed to support water management decision-making. Using the Murray-Darling Basin as a case study, a technique for developing both streamflow reconstructions and future projections is presented based on gridded estimates of the Palmer drought severity index. To verify the method, gridded reconstructions of the Darling and Murray rivers are compared to reconstructions developed using the more traditional, tree-ring method, and show similar reconstruction statistics. The future projections, based on an ensemble of 14 climate models and 30 individual simulations, are compared to an existing ensemble of downscaled and bias-corrected climate model outputs for the MDB, and produce similar streamflow characteristics as these ‘best available’ estimates. The gridded method is therefore found to be suitable for the MBD and could be extended to a regional study with minimal additional development.

We fit joint probability models to characteristics of drought events (duration, magnitude, and peak) identified in the reconstructions and analysed the likelihood that the most severe historical drought events could be exceeded in the future. The Millennium Drought, the most severe recorded drought in the Murray catchment, is shown to be exceptional compared to the 500-year paleorecord, with a return period exceeding 900 years. This suggests increasing temperatures likely amplified precipitation anomalies during this drought. The future projections show that droughts of this severity are more likely to occur in future, with the return period decreasing to 280 years under the driest future projection. Droughts as or more severe (longer duration and/or greater magnitude) than the Millennium Drought should be considered in future scenario planning.

In contrast, events as severe as the 2017-2019 drought in the Darling catchment have a return period of only ~42 years based on the paleorecord. The impact of such events in the past was probably much smaller in the absence of extreme temperatures and the water management infrastructure which contributed to the catastrophic environmental outcomes of that drought in the summer of 2018/19. Based on the model projections, such events are likely to occur with greater frequency in future. Whether future events will have similar impacts will depend on the management decisions that are made in the short term to mitigate this risk.

The visual presentation of the joint probability model results, which demonstrate an alarming future for the Darling and Murray rivers, are a powerful tool to communicate the drought projections and their uncertainties. However, as CMIP5 models tend to underestimate rainfall

persistence, it is possible that drought duration and magnitude are also underestimated in the gridded projections. Further work is therefore needed to validate the representation of drought characteristics in the gridded projections.

Chapter 7 Conclusions

To achieve sustainable water resource planning, a robust understanding of long-term natural climate variability as well as the likely impacts of climate change are urgently required. However, short instrumental records are insufficient to fully understand natural trends and variability in climate. This thesis aimed to use remote tree-ring chronologies to reconstruct past hydroclimate in the South Pacific to address uncertainty around past and future trends and detect the occurrence of extreme events. This broad objective, and the specific aims outlined in Section 1.4, were addressed across five case studies, each reconstructing and analysing a different aspect of South Pacific hydroclimate.

Overall, this thesis highlights the enormous potential of remote tree-rings for improving our understanding of past climate in the South Pacific. The reconstructions consistently demonstrate that the instrumental period underestimates the full range of natural climate variability and demonstrates how century-long records provided by tree rings can help us better understand past climate drivers, contextualise the instrumental period, and refine estimates of future climate risks. Existing methods for tree-ring reconstructions have been applied with success in the region (Chapter 2); however, overcoming the challenges posed by very short and non-continuous records required adaptations to existing methods (Chapter 3) and the development of new methods (Chapter 5). The new baselines generated by this research allow scientists, academics, and policymakers from across the region to analyse and address climate impacts and risks over time spans not previously possible. The specific achievements of this thesis are described in more detail below.

7.1 Summary of main findings

The South Pacific Convergence Zone (SPCZ) is the largest rain belt in the Southern Hemisphere and a key driver of precipitation variability impacting South Pacific Island communities. In **Chapter 2**, a 1300-year-long record of precipitation variability in the SPCZ region was presented, providing an important context for understanding historic changes captured by instrumental period. We found that during the medieval climate anomaly (MCA, ~1000–1200 CE), a period when the climate was warmer on average than during the instrumental period, the main axis of convergence in the SPCZ was to the east of its current position. This suggests that during the MCA the southwest Pacific experienced a period of sustained dry conditions, similar to an El Niño event. This could have important implications for our understanding of colonization processes in East Polynesia and supports the ‘El Niño hypothesis’ of Pacific migration. The distinct behaviour of the SPCZ during the MCA can also be used to assess general circulation model projections for Pacific Island communities and the wider region. The success of the SPCZ reconstruction, indicated by its length and positive verification statistics, showed that robust

reconstructions of South Pacific climate variability are possible using remote chronologies sensitive to changes in the El Niño-Southern Oscillation (ENSO). This case study provides the ‘proof-of-concept’ for using remote tree rings for hydroclimatic reconstructions in the South Pacific in Chapters 3, 5, and 6.

Following from the SPCZ case study, the same methods, with some modification, were applied to produce spatially resolved reconstructions of drought for the South Pacific Islands. Small Pacific Islands are particularly susceptible to droughts, yet due to data limitations, quantifying and attributing historical drought trends and variability is still a research gap. In **Chapter 3**, considerable progress was made towards producing a drought atlas for the South Pacific (called the SPaDA), describing variability in the November-April Standardized Precipitation Evapotranspiration Index for the period 1640-1998 CE. The suitability of using a trans-Pacific network of tree rings to produce the SPaDA is demonstrated by its ability to reproduce four known historical drought events, and the strong and stable correlation between the first principal component of the SPaDA and previously published tree-ring and multi-proxy (tree ring, coral, ice core) ENSO reconstructions. A random forest classifier, a supervised machine learning algorithm, was used to identify extreme El Niño events based on the spatial drought patterns in the SPaDA. Nevertheless, the SPaDA has some limitations. The extremely short meteorological data records for many of the Pacific Islands precludes statistical verification over much of the reconstruction domain. In addition, ENSO events in the SPaDA have little correspondence to previously published coral-based ENSO reconstructions, which means the SPaDA is without truly independent verification (i.e., no proxy overlap) over the first ~ 140 years of the reconstruction. Further work is therefore needed to improve the SPaDA before it can be used to support drought attribution analysis for the Pacific Islands.

In **Chapter 4** one of the unresolved questions identified in Chapter 2 was thoroughly investigated: do Southern Hemisphere tree rings record volcanic signals? Data from eight New Zealand dendrochronological species was used to test whether volcanic events could be identified in tree rings. We found that New Zealand dendrochronological species are reliable recorders of volcanic cooling, but that response varies across species. In general, volcanic events can be more readily observed in the ring widths of “fast-responder” species, those which rapidly respond to climate changes. These species should be prioritised for future regional or hemispheric studies. However, volcanic responses are not consistent within a species, and site-related factors was found to have greater control over the displayed volcanic response than the species. Two new reconstructions of New Zealand summer temperature were developed which showed anomalies remarkably consistent with the ensemble mean response of CMIP5 climate models. Based on these results, New Zealand ring widths are reliable indicators of regional volcanic climate response, which supports the findings of Chapter 2. However, carefully site selection is required when developing

chronologies to study volcanic impacts. More broadly, the findings of this study have important implications for the development of future tree-ring or multiproxy hemispheric temperature reconstructions from the Southern Hemisphere, which often incorporate species-specific “master” chronologies (i.e., composite chronologies developed from across many sites) into their predictor pool. As shown in this case study, the compositing process can result in reduced volcanic signals when more than one type of response is recorded by a single species.

In the second half of the thesis, the research focus narrowed to developing decision-relevant tree-ring reconstructions of streamflow, looking at two catchment-scale case studies from Australia. **Chapter 5** provides a long-term perspective on past streamflow variability in the Daly catchment and is one of the few high-resolution streamflow proxy reconstructions produced for the Indo-Australian monsoon region. Tree-rings from Australia and monsoon Asia were used to create the reconstruction, leveraging the teleconnection between the regional monsoons. This case study demonstrates the utility of remote tree rings in a region where ENSO is not the primary target climate teleconnection. The Daly River gauge data is short and non-continuous, sharing similar characteristics and shortcomings to the data used to calibrate the SPaDA. In this chapter, several methodological advancements were proposed to overcome the shortcomings of the data: a novel variance transformation of the tree-ring predictors that maximises the ability of the tree-ring predictors to characterise the hydroclimate, hierarchical Bayesian regression to account for the short data and gaps, and a ‘moving-block’ verification scheme to ensure independent statistical verification of the reconstruction. Together, these methodological advancements resulted in a streamflow reconstruction that better matches the instrumental data and extends back much further than would otherwise be possible. The Daly River reconstruction extends the streamflow record by more than five centuries. The length and robustness of the reconstruction, ability to identify historical flood events, and coherence with other proxy reconstructions demonstrate the utility of the new method. We found that the recent magnitude and frequency of high streamflow events are unmatched over the past five centuries and closely follow observed trends in summer monsoon rainfall. Our reconstruction shows that current resource allocations in the Daly have been set during a period of unprecedented high river and aquifer levels which should be carefully considered by water managers when deciding on sustainable future allocations.

Chapter 5 demonstrates how long time series of annual streamflow can provide relevant information for water management decisions. Water managers also need information on plausible future trends in streamflow and the likely occurrence of hydrological extremes for resource planning. In **Chapter 6**, we continue identifying methods for translating paleoclimate information into useful scenarios for water management. Using the Murray-Darling Basin (MDB) as a case study, a technique for developing both streamflow reconstructions and future projections is presented, based on gridded estimates of the Palmer drought severity index. To verify the method,

the reconstruction is compared to a reconstruction developed using the more traditional, tree-ring method, with predictors selected from the same trans-Pacific network of tree rings used in Chapter 3. The future projections are compared to an existing ensemble of downscaled and bias-corrected climate model outputs for the MDB. The gridded method is shown to be suitable for the MDB and could be extended to any other region globally with a similar existing dataset. To show how water managers could utilise the reconstructions, we fit joint probability models to characteristics of drought events and analyse the likelihood that the most severe historical drought events could be exceeded in the future. Emphasis is placed on visual presentation of the joint probability model results, which is a powerful tool to communicate the drought projections and their uncertainties.

7.2 Recommendations for future work

Several topics covered in this thesis would benefit from further research to improve climate reconstructions for the South Pacific region and ensure paleoclimate information is relevant for water management. Based on the outcomes of this thesis, the following research priorities are suggested.

Remote tree rings present an enormous opportunity to produce paleo-reconstructions for regions with few or no terrestrial proxies. Nevertheless, as demonstrated in Chapters 2, 3, and 6, there is a limit to the amount of instrumental variance remote tree-ring reconstructions can explain. Even with noise-free proxies and perfect reconstruction methods, the proportion of explained variance is related to how well the large-scale climate driver/s explain local climate variability. Thus, resources should be invested in producing new chronologies from target locations such as the Pacific Islands and mainland Australia, to capture local climate variability and improve the skill of climate reconstructions. In addition, most of the available tree-ring chronologies from the Southern Hemisphere ended during (or before) the late 1990s, which is problematic because of the short period of overlap between the proxies and the instrumental period. Updating older collections should be undertaken with priority. Continued efforts to digitise documentary climate records and develop other proxy records such as corals and speleothems will also contribute to the understanding of South Pacific climate; however, dating errors must be minimised to allow for inter-proxy comparisons, reconcile discrepancies between different proxies (see Chapter 3), and support multi-proxy reconstructions.

In Chapter 4 we present the first conclusive evidence that large volcanic eruptions impact tree growth in the Southern Hemisphere. We introduced a suite of plausible, testable hypotheses explaining how site-related factors affect the magnitude and direction of the observed volcanic response. In future research, these hypotheses can be tested either directly (e.g., via dendroband studies) or indirectly (e.g., using process-based forward models and site-specific climate data).

The climate response to eruptions is known to vary regionally and therefore revisiting the data from other major Southern Hemisphere dendrochronology regions (e.g., Tasmania, South America) is an important aspect for future research. A good understanding of the factors affecting whether tree rings record volcanic signals across the Southern Hemisphere, considering ring width and other wood properties, is needed to elucidate the proxy contribution to the proxy-model discrepancy in hemispheric temperature reconstructions.

The value of tree-ring reconstructions of streamflow has been well demonstrated in previous research (e.g., Rice et al., 2009; Woodhouse et al., 2017) and again in Chapters 5 and 6 of this study. However, ongoing work is required to maximise the benefits of tree-ring streamflow reconstructions for water resources management. A major hurdle to overcome is the seasonality of reconstructions, which are generally produced for the water year, and may not have a suitable resolution for water managers. For example, in Chapter 5, dry season streamflow is extremely important for the ecological function of the Daly River, yet since the wet season dominates the water year reconstruction, no trends in dry season streamflow can be inferred. Producing sub-annual streamflow reconstructions from tree rings is an emerging field of study, and studies reported to date rely on wood properties other than ring widths to target high streamflow (Nguyen et al., 2021). Development of alternative wood properties (such as stable isotopes) may also aid in better capturing the high-flow portion (extremes) in reconstructions, a limitation to the record produced in Chapter 6.

This thesis builds upon a growing body of work that demonstrates the considerable value of tree-ring based reconstructions in the analysis of trends, extremes, and allocations of water resources for current and future decision making, most notably in remote regions where there are limited instrumental records and that are highly vulnerable to climate change. Maximising the potential of tree-ring data for water management will require continued collaboration between dendrochronologists and water managers. Future work should prioritise the communication of this rich data resource to users in industry, government, and communities.

References

- Adams, J. B., Mann, M. E., & Ammann, C. M. (2003). Proxy evidence for an El Niño-like response to volcanic forcing. *Nature*, 426, 274–278. <https://doi.org/10.1038/nature02101>
- Adler, R. F., Huffman, G. J., Chang, A., Ferraro, R., Xie, P. P., Janowiak, J., Rudolf, B., Schneider, U., Curtis, S., Bolvin, D., Gruber, A., Susskind, J., Arkin, P., & Nelkin, E. (2003). The version-2 global precipitation climatology project (GPCP) monthly precipitation analysis (1979-present). *Journal of Hydrometeorology*, 4(6), 1147–1167. [https://doi.org/10.1175/1525-7541\(2003\)004<1147:TVGPCP>2.0.CO;2](https://doi.org/10.1175/1525-7541(2003)004<1147:TVGPCP>2.0.CO;2)
- Allen, K. J. (1998). A Dendroclimatological Investigation of *Phyllocladus*. University of Tasmania, PhD thesis, 343 pp.
- Allen, K. J., Brookhouse, M., French, B. J., Nichols, S. C., Dahl, B., Norrie, D., Prior, L. D., Palmer, J. G., & Bowman, D. J. M. S. (2019). Two climate-sensitive tree-ring chronologies from Arnhem Land, monsoonal Australia. *Austral Ecology*, 44(4), 581–596. <https://doi.org/10.1111/aec.12699>
- Allen, K. J., Cook, E. R., Evans, R., Francey, R., Buckley, B. M., Palmer, J. G., Peterson, M. J., & Baker, P. J. (2018). Lack of cool, not warm, extremes distinguishes late 20th Century climate in 979-year Tasmanian summer temperature reconstruction. *Environmental Research Letters*, 13(3). <https://doi.org/10.1088/1748-9326/aaafd7>
- Allen, K. J., Freund, M. B., Palmer, J. G., Simkin, R., Williams, L., Brookhouse, M., Cook, E. R., Stewart, S., & Baker, P. J. (2020). Hydroclimate extremes in a north Australian drought reconstruction asymmetrically linked with Central Pacific Sea surface temperatures. *Global and Planetary Change*, 195(July), 103329. <https://doi.org/10.1016/j.gloplacha.2020.103329>
- Allen, K. J., Lee, G., Ling, F., Allie, S., Willis, M., & Baker, P. J. (2015). Palaeohydrology in climatological context: Developing the case for use of remote predictors in Australian streamflow reconstructions. *Applied Geography*, 64, 132–152. <https://doi.org/10.1016/j.apgeog.2015.09.007>
- Alston, M., & Whittenbury, K. (2013). Does climatic crisis in Australia's food bowl create a basis for change in agricultural gender relations? *Agriculture and Human Values*, 30(1), 115–128. <https://doi.org/10.1007/s10460-012-9382-x>
- Álvarez-Romero, J., Adams, V., & Pressey, R. (2016). Using Optimal Land-Use Scenarios to Assess Trade-Offs between Conservation, Development, and Social Values. *PLoS ONE*, 11(6). <https://doi.org/https://doi.org/10.1371/journal.pone.0158350>
- Armstrong, M. S., Kiem, A. S., & Vance, T. R. (2020). Comparing instrumental, palaeoclimate, and projected rainfall data: Implications for water resources management and hydrological modelling. *Journal of Hydrology: Regional Studies*, 31(July), 100728. <https://doi.org/10.1016/j.ejrh.2020.100728>
- Azarnivand, A., Sharples, W., Bende-michl, U., Shokri, A., & Srikanthan, S. (2022). Analysing the uncertainty of modelling hydrologic states of AWRA-L – understanding impacts from parameter uncertainty for the National Hydrological Projections. In *Bureau Research Report No. 060* (Issue February).
- Baker, P. J., Palmer, J. G., & D'Arrigo, R. (2008). The dendrochronology of *Callitris intratropica* in northern Australia: Annual ring structure, chronology development and climate correlations. *Australian Journal of Botany*, 56(4), 311–320. <https://doi.org/10.1071/BT08040>
- Batehup, R., McGregor, S., & Gallant, A. J. E. (2015). The influence of non-stationary teleconnections on palaeoclimate reconstructions of ENSO variance using a pseudoproxy framework. *Climate of the Past*, 11(12), 1733–1749. <https://doi.org/10.5194/cp-11-1733-2015>
- Berry, G., & Reeder, M. (2016). The dynamics of Australian monsoon bursts. *Journal of the Atmospheric Sciences*, 73(1), 55–69. <https://doi.org/10.1175/JAS-D-15-0071.1>
- Berry, G., Reeder, M. J., & Jakob, C. (2011). Physical mechanisms regulating summertime rainfall over Northwestern Australia. *Journal of Climate*, 24(14), 3705–3717. <https://doi.org/10.1175/2011JCLI3943.1>

- Biondi, F., Kozubowski, T. J., & Panorska, A. K. (2005). A new model for quantifying climate episodes. *International Journal of Climatology*, 25(9), 1253–1264. <https://doi.org/10.1002/joc.1186>
- Biondi, F., Kozubowski, T. J., Panorska, A. K., & Saito, L. (2008). A new stochastic model of episode peak and duration for eco-hydro-climatic applications. *Ecological Modelling*, 211(3–4), 383–395. <https://doi.org/10.1016/j.ecolmodel.2007.09.019>
- Biondi, F., & Meko, D. M. (2019). Long-Term Hydroclimatic Patterns in the Truckee-Carson Basin of the Eastern Sierra Nevada, USA. *Water Resources Research*, 55(7), 5559–5574. <https://doi.org/10.1029/2019WR024735>
- Biondi, F., & Qeadan, F. (2008). Inequality in paleorecords. *Ecology*, 89(4), 1056–1067. <https://doi.org/10.1890/07-0783.1>
- Blake, S. A. P., Palmer, J. G., Björklund, J., Harper, J. B., & Turney, C. S. M. (2020). Palaeoclimate potential of New Zealand *Manoao colensoi* (silver pine) tree rings using Blue-Intensity (BI). *Dendrochronologia*, 60. <https://doi.org/10.1016/j.dendro.2020.125664>
- BOM. (2012). *Record-breaking La Niña events. An analysis of the La Niña life cycle and the impacts and significance of the 2010–11 and 2011–12 La Niña events in Australia*. <http://www.bom.gov.au/climate/enso/history/La-Nina-2010-12.pdf>, Last accessed 17/5/2021.
- BOM. (2019). *Climate of the 2018–19 financial year*. Australian Government Bureau of Meteorology Climate Updates. <http://www.bom.gov.au/climate/updates/articles/a034.shtml>
- BOM. (2020a). *Climate of the 2019–20 financial year*. Australian Government Bureau of Meteorology Climate Updates. <http://www.bom.gov.au/climate/updates/articles/a037.shtml>
- BOM. (2020b). *Special Climate Statement 70 update — drought conditions in Australia and impact on water resources in the Murray–Darling Basin*. Commonwealth of Australia Bureau of Meteorology Technical Report. 18pp. <http://www.bom.gov.au/climate/current/statements/scs70.pdf>
- BOM. (2020c). Trends and historical conditions in the Murray-Darling Basin. Commonwealth of Australia Bureau of Meteorology Technical Report. 18pp. <https://www.mdba.gov.au/sites/default/files/pubs/bp-eval-2020-BOM-trends-and-historical-conditions-report.pdf>
- Boswijk, G., Fowler, A., Lorrey, A., Palmer, J., & Ogden, J. (2006). Extension of the New Zealand kauri (*Agathis australis*) chronology to 1724 BC. *The Holocene*, 16(2), 188–199. <https://doi.org/10.1191/0959683606hl919rp>
- Breiman, L. (2001). Random forests. *Machine Learning*, 45, 5–32. <https://doi.org/10.1201/9780429469275-8>
- Briffa, K. R., Bartholint, T. S., Eckstein, D., Jones, P. D., Karlen, W., Schweingruberll, F. H., & Zetterberg, P. (1990). A 1,400-year tree-ring record of summer temperatures in Fennoscandia. *Nature*, 346, 434–439. <https://doi.org/10.1038/346434a0>
- Briffa, K. R., Jones, P. D., Bartholin, T. S., Eckstein, D., Schweingruber, F. H., Karlén, W., Zetterberg, P., & Eronen, M. (1992). Fennoscandian summers from ad 500: temperature changes on short and long timescales. *Climate Dynamics*, 7(3), 111–119. <https://doi.org/10.1007/BF00211153>
- Briffa, K. R., Jones, P. D., & Osborn, T. J. (1998). Influence of volcanic eruptions on Northern Hemisphere summer temperature over the past 600 years. *Nature*, 393, 2–7. <https://doi.org/10.1038/30943>
- Brown, J. R., Moise, A. F., & Colman, R. A. (2017). Projected increases in daily to decadal variability of Asian-Australian monsoon rainfall. *Geophysical Research Letters*, 44(11), 5683–5690. <https://doi.org/10.1002/2017GL073217>
- Buckley, B. M., Ogden, J., Palmer, J., Fowler, A., & Salinger, J. (2000). Dendroclimatic interpretation of tree-rings in *Agathis australis* (kauri). 1. Climate correlation functions and master chronology. *Journal of the Royal Society of New Zealand*, 30(3), 263–276. <https://doi.org/10.1080/03014223.2000.9517621>
- Buckley, B. M., Ummenhofer, C. C., D'Arrigo, R. D., Hansen, K. G., Truong, L. H., Le, C. N., & Stahle, D. K. (2019). Interdecadal Pacific Oscillation reconstructed from trans-Pacific tree rings: 1350–2004 CE. *Climate Dynamics*, 3181–3196. <https://doi.org/10.1007/s00382-019-04694-4>

- Büntgen, U., Allen, K., Anchukaitis, K. J., Arseneault, D., Boucher, É., Bräuning, A., Chatterjee, S., Cherubini, P., Churakova (Sidorova), O. V., Corona, C., Gennaretti, F., Griebinger, J., Guillet, S., Guiot, J., Gunnarson, B., Helama, S., Hochreuther, P., Hughes, M. K., Huybers, P., ... Esper, J. (2021). The influence of decision-making in tree ring-based climate reconstructions. *Nature Communications*, 12(1). <https://doi.org/10.1038/s41467-021-23627-6>
- Büntgen, U., Arseneault, D., Boucher, É., Churakova (Sidorova), O. V., Gennaretti, F., Crivellaro, A., Hughes, M. K., Kirdyanov, A. V., Klippel, L., Krusic, P. J., Linderholm, H. W., Ljungqvist, F. C., Ludescher, J., McCormick, M., Myglan, V. S., Nicolussi, K., Piermattei, A., Oppenheimer, C., Reinig, F., ... Esper, J. (2020). Prominent role of volcanism in Common Era climate variability and human history. *Dendrochronologia*, 64(March). <https://doi.org/10.1016/j.dendro.2020.125757>
- Burke, E. J. (2011). Understanding the sensitivity of different drought metrics to the drivers of drought under increased atmospheric CO₂. *Journal of Hydrometeorology*, 12(6), 1378–1394. <https://doi.org/10.1175/2011JHM1386.1>
- Cai, W., & Cowan, T. (2008). Evidence of impacts from rising temperature on inflows to the Murray-Darling Basin. *Geophysical Research Letters*, 35(7), 2–6. <https://doi.org/10.1029/2008GL033390>
- Cai, W., & van Rensch, P. (2013). Austral summer teleconnections of indo-pacific variability: Their nonlinearity and impacts on australian climate. *Journal of Climate*, 26(9), 2796–2810. <https://doi.org/10.1175/JCLI-D-12-00458.1>
- Callaghan, J. (2019). A comparison of weather systems in 1870 and 1956 leading to extreme floods in the Murray–Darling Basin. *Journal of Southern Hemisphere Earth Systems Science*, 69(1), 84. <https://doi.org/10.1071/es19003>
- Chappell, J., & Bardsley, K. (1985). *Hydrology of the lower Daly River, Northern Territory*. Australian National University North Australia Research Unit.
- Chen, C., Liaw, A., & Breiman, L. (2004). Using Random Forest to Learn Imbalanced Data. In *Berkeley Statistics Technical Reports*. <https://statistics.berkeley.edu/tech-reports/666>
- Chen, X., & Wallace, J. M. (2016). Orthogonal PDO and ENSO indices. *Journal of Climate*, 29(10), 3883–3892. <https://doi.org/10.1175/JCLI-D-15-0684.1>
- Chen, X., Wallace, J. M., & Tung, K. K. (2017). Pairwise-rotated EOFs of global SST. *Journal of Climate*, 30(14), 5473–5489. <https://doi.org/10.1175/JCLI-D-16-0786.1>
- Chiew, F. H. S., & McMahon, T. A. (2003). El Niño/Southern Oscillation and Australian rainfall and streamflow. *Australasian Journal of Water Resources*, 6(2), 115–129. <https://doi.org/10.1080/13241583.2003.11465216>
- Christensen, J. H., Krishna Kumar, K., Aldrian, E., An, S.-I., Cavalcanti, I. F. A., de Castro, M., Dong, W., Goswami, P., Hall, A., Kanyanga, J. K., Kitoh, A., Kossin, J., Lau, N.-C., Renwick, J., Stephenson, D. B., Xie, S.-P., & Zhou, T. (2013). Climate Phenomena and their Relevance for Future Regional Climate Change. In V. B. and Stocker, T.F., D. Qin, G.-K. Plattner, M. Tignor, S.K. Allen, J. Boschung, A. Nauels, Y. Xia & P. M. Midgley (Eds.), *Climate Change 2013: The Physical Science Basis. Contribution of Working Group I to the Fifth Assessment Report of the Intergovernmental Panel on Climate Change*. Cambridge University Press.
- Christiansen, B. (2008). Volcanic eruptions, large-scale modes in the Northern Hemisphere, and the El Niño-Southern Oscillation. *Journal of Climate*, 21(5), 910–922. <https://doi.org/10.1175/2007JCLI1657.1>
- Christiansen, B., & Ljungqvist, F. C. (2017). Challenges and perspectives for large-scale temperature reconstructions of the past two millennia. *Reviews of Geophysics*, 55(1), 40–96. <https://doi.org/10.1002/2016RG000521>
- Clark, S., Reeder, M. J., & Jakob, C. (2018). Rainfall regimes over northwestern Australia. *Quarterly Journal of the Royal Meteorological Society*, 144(711), 458–467. <https://doi.org/10.1002/qj.3217>
- Cleverly, J., Eamus, D., Luo, Q., Coupe, N. R., Kljun, N., Ma, X., Ewenz, C., Li, L., Yu, Q., & Huete, A. (2016). The importance of interacting climate modes on Australia's contribution to global carbon cycle extremes. *Scientific Reports*, 6, 1–10. <https://doi.org/10.1038/srep23113>

- Cobb, K. M., Charles, C. D., Cheng, H., & Edwards, R. L. (2003). El Niño/Southern Oscillation and tropical Pacific climate during the last millennium. *Nature*, 424(6946), 271–276. <https://doi.org/10.1038/nature01779>
- Cook, B. I., Ault, T. R., & Smerdon, J. E. (2015). Unprecedented 21st century drought risk in the American Southwest and Central Plains. *Science Advances*, 1(1), 1–8. <https://doi.org/10.1126/sciadv.1400082>
- Cook, B. I., Palmer, J. G., Cook, E. R., Turney, C. S. M., Allen, K., Fenwick, P., O'Donnell, A., Lough, J. M., Grierson, P. F., Ho, M., & Baker, P. J. (2016). The paleoclimate context and future trajectory of extreme summer hydroclimate in eastern Australia. *Journal of Geophysical Research*, 121(21), 12,820–12,838. <https://doi.org/10.1002/2016JD024892>
- Cook, B. I., Smerdon, J. E., Seager, R., & Coats, S. (2014). Global warming and 21st century drying. *Climate Dynamics*, 43(9–10), 2607–2627. <https://doi.org/10.1007/s00382-014-2075-y>
- Cook, B. I., Williams, A. P., Smerdon, J. E., Palmer, J. G., Cook, E. R., Stahle, D. W., & Coats, S. (2018). Cold Tropical Pacific Sea Surface Temperatures During the Late Sixteenth-Century North American Megadrought. *Journal of Geophysical Research: Atmospheres*, 123(20), 11307–11320. <https://doi.org/10.1029/2018JD029323>
- Cook, E. R., Anchukaitis, K. J., Buckley, B. M., D'Arrigo, R. D., Jacoby, G. C., & Wright, W. E. (2010a). Asian monsoon failure and megadrought during the last millennium: Supporting Information. *Science*, 328, 486–489. <https://doi.org/10.1126/science.1185188>
- Cook, E. R., Anchukaitis, K. J., Buckley, B. M., D'Arrigo, R. D., Jacoby, G. C., & Wright, W. E. (2010b). Asian monsoon failure and megadrought during the last millennium. *Science*, 328, 486–489. <https://doi.org/10.1126/science.1185188>
- Cook, E. R., Bird, T., Peterson, M., Barbetti, M., Buckley, B., D'Arrigo, R., & Francey, R. (1992). Climatic change over the last millennium in Tasmania reconstructed from tree-rings. *Holocene*, 2(3), 205–217. <https://doi.org/10.1177/095968369200200302>
- Cook, E. R., & Kairiukstis, L. A. (Eds.). (1990). *Methods of dendrochronology: applications in the environmental sciences*. Kluwer Academic Publishers, Amsterdam, 394 pp. <https://doi.org/10.2307/1551446>
- Cook, E. R., Meko, D. M., Stahle, D. W., & Cleaveland, M. K. (1999). Drought reconstructions for the continental United States. *Journal of Climate*, 12(4), 1145–1163. [https://doi.org/10.1175/1520-0442\(1999\)012<1145:drftcu>2.0.co;2](https://doi.org/10.1175/1520-0442(1999)012<1145:drftcu>2.0.co;2)
- Cook, E. R., Palmer, J. G., Cook, B. I., Hogg, A., & D'Arrigo, R. D. (2002). A multi-millennial palaeoclimatic resource from *Lagarostrobos colensoi* tree-rings at Oroko Swamp, New Zealand. *Global and Planetary Change*, 33(3–4), 209–220. [https://doi.org/10.1016/S0921-8181\(02\)00078-4](https://doi.org/10.1016/S0921-8181(02)00078-4)
- Cook, E. R., Seager, R., Cane, M. A., & Stahle, D. W. (2007). North American drought: Reconstructions, causes, and consequences. *Earth-Science Reviews*, 81(1–2), 93–134. <https://doi.org/10.1016/j.earscirev.2006.12.002>
- Cook, E. R., Seager, R., Heim, R. R., Vose, R. S., Herweijer, C., & Woodhouse, C. (2010). Megadroughts in North America: Placing IPCC projections of hydroclimatic change in a long-term palaeoclimate context. *Journal of Quaternary Science*, 25(1), 48–61. <https://doi.org/10.1002/jqs.1303>
- Coulthard, B., Smith, D. J., & Meko, D. M. (2016). Is worst-case scenario streamflow drought underestimated in British Columbia? A multi-century perspective for the south coast, derived from tree-rings. *Journal of Hydrology*, 534, 205–218. <https://doi.org/10.1016/j.jhydrol.2015.12.030>
- Cox, D. R., & Lewis, P. A. W. (1966). *The Statistical Analysis of Series of Events*. Methuen, London, 285 pp.
- Crowley, T. J., & Unterman, M. B. (2013). Technical details concerning development of a 1200 yr proxy index for global volcanism. *Earth System Science Data*, 5(1), 187–197. <https://doi.org/10.5194/essd-5-187-2013>

- CSIRO. (2009). *Water in the Daly region of the Timor Sea Drainage Division. A report to the Australian Government from the CSIRO Northern Australia Sustainable Yields Project*. (Issue August). CSIRO Water for a Healthy Country Flagship. <https://doi.org/10.4225/08/5859722f95216>
- CSIRO, BOM, & SPREP. (2015). Climate in the Pacific: A regional summary of new science and management tools. In *Pacific-Australia Climate Change Science and Adaptation Planning Program Summary Report*. Commonwealth Scientific and Industrial Research Organisation.
- D'Arrigo, R. D., Abram, N., Ummenhofer, C., Palmer, J., & Mudelsee, M. (2011). Reconstructed streamflow for Citarum River, Java, Indonesia: Linkages to tropical climate dynamics. *Climate Dynamics*, 36(3), 451–462. <https://doi.org/10.1007/s00382-009-0717-2>
- D'Arrigo, R. D., Baker, P., Palmer, J., Anchukaitis, K., & Cook, G. (2008). Experimental reconstruction of monsoon drought variability for Australasia using tree rings and corals. *Geophysical Research Letters*, 35(12), 1–6. <https://doi.org/10.1029/2008GL034393>
- D'Arrigo, R. D., Buckley, B. M., Cook, E. R., & Wagner, W. S. (1996). Temperature-sensitive tree-ring width chronologies of pink pine (*Halocarpus biformis*) from Stewart Island, New Zealand. *Palaeogeography, Palaeoclimatology, Palaeoecology*, 119(3–4), 293–300. [https://doi.org/10.1016/0031-0182\(95\)00014-3](https://doi.org/10.1016/0031-0182(95)00014-3)
- D'Arrigo, R. D., Cook, E. R., Salinger, M. J., Palmer, J., Krusic, P. J., Buckley, B. M., & Villalba, R. (1998). Tree-ring records from New Zealand: Long-term context for recent warming trend. *Climate Dynamics*, 14(3), 191–199. <https://doi.org/10.1007/s003820050217>
- D'Arrigo, R. D., Cook, E. R., Wilson, R. J., Allan, R., & Mann, M. E. (2005). On the variability of ENSO over the past six centuries. *Geophysical Research Letters*, 32(3), 1–4. <https://doi.org/10.1029/2004GL022055>
- D'Arrigo, R. D., Wilson, R., & Anchukaitis, K. J. (2013). Volcanic cooling signal in tree ring temperature records for the past millennium. *Journal of Geophysical Research Atmospheres*, 118(16), 9000–9010. <https://doi.org/10.1002/jgrd.50692>
- D'Arrigo, R. D., Wilson, R., & Tudhope, A. (2009). The impact of volcanic forcing on tropical temperatures during the past four centuries. *Nature Geoscience*, 2(1), 51–56. <https://doi.org/10.1038/ngeo393>
- D'Aubert, A., & Nunn, P. D. (2012). *Furious Winds and Parched Islands: Tropical Cyclones (1558–1970) and Droughts (1722–1987) in the Pacific*. Xlibris Corporation.
- da Silva, G. A. M., Drumond, A., & Ambrizzi, T. (2011). The impact of El Niño on South American summer climate during different phases of the Pacific Decadal Oscillation. *Theoretical and Applied Climatology*, 106(3–4), 307–319. <https://doi.org/10.1007/s00704-011-0427-7>
- Dang, H., Jiang, M., Zhang, Q., & Zhang, Y. (2007). Growth responses of subalpine fir (*Abies fargesii*) to climate variability in the Qinling Mountain, China. *Forest Ecology and Management*, 240(1–3), 143–150. <https://doi.org/10.1016/j.foreco.2006.12.021>
- Davis, M. (2002). PART I The Great Droughts, 1876–1878. In *Late Victorian holocausts: El Niño famines and the making of the third world* (p. 470). Verso Books.
- De Loe, R. C., & Kreutzweiser, R. D. (2000). Climate variability, climate change and water resource management in the Great Lakes. *Climatic Change*, 45, 163–179. <https://doi.org/10.1023/A:1005649219332>
- Dee, S. G., Cobb, K. M., Emile-geay, J., Ault, T. R., Edwards, R. L., Cheng, H., & Charles, C. D. (2020). No consistent ENSO response to volcanic forcing over the last millennium. *Science*, 367(6485), 1477–1481. <https://doi.org/10.1126/science.aax2000>
- DeLong, K. L., Quinn, T. M., Taylor, F. W., Shen, C.-C., & Lin, K. (2013). Improving coral-base paleoclimate reconstructions by replicating 350 years of coral Sr/Ca variations. *Palaeogeography, Palaeoclimatology, Palaeoecology*, 373, 6–24. <https://doi.org/10.1016/j.palaeo.2012.08.019>
- Denniston, R. F., Ummenhofer, C. C., Wanamaker, A. D., Lachniet, M. S., Villarini, G., Asmerom, Y., Polyak, V. J., Passaro, K. J., Cugley, J., Woods, D., & Humphreys, W. F. (2016). Expansion and contraction of the Indo-Pacific tropical rain belt over the last three millennia. *Scientific Reports*, 6, 1–9. <https://doi.org/10.1038/srep34485>

- Deser, C., & Phillips, A. (2017). An overview of decadal-scale sea surface temperature variability in the observational record. *Past Global Changes Magazine*, 25(1), 2–6. <https://doi.org/10.22498/pages.25.1.2>
- Devineni, N., Lall, U., Pederson, N., & Cook, E. (2013). A tree-ring-based reconstruction of Delaware river basin streamflow using hierarchical Bayesian regression. *Journal of Climate*, 26(12), 4357–4374. <https://doi.org/10.1175/JCLI-D-11-00675.1>
- Dey, R., Gallant, A. J. E., & Lewis, S. C. (2020). Evidence of a continent-wide shift of episodic rainfall in Australia. *Weather and Climate Extremes*, 29, 100274. <https://doi.org/10.1016/j.wace.2020.100274>
- Ding, C., & He, X. (2004). K-means Clustering via Principal Component Analysis. *Proceedings of the 21st International Conference on Machine Learning*. <https://doi.org/10.1145/1015330.1015408>
- Duncan, R. P., Fenwick, P., Palmer, J. G., McGlone, M. S., & Turney, C. S. M. (2010). Non-uniform interhemispheric temperature trends over the past 550 years. *Climate Dynamics*, 35(7), 1429–1438. <https://doi.org/10.1007/s00382-010-0794-2>
- Dunwiddie, P. W. (1979). Dendrochronological studies of indigenous New Zealand trees. *New Zealand Journal of Botany*, 17(3), 251–266. <https://doi.org/10.1080/0028825X.1979.10426899>
- Efron, B. (1987). Better Bootstrap Confidence Intervals. *Journal of the American Statistical Association*, 82(397), 171–185. <https://doi.org/10.2307/2289144>
- Ekström, M., Abbs, D., Bhend, J., Chiew, F., Kirono, D., Lucas, C., McInnes, K., Moise, A., Mpelasoka, F., Webb, L., & Whetton, P. (2015). *Central slopes cluster report, Climate change in Australia projections for Australia's natural resource regions*.
- Emile-Geay, J., Cobb, K. M., Mann, M. E., & Wittenberg, A. T. (2013). Estimating central equatorial Pacific SST variability over the past millennium. part II: Reconstructions and implications. *Journal of Climate*, 26(7), 2329–2352. <https://doi.org/10.1175/JCLI-D-11-00511.1>
- Emile-Geay, J., Seager, R., Cane, M. A., Cook, E. R., & Haug, G. H. (2008). Volcanoes and ENSO over the past millennium. *Journal of Climate*, 21(13), 3134–3148. <https://doi.org/10.1175/2007JCLI1884.1>
- Esper, J., Cook, E. R., & Schweingruber, F. H. (2002). Low-Frequency Signals in Long Tree-Ring Chronologies for Reconstructing Past Temperature Variability. *Science*, 295(5563), 2250–2253. <https://doi.org/10.1126/science.1066208>
- Esper, J., Schneider, L., Krusic, P. J., Luterbacher, J., Büntgen, U., Timonen, M., Sirocko, F., & Zorita, E. (2013). European summer temperature response to annually dated volcanic eruptions over the past nine centuries. *Bulletin of Volcanology*, 75(7), 1–14. <https://doi.org/10.1007/s00445-013-0736-z>
- Fatih, S., Pappas, C., Zscheischler, J., & Leuzinger, S. (2019). Modelling carbon sources and sinks in terrestrial vegetation. *New Phytologist*, 221(2), 652–668. <https://doi.org/10.1111/nph.15451>
- Fenwick, P. (2003). Reconstruction of past climates using pink pine (*Halocarpus biformis*) tree-ring chronologies. Lincoln University, PhD thesis, 183pp.
- Flack, A. L., Kiem, A. S., Vance, T. R., Tozer, C. R., & Roberts, J. L. (2020). Comparison of published palaeoclimate records suitable for reconstructing annual to sub-decadal hydroclimatic variability in eastern Australia: implications for water resource management and planning. *Hydrology and Earth System Sciences*, 24(12), 5699–5712. <https://doi.org/10.5194/hess-24-5699-2020>
- Fowler, A. M., Boswijk, G., Gergis, J., & Lorrey, A. (2008). ENSO history recorded in *Agathis australis* (kauri) tree rings. Part A: kauri's potential as an ENSO proxy. *International Journal of Climatology*, 28, 1–20. <https://doi.org/10.1002/joc>
- Fowler, A. M., Lorrey, A., & Crossley, P. (2005). Seasonal growth characteristics of kauri. *Tree-Ring Research*, 61(1), 3–19. <https://doi.org/10.3959/1536-1098-61.1.3>
- Fowler, A. M., Palmer, J., Salinger, J., & Ogden, J. (2000). Dendroclimatic interpretation of tree-rings in *Agathis australis* (kauri): 2. Evidence of a significant relationship with ENSO. *Journal of the Royal Society of New Zealand*, 30(3), 277–292. <https://doi.org/10.1080/03014223.2000.9517622>

- Frank, D., Esper, J., & Cook, E. R. (2006). On Variance Adjustment in Tree-Ring Chronology Development. In H. H. Gärtner, M. Monbaron, & G. Schleser (Eds.), *TRACE. Tree Rings in Archaeology, Climatology and Ecology. Volume 4*. (pp. 56–66).
- Franke, J., Frank, D., Raible, C. C., Esper, J., & Brönnimann, S. (2013). Spectral biases in tree-ring climate proxies. *Nature Climate Change*, 3(4), 360–364. <https://doi.org/10.1038/nclimate1816>
- Freund, M. B., Henley, B. J., Karoly, D. J., McGregor, H. V., Abram, N. J., & Dommenges, D. (2019). Higher frequency of Central Pacific El Niño events in recent decades relative to past centuries. *Nature Geoscience*, 12(6), 450–455. <https://doi.org/10.1038/s41561-019-0353-3>
- Freund, M. B., Henley, B. J., Karoly, D. J., Allen, K. J., & Baker, P. J. (2017). Multi-century cool- and warm-season rainfall reconstructions for Australia’s major climatic regions. *Climate of the Past*, 13(12), 1751–1770. <https://doi.org/10.5194/cp-13-1751-2017>
- Fritts, H. C. (1976). *Tree Rings and Climate*. Academic Press. 582 pp., ISBN 978-0122684500
- Fritts, H. C. (1991). *Reconstructing Large-scale Climatic Patterns from Tree-Ring Data*. University of Arizona Press. ISBN 978-0816512188.
- Frost, A. J., & Wright, D. P. (2018). *Evaluation of the Australian Landscape Water Balance model : AWRA-L v6. A comparison of AWRA-L v6 against Observed Hydrological Data and Peer Models*. Bureau of Meteorology: Sydney, Australia.
- Galelli, S., Nguyen, H. T. T., Turner, S. W. D., & Buckley, B. M. (2021). Time to Use Dendrohydrological Data in Water Resources Management? *Journal of Water Resources Planning and Management*, 147(8), 01821001. [https://doi.org/10.1061/\(asce\)wr.1943-5452.0001422](https://doi.org/10.1061/(asce)wr.1943-5452.0001422)
- Gallant, A. J. E., & Gergis, J. (2011). An experimental streamflow reconstruction for the River Murray, Australia, 1783–1988. *Water Resources Research*, 47(4), 1–15. <https://doi.org/10.1029/2010WR009832>
- Gallant, A. J. E., Kiem, A. S., Verdon-Kidd, D. C., Stone, R. C., & Karoly, D. J. (2012). Understanding hydroclimate processes in the Murray-Darling Basin for natural resources management. *Hydrology and Earth System Sciences*, 16(7), 2049–2068. <https://doi.org/10.5194/hess-16-2049-2012>
- Gallant, A. J. E., Phipps, S. J., Karoly, D. J., Mullan, A. B., & Lorrey, A. M. (2013). Nonstationary Australasian teleconnections and implications for paleoclimate reconstructions. *Journal of Climate*, 26(22), 8827–8849. <https://doi.org/10.1175/JCLI-D-12-00338.1>
- Gallego, D., García-Herrera, R., Peña-Ortiz, C., & Ribera, P. (2017). The steady enhancement of the Australian Summer Monsoon in the last 200 years. *Scientific Reports*, 7(1), 1–7. <https://doi.org/10.1038/s41598-017-16414-1>
- Gao, C., Robock, A., & Ammann, C. (2008). Volcanic forcing of climate over the past 1500 years: An improved ice core-based index for climate models. *Journal of Geophysical Research Atmospheres*, 113(23). <https://doi.org/10.1029/2008JD010239>
- Garrison, C. S., Kilburn, C. R. J., & Edwards, S. J. (2018). The 1831 eruption of Babuyan Claro that never happened: has the source of one of the largest volcanic climate forcing events of the nineteenth century been misattributed? *Journal of Applied Volcanology*, 7(1), 8. <https://doi.org/10.1186/s13617-018-0078-9>
- Gelman, A., Goodrich, B., Gabry, J., & Vehtari, A. (2019). R-squared for Bayesian Regression Models. *American Statistician*, 73(3), 307–309. <https://doi.org/10.1080/00031305.2018.1549100>
- Gergis, J. L., Gallant, A. J. E., Braganza, K., Karoly, D. J., Allen, K., Cullen, L., D’Arrigo, R., Goodwin, I., Grierson, P., & McGregor, S. (2012). On the long-term context of the 1997–2009 “Big Dry” in South-Eastern Australia: Insights from a 206-year multi-proxy rainfall reconstruction. *Climatic Change*, 111(3), 923–944. <https://doi.org/10.1007/s10584-011-0263-x>
- Gergis, J. L., & Fowler, A. M. (2009). A history of ENSO events since A.D. 1525: Implications for future climate change. *Climatic Change*, 92(3–4), 343–387. <https://doi.org/10.1007/s10584-008-9476-z>
- Gershunov, A., & Barnett, T. P. (1998). Interdecadal Modulation of ENSO Teleconnections. *Bulletin of the American Meteorological Society*, 79(12), 2715–2725. [https://doi.org/10.1175/1520-0477\(1998\)079<2715:IMOET>2.0.CO;2](https://doi.org/10.1175/1520-0477(1998)079<2715:IMOET>2.0.CO;2)

- Grime, J. P. (1979). *Plant Strategies and Vegetation Processes*. John Wiley & Sons, Ltd., Chichester-New York-Brisbane-Toronto, 222 pp., ISBN 978047199695.
- Grove, J. M. (1988). *The Little Ice Age*. Methuen, London. <https://doi.org/10.4324/9780203505205>
- Grove, R. H. (2007). The Great El Niño of 1789-93 and its global consequences: Reconstructing an extreme climate event in world environmental history. *Medieval History Journal*, 10(1–2), 75–98. <https://doi.org/10.1177/097194580701000203>
- Gruber, A. (1972). Fluctuations in the Position of the ITCZ in the Atlantic and Pacific Oceans. *Journal of the Atmospheric Sciences*, 29(1), 193–197. [https://doi.org/https://doi.org/10.1175/1520-0469\(1972\)029<0193:FITPOT>2.0.CO;2](https://doi.org/10.1175/1520-0469(1972)029<0193:FITPOT>2.0.CO;2)
- Gu, L., Baldocchi, D. D., Wofsy, S. C., William Munger, J., Michalsky, J. J., Urbanski, S. P., & Boden, T. A. (2003). Response of a deciduous forest to the Mount Pinatubo eruption: Enhanced photosynthesis. *Science*, 299(5615), 2035–2038. <https://doi.org/10.1126/science.1078366>
- Hameed, S. N., Jin, D., & Thilakan, V. (2018). A model for super El Niños. *Nature Communications*, 9(1), 1–15. <https://doi.org/10.1038/s41467-018-04803-7>
- Harper, J. L. (1977). *Population biology of plants*. Academic Press, New York, 892 pp., ISBN 9780123258502.
- Haurwitz, M. W., & Brier, G. W. (1981). A Critique of the Superposed Epoch Analysis Method: Its Application to Solar-Weather Relations. *Monthly Weather Review*, 109, 2074–2079.
- Heidemann, H., Ribbe, J., Cowan, T., Henley, B. J., Pudmenzky, C., Stone, R., & Cobon, D. H. (2021). The influence of interannual and decadal Indo-Pacific sea surface temperature variability on Australian monsoon rainfall. *Journal of Climate*, 1–58. <https://doi.org/10.1175/jcli-d-21-0264.1>
- Henley, B. J. (2017). Pacific decadal climate variability: Indices, patterns and tropical-extratropical interactions. *Global and Planetary Change*, 155(June), 42–55. <https://doi.org/10.1016/j.gloplacha.2017.06.004>
- Henley, B. J., Gergis, J., Karoly, D. J., Power, S., Kennedy, J., & Folland, C. K. (2015). A Tripole Index for the Interdecadal Pacific Oscillation. *Climate Dynamics*, 45(11), 3077–3090. <https://doi.org/10.1007/s00382-015-2525-1>
- Hernández, A., Martín-Puertas, C., Moffa-Sánchez, P., Moreno-Chamarro, E., Ortega, P., Blockley, S., Cobb, K. M., Comas-Bru, L., Giral, S., Goosse, H., Luterbacher, J., Martrat, B., Muscheler, R., Parnell, A., Pla-Rabes, S., Sjolte, J., Scaife, A. A., Swingedouw, D., Wise, E., & Xu, G. (2020). Modes of climate variability: Synthesis and review of proxy-based reconstructions through the Holocene. *Earth-Science Reviews*, 209. <https://doi.org/10.1016/j.earscirev.2020.103286>
- Hessl, A. E., Anchukaitis, K. J., Jelsema, C., Cook, B., Byambasuren, O., Leland, C., Nachin, B., Pederson, N., Tian, H., & Hayles, L. A. (2018). Past and future drought in Mongolia. *Science Advances*, 4(3), 1–8. <https://doi.org/10.1126/sciadv.1701832>
- Ho, M., Kiem, A. S., & Verdon-Kidd, D. C. (2015a). A paleoclimate rainfall reconstruction in the Murray-Darling Basin (MDB), Australia: 1. Evaluation of different paleoclimate archives, rainfall networks, and reconstruction techniques. *Water Research*, 51, 8362–8379. [https://doi.org/doi:10.1002/2015WR017058](https://doi.org/10.1002/2015WR017058)
- Ho, M., Kiem, A. S., & Verdon-Kidd, D. C. (2015b). A paleoclimate rainfall reconstruction in the Murray-Darling Basin (MDB), Australia: 2. Assessing hydroclimatic risk using paleoclimate records of wet and dry epochs. *Water Resources Research*, 51, 8380–8396. [https://doi.org/doi:10.1002/2015WR017059](https://doi.org/10.1002/2015WR017059)
- Ho, M., Lall, U., & Cook, E. R. (2016). Can a paleodrought record be used to reconstruct streamflow?: A case study for the Missouri River Basin. *Water Resources Research*, 52(7), 5195–5212. <https://doi.org/10.1111/j.1752-1688.1969.tb04897.x>
- Ho, M., Lall, U., Sun, X., & Cook, E. R. (2017). Multiscale temporal variability and regional patterns in 555 years of conterminous U.S. streamflow. *Water Resources Research*, 53, 3047–3066. <https://doi.org/10.1002/2016WR019632>

- Holgate, C., Evans, J. P., Taschetto, A. S., Sen Gupta, A., & Santoso, A. (2022). The impact of interacting climate modes on east Australian precipitation moisture sources. *Journal of Climate*, 35(10), 1–31. <https://doi.org/10.1175/jcli-d-21-0750.1>
- Holland, G. J. (1988). Interannual Variability of the Australian Summer Monsoon at Darwin: 1952–82. *Monthly Weather Review*, 114, 594–604. [https://doi.org/10.1175/1520-0493\(1986\)114<0594:IVOTAS>2.0.CO;2](https://doi.org/10.1175/1520-0493(1986)114<0594:IVOTAS>2.0.CO;2)
- Holmes, R. L. (1983). Computer-Assisted Quality Control in Tree-Ring Dating and Measurement. *Tree-Ring Bulletin*, 43, 69–78.
- Iese, V., Kiem, A. S., Mariner, A., Malsale, P., Tofaeono, T., Kirono, D. G. C., Round, V., Heady, C., Tigona, R., Veisa, F., Posanau, K., Aiono, F., Haruhiru, A., Daphne, A., Vainikolo, V., & Iona, N. (2021). Historical and future drought impacts in the Pacific islands and atolls. *Climatic Change*, 166(1–2), 1–24. <https://doi.org/10.1007/s10584-021-03112-1>
- Iles, C. E., Hegerl, G. C., Schurer, A. P., & Zhang, X. (2013). The effect of volcanic eruptions on global precipitation. *Journal of Geophysical Research Atmospheres*, 118(16), 8770–8786. <https://doi.org/10.1002/jgrd.50678>
- Jaume-Santero, F., Barriopedro, D., García-Herrera, R., Calvo, N., & Salcedo-Sanz, S. (2020). Selection of optimal proxy locations for temperature field reconstructions using evolutionary algorithms. *Scientific Reports*, 10(1), 1–12. <https://doi.org/10.1038/s41598-020-64459-6>
- Jiang, Z., Rashid, M. M., Johnson, F., & Sharma, A. (2021). A wavelet-based tool to modulate variance in predictors: An application to predicting drought anomalies. *Environmental Modelling and Software*, 135(October 2020), 104907. <https://doi.org/10.1016/j.envsoft.2020.104907>
- Jiang, Z., Sharma, A., & Johnson, F. (2020). Refining Predictor Spectral Representation Using Wavelet Theory for Improved Natural System Modeling. *Water Resources Research*, 53(3), 1–17. <https://doi.org/10.1029/2019WR026962>
- Johnson, F., Higgins, P., & Stephens, C. (2021). Climate change and hydrological risk in the Pacific: a Humanitarian Engineering perspective. *Journal of Water and Climate Change*, 1–32. <https://doi.org/10.2166/wcc.2021.277>
- Johnson, F., & Sharma, A. (2012). A nesting model for bias correction of variability at multiple time scales in general circulation model precipitation simulations. *Water Resources Research*, 48(1), 1–16. <https://doi.org/10.1029/2011WR010464>
- Jones, P. D., & Mann, M. E. (2004). Climate over past millennia. *Reviews of Geophysics*, 42(2), 1–42. <https://doi.org/10.1029/2003RG000143>
- Jourdain, N. C., Gupta, A. Sen, Taschetto, A. S., Ummenhofer, C. C., Moise, A. F., & Ashok, K. (2013). The Indo-Australian monsoon and its relationship to ENSO and IOD in reanalysis data and the CMIP3/CMIP5 simulations. *Climate Dynamics*, 41(11–12), 3073–3102. <https://doi.org/10.1007/s00382-013-1676-1>
- Khider, D., Stott, L. D., Emile-Geay, J., Thunell, R., & Hammond, D. E. (2011). Assessing El Niño Southern Oscillation variability during the past millennium. *Paleoceanography*, 26(3). <https://doi.org/10.1029/2011PA002139>
- Khodri, M., Izumo, T., Vialard, J., Janicot, S., Cassou, C., Lengaigne, M., Mignot, J., Gastineau, G., Guilyardi, E., Lebas, N., Robock, A., & McPhaden, M. J. (2017). Tropical explosive volcanic eruptions can trigger El Niño by cooling tropical Africa. *Nature Communications*, 8(1), 1–12. <https://doi.org/10.1038/s41467-017-00755-6>
- Kiem, A. S., Johnson, F., Westra, S., van Dijk, A., Evans, J. P., O'Donnell, A., Rouillard, A., Barr, C., Tyler, J., Thyer, M., Jakob, D., Woldemeskel, F., Sivakumar, B., & Mehrotra, R. (2016). Natural hazards in Australia: droughts. *Climatic Change*, 139(1), 37–54. <https://doi.org/10.1007/s10584-016-1798-7>
- Kiem, A. S., Vance, T. R., Tozer, C. R., Roberts, J. L., Dalla Pozza, R., Vitkovsky, J., Smolders, K., & Curran, M. A. J. (2020). Learning from the past – Using palaeoclimate data to better understand and manage drought in South East Queensland (SEQ), Australia. *Journal of Hydrology: Regional Studies*, 29. <https://doi.org/10.1016/j.ejrh.2020.100686>

- Kiem, A. S., & Verdon-Kidd, D. C. (2011). Steps toward “useful” hydroclimatic scenarios for water resource management in the Murray-Darling Basin. *Water Resources Research*, 47(6), 1–14. <https://doi.org/10.1029/2010WR009803>
- Kim, T.-W., Valdés, J. B., & Yoo, C. (2003). Nonparametric Approach for Estimating Return Periods of Droughts in Arid Regions. *Journal of Hydrologic Engineering*, 8(5), 237–246. [https://doi.org/10.1061/\(asce\)1084-0699\(2003\)8:5\(237\)](https://doi.org/10.1061/(asce)1084-0699(2003)8:5(237))
- King, A. D., Alexander, L. V., & Donat, M. G. (2013). Asymmetry in the response of eastern Australia extreme rainfall to low-frequency Pacific variability. *Geophysical Research Letters*, 40(10), 2271–2277. <https://doi.org/10.1002/grl.50427>
- King, A. D., Pitman, A. J., Henley, B. J., Ukkola, A. M., & Brown, J. R. (2020). The role of climate variability in Australian drought. *Nature Climate Change*, 10(3), 173–183. <https://doi.org/10.1038/s41558-020-0712-5>
- Kirono, D. G. C., Round, V., Heady, C., Chiew, F. H. S., & Osbrough, S. (2020). Drought projections for Australia: Updated results and analysis of model simulations. *Weather and Climate Extremes*, 30, 100280. <https://doi.org/10.1016/j.wace.2020.100280>
- Kozubowski, T. J., & Panorska, A. K. (2005). A mixed bivariate distribution with exponential and geometric marginals. *Journal of Statistical Planning and Inference*, 134(2), 501–520. <https://doi.org/https://doi.org/10.1016/j.jspi.2004.04.010>
- Kozubowski, T. J., & Panorska, A. K. (2008). A Mixed Bivariate Distribution Connected with Geometric Maxima of Exponential Variables. *Communications in Statistics - Theory and Methods*, 37(18), 2903–2923. <https://doi.org/10.1080/03610920802162680>
- Krakauer, N. Y., & Randerson, J. T. (2003). Do volcanic eruptions enhance or diminish net primary production? Evidence from tree rings. *Global Biogeochemical Cycles*, 17(4). <https://doi.org/10.1029/2003gb002076>
- Kreibich, H., Van Loon, A. F., Schröter, K., Ward, P. J., Mazzoleni, M., Sairam, N., Abeshu, G. W., Agafonova, S., AghaKouchak, A., Aksoy, H., Alvarez-Garreton, C., Aznar, B., Balkhi, L., Barendrecht, M. H., Biancamaria, S., Bos-Burginger, L., Bradley, C., Budiyo, Y., Buytaert, W., ... Di Baldassarre, G. (2022). The challenge of unprecedented floods and droughts in risk management. *Nature*, 608, 80–86. <https://doi.org/10.1038/s41586-022-04917-5>
- Kuleshov, Y., Ming, F. C., Qi, L., Chouaibou, I., Hoareau, C., & Roux, F. (2009). Tropical cyclone genesis in the Southern Hemisphere and its relationship with the ENSO. *Annales Geophysicae*, 27(6), 2523–2538. <https://doi.org/10.5194/angeo-27-2523-2009>
- Kundzewicz, Z. W., Krysanova, V., Benestad, R. E., Hov, Piniewski, M., & Otto, I. M. (2018). Uncertainty in climate change impacts on water resources. *Environmental Science and Policy*, 79(June 2017), 1–8. <https://doi.org/10.1016/j.envsci.2017.10.008>
- LaMarche, V. C., Holmes, R. L., Dunwiddie, P. W., & Drew, L. G. (1979). *Tree-ring chronologies of the Southern Hemisphere 3. New Zealand* (Issue Chronology Series V). Laboratory of Tree-Ring Research, University of Arizona. Tucson, Arizona.
- Leblanc, M., Tweed, S., Van Dijk, A., & Timbal, B. (2012). A review of historic and future hydrological changes in the Murray-Darling Basin. *Global and Planetary Change*, 80–81, 226–246. <https://doi.org/10.1016/j.gloplacha.2011.10.012>
- Lenssen, N. J. L., Goddard, L., & Mason, S. (2020). Seasonal forecast skill of ENSO teleconnection maps. *Weather and Forecasting*, 35(6), 2387–2406. <https://doi.org/10.1175/WAF-D-19-0235.1>
- Li, J., Xie, S. P., Cook, E. R., Morales, M. S., Christie, D. A., Johnson, N. C., Chen, F., D’Arrigo, R., Fowler, A. M., Gou, X., & Fang, K. (2013). El Niño modulations over the past seven centuries. *Nature Climate Change*, 3(9), 822–826. <https://doi.org/10.1038/nclimate1936>
- Linsley, B. K., Kaplan, A., Gouriou, Y., Salinger, J., DeMenocal, P. B., Wellington, G. M., & Howe, S. S. (2006). Tracking the extent of the South Pacific Convergence Zone since the early 1600s. *Geochemistry, Geophysics, Geosystems*, 7(5), 1–15. <https://doi.org/10.1029/2005GC001115>

- Linsley, B. K., Wellington, G. M., Schrag, D. P., Ren, L., Salinger, M. J., & Tudhope, A. W. (2004). Geochemical evidence from corals for changes in the amplitude and spatial pattern of South Pacific interdecadal climate variability over the last 300 years. *Climate Dynamics*, 22(1), 1–11. <https://doi.org/10.1007/s00382-003-0364-y>
- Liu, F., Chai, J., Wang, B., Liu, J., Zhang, X., & Wang, Z. (2016). Global monsoon precipitation responses to large volcanic eruptions. *Scientific Reports*, 6. <https://doi.org/10.1038/srep24331>
- Ljungqvist, F. C., Piermattei, A., Seim, A., Krusic, P. J., Büntgen, U., He, M., Kirdyanov, A. V., Luterbacher, J., Schneider, L., Seftigen, K., Stahle, D. W., Villalba, R., Yang, B., & Esper, J. (2020). Ranking of tree-ring based hydroclimate reconstructions of the past millennium. *Quaternary Science Reviews*, 230, 106074. <https://doi.org/10.1016/j.quascirev.2019.106074>
- Lough, J. M., & Fritts, H. C. (1985). The Southern Oscillation and tree rings: 1600–1961. *Journal of Applied Meteorology and Climatology*, 24, 952–966. [https://doi.org/10.1175/1520-0450\(1985\)024<0952:TSOATR>2.0.CO;2](https://doi.org/10.1175/1520-0450(1985)024<0952:TSOATR>2.0.CO;2)
- Lough, J. M., Lewis, S. E., & Cantin, N. E. (2015). Freshwater impacts in the central Great Barrier Reef: 1648–2011. *Coral Reefs*, 34(3), 739–751. <https://doi.org/10.1007/s00338-015-1297-8>
- Ludert, A., Wang, B., & Merrifield, M. A. (2018). Characterization of dry conditions across the U.S.-Affiliated Pacific Islands during near-neutral ENSO phases. *Journal of Climate*, 31(16), 6461–6480. <https://doi.org/10.1175/JCLI-D-17-0561.1>
- Luo, J. J., Zhang, R., Behera, S. K., Masumoto, Y., Jin, F. F., Lukas, R., & Yamagata, T. (2010). Interaction between El Niño and extreme Indian Ocean dipole. *Journal of Climate*, 23(3), 726–742. <https://doi.org/10.1175/2009JCLI13104.1>
- MacDonald, G. M., & Case, R. A. (2005). Variations in the Pacific Decadal Oscillation over the past millennium. *Geophysical Research Letters*, 32(8), 1–4. <https://doi.org/10.1029/2005GL022478>
- Magee, A. D., Lorrey, A. M., Kiem, A. S., & Colyvas, K. (2020). A new island-scale tropical cyclone outlook for southwest Pacific nations and territories. *Scientific Reports*, 10(1), 1–13. <https://doi.org/10.1038/s41598-020-67646-7>
- Man, W., Zhou, T., & Jungelaus, J. H. (2014). Effects of large volcanic eruptions on global summer climate and east asian monsoon changes during the last millennium: Analysis of MPI-ESM simulations. *Journal of Climate*, 27(19), 7394–7409. <https://doi.org/10.1175/JCLI-D-13-00739.1>
- Mann, M. E. (2000). Long-Term Variability in the El Niño/Southern Oscillation and Associated Teleconnections. In H. F. Diaz & V. Markgraf (Eds.), *El Niño and the Southern Oscillation Multiscale Variability and Global and Regional Impacts* (pp. 357–410). Cambridge University Press.
- Mann, M. E., & Lees, J. M. (1996). Robust estimation of background noise and signal detection in climatic time series. *Climatic Change*, 33(3), 409–445. <https://doi.org/10.1007/BF00142586>
- Mann, M. E., Steinman, B. A., & Miller, S. K. (2020). Absence of internal multidecadal and interdecadal oscillations in climate model simulations. *Nature Communications*, 11(1), 1–9. <https://doi.org/10.1038/s41467-019-13823-w>
- Manson, B. R. (1974). The life history of silver beech (*Nothofagus menziesii*). *Proceedings of the New Zealand Ecological Society*, 21, 27–31. <http://www.jstor.org/stable/24061487>
- McBride, J. L., & Nicholls, N. (1983). Seasonal Relationships between Australian Rainfall and the Southern Oscillation. *Monthly Weather Review*, 111, 1998–2004. [https://doi.org/10.1175/1520-0493\(1983\)111<1998:SRBARA>2.0.CO;2](https://doi.org/10.1175/1520-0493(1983)111<1998:SRBARA>2.0.CO;2)
- McCallum, J. L., Crosbie, R. S., Walker, G. R., & Dawes, W. R. (2010). Impacts of climate change on groundwater in Australia: A sensitivity analysis of recharge. *Hydrogeology Journal*, 18(7), 1625–1638. <https://doi.org/10.1007/s10040-010-0624-y>
- McGlone, M. S., Richardson, S. J., Burge, O. R., Perry, G. L. W., & Wilmshurst, J. M. (2017). Palynology and the ecology of the New Zealand conifers. *Frontiers in Earth Science*, 5, 1–23. <https://doi.org/10.3389/feart.2017.00094>

- McGowan, H. A., Marx, S. K., Denholm, J., Soderholm, J., & Kamber, B. S. (2009). Reconstructing annual inflows to the headwater catchments of the Murray River, Australia, using the Pacific Decadal Oscillation. *Geophysical Research Letters*, 36(6). <https://doi.org/10.1029/2008GL037049>
- McGree, S., Schreider, S., & Kuleshov, Y. (2016). Trends and variability in droughts in the Pacific islands and Northeast Australia. *Journal of Climate*, 29(23), 8377–8397. <https://doi.org/10.1175/JCLI-D-16-0332.1>
- McGregor, S., Timmermann, A., & Timm, O. (2010). A unified proxy for ENSO and PDO variability since 1650. *Climate of the Past*, 6(1), 1–17. <https://doi.org/10.5194/cp-6-1-2010>
- Mehrotra, R., & Sharma, A. (2016). A multivariate quantile-matching bias correction approach with auto- and cross-dependence across multiple time scales: implications for downscaling. *Journal of Climate*, 29(10), 3519–3539. <https://doi.org/10.1175/JCLI-D-15-0356.1>
- Meko, D. M. (1997). Dendroclimatic reconstruction with time varying predictor subsets of tree indices. *Journal of Climate*, 10(4), 687–696. [https://doi.org/10.1175/1520-0442\(1997\)010<0687:DRWTVP>2.0.CO;2](https://doi.org/10.1175/1520-0442(1997)010<0687:DRWTVP>2.0.CO;2)
- Meko, D. M., Stockton, C. W., & Boggess, W. R. (1995). The Tree-Ring Record of Severe Sustained Drought. *JAWRA Journal of the American Water Resources Association*, 31(5), 789–801. <https://doi.org/10.1111/j.1752-1688.1995.tb03401.x>
- Meko, D. M., & Woodhouse, C. A. (2011). Application of Streamflow Reconstruction to Water Resources Management. In M. Hughes, T. Swetnam, & H. Diaz (Eds.), *Dendroclimatology. Developments in Paleoenvironmental Research* (pp. 231–261). Springer. https://doi.org/10.1007/978-1-4020-5725-0_8
- Melvin, T. M., & Briffa, K. R. (2008). A “signal-free” approach to dendroclimatic standardisation. *Dendrochronologia*, 26(2), 71–86. <https://doi.org/10.1016/j.dendro.2007.12.001>
- Meyers, G., McIntosh, P., Pigot, L., & Pook, M. (2007). The years of El Niño, La Niña and interactions with the tropical Indian Ocean. *Journal of Climate*, 20(13), 2872–2880. <https://doi.org/10.1175/JCLI4152.1>
- Miao, J., Wang, T., Wang, H., & Sun, J. (2018). Interannual Weakening of the Tropical Pacific Walker Circulation Due to Strong Tropical Volcanism. *Advances in Atmospheric Sciences*, 35(6), 645–658. <https://doi.org/10.1007/s00376-017-7134-y>
- Miller, A. (2019). *Subset Selection in Regression* (Second Ed.). Chapman and Hall, New York. ISBN 9780367396220
- Moise, A., Bhend, J., Watterson, I., & Wilson, L. (2015). Evaluation of Climate Models. In *Climate Change in Australia Information for Australia's Natural Resource Management Regions: Technical Report*. CSIRO and Bureau of Meteorology: Canberra. pp. 52–76.
- Morales, M. S., Cook, E. R., Barichivich, J., Christie, D. A., Matskovsky, V., Aravena, J. C., Lara, A., Mundo, I. A., Alvarez, C., Lopez, L., Luckman, B., Lister, D., Harris, I., Philip, D., Williams, P., Velazquez, G., Aliste, D., & Aguilera-betti, I. (2020). 600 years of South American tree rings reveal an increase in severe hydroclimatic events since mid-20th century. *PNAS*, 117(29). <https://doi.org/10.1073/pnas.2002411117>
- Morrison, R. E. (1970). Water resources of the Daly River Basin - a study of a proposed dam at Mt. Nancar. The University of New South Wales, Sydney, Master's thesis.
- Mudelsee, M., Börngen, M., Tetzlaff, G., & Grünwald, U. (2003). No upward trends in the occurrence of extreme floods in central Europe. *Nature*, 425(6954), 166–169. <https://doi.org/10.1038/nature01928>
- Mudelsee, M., Börngen, M., Tetzlaff, G., & Grünwald, U. (2004). Extreme floods in central Europe over the past 500 years: Role of cyclone pathway “Zugstrasse Vb.” *Journal of Geophysical Research D: Atmospheres*, 109(23), 1–21. <https://doi.org/10.1029/2004JD005034>
- Mullan, B. (2012). Applying the Rhoades and Salinger Method to New Zealand's “Seven-Station” Temperature Series. *Weather and Climate*, 32(1), 23. <https://doi.org/10.2307/26169723>
- Murphy, B. F., Power, S. B., & McGree, S. (2014). The varied impacts of El Niño-southern oscillation on pacific Island climates. *Journal of Climate*, 27(11), 4015–4036. <https://doi.org/10.1175/JCLI-D-13-00130.1>

- Nash, J. E., & Sutcliffe, J. V. (1970). River Flow Forecasting through Conceptual Models. Part 1—A Discussion of Principles. *Journal of Hydrology*, 10, 282–290. [https://doi.org/http://dx.doi.org/10.1016/0022-1694\(70\)90255-6](https://doi.org/http://dx.doi.org/10.1016/0022-1694(70)90255-6)
- Neukom, R., Barboza, L. A., Erb, M. P., Shi, F., Emile-Geay, J., Evans, M. N., Franke, J., Kaufman, D. S., Lücke, L., Rehfeld, K., Schurer, A., Zhu, F., Brönnimann, S., Hakim, G. J., Henley, B. J., Ljungqvist, F. C., McKay, N., Valler, V., & von Gunten, L. (2019). Consistent multidecadal variability in global temperature reconstructions and simulations over the Common Era. *Nature Geoscience*, 12(8), 643–649. <https://doi.org/10.1038/s41561-019-0400-0>
- Neukom, R., Gergis, J., Karoly, D. J., Wanner, H., Curran, M., Elbert, J., González-Rouco, F., Linsley, B. K., Moy, A. D., Mundo, I., Raible, C. C., Steig, E. J., van Ommen, T., Vance, T., Villalba, R., Zinke, J., & Frank, D. (2014). Inter-hemispheric temperature variability over the past millennium. *Nature Climate Change*, 4(5), 362–367. <https://doi.org/10.1038/nclimate2174>
- Neukom, R., Schurer, A. P., Steiger, N. J., & Hegerl, G. C. (2018). Possible causes of data model discrepancy in the temperature history of the last Millennium /704/106/694/674 /704/106/694/1108 /704/106/413 /141 article. *Scientific Reports*, 8(1), 1–15. <https://doi.org/10.1038/s41598-018-25862-2>
- Nguyen, H. T. T., Galelli, S., Xu, C., & Buckley, B. M. (2021). Multi-Proxy, Multi-Season Streamflow Reconstruction With Mass Balance Adjustment. *Water Resources Research*, 57(8). <https://doi.org/10.1029/2020WR029394>
- Nguyen, H. T. T., Turner, S. W. D., Buckley, B. M., & Galelli, S. (2020). Coherent Streamflow Variability in Monsoon Asia Over the Past Eight Centuries—Links to Oceanic Drivers. *Water Resources Research*, 56(12), 1–20. <https://doi.org/10.1029/2020WR027883>
- Nguyen, H., Wheeler, M. C., Hendon, H. H., Lim, E. P., & Otkin, J. A. (2021). The 2019 flash droughts in subtropical eastern Australia and their association with large-scale climate drivers. *Weather and Climate Extremes*, 32, 100321. <https://doi.org/10.1016/j.wace.2021.100321>
- Nicholls, N. (2004). The changing nature of Australian droughts. *Climatic Change*, 63(3), 323–336. <https://doi.org/10.1023/B:CLIM.0000018515.46344.6d>
- Norton, D. A. (1983a). Modern New Zealand Tree-Ring Chronologies I. *Nothofagus solandri*. *Tree Ring Bulletin*, 43, 39–49.
- Norton, D. A. (1983b). Modern New Zealand Tree-Ring Chronologies II. *Nothofagus mezeisii*. *Tree-Ring Bulletin*, 43, 31–38.
- Norton, D. A. (1984). Tree-growth-climate relationships in subalpine *Nothofagus* forests, South Island, New Zealand. *New Zealand Journal of Botany*, 22(4), 471–481. <https://doi.org/10.1080/0028825X.1984.10425281>
- Norton, D. A. (1992). New Zealand Temperatures, 1800–30. In C. R. Harington (Ed.), *The Year without a summer?: World climate in 1816* (pp. 516–520). Canadian Museum of Nature.
- Norton, D. A., Briffa, K. R., & Salinger, M. J. (1989). Reconstruction of New Zealand summer temperatures to 1730 AD using dendroclimatic techniques. *International Journal of Climatology*, 9(6), 633–644. <https://doi.org/10.1002/joc.3370090607>
- Norton, D. A., & Kelly, D. (1988). Mast Seeding Over 33 Years by *Dacrydium cupressinum* Lamb. (rimu) (Podocarpaceae) in New Zealand: The Importance of Economies of Scale. *Functional Ecology*, 2(3), 399. <https://doi.org/10.2307/2389413>
- Norton, D. A., & Ogden, J. (1987). Dendrochronology: a review with emphasis on New Zealand applications. *New Zealand Journal of Ecology*, 10, 77–95.
- O'Donnell, A. J., Cook, E. R., Palmer, J. G., Turney, C. S. M., Page, G. F. M., & Grierson, P. F. (2015). Tree rings show recent high summer-autumn precipitation in northwest Australia is unprecedented within the last two centuries. *PLoS ONE*, 10(6), 1–18. <https://doi.org/10.1371/journal.pone.0128533>
- Ogden, J., & Ahmed, M. (1989). Climate response function analyses of kauri (*Agathis australis*) tree-ring chronologies in northern New Zealand. *Journal of the Royal Society of New Zealand*, 19(2), 205–221. <https://doi.org/10.1080/03036758.1989.10426449>

- Ogden, J., & Dunwiddie, P. W. (1982). Australasia. In Malcolm K. Hughes et al. (Ed.), *Climate from tree rings* (pp. 90–104). Cambridge University Press, Cambridge.
- Olafsdottir, K., & Mudelsee, M. (2014). More accurate, calibrated bootstrap confidence intervals for estimating the correlation between two time series. *Mathematical Geosciences*, 46(4), 411–427. <https://doi.org/10.1007/s11004-014-9523-4>
- Osborn, T. J., & Briffa, K. R. (2004). The Real Color of Climate Change? *Science*, 306(5696), 621–622. <https://doi.org/10.1126/science.1104416>
- Osborn, T. J., Briffa, K. R., & Jones, P. D. (1997). Adjusting Variance for Sample-Size in Tree-Ring Chronologies and Other Regional Mean Time Series. *Dendrochronologia*, 15, 89–99.
- Palmer, J. G. (1989). A dendroclimatic study of tanekaha (*Phyllocladus frichomanoides*). University of Auckland, PhD thesis.
- Palmer, J. G., Cook, E. R., Turney, C. S. M., Allen, K., Fenwick, P., Cook, B. I., O'Donnell, A., Lough, J., Grierson, P., & Baker, P. (2015). Drought variability in the eastern Australia and New Zealand summer drought atlas (ANZDA, CE 1500-2012) modulated by the Interdecadal Pacific Oscillation. *Environmental Research Letters*, 10(12). <https://doi.org/10.1088/1748-9326/10/12/124002>
- Palmer, J. G., Lorrey, A., Turney, C. S. M., Hogg, A., Baillie, M., Fifield, K., & Ogden, J. (2006). Extension of New Zealand kauri (*Agathis australis*) tree-ring chronologies into Oxygen Isotope Stage (OIS) 3. *Journal of Quaternary Science*, 21(7), 779–787. <https://doi.org/10.1002/jqs>
- Palmer, J. G., & Ogden, J. (1992). Tree-Ring Chronologies from Endemic Australian and New Zealand Conifers 1800-30. In C. R. Harington (Ed.), *The Year without a summer?: World climate in 1816* (pp. 510–515). Canadian Museum of Nature.
- Palmer, J. G., & Xiong, L. (2004). New Zealand climate over the last 500 years reconstructed from *Libocedrus bidwillii* Hook. f. tree-ring chronologies. *Holocene*, 14(2), 282–289. <https://doi.org/10.1191/0959683604hl679rr>
- Partin, J. W., Quinn, T. M., Shen, C. C., Emile-Geay, J., Taylor, F. W., Maupin, C. R., Lin, K., Jackson, C. S., Banner, J. L., Sinclair, D. J., & Huh, C. A. (2013). Multidecadal rainfall variability in south pacific convergence zone as revealed by stalagmite geochemistry. *Geology*, 41(11), 1143–1146. <https://doi.org/10.1130/G34718.1>
- Paton, J. G. (1893). *The Story of John G. Paton Told for Young Folks or Thirty Years among South Sea Cannibals*. Hodder and Stoughton, London.
- Peterson, T. J., Saft, M., Peel, M. C., & John, A. (2021). Watersheds may not recover from drought. *Science*, 372(6543), 745–749. <https://doi.org/10.1126/science.abd5085>
- Petheram, C., McMahon, T. A., & Peel, M. C. (2008). Flow characteristics of rivers in northern Australia: Implications for development. *Journal of Hydrology*, 357(1–2), 93–111. <https://doi.org/10.1016/j.jhydrol.2008.05.008>
- Phipps, R. (1982). Comments on interpretation of climatic information from tree rings, eastern North America. *Tree Ring Bulletin*, 42, 11–22.
- Pieper, H., Heinrich, I., Heußner, K. U., & Helle, G. (2014). The influence of volcanic eruptions on growth of central European lowland trees in NE-Germany during the last millennium. *Palaeogeography, Palaeoclimatology, Palaeoecology*, 411, 155–166. <https://doi.org/10.1016/j.palaeo.2014.06.012>
- Potter, N. J., Chiew, F. H. S., & Frost, A. J. (2010). An assessment of the severity of recent reductions in rainfall and runoff in the Murray-Darling Basin. *Journal of Hydrology*, 381(1–2), 52–64. <https://doi.org/10.1016/j.jhydrol.2009.11.025>
- Power, S. B., Casey, T., Folland, C., Colman, A., & Mehta, V. (1999). Inter-decadal modulation of the impact of ENSO on Australia. *Climate Dynamics*, 15(5), 319–324. <https://doi.org/10.1007/s003820050284>
- Power, S. B., Haylock, M., Colman, R., & Wang, X. (2006). The predictability of interdecadal changes in ENSO activity and ENSO teleconnections. *Journal of Climate*, 19(19), 4755–4771. <https://doi.org/10.1175/JCLI3868.1>

- Prosser, I. P., Chiew, F. H. S., & Smith, M. S. (2021). Adapting water management to climate change in the Murray–Darling Basin, Australia. *Water (Switzerland)*, 13(18), 1–19. <https://doi.org/10.3390/w13182504>
- Quinn, T. M., Crowley, T. J., & Taylor, F. W. (1996). New stable isotope results from a 173-year coral from Espiritu Santo, Vanuatu. *Geophysical Research Letters*, 23(23), 3413–3416. <https://doi.org/10.1029/96GL03169>
- Quinn, T. M., Crowley, T. J., Taylor, F. W., Henin, C., Joannot, P., & Join, Y. (1998). A multicentury stable isotope record from a New Caledonia coral: Interannual and decadal sea surface temperature variability in the southwest Pacific since 1657 A.D. *Paleoceanography*, 13(4), 412–426. <https://doi.org/10.1029/98PA00401>
- Raible, C. C., Brönnimann, S., Auchmann, R., Brohan, P., Frölicher, T. L., Graf, H. F., Jones, P., Luterbacher, J., Muthers, S., Neukom, R., Robock, A., Self, S., Sudrajat, A., Timmreck, C., & Wegmann, M. (2016). Tambora 1815 as a test case for high impact volcanic eruptions: Earth system effects. *Wiley Interdisciplinary Reviews: Climate Change*, 7(4), 569–589. <https://doi.org/10.1002/wcc.407>
- Rao, M. P., Cook, E. R., Cook, B. I., Anchukaitis, K. J., D’Arrigo, R. D., Krusic, P. J., & LeGrande, A. N. (2019). A double bootstrap approach to Superposed Epoch Analysis to evaluate response uncertainty. *Dendrochronologia*, 55(February), 119–124. <https://doi.org/10.1016/j.dendro.2019.05.001>
- Rao, M. P., Cook, E. R., Cook, B. I., D’Arrigo, R. D., Palmer, J. G., Lall, U., Woodhouse, C. A., Buckley, B. M., Uriarte, M., Bishop, D. A., Jian, J., & Webster, P. J. (2020). Seven centuries of reconstructed Brahmaputra River discharge demonstrate underestimated high discharge and flood hazard frequency. *Nature Communications*, 11(1). <https://doi.org/10.1038/s41467-020-19795-6>
- Rao, M. P., Cook, E. R., Cook, B. I., Palmer, J. G., Uriarte, M., Devineni, N., Lall, U., D’Arrigo, R. D., Woodhouse, C. A., Ahmed, M., Zafar, M. U., Khan, N., Khan, A., & Wahab, M. (2018). Six Centuries of Upper Indus Basin Streamflow Variability and Its Climatic Drivers. *Water Resources Research*, 54(8), 5687–5701. <https://doi.org/10.1029/2018WR023080>
- Renwick, J., & Thompson, D. (2006). The Southern Annular Mode and New Zealand Climate. *Water & Atmosphere*, 14(2), 24–25. <https://doi.org/10.1029/1998RG000054>
- Rice, J. L., Woodhouse, C. A., & Lukas, J. J. (2009). Science and decision making: Water management and tree-ring data in the western United States. *Journal of the American Water Resources Association*, 45(5), 1248–1259. <https://doi.org/10.1111/j.1752-1688.2009.00358.x>
- Riedwyl, N., Küttel, M., Luterbacher, J., & Wanner, H. (2009). Comparison of climate field reconstruction techniques: Application to Europe. *Climate Dynamics*, 32(2–3), 381–395. <https://doi.org/10.1007/s00382-008-0395-5>
- Rifai, S. W., Li, S., & Malhi, Y. (2019). Coupling of El Niño events and long-term warming leads to pervasive climate extremes in the terrestrial tropics. *Environmental Research Letters*, 14(10). <https://doi.org/10.1088/1748-9326/ab402f>
- Risbey, J. S., Pook, M. J., McIntosh, P. C., Wheeler, M. C., & Hendon, H. H. (2009). On the remote drivers of rainfall variability in Australia. *Monthly Weather Review*, 137(10), 3233–3253. <https://doi.org/10.1175/2009MWR2861.1>
- Robock, A. (2000). Volcanic eruptions and climate. *Reviews of Geophysics*, 38(2), 191–219.
- Robock, A. (2005). Cooling following large volcanic eruptions corrected for the effect of diffuse radiation on tree rings. *Geophysical Research Letters*, 32(6), 1–4. <https://doi.org/10.1029/2004GL022116>
- Rocheta, E., Sugiyanto, M., Johnson, F., Evans, J., & Sharma, A. (2014). How well do general circulation models represent low frequency rainfall variability? *Water Resources Research*, 50, 2108–2123. <https://doi.org/10.1002/2012WR013085>
- Rodionov, S., & Overland, J. E. (2005). Application of a sequential regime shift detection method to the Bering Sea ecosystem. *ICES Journal of Marine Science*, 62(3), 328–332. <https://doi.org/10.1016/j.icesjms.2005.01.013>

- Rotstayn, L. D., Cai, W., Dix, M. R., Farquhar, G. D., Feng, Y., Ginoux, P., Herzog, M., Ito, A., Penner, J. E., Roderick, M. L., & Wang, M. (2007). Have Australian rainfall and cloudiness increased due to the remote effects of Asian anthropogenic aerosols? *Journal of Geophysical Research Atmospheres*, 112(9), 1–28. <https://doi.org/10.1029/2006JD007712>
- Rozas, V., García-González, I., Pérez-De-Lis, G., & Arévalo, J. R. (2013). Local and large-scale climatic factors controlling tree-ring growth of *Pinus canariensis* on an oceanic island. *Climate Research*, 56(3), 197–207. <https://doi.org/10.3354/cr01158>
- Rozendaal, D. M. A., & Zuidema, P. A. (2011). Dendroecology in the tropics: A review. *Trees - Structure and Function*, 25(1), 3–16. <https://doi.org/10.1007/s00468-010-0480-3>
- Russell-Smith, J., Lucas, D., Gapindi, M., Gunbunuka, B., Kapirigi, N., Namingum, G., Lucas, K., Giuliani, P., & Chaloupka, G. (1997). Aboriginal Resource Utilization and Fire Management Practice in Western Arnhem Land, Monsoonal Northern Australia: Notes for Prehistory, Lessons for the Future. *Human Ecology*, 25(2), 159–195.
- Saft, M., Western, A. W., Zhang, L., Peel, M. C., & Potter, N. J. (2015). The influence of multiyear drought on the annual rainfall-runoff relationship: An Australian perspective. *Water Resources Research*, 51, 2444–2463. <https://doi.org/doi:10.1002/2014WR015348>
- Salinger, M. J. (1980). New Zealand Climate: 1. Precipitation Patterns. *Monthly Weather Review*, 108, 1892–1904. [https://doi.org/10.1175/1520-0493\(1980\)108<1892:NZCIPP>2.0.CO;2](https://doi.org/10.1175/1520-0493(1980)108<1892:NZCIPP>2.0.CO;2)
- Salinger, M. J. (1981). *New Zealand Climate: The instrumental record*. Victoria University of Wellington, PhD thesis.
- Salinger, M. J. (1998). New Zealand Climate: The Impact of Major Volcanic Eruptions. *Weather and Climate*, 18(1), 11–19. <https://doi.org/10.2307/44280024>
- Salinger, M. J., Palmer, J. G., Jones, P. D., & Briffa, K. R. (1994). Reconstruction of New Zealand climate indices back to AD 1731 using dendroclimatic techniques: Some preliminary results. *International Journal of Climatology*, 14(10), 1135–1149. <https://doi.org/10.1002/joc.3370141005>
- Santoso, A., Mcphaden, M. J., & Cai, W. (2017). The Defining Characteristics of ENSO Extremes and the Strong 2015/2016 El Niño. *Reviews of Geophysics*, 55(4), 1079–1129. <https://doi.org/10.1002/2017RG000560>
- Satoh, Y., Yoshimura, K., Pokhrel, Y., Kim, H., Shiogama, H., Yokohata, T., Hanasaki, N., Wada, Y., Burek, P., Byers, E., Schmied, H. M., Gerten, D., Ostberg, S., Gosling, S. N., Eric, J., Boulange, S., & Oki, T. (2022). The timing of unprecedented hydrological drought under climate change. *Nature Communications*, 13(3287), 1–11. <https://doi.org/10.1038/s41467-022-30729-2>
- Schneider, T., Bischoff, T., & Haug, G. H. (2014). Migrations and dynamics of the intertropical convergence zone. *Nature*, 513(7516), 45–53. <https://doi.org/10.1038/nature13636>
- Scuderi, L. A. (1990). Tree-ring evidence for climatically effective volcanic eruptions. *Quaternary Research*, 34(1), 67–85. [https://doi.org/10.1016/0033-5894\(90\)90073-T](https://doi.org/10.1016/0033-5894(90)90073-T)
- Sheather, S. J., & Jones, M. C. (1991). A Reliable Data-Based Bandwidth Selection Method for Kernel Density Estimation. *Journal of the Royal Statistical Society*, 53(3), 683–690. <https://www.jstor.org/stable/2345597>
- Sheffield, J., Wood, E. F., & Roderick, M. L. (2012). Little change in global drought over the past 60 years. *Nature*, 491(7424), 435–438. <https://doi.org/10.1038/nature11575>
- Shi, G., Cai, W., Cowan, T., Ribbe, J., Rotstayn, L., & Dix, M. (2008). Variability and trend of North West Australia rainfall: Observations and coupled climate modeling. *Journal of Climate*, 21(12), 2938–2959. <https://doi.org/10.1175/2007JCLI1908.1>
- Sigl, M., McConnell, J. R., Toohey, M., Curran, M., Das, S. B., Edwards, R., Isaksson, E., Kawamura, K., Kipfstuhl, S., Krüger, K., Layman, L., Maselli, O. J., Motizuki, Y., Motoyama, H., Pasteris, D. R., & Severi, M. (2014). Insights from antarctica on volcanic forcing during the common era. *Nature Climate Change*, 4(8), 693–697. <https://doi.org/10.1038/nclimate2293>

- Sigl, M., Winstrup, M., McConnell, J. R., Welten, K. C., Plunkett, G., Ludlow, F., Büntgen, U., Caffee, M., Chellman, N., Dahl-Jensen, D., Fischer, H., Kipfstuhl, S., Kostick, C., Maselli, O. J., Mekhaldi, F., Mulvaney, R., Muscheler, R., Pasteris, D. R., Pilcher, J. R., ... Woodruff, T. E. (2015). Timing and climate forcing of volcanic eruptions for the past 2,500 years. *Nature*, 523(7562), 543–549. <https://doi.org/10.1038/nature14565>
- Singh, D., Ghosh, S., Roxy, M. K., & McDermid, S. (2019). Indian summer monsoon: Extreme events, historical changes, and role of anthropogenic forcings. *Wiley Interdisciplinary Reviews: Climate Change*, 10(2), 1–35. <https://doi.org/10.1002/wcc.571>
- Singh, D., Seager, R., Cook, B. I., Cane, M., Ting, M., Cook, E., & Davis, M. (2018). Climate and the Global Famine of 1876–78. *Journal of Climate*, 31(23), 9445–9467. <https://doi.org/10.1175/JCLI-D-18-0159.1>
- Skertchly, A., & Skertchly, K. (1999). The Katherine-Daly flood disaster 1998. *Australian Journal of Emergency Management*, 31–36.
- Smerdon, J. E., Coats, S., & Ault, T. R. (2016). Model-dependent spatial skill in pseudoproxy experiments testing climate field reconstruction methods for the Common Era. *Climate Dynamics*, 46(5–6), 1921–1942. <https://doi.org/10.1007/s00382-015-2684-0>
- Smith, I. N., Wilson, L., & Suppiah, R. (2008). Characteristics of the northern Australian rainy season. *Journal of Climate*, 21(17), 4298–4311. <https://doi.org/10.1175/2008JCLI2109.1>
- St. George, S., Meko, D. M., & Cook, E. R. (2010). The seasonality of precipitation signals embedded within the North American Drought Atlas. *Holocene*, 20(6), 983–988. <https://doi.org/10.1177/0959683610365937>
- Stahle, D. W., Cook, E. R., Burnette, D. J., Villanueva, J., Cerano, J., Burns, J. N., Griffin, D., Cook, B. I., Acuña, R., Torbenson, M. C. A., Sjezner, P., & Howard, I. M. (2016). The Mexican Drought Atlas: Tree-ring reconstructions of the soil moisture balance during the late pre-Hispanic, colonial, and modern eras. *Quaternary Science Reviews*, 149, 34–60. <https://doi.org/10.1016/j.quascirev.2016.06.018>
- Stahle, D. W., D'Arrigo, R. D., Krusic, P. J., Cleaveland, M. K., Cook, E. R., Allan, R. J., Cole, J. E., Dunbar, R. B., Therrell, M. D., Gay, D. A., Moore, M. D., Stokes, M. A., Burns, B. T., Villanueva-Diaz, J., & Thompson, L. G. (1998). Experimental Dendroclimatic Reconstruction of the Southern Oscillation. *Bulletin of the American Meteorological Society*, 79(10), 2137–2152. [https://doi.org/10.1175/1520-0477\(1998\)079<2137:EDROTS>2.0.CO;2](https://doi.org/10.1175/1520-0477(1998)079<2137:EDROTS>2.0.CO;2)
- Stevenson, S., Otto-Bliesner, B., Fasullo, J., & Brady, E. (2016). “El Niño Like” hydroclimate responses to last millennium volcanic eruptions. *Journal of Climate*, 29(8), 2907–2921. <https://doi.org/10.1175/JCLI-D-15-0239.1>
- Stewart, G. H. (2002). *Structure and canopy tree species regeneration requirements in indigenous forests, Westland, New Zealand*. Department of Conservation, Wellington, New Zealand, Doc Science Internal Series 66, 1–33.
- Suppiah, R. (1992). The Australian summer monsoon: a review. *Progress in Physical Geography: Earth and Environment*, 16(3), 283–318. <https://doi.org/10.1177/030913339201600302>
- Taschetto, A. S., & England, M. H. (2009). An analysis of late twentieth century trends in Australian rainfall. *International Journal of Climatology*, 29, 791–807. <https://doi.org/10.1002/joc.1736>
- Taschetto, A. S., Haarsma, R. J., Sen Gupta, A., Ummenhofer, C. C., & England, M. H. (2010). Teleconnections associated with the intensification of the Australian monsoon during El Niño Modoki events. *IOP Conference Series: Earth and Environmental Science*, 11, 012031. <https://doi.org/10.1088/1755-1315/11/1/012031>
- Tejedor, E., Steiger, N., Smerdon, J. E., Serrano-Notivol, R., & Vuille, M. (2021). Global Temperature Responses to Large Tropical Volcanic Eruptions in Paleo Data Assimilation Products and Climate Model Simulations Over the Last Millennium. *Paleoceanography and Paleoclimatology*, 36(4), 1–17. <https://doi.org/10.1029/2020PA004128>
- Therrell, M. D. (2005). Tree rings and “El Año del Hambre” in Mexico. *Dendrochronologia*, 22(3), 203–207. <https://doi.org/10.1016/j.dendro.2005.04.006>

- Thompson, C. S. (2006). Relative Influence of the Interdecadal Pacific Oscillation on Drought Occurrence and Severity. *Weather and Climate*, 26(August), 35–66. <https://www.jstor.org/stable/10.2307/26169685>
- Thoms, M. C., & Sheldon, F. (2000). Water resource development and hydrological change in a large dryland river: The Barwon-Darling River, Australia. *Journal of Hydrology*, 228(1–2), 10–21. [https://doi.org/10.1016/S0022-1694\(99\)00191-2](https://doi.org/10.1016/S0022-1694(99)00191-2)
- Timbal, B., Abbs, D., Bhend, J., Chiew, F. H. S., Church, J., Ekstrom, M., Kirono, D., Lenton, A., Lucas, C., McInnes, K., Moise, A. F., Monselesan, D., Mpelasoka, F., Webb, L., & Whetton, P. H. (2015). Murray Basin Cluster Report. In *Climate Change in Australia Projections for Australia's Natural Resource Management Regions: Cluster Reports*. CSIRO and Bureau of Meteorology: Canberra.
- Timmreck, C. (2012). Modeling the climatic effects of large explosive volcanic eruptions. *Wiley Interdisciplinary Reviews: Climate Change*, 3(6), 545–564. <https://doi.org/10.1002/wcc.192>
- Timmreck, C., Toohey, M., Zanchettin, D., Brönnimann, S., Lundstadt, E., & Wilson, R. (2021). The unidentified volcanic eruption of 1809: why it remains a climatic cold case. *Climate of the Past Discussions, April 1815*, 1–39. <https://doi.org/10.5194/cp-2021-4>
- Tingley, M. P., Stine, A. R., & Huybers, P. (2014). Temperature reconstructions from tree-ring densities overestimate volcanic cooling. *Geophysical Research Letters*, 41(22), 7838–7845. <https://doi.org/10.1002/2014GL061268>
- Toohey, M., & Sigl, M. (2017). Volcanic stratospheric sulfur injections and aerosol optical depth from 500BCE to 1900CE Matthew. *Earth Syst. Sci. Data*, 9, 809–831. <https://doi.org/10.1108/eb058541>
- Toohey, M., Stevens, B., Schmidt, H., & Timmreck, C. (2016). Easy Volcanic Aerosol (EVA v1.0): an idealized forcing generator for climate simulations. *Geoscientific Model Development*, 9(11), 4049–4070. <https://doi.org/10.5194/gmd-9-4049-2016>
- Turney, C., & Fogwill, C. (2021). The implications of the recently recognized mid-20th century shift in the Earth system. *Anthropocene Review*. <https://doi.org/10.1177/2053019621995526>
- Ukkola, A. M., De Kauwe, M. G., Roderick, M. L., Abramowitz, G., & Pitman, A. J. (2020). Robust Future Changes in Meteorological Drought in CMIP6 Projections Despite Uncertainty in Precipitation. *Geophysical Research Letters*, 47(11), 1–9. <https://doi.org/10.1029/2020GL087820>
- Ummenhofer, C. C., D'Arrigo, R. D., Anchukaitis, K. J., Buckley, B. M., & Cook, E. R. (2013). Links between Indo-Pacific climate variability and drought in the Monsoon Asia Drought Atlas. *Climate Dynamics*, 40(5–6), 1319–1334. <https://doi.org/10.1007/s00382-012-1458-1>
- Ummenhofer, C. C., England, M. H., McIntosh, P. C., Meyers, G. A., Pook, M. J., Risbey, J. S., Gupta, A. Sen, & Taschetto, A. S. (2009). What causes southeast Australia's worst droughts? *Geophysical Research Letters*, 36(4), 1–5. <https://doi.org/10.1029/2008GL036801>
- Van Dijk, A. I. J. M., Beck, H. E., Crosbie, R. S., De Jeu, R. A. M., Liu, Y. Y., Podger, G. M., Timbal, B., & Viney, N. R. (2013). The Millennium Drought in southeast Australia (2001–2009): Natural and human causes and implications for water resources, ecosystems, economy, and society. *Water Resources Research*, 49(2), 1040–1057. <https://doi.org/10.1002/wrcr.20123>
- Vance, T. R., Roberts, J. L., Plummer, C. T., Kiem, A. S., & Van Ommen, T. D. (2015). Interdecadal Pacific variability and eastern Australian megadroughts over the last millennium. *Geophysical Research Letters*, 42(1), 129–137. <https://doi.org/10.1002/2014GL062447>
- Verdon-Kidd, D. C., Kiem, A. S., & Moran, R. (2014). Links between the big dry in Australia and hemispheric multi-decadal climate variability-implications for water resource management. *Hydrology and Earth System Sciences*, 18(6), 2235–2256. <https://doi.org/10.5194/hess-18-2235-2014>
- Verdon-Kidd, D. C., Hancock, G. R., & Lowry, J. B. (2017). A 507-year rainfall and runoff reconstruction for the Monsoonal North West, Australia derived from remote paleoclimate archives. *Global and Planetary Change*, 158(September), 21–35. <https://doi.org/10.1016/j.gloplacha.2017.09.003>

- Verdon, D. C., & Franks, S. W. (2005). Indian Ocean sea surface temperature variability and winter rainfall: Eastern Australia. *Water Resources Research*, 41(9), 1–10. <https://doi.org/10.1029/2004WR003845>
- Verdon, D. C., & Franks, S. W. (2007). Long-term drought risk assessment in the Lachlan River Valley – a paleoclimate perspective. *Australasian Journal of Water Resources*, 11(2), 145–152. <https://doi.org/10.1080/13241583.2007.11465319>
- Vertessy, R., Barma, D., Baumgartner, L., Mitrovic, S., Sheldon, F., & Bond, N. (2019). *Independent Assessment of the 2018-19 fish deaths in the lower Darling*. Report to the Minister for Agriculture and Water Resources. 1–99.
- Villalba, R., & Boninsegna, J. A. (1992). Changes in Southern South American Tree-Ring Chronologies following Major Volcanic Eruptions between 1750-1970. *The Year without a Summer? World Climate in 1816, January*, 493–509.
- Vincent, D. G. (1994). The South Pacific Convergence Zone (SPCZ): A Review. *Monthly Weather Review*, 122, 1949–1970. [https://doi.org/10.1175/1520-0493\(1994\)122<1949:TSPCZA>2.0.CO;2](https://doi.org/10.1175/1520-0493(1994)122<1949:TSPCZA>2.0.CO;2)
- Vincent, E. M., Lengaigne, M., Menkes, C. E., Jourdain, N. C., Marchesiello, P., & Madec, G. (2011). Interannual variability of the South Pacific Convergence Zone and implications for tropical cyclone genesis. *Climate Dynamics*, 36(9–10), 1881–1896. <https://doi.org/10.1007/s00382-009-0716-3>
- Vinod, H. D., & López-de-Lacalle, J. (2009). Maximum entropy bootstrap for time series: The meboot R package. *Journal of Statistical Software*, 29(5), 1–19. <https://doi.org/10.18637/jss.v029.i05>
- Wang, P. X., Wang, B., Cheng, H., Fasullo, J., Guo, Z. T., Kiefer, T., & Liu, Z. Y. (2014). The global monsoon across timescales: Coherent variability of regional monsoons. *Climate of the Past*, 10(6), 2007–2052. <https://doi.org/10.5194/cp-10-2007-2014>
- Wardle, J. (1970). The ecology of *Nothofagus solandri*, New Zealand. *New Zealand Journal of Botany*, 8(4), 609–646. <https://doi.org/10.1080/0028825X.1970.10430162>
- Wardle, P. (1977). Plant communities of Westland National Park (New Zealand) and neighbouring lowland and coastal areas. *New Zealand Journal of Botany*, 15(2), 323–398. <https://doi.org/10.1080/0028825X.1977.10432549>
- Wardle, R., & Smith, I. (2004). Modeled response of the Australian monsoon to changes in land surface temperatures. *Geophysical Research Letters*, 31(16). <https://doi.org/10.1029/2004GL020157>
- Wasko, C., Shao, Y., Vogel, E., Wilson, L., Wang, Q. J., Frost, A., & Donnelly, C. (2021). Understanding trends in hydrologic extremes across Australia. *Journal of Hydrology*, 593, 125877. <https://doi.org/https://doi.org/10.1016/j.jhydrol.2020.125877>
- Wasson, R. J., Furlonger, L., Parry, D., Pietsch, T., Valentine, E., & Williams, D. (2010). Sediment sources and channel dynamics, Daly River, Northern Australia. *Geomorphology*, 114(3), 161–174. <https://doi.org/10.1016/j.geomorph.2009.06.022>
- Water Studies Pty Ltd. (2000). *Katherine River Flood Study*. Report No. 02/2000D. NT Department of Lands, Planning and the Environment.
- Williams, C. A., & Hanan, N. P. (2011). ENSO and IOD teleconnections for African ecosystems: Evidence of destructive interference between climate oscillations. *Biogeosciences*, 8(1), 27–40. <https://doi.org/10.5194/bg-8-27-2011>
- Wilson, R., Anchukaitis, K., Briffa, K. R., Büntgen, U., Cook, E., D'Arrigo, R., Davi, N., Esper, J., Frank, D., Gunnarson, B., Hegerl, G., Helama, S., Klesse, S., Krusic, P. J., Linderholm, H. W., Myglan, V., Osborn, T. J., Rydval, M., Schneider, L., ... Zorita, E. (2016). Last millennium Northern Hemisphere summer temperatures from tree rings: Part I: The long term context. *Quaternary Science Reviews*, 134, 1–18. <https://doi.org/10.1016/j.quascirev.2015.12.005>
- Wilson, R., Cook, E., D'arrigo, R., Riedwyl, N., Evans, M., Tudhope, A., & Allan, R. (2009). Reconstructing ENSO: the influence of method, proxy data, climate forcing and teleconnections. *J. Quaternary Science*, 25, 62–78. <https://doi.org/10.1002/jqs.1297>
- Wise, E. K., & Dannenberg, M. P. (2019). Climate Factors Leading to Asymmetric Extreme Capture in the Tree-Ring Record. *Geophysical Research Letters*, 46(6), 3408–3416. <https://doi.org/10.1029/2019GL082295>

- Woodhouse, C. A. (1997). Tree-ring reconstructions of circulation indices. *Climate Research*, 8(2), 117–127. <https://doi.org/10.3354/cr008117>
- Woodhouse, C. A., Gray, S. T., & Meko, D. M. (2006). Updated streamflow reconstructions for the Upper Colorado River Basin. *Water Resources Research*, 42(5), 1–16. <https://doi.org/10.1029/2005WR004455>
- Woodhouse, C. A., Lukas, J. J., Morino, K., Meko, D. M., & Hirschboeck, K. K. (2017). Using the past to plan for the future-the value of paleoclimate reconstructions for water resource planning. *Water Policy and Planning in a Variable and Changing Climate*, 161–182. <https://doi.org/10.1201/b19534>
- Wright, W. J. (1997). Tropical-extratropical cloudbands and Australian rainfall: I. Climatology. *International Journal of Climatology*, 17(8), 807–829. [https://doi.org/10.1002/\(sici\)1097-0088\(19970630\)17:8<807::aid-joc162>3.0.co;2-j](https://doi.org/10.1002/(sici)1097-0088(19970630)17:8<807::aid-joc162>3.0.co;2-j)
- Xiong, L., Okada, N., Fujiwara, T., Ohta, S., & Palmer, J. G. (1998). Chronology development and climate response analysis of different New Zealand pink pine (*Halocarpus biformis*) tree-ring parameters. *Canadian Journal of Forest Research*, 28(4), 566–573. <https://doi.org/10.1139/cjfr-28-4-566>
- Xiong, L., & Palmer, J. G. (2000). *Libocedrus Bidwillii* Tree-ring Chronologies in New Zealand. *Tree-Ring Bulletin*, 56, 1–16.
- Yan, H., Wei, W., Soon, W., An, Z., Zhou, W., Liu, Z., Wang, Y., & Carter, R. M. (2015). Dynamics of the intertropical convergence zone over the western Pacific during the Little Ice Age. *Nature Geoscience*, 8(4), 315–320. <https://doi.org/10.1038/ngeo2375>
- Yang, S., Li, Z., Yu, J. Y., Hu, X., Dong, W., & He, S. (2018). El Niño-Southern Oscillation and its impact in the changing climate. *National Science Review*, 5(6), 840–857. <https://doi.org/10.1093/nsr/nwy046>
- Yeates, S. J., Strickland, G. R., & Grundy, P. R. (2013). Can sustainable cotton production systems be developed for tropical northern Australia? *Crop and Pasture Science*, 64, 1127–1140. <https://doi.org/https://doi.org/10.1071/CP13220>
- Yun, K. S., & Timmermann, A. (2019). Calibration uncertainties of tropical Pacific climate reconstructions over the Last Millennium. *Journal of Climate*, 32(14), 4547–4566. <https://doi.org/10.1175/JCLI-D-18-0524.1>
- Zhang, X. S., Amirthanathan, G. E., Bari, M. A., Laugesen, R. M., Shin, D., Kent, D. M., MacDonald, A. M., Turner, M. E., & Tuteja, N. K. (2016). How streamflow has changed across Australia since the 1950s: Evidence from the network of hydrologic reference stations. *Hydrology and Earth System Sciences*, 20(9), 3947–3965. <https://doi.org/10.5194/hess-20-3947-2016>
- Zhu, F., Emile-geay, J., Anchukaitis, K. J., Hakim, G. J., Wittenberg, A. T., Morales, M. S., Toohey, M., & King, J. (2022). A re-appraisal of the ENSO response to volcanism with paleoclimate data assimilation. *Nature Communications*, 747(13), 1–9. <https://doi.org/10.1038/s41467-022-28210-1>
- Zhu, F., Emile-Geay, J., Hakim, G. J., King, J., & Anchukaitis, K. J. (2020). Resolving the Differences in the Simulated and Reconstructed Temperature Response to Volcanism. *Geophysical Research Letters*, 47(8), 1–12. <https://doi.org/10.1029/2019GL086908>
- Zweifel, R., Sterck, F., Braun, S., Buchmann, N., Eugster, W., Gessler, A., Häni, M., Peters, R. L., Walthert, L., Wilhelm, M., Ziemnińska, K., & Etzold, S. (2021). Why trees grow at night. *New Phytologist*, 231(6), 2174–2185. <https://doi.org/10.1111/nph.17552>

Appendix A. Supplementary information for Chapter 2

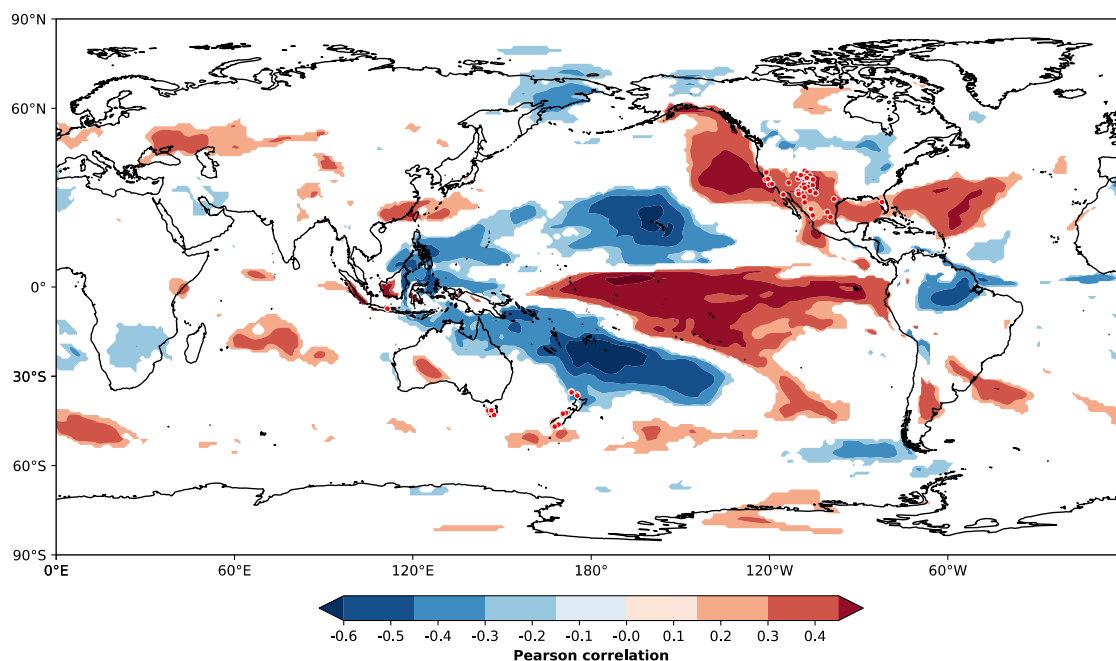


Figure A-1 Correlation ($P < 0.05$) between Nov-Apr instrumental SPCZI anomalies and 20th Century Reanalysis v3 Nov-Apr precipitation anomalies for 1911-1998, showing teleconnections between SPCZ convergence and precipitation in the ANZDA and MXDA tree-ring regions. Red dots indicate the location of tree-ring predictors used in the SPCZI reconstruction.

Full calibration and validation statistics for the South Pacific Convergence Zone Index reconstruction (SPCZI_r) are provided in Figure A-1 and Table A-1. Following standard procedures in dendrochronology, the split calibration/verification period was verified both ways, using first the 1955-1998 period for calibration and the 1911-1954 period for verification and then repeating with the periods reversed. Successful verification both ways indicates stability in the reconstruction. The final SPCZI_r used the full instrumental period (1911-1998) for calibration to maximise the timescale of variability against which the final regression equation could be fitted.

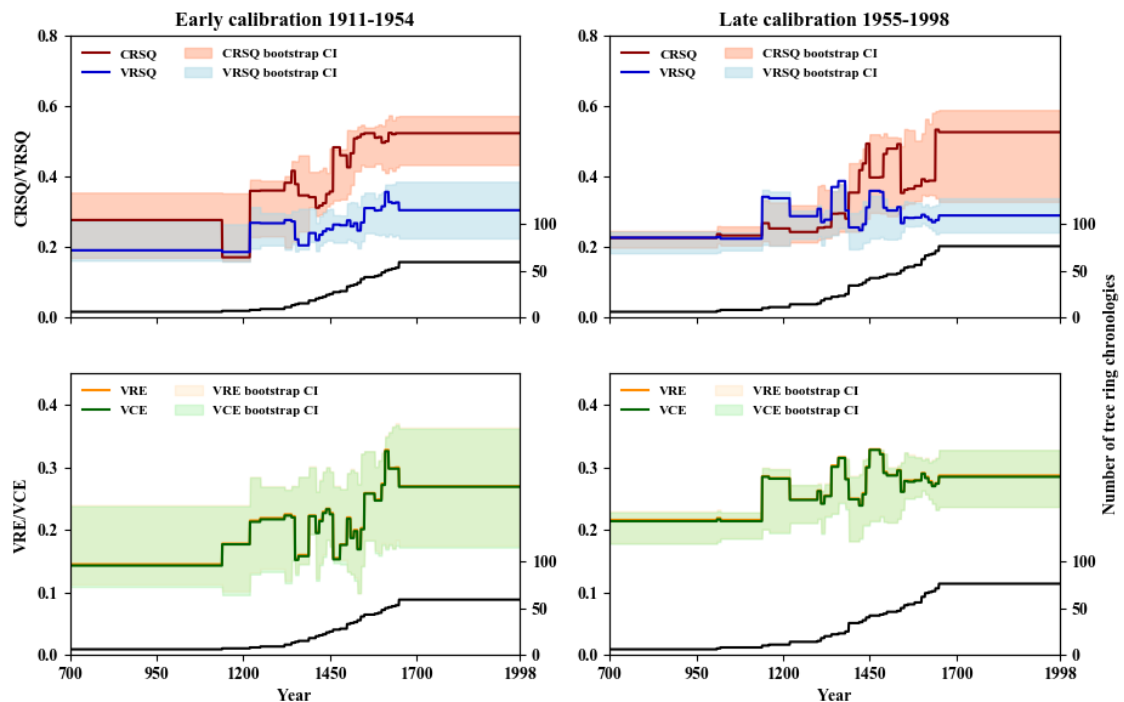


Figure A-2 Calibration and validation statistics for the Nov-Apr mean SPCZI reconstruction along with the number of tree ring series (black line) used as predictors in each nest. The shaded uncertainties represent the 5-95% confidence interval for each statistic based on 300 maximum entropy bootstrap replications. CRSQ - calibration period coefficient of multiple determination; VRSQ - validation period square of the Pearson correlation; VRE - validation period reduction of error; and VCE validation period coefficient of efficiency. VRE and VCE values consistently greater than 0 indicate skill in the reconstruction.

Table A-1 November to April SPCZ reconstruction calibration (c) and validation (v) statistics for early calibration (1911–1954) and late calibration (1955–1998) models, restricted to those tree-ring predictors correlated to the entire instrumental period (1911–1998).

Test	Score-c	Probability-c	Score-v	Probability-v
<i>Early calibration (1911–1954) and late verification (1955–1998)</i>				
Pearson correlation	0.724	0.000	0.551	0.000
Spearman correlation	0.678	0.000	0.554	0.000
Kendall Tau	0.502	0.000	0.410	0.000
Reduction of error	0.270			
Coefficient of efficiency	0.269			
<i>Late calibration (1955–1998) and early verification (1911–1954)</i>				
Pearson correlation	0.719	0.000	0.539	0.000
Spearman correlation	0.718	0.000	0.543	0.000
Kendall Tau	0.528	0.000	0.373	0.000
Reduction of error	0.287			
Coefficient of efficiency	0.285			

Table A-2 Pearson correlation (R) between instrumental SPCZI and annually resolved coral proxies from the SPCZ region over the common instrumental period. Significant correlations $P < 0.05$ are shown in bold.

Coral proxy ($\delta^{18}\text{O}$)	Location	Common period	R	P	Reference
Rarotonga <i>Porites lutea</i>	Cook Islands	1911-1996	-0.339	0.001	Linsley et al., 2004
Savusavu Bay <i>Porites lutea</i> AB	Fiji	1911-2001	0.361	0.000	Linsley et al., 2008
Savusavu Bay <i>Porites lutea</i> 1F	Fiji	1911-1996	0.470	0.000	Linsley et al., 2006
Savusavu Bay <i>Diploastrea</i>	Fiji	1911-2001	0.506	0.000	Bagnato et al., 2005
Amedee Lighthouse <i>Porites lutea</i>	New Caledonia	1911-1992	-0.273	0.013	Quinn et al., 1998
Ha'afera Island, <i>Porites lutea</i> TH1*	Tonga	1911-2004	0.220	0.033	Linsley et al., 2006
Malinoa Island, <i>Porites lutea</i> TN12*	Tonga	1911-2004	0.082	0.433	Linsley et al., 2006
Santo <i>Platygyra lamellina</i>	Vanuatu	1911-1979	0.010	0.934	Quinn et al., 1996
Sabine Bank <i>Porites lutea</i>	Vanuatu	1911-1989	-0.434	0.000	Gorman et al., 2012

*TH1 and TN12 are not annual average isotope records but reconstructions based on the multi-decadal (~9-55 year) variance of the isotope data. Tonga *Porites lutea* TM1 from Linsley et al. (2006) has not been included due to fungal infestation which inhibited growth (Linsley et al., 2008).

Independent verification of the reconstruction was undertaken using local coral proxies from the SPCZ region. The three-core average of the two Savusavu Bay *Porites lutea* and the Savusavu Bay *Diploastrea* core was selected as the verification series. Averaging multiple cores reduces the impact of potential dating errors which can result in very low correlations between proxies that otherwise contain a coherent signal. The Pearson correlation over the common reconstruction period (1781-1996; $R = 0.347$, $P < 0.01$) is similar to the correlations between coral proxies and instrumental SPCZI (Table A-3) demonstrating the ability of the reconstruction to represent local climate.

Table A-3 Comparison between the Nov-Apr SPCZI reconstruction and mean Nov-Apr values of published instrumental indices over the calibration/verification period 1911-1998. Indices for comparison are the Niño3.4 index (<https://climatedataguide.ucar.edu>), Multivariate ENSO Index (MEI; <https://www.esrl.noaa.gov/psd/enso/mei/>), Tripole Index (Henley et al., 2015), and Interdecadal Pacific Oscillation (IPO) index (<http://cola.gmu.edu/c20c/>). All Pearson RSQ values are significant at $P < 0.001$.

	Niño3.4 (Nov-Apr)	MEI (Nov-Apr)	TPI (Nov-Apr)	IPO (Nov-Apr)
SPCZI (Nov-Apr)	0.713	0.737	0.747	0.729
MEI (Nov-Apr)	0.942		0.861	0.806
TPI (Nov-Apr)	0.861	0.861		0.967
IPO (Nov-Apr)	0.806	0.806	0.967	

Table A-4 Comparison between the Nov-Apr SPCZI reconstruction and related paleoclimate reconstructions over the common reconstruction period 1650-1998: Buckley IPO (Buckley et al., 2019), Vance piecewise linear fit (PLF) IPO (Vance et al., 2015), and the Fiji-Tonga Interdecadal-decadal Pacific Oscillation (FT-IDPO; (Linsley et al., 2006)). Pearson correlations for unfiltered reconstructions significant at $P \leq 0.05$ are shown in bold. For comparisons with the PLF IPO (for which only the filtered data has been made publicly available), the remaining reconstructions were smoothed with a 13-year Gaussian low-pass filter. The correlation coefficients for filtered series were calculated with bootstrapped confidence intervals using the PearsonT3 software (Olafsdottir & Mudelsee, 2014) which accounts for autocorrelation in the smoothed time series. Correlations are significant at $P < 0.05$ if the 95% confidence interval does not span 0 (bold values).

	Buckley IPO	F-T IDPO	Vance PLF IPO
SPCZI	0.182	0.127	<i>na</i>
Buckley IPO		0.137	<i>na</i>
F-T IDPO			<i>na</i>
SPCZI (filtered)	0.377 [0.06, 0.63]	0.187 [-0.16, 0.49]	0.199 [-0.16, 0.38]
Buckley IPO (filtered)		0.262 [-0.03, 0.51]	0.199 [0.03, 0.36]
F-T IDPO (filtered)			0.181 [-0.01, 0.36]
	Buckley IPO (filtered)	F-T IDPO (filtered)	Vance PLF IPO

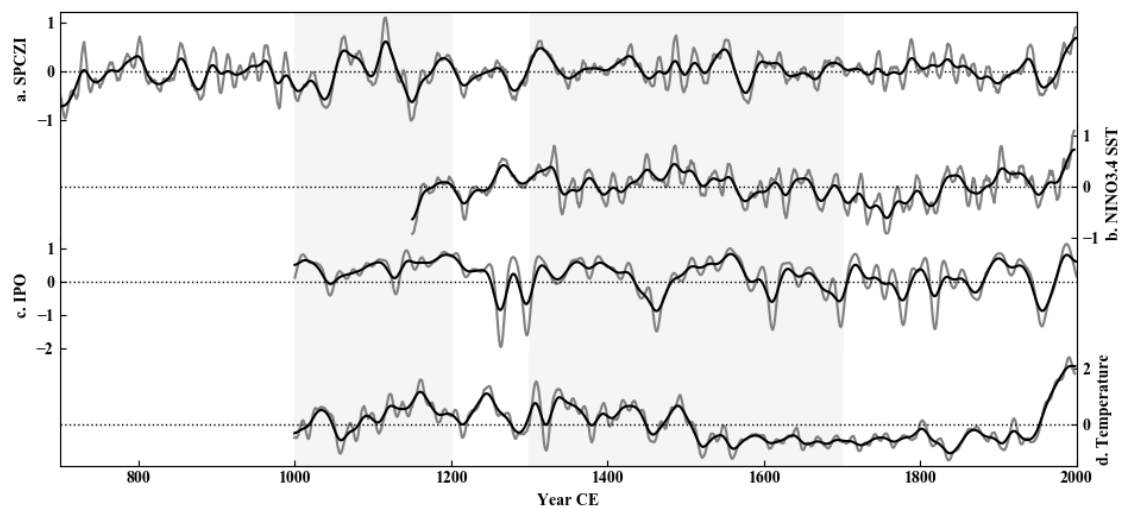


Figure A-3 Stacked plot comparing SPCZI to Southern Hemisphere reconstructions of ocean-atmosphere climate modes stretching back to the Medieval Climate Anomaly (MCA); a) SPCZI, b) Niño3.4 sea surface temperatures (Emile-Geay et al., 2013), c) PLF IPO (Vance et al., 2015), d) temperature (Neukom et al., 2014). The records have been smoothed with a 13-year (grey line) and 50-year (black line) Gaussian filters. Vertical bars indicate the approximate timing of the MCA and LIA.

Regime shift analysis (Rodionov & Overland, 2005) was used to identify significant shifts in the reconstruction mean (at the 95% confidence limit). Mean values of 15-year periods were compared on either side of each year throughout the reconstruction. The analysis successfully identified the well-reported shifts in climate associated with changing IPO mode in 1944 and 1973. Significant regime shifts were also identified in CE 725, 991, 1049, 1130, 1162, 1212, 1300, and 1333.

The presence of a likely El Niño (or La Niña) event in a given reconstruction year was estimated by an SPCZI at least one standard deviation above (below) the mean. These threshold values are

very close to the average SPCZI for recorded ENSO events during the instrumental period. An extreme shift eastwards (westwards) was defined by a period of three or more years of sustained positive (negative) SPCZI where the average of the period was above the El Niño (La Niña) threshold. Table A-5 displays the results of the frequency analysis.

Table A-5 Number of extreme events per 100 years with sustained eastward (dry) and westward (wet) shifts in the SPCZ: for the whole reconstruction period (700-1998), for the MCA envelope period (1000-1400), and for the LIA (1450-1850).

	Dry events	Wet events	Total
CE 700-1998	3.08	2.62	5.7
MCA envelope	2.5	3.75	6.25
LIA	2.75	0.75	3.5

Large tropical volcanic eruption key years since 700 CE were taken from Toohey & Sigl (2017). Eruptions with VSSI > 10 Tg [S] occurred in 1107, 1170, 1229, 1257, 1285, 1344, 1452, 1457, 1585, 1600, 1694, 1640, 1808, 1815, 1831, 1835, 1883, 1887, 1902. The eruption in Parker, Philippines occurred in December 1640 and has been designated 1641 in the key event year list for consistency with the designation of years in the SPCZI reconstruction.

There are several potential factors contributing to the lack of volcanic fingerprinting in the Southern Hemisphere-only reconstruction in year $t+1$. Even limiting the analysis to very large eruptions (VSSI > 10 Tg [S]), all trees may not record every event. The location of events (14/18 in the Northern Hemisphere) suggests that volcanic dimming may often be too weak to force a Southern Hemisphere tree-ring response. The maritime climate effect also likely reduces the temperature response of the Southern Hemisphere chronologies compared to the largely continental Northern Hemisphere chronologies (Fritts, 1991).

Nevertheless, the Southern Hemisphere trees strengthen the volcanic response in the combined SPCZI reconstruction. Therefore, we further investigated the Southern Hemisphere response by undertaking superposed epoch analysis (SEA) for the same set of volcanic key years on the standardised tree-ring chronologies underlying the reconstruction (Table A-6). Composites were calculated for chronologies of the same species, and SEA was only undertaken for species with at least two chronologies. The species composites are also representative of discrete geographical locations, and therefore local climate effects.

Of the six species composites studied, three show a significant volcanic impact. The New Zealand pink pine (HABI) composite shows a typical volcanic imprint at $t+1$. The kauri pine (AGAU) actually increases in $t+1$, suggesting it receives a secondary benefit from volcanism. The location of the AGAU chronologies in the subtropical/temperate transition zone on the northern coast of

New Zealand (latitude $\sim 35^{\circ}\text{S}$) suggests a decrease in summer evapotranspiration following a volcanic event may provide a growth benefit to this species.

Tasmania cedar (ATCU) is the only Tasmanian species composite which shows a significant volcanic signal; a lagged response which persists over several years. Biological persistence, particularly in ring width indices, has been shown to result in a lagged volcanic response in several tree species, underestimating both the abruptness and magnitude of cooling (e.g. D'Arrigo et al., 2009 and references within). The lack of response in the other Tasmanian species is an interesting question for future research.

Table A-6 Species and location of the Southern Hemisphere chronologies included in the reconstruction.

Tree Species	Common name	Abbreviation	Chronologies	
			Number	*Geographic location
<i>Agathis australis</i>	Kauri pine	AGAU	5	North coast NZ
<i>Athrotaxis cupressoides</i>	Tasmanian cedar	ATCU	10	Tasmania
<i>Athrotaxis seaginoides</i>	King Billy pine	ATSE	2	Tasmania
<i>Phyllocladus aspleniifolius</i>	Celery-top pine	CTOP	1	Tasmania
<i>Haocarpus biformis</i>	Pink pine	HABI	9	West- and south coast NZ
<i>Lagarostrobos colensoi</i>	Silver pine	LACO	1	Westcoast NZ
<i>Lagarostrobos franklinii</i>	Huon pine	LGFR	4	Tasmania
<i>Libocedrus bidwillii</i>	New Zealand cedar	LIBI	3	Westcoast NZ
<i>Tectona grandis</i>	Teak	TEGR	1	Indonesia

*Refers only to geographic location of chronologies used in the reconstruction.

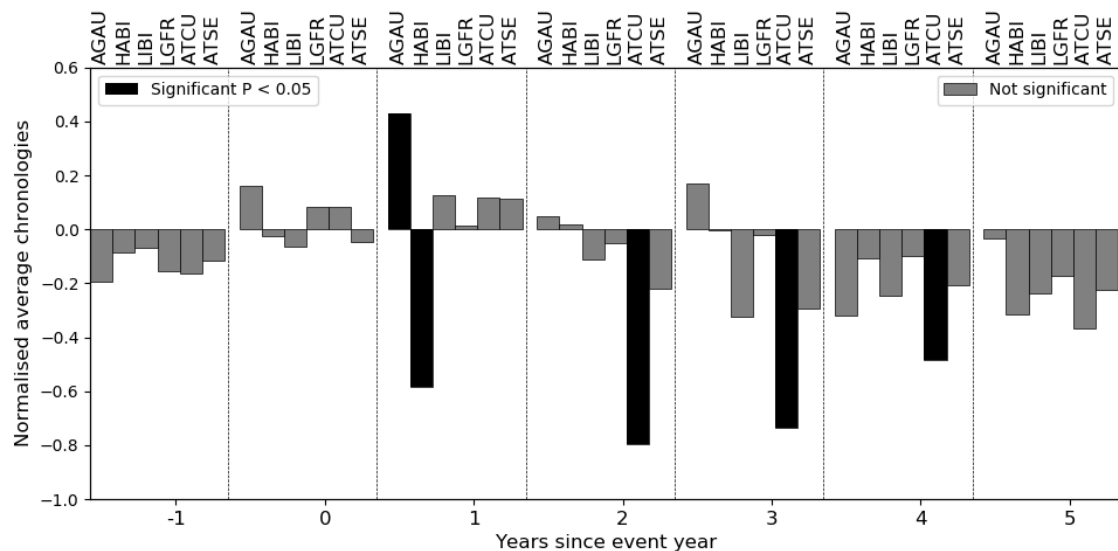


Figure A-4 Results of SEA analysis for species composites based on 18 large tropical volcanic events. SEA was carried out on a 21-year window (-10 to +10 years) but only results for -1 to +5 years are shown. The response shows the sensitivity of the species growth (ring width or density) to changing climate conditions after a large event. Significant results at $P < 0.05$ are shown by black bars; the results for ATCU in year $t+2$ and $t+3$ are significant at $P < 0.01$.

The effect of the 11-year Schwabe solar cycle on SPCZI was assessed using the ‘double-bootstrap’ SEA methodology of Rao et al. (2019) where the 5th to 95th uncertainty interval is

based on multiple unique draws of key event years. Key event years were defined as the maxima of the solar cycle calculated using a 24-month FWHM Gaussian with sunspot number data, sunspot area data, and 10.7 cm radio flux data (Hathaway, 2015). Cycles -4 to -1 were calculated using the 13-month mean of Group Sunspot Number due to limited data availability. The results with and without groups -4 to -1 were not significantly different. For consistency with the definition of the years of the SPCZI reconstruction (November to April, year starting January), years in which the solar maximum fell in November or December (cycles 11, 12, 15, 16 and 17) were labelled year+1. Solar maxima occurring within five years of a major volcanic eruption were removed from the key event list to maintain distinct signals. No response to solar maxima was identified (Figure A-5).

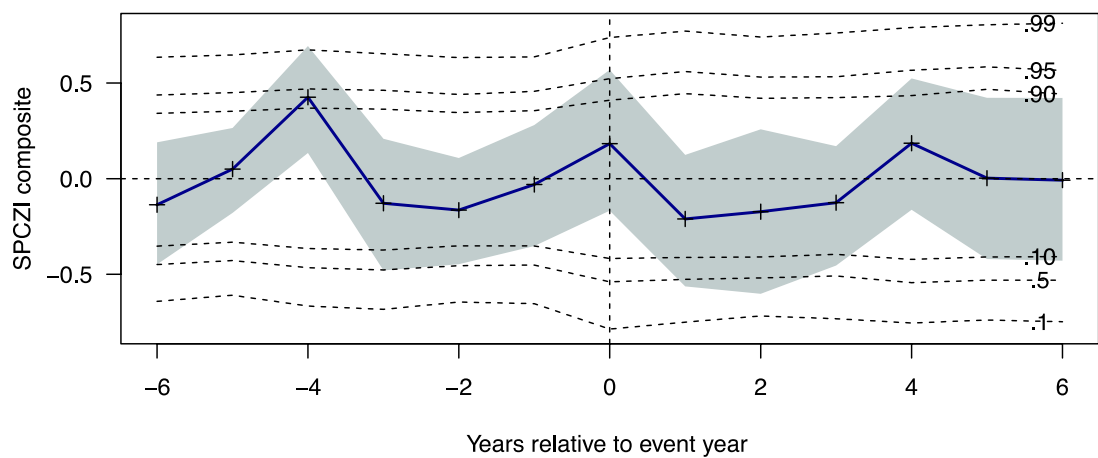


Figure A-5 Superposed epoch analysis showing the mean SPCZI response (blue line) to solar peak years, and the 5th to 95th percentiles of the SPCZI response (grey shading) based on 1000 unique draws of 10 key years.

Appendix B. Supplementary information for Chapter 3

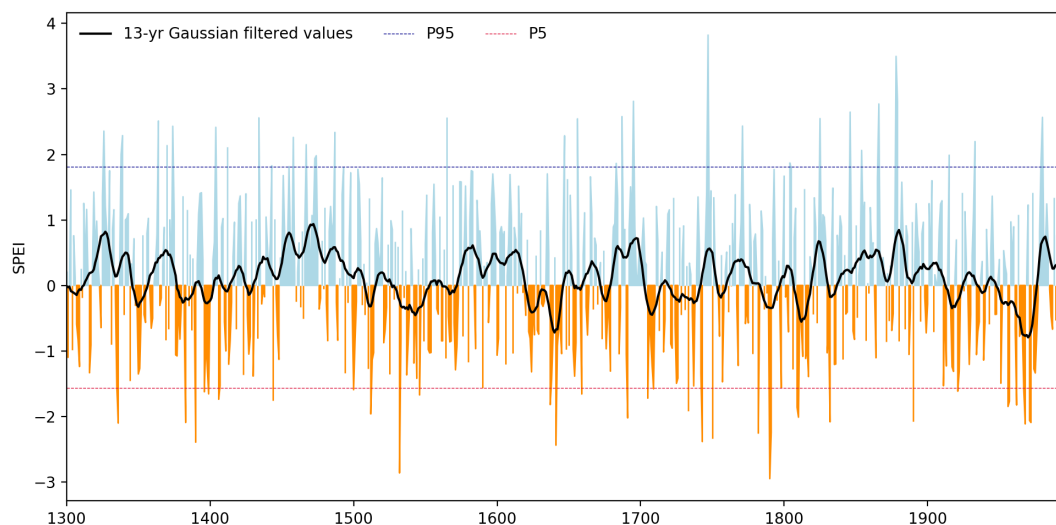


Figure B-1 Time series of reconstructed 12-month SPEI for Rapa Nui, with 13-year Gaussian filtered values (black lines). The 5th and 95th percentiles of the reconstruction are shown as dashed lines.

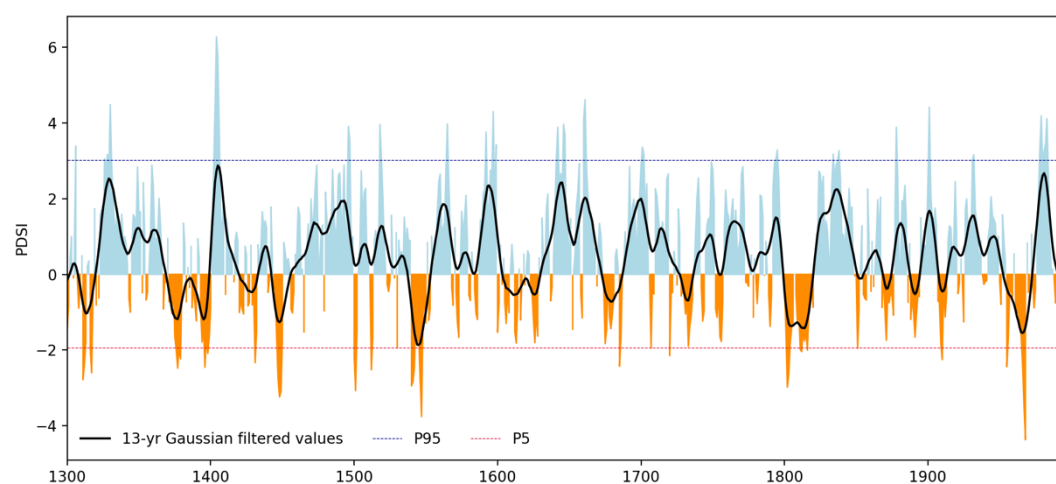


Figure B-2 Time series of reconstructed 12-month PDSI for Rapa Nui, with 13-year Gaussian filtered values (black lines). The 5th and 95th percentiles of the reconstruction are shown as dashed lines. Compared to Figure B-1 above, the PDSI reconstruction shows an unusual periodicity.

Appendix C. Supplementary information for Chapter 4

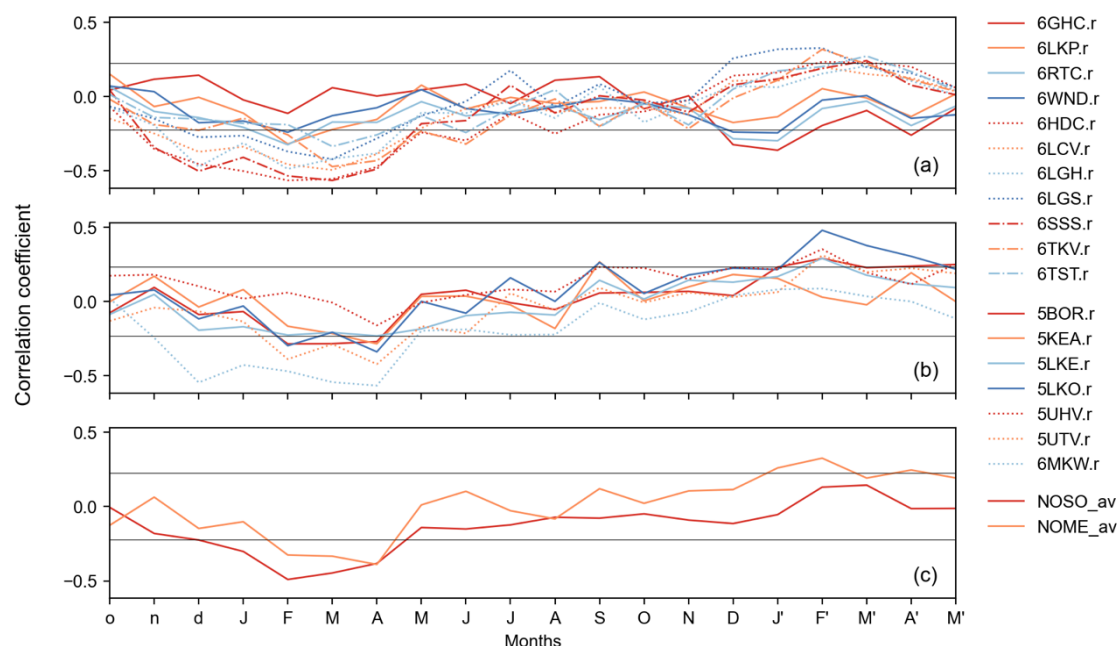


Figure C-1 Correlation between beech ring widths and monthly New Zealand seven-station average monthly temperature from for the 20-month window extending from October of the previous growing season to May at the end of the current austral growing season: a) Mountain beech (*Fuscopora cliffortioides*), b) Silver beech (*Lophozonia menziesii*), c) Average of all mountain beech chronologies (NOSO_av) and average of all silver beech chronologies (NOME_av). Horizontal lines indicate the approximate threshold for significance at $p < 0.05$ calculated for the average length of all chronologies intersecting with the temperature data ($n = 73$ for mountain beech, $n = 78$ for silver beech) although series have different lengths and thus thresholds for significance.

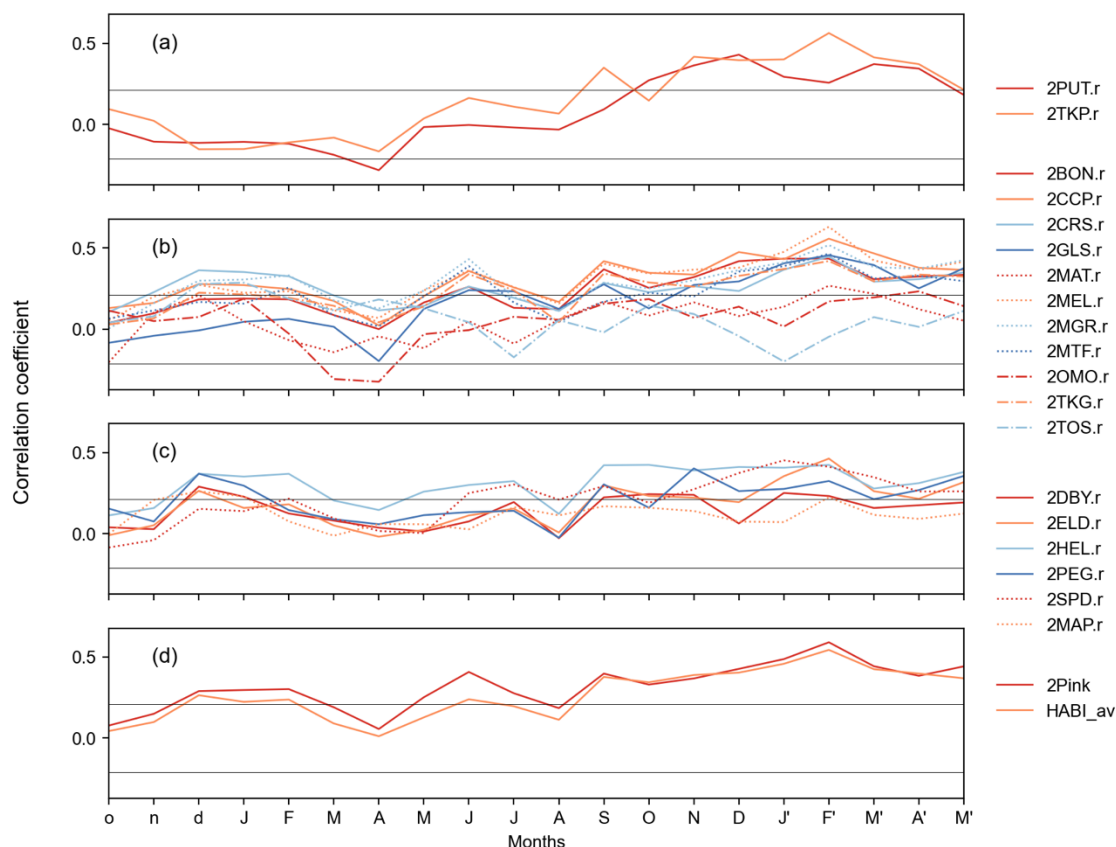


Figure C-2 Correlation between pink pine (*Halocarpus biformis*) ring widths and monthly New Zealand seven-station average monthly temperature for the 20-month window extending from October of the previous growing season to May at the end of the current austral growing season: a) Chronologies from the North Island, b) Chronologies from the western coast of the South Island, c) Chronologies south of latitude -45° on the South Island, d) Pink pine master chronology (2Pink) and average of all chronologies (HABI_av). Horizontal lines indicate the approximate threshold for significance at $p < 0.05$ calculated for the average length of all chronologies intersecting with the temperature data ($n = 87$) although series have different lengths and thus thresholds for significance.

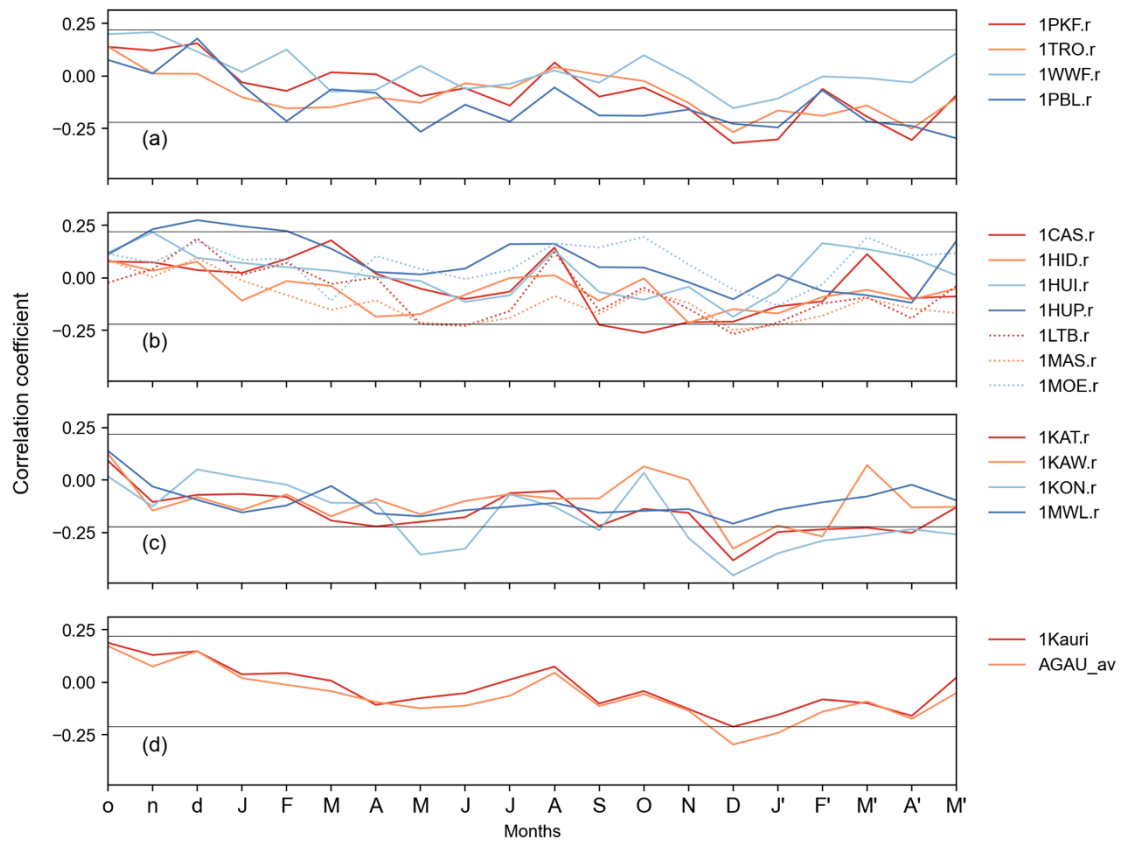


Figure C-3 Correlation between kauri (*Agathis australis*) ring widths and monthly New Zealand seven-station average monthly temperature for the 20-month window extending from October of the previous growing season to May at the end of the current austral growing season: a) Chronologies north of latitude -36° on the North Island, b) Chronologies south of -36° but north of 37° latitude c) Chronologies south of -37° , d) Kauri master chronology (1Kauri) and average of all chronologies (AGAU_av). Horizontal lines indicate the approximate threshold for significance at $p < 0.05$ calculated for the average length of all chronologies intersecting with the temperature data ($n = 80$) although series have different lengths and thus thresholds for significance. Chronologies 1HUI.r, 1MOE.r, and 1MWL.r are not significantly correlated with New Zealand average temperatures in any month. Chronology 1WFD.r does not overlap with instrumental temperature and is not plotted.

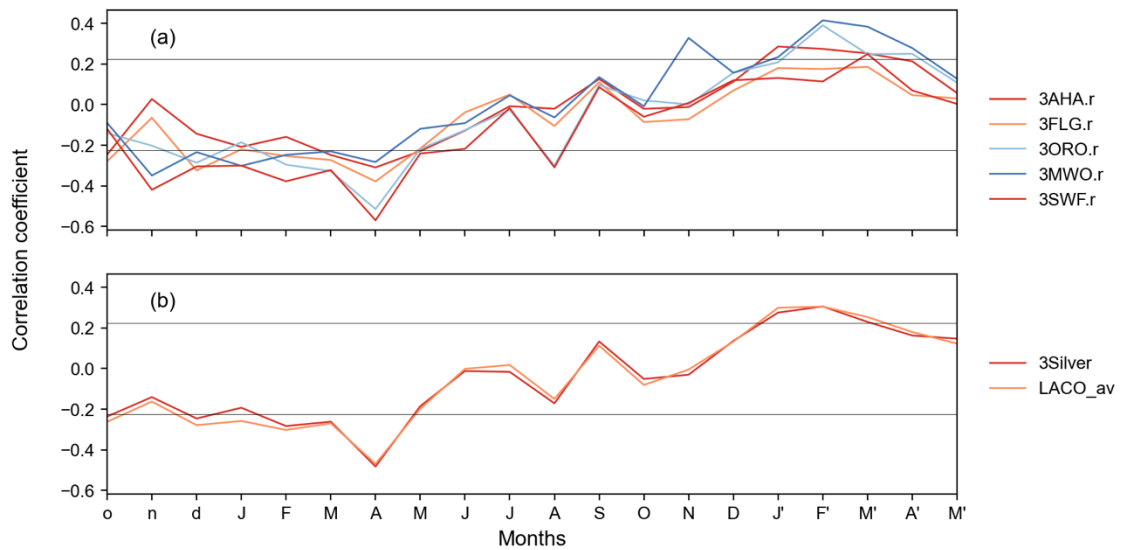


Figure C-4 Correlation between silver pine (*Manoao colensoi*) ring widths and monthly New Zealand seven-station average monthly temperature for the 20-month window extending from October of the previous growing season to May at the end of the current austral growing season. a) All silver pine chronologies, b) Silver pine master chronology (3Silver) and average of all chronologies (LACO_av). Horizontal lines indicate the approximate threshold for significance at $p < 0.05$ calculated for the average length of all chronologies intersecting with the temperature data ($n = 78$) although series have different lengths and thus thresholds for significance.

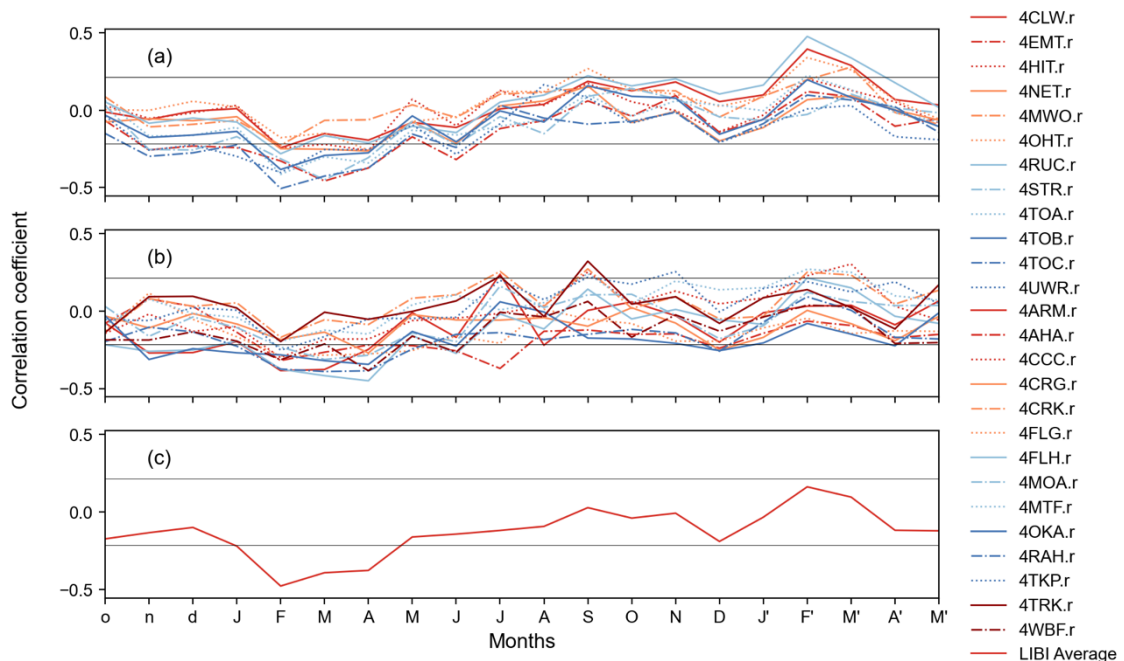


Figure C-5 Correlation between cedar (*Libocedrus bidwillii*) ring widths and monthly New Zealand seven-station average monthly temperature for the 20-month window extending from October of the previous growing season to May at the end of the current austral growing season: a) Chronologies from the North Island, b) Chronologies from the South Island, c) average of all cedar chronologies. Horizontal lines indicate the approximate threshold for significance at $p < 0.05$ calculated for the average length of all chronologies intersecting with the temperature data ($n = 84$) although series have different lengths and thus thresholds for significance.

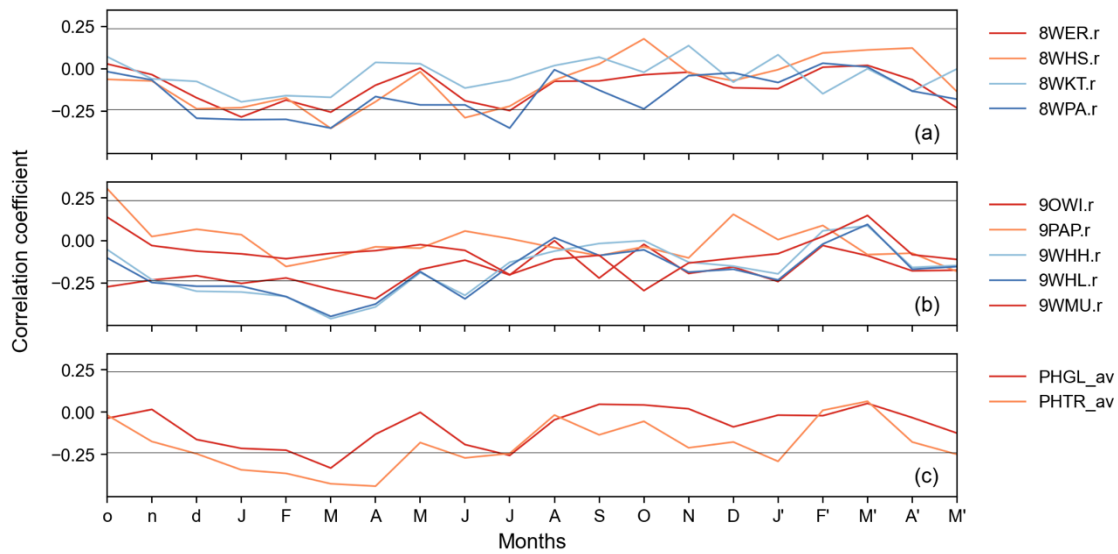


Figure C-6 Correlation between *Phyllocladus* ring widths and monthly New Zealand seven-station average monthly temperature for the 20-month window extending from October of the previous growing season to May at the end of the current austral growing season: a) Toatoa (*Phyllocladus toatoa*), b) Tanekaha (*Phyllocladus trichomanoides*), c) Average of all toatoa chronologies (PHGL_av) and average of all tanekaha chronologies (PHTR_av). Horizontal lines indicate the approximate threshold for significance at $p < 0.05$ calculated for the average length of all chronologies intersecting with the temperature data ($n = 68$ for toatoa, $n = 69$ for tanekaha) although series have different lengths and thus thresholds for significance. Chronology 8WKT.r is not significantly correlated with New Zealand average temperatures in any month.

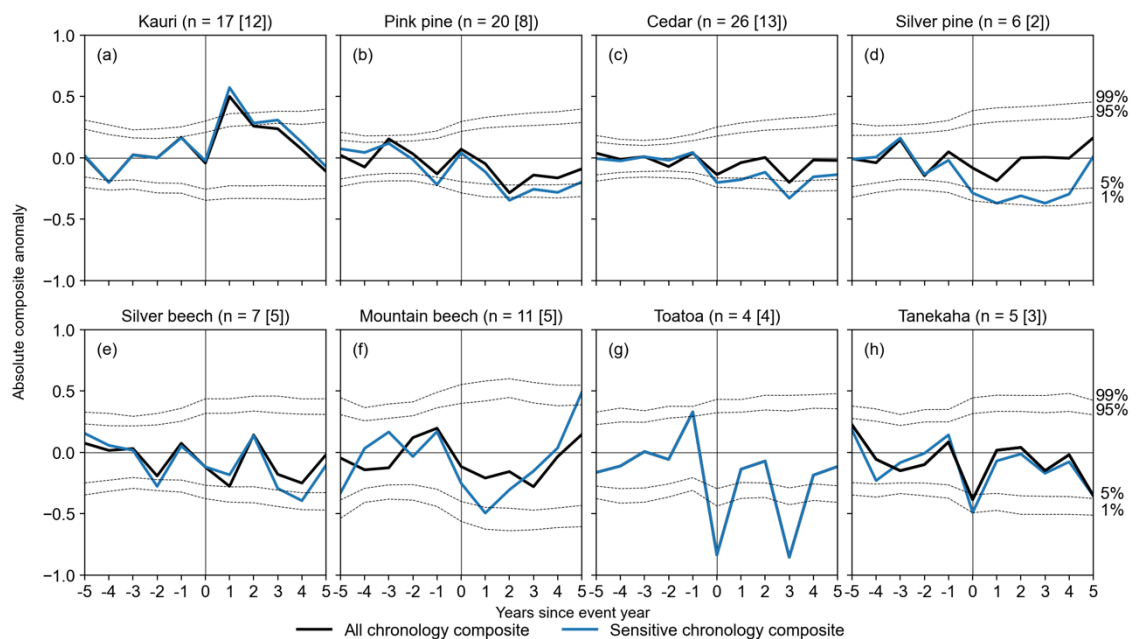


Figure C-7 Mean chronology departures five years before and after 21 eruption years with SAOD > 0.04 (year 0), separated by tree species. The chronologies contributing to the species-wide composite are shown in black, with the number of chronologies indicated in the round brackets. The sensitive chronology composite is shown in blue and the number of contributing chronologies is shown in the square brackets. Significance bands (dotted grey lines) are the 1st, 5th, 95th, and 99th percentile of 10,000 random samples of non-event years from the species-wide composite.

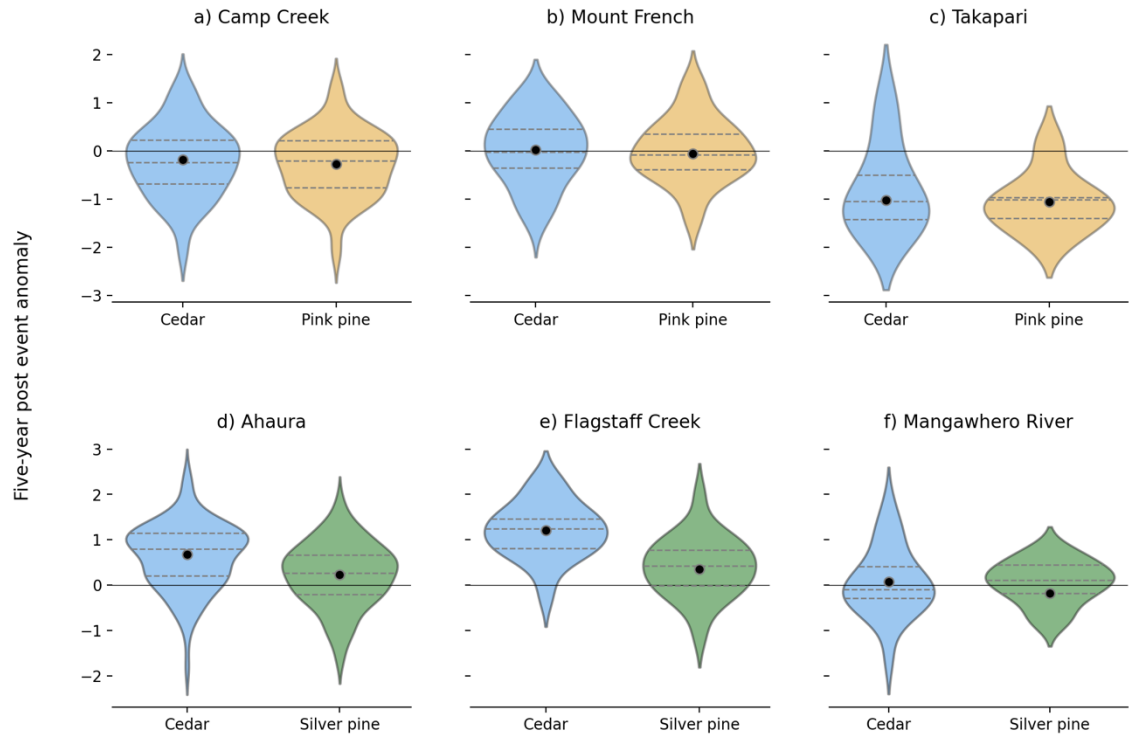


Figure C-8 Kernel density (violin) plots of the five-year post event anomaly for the standardised ring-width series contributing to the chronologies at six sites, three sites where cedar is co-located with pink pine (a-c) and three sites where cedar is co-located with silver pine (d-f). Dashed lines indicate the 25th, 50th, and 75th percentiles of the distributions of the response to the 21-volcanic event series, with the mean series response shown by the black dot. At some sites (a - Camp Creek, b - Mount French, f - Mangawhero River) neither species shows a significant volcanic response, indicating that the change in conditions following an eruption is not sufficient to be recorded. At the remaining three sites, significant responses are recorded by one or both species. Both pink pine and cedar recorded significant negative volcanic responses at Takapari (c), with a significantly larger response from cedar (Mann-Whitney U-test, $p < 0.05$). At Ahaura and Flagstaff Creek, only cedar recorded a significant positive growth response compared to a neutral silver pine response. At both these sites, the difference between the species' response is significant (Mann-Whitney U-test, $p < 0.001$; d-e).

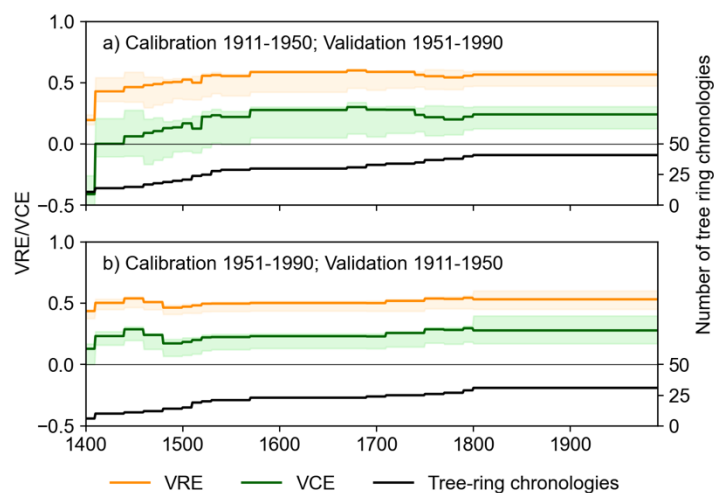


Figure C-9 Verification statistics for the NZall temperature reconstruction: using a) the early calibration window and b) the late calibration window. The 90% uncertainty interval around the verification period reduction of error (VRE; orange) and verification period coefficient of efficiency (VCE; green) were calculated from 300 maximum entropy bootstrap replications. The secondary axis shows the number of tree-ring chronologies contributing to the reconstruction over time.

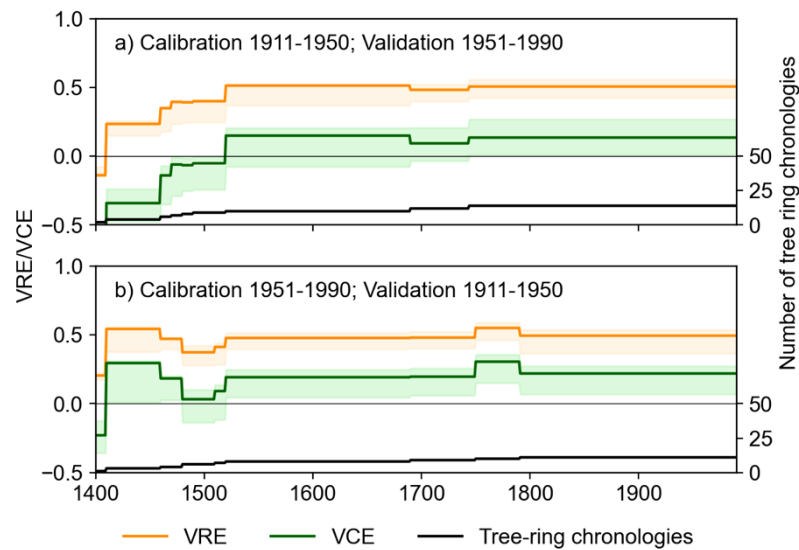


Figure C-10 Verification statistics for the NZsens temperature reconstruction: a) using the early calibration window and b) using the late calibration window. The 90% uncertainty interval around the verification period reduction of error (VRE; orange) and verification period coefficient of efficiency (VCE; green) were calculated from 300 maximum entropy bootstrap replications. The secondary axis shows the number of tree-ring chronologies contributing to the reconstruction over time.

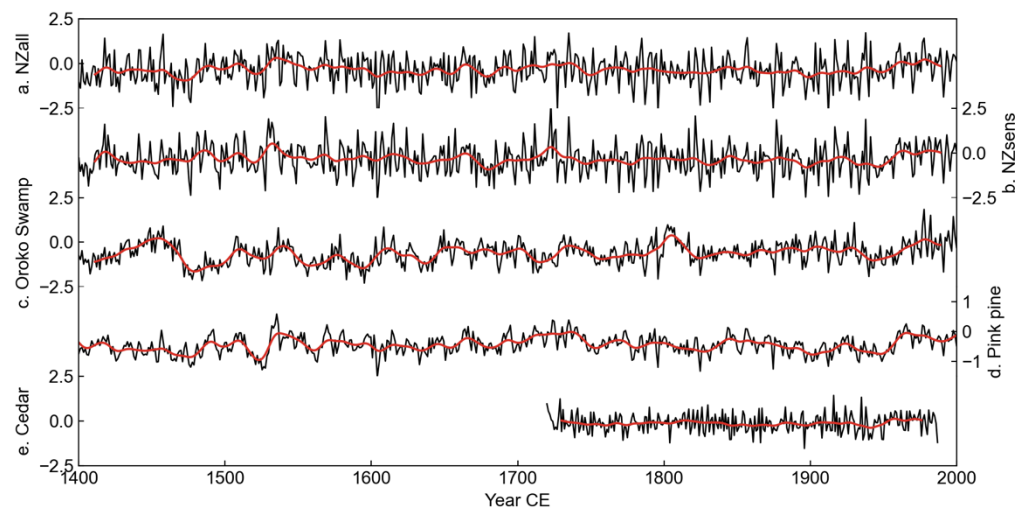


Figure C-11 New Zealand summer temperature reconstructions: a, b) DJF New Zealand average temperatures (this study) for all (a) and sensitive chronologies (b); c) January-March temperature at Hokitika, Westland, based on Oroko Swamp silver pine (Cook et al., 2002); d) Annual average New Zealand temperature based on pink pine chronologies (Duncan et al., 2010); e) February-March average New Zealand temperature based on cedar chronologies (Palmer & Xiong, 2004). Reconstructed temperature is shown in black, and the 20-year filtered series is in red. All series were transformed into anomalies using a baseline of reconstructed temperature over 1961-1990, except for the pink pine reconstruction which was calibrated directly against instrumental temperature anomalies for the same period and therefore not transformed.

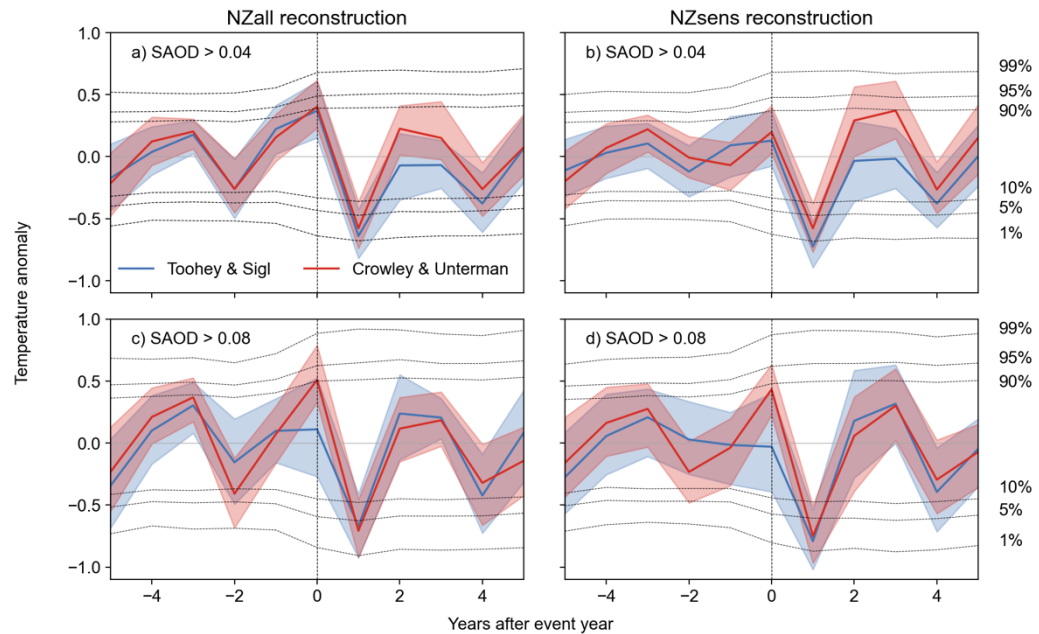


Figure C-12 Comparison of SEA analysis of the NZall and NZsens temperature reconstructions use two sets of volcanic event years (Table C-3): a) the ice core analysis of Toohey and Sigl (2017) using a regional threshold of SAOD > 0.04 or 0.08 averaged over the New Zealand latitudinal range (30–50°S), and b) the ice core analysis of Crowley and Unterman (2013) using a threshold of SAOD > 0.04 or 0.08 averaged over the Southern Hemisphere (0–90°S). Both datasets show that the New Zealand temperature reconstructions significantly respond to volcanic events in year t+1. However, there are some differences, most notably a larger response to the Toohey & Sigl event list in b). There are also some issues with the compositing in c), with values in the normalisation period not close to 0, and the volcanic response of NZall is not significant at $p < 0.05$ when tested against the event list of Crowley and Unterman (2013).

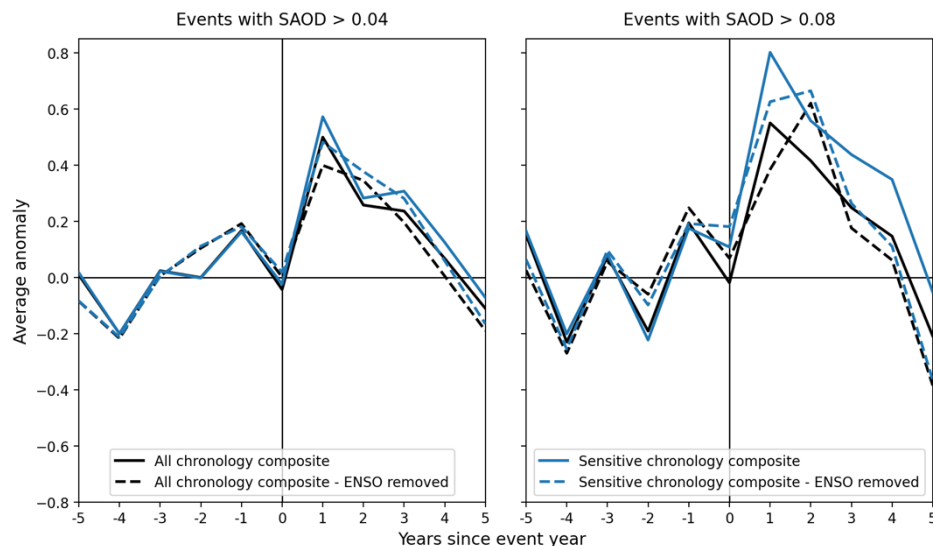


Figure C-13 Impact of removing volcanic events occurring simultaneously with a known El Niño event (1902, 1963, and 1982) from the key event list on the SEA results for kauri. All results are significant in year t+1 except for the ‘All chronology composite’ for the events with SAOD > 0.08 after the known El Niño events are removed ($n = 10$). For this series, only the t+2 anomaly is significant.

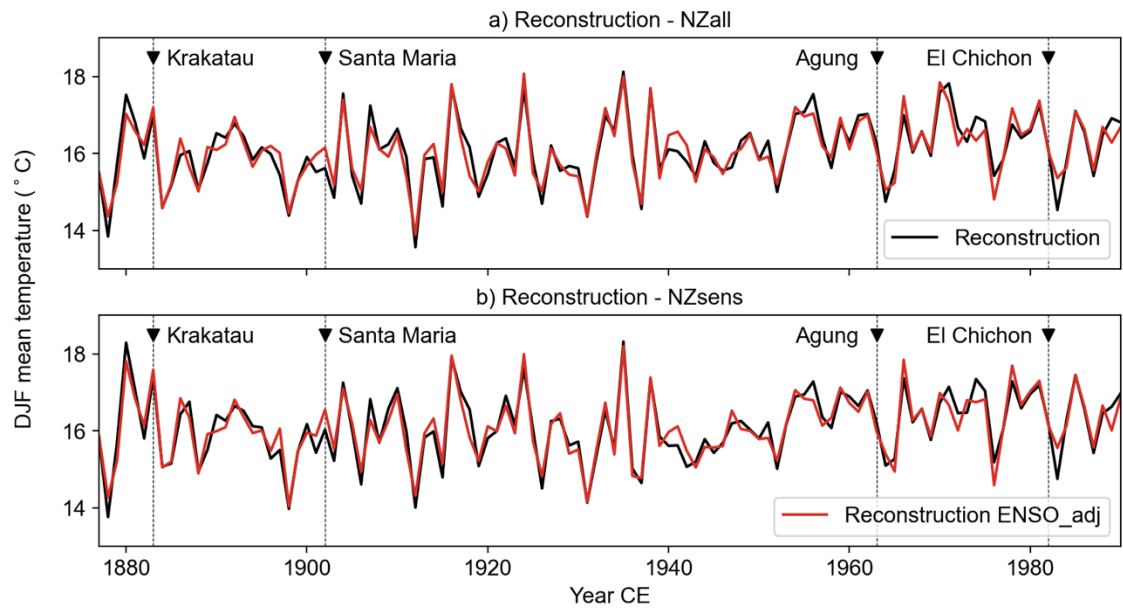


Figure C-14 Reconstructed temperatures in black and the same data with ENSO removed in red for a) reconstruction NZall and b) reconstruction NZsens. The eruption years for the four large volcanic eruptions occurring during the period for which instrumental ENSO indices are available (Southern Oscillation Index; 1778 CE to present) are also shown.

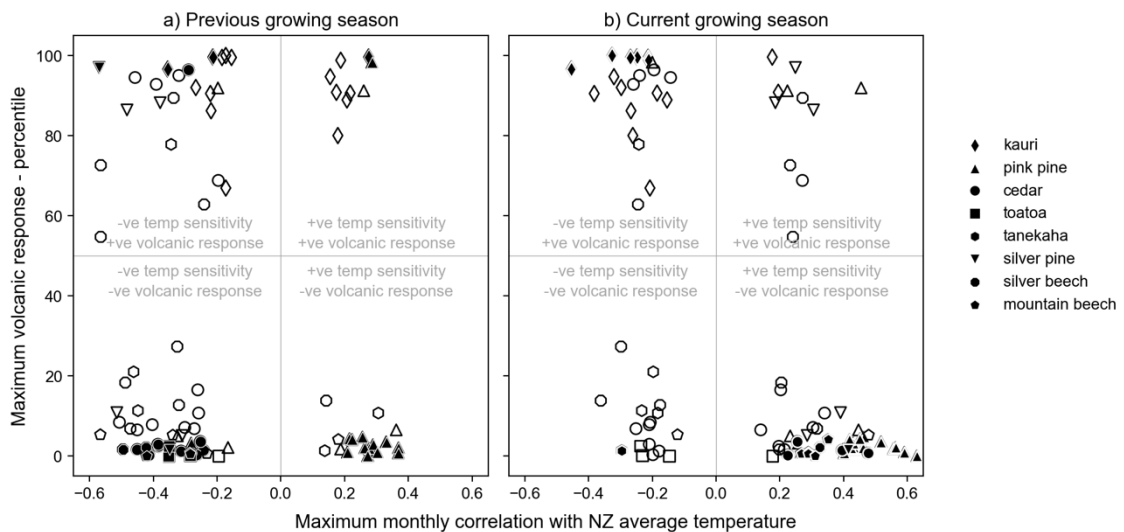


Figure C-15 Summary of the relationship between sensitivity to temperature and magnitude of the volcanic response for the eight species. Left: maximum temperature correlation in any month of the prior growing season against maximum volcanic response in the five years following an eruption for the 13 largest events. Right: Same plot but for the current growing season. Filled markers indicate that a site has a significant temperature correlation ($p < 0.05$) and a significant volcanic response ($< 5\text{th}$ or $> 95\text{th}$ percentile of bootstrapped responses). Open markers are not significant for either the temperature or volcanic response, or both.

Table C-1 Meta data for New Zealand chronologies used in the analysis.

Site	Species	Start	End	Longitude	Latitude	Altitude (m asl)	ITRDB Code	Notes
1CAS	AGAU	1559	1982	-36.88	174.53	180	newz082	Cascades
1HID	AGAU	1679	2002	-36.20	175.43	220	newz083	Hidden Valley
1HUI	AGAU	1720	1981	-36.97	174.57	274	newz085	Huia
1HUP	AGAU	1483	1997	-36.82	174.50	90	newz084	Huapai
1KAT	AGAU	1698	1996	-37.60	175.87	350	newz091	Katikati
1KAW	AGAU	1710	1996	-37.92	174.92	80	newz087	Kawhia
1KON	AGAU	1770	1976	-37.07	175.13	335	newz008	Konini Forks Little Barrier Island
1LTB	AGAU	1790	1981	-36.20	175.13	274	newz086	Island
1MAS	AGAU	1269	1998	-36.90	175.55	350	newz088	Manaia Sanctuary
1MOE	AGAU	1360	1980	-36.53	175.55	630	newz089	Mount Mochau
1MWL	AGAU	1580	1981	-37.22	175.03	350	newz090	Mount William
1PBL	AGAU	1675	1981	-35.18	173.75	305	newz078	Puketi Bluff
1PKF	AGAU	1504	2002	-35.27	173.73	290	newz079	Puketi Forest Trounson Kauri Park
1TRO	AGAU	1408	2002	-35.72	173.65	175	2	
1WFD	AGAU	1628	1903	-35.65	173.57	180	newz022	Waipoua Forest
1WWF	AGAU	1462	2002	-35.37	173.28	468	newz081	Warawara Plateau
2BON	HABI	1463	1999	-43.08	170.65	850	1	Mount Bonar
2CCP	HABI	1410	1998	-42.72	171.57	970	1	Camp Creek
2CRS	HABI	1483	1999	-42.28	171.38	900	1	Croesus Track Doughboy - Adams Hill
2DBY	HABI	1457	2010	-47.03	167.72	100	newz118	
2ELD	HABI	1338	1999	-45.75	167.47	750	1	Eldrig Peak
2GLS	HABI	1461	1999	-41.62	172.03	950	1	Mount Glasgow Hellfire Ruggedy Mt
2HEL	HABI	1407	2013	-46.98	167.75	100	newz119	
2MAP	HABI	1567	1976	-45.53	167.30	305	newz010	Manapouri Dam
2MAT	HABI	1508	1999	-41.57	172.32	1060	1	Matiri Range
2MEL	HABI	1440	1999	-42.50	171.83	1050	1	Mount Elliot
2MGR	HABI	1400	1999	-42.95	170.82	865	1	Mount Greenland
2MTF	HABI	1367	1999	-42.67	171.33	750	1	Mount French
2OMO	HABI	1578	1999	-43.40	170.10	320	1	Omoeroa Saddle Pegasus Stewart Island
2PEG	HABI	1667	1991	-46.92	167.73	450	2	
2PUT	HABI	1646	1993	-40.67	175.52	650	newz010	Putara
2SPD	HABI	1447	1999	-46.37	169.05	560	1	Slopedown Hill
2TKG	HABI	1450	1999	-42.65	171.50	950	1	Mount Tekinga
2TKP	HABI	1708	1995	-40.08	176.00	800	NEWZ076	Takapari
2TOS	HABI	1590	1998	-42.98	170.85	210	1	Totara Saddle
3AHA	LACO	1209	2000	-42.38	171.80	244	newz005	Ahaura
3FLG	LACO	1230	2003	-42.50	171.72	200	newz120	Flagstaff Creek

Site	Species	Start	End	Longitude	Latitude	Altitude (m asl)	ITRDB Code	Notes
3MWO	LACO	1464	1976	-39.35	175.48	1000	newz011	Mangawhero River Bridge
3ORO	LACO	470	1999	-43.23	170.28	110	newz121	Oroko Swamp
3SWF	LACO	1130	1969	-43.13	170.40	200	newz122	Saltwater Forest
4AHA	LIBI	1303	2009	-42.38	171.80	244	newz127	Ahaura Armstrong Reserve
4ARM	LIBI	1446	1958	-43.83	173.00	731	newz007	Reserve
4CCC	LIBI	1064	2010	-42.72	171.57	965	newz124	Camp Creek
4CLW	LIBI	1450	1991	-39.63	176.10	1220	newz064	Clearwater
4CRG	LIBI	1492	2010	-45.83	170.53	576	newz128	Mount Cargill
4CRK	LIBI	1460	1978	-43.08	170.98	800	newz039	Cream Creek
4EMT	LIBI	1616	1990	-39.25	174.08	1050	newz003	Mount Egmont
4FLG	LIBI	1464	2004	-42.50	171.72	200	newz125	Flagstaff Creek
4FLH	LIBI	1683	1991	-41.27	172.60	950	newz065	Flanagans Hut
4HIT	LIBI	1431	1991	-39.53	175.73	976	newz066	Hihitahi
4MOA	LIBI	1490	1991	-40.93	172.93	1036	newz067	Moa Park
4MTF	LIBI	1330	1999	-42.67	171.33	855	newz126	Mount French Mangawhero River Bridge
4MWO	LIBI	1662	1976	-39.35	175.48	1000	newz012	River Bridge
4NET	LIBI	1625	1990	-39.28	174.10	991	newz014	North Egmont
4OHT	LIBI	1585	1991	-39.62	176.12	1140	newz068	Ohutu Ridge
4OKA	LIBI	1732	1976	-46.38	169.45	305	newz016	Owaka
4RAH	LIBI	1480	2012	-42.32	172.12	672	newz129	Rahu Saddle
4RUC	LIBI	1473	1991	-39.63	176.18	1200	newz069	Ruahine Corner Stratford side - East Egmont
4STR	LIBI	1626	1990	-39.32	174.12	860	newz071	East Egmont
4TKP	LIBI	1256	1992	-40.07	175.98	838	newz062	Takapari Road Hauhangatahi Site A
4TOA	LIBI	1511	1992	-39.23	175.43	1160	newz072	Hauhangatahi Site B
4TOB	LIBI	1332	1992	-39.23	175.43	1100	newz073	Hauhangatahi Site C
4TOC	LIBI	1213	1992	-39.23	175.43	1000	newz074	
4TRK	LIBI	1526	1978	-43.08	170.97	925	newz055	Tarkus Knob
4UWR	LIBI	1140	1992	-38.68	177.20	854	newz063	Urewera
4WBF	LIBI	1674	1992	-43.07	171.28	780	newz075	Wilberforce
5BOR	NOME	1389	2007	-45.78	167.37	200	2	Borland
5KEA	NOME	1580	1980	-43.87	169.78	1150	newz036	Kea Flat
5LKE	NOME	1676	1980	-45.25	167.48	950	newz048	Lake Eyles
5LKO	NOME	1584	1980	-45.30	167.68	1000	newz051	Lake Orbell Upper Hollyford Valley
5UHV	NOME	1710	1980	-44.77	168.00	950	newz033	Upper Takahe Valley
5UTV	NOME	1622	1979	-45.20	167.65	1000	newz054	
6GHC	NOSO	1795	2006	-43.25	171.75	870	newz046	Ghost Creek
6HDC	NOSO	1730	1979	-43.13	171.60	1350	newz037	Hidden Creek

Site	Species	Start	End	Longitude	Latitude	Altitude (m asl)	ITRDB Code	Notes
6LCV	NOSO	1730	1979	-43.08	171.72	1350	newz035	Lower Cass Valley
6LGH	NOSO	1740	1979	-43.08	171.70	1400	newz031	Logos Hill
6LGS	NOSO	1760	1979	-43.05	171.60	1300	newz024	Lagoon Saddle
6LKP	NOSO	1713	2006	-43.12	171.78	970	newz049	Lake Pearson
6MKW	NOME	1730	1979	-43.05	171.68	1275	newz023	Mirkwood
6RTC	NOSO	1787	2006	-43.15	171.80	950	newz052	Rata Creek
6SSS	NOSO	1760	1979	-43.05	171.72	1250	newz030	Snowslide Stream
6TKV	NOSO	1630	1979	-45.30	167.68	1100	newz031	Takahe Valley
6TST	NOSO	1840	1979	-45.28	167.65	1000	newz032	Takahe Stream
6WND	NOSO	1760	2006	-43.08	171.58	1350	newz053	Windy Creek
7PLC	PHAL	1717	2015	-42.90	171.57	915	newz130	Pegleg Creek Waimanoa Ecological Reserve
8WER	PHGL	1740	1976	-38.57	175.70	518	newz020	Waihora Stream
8WHS	PHGL	1550	1986	-38.65	175.63	780	newz056	Lake Waikareiti
8WKT	PHGL	1535	1976	-38.70	177.20	853	newz009	Waipoua Forest
8WPA	PHGL	1585	1976	-35.68	173.55	244	newz022	Okiwi
9OWI	PHTR	1709	1976	-41.12	173.67	15	newz015	Paparoa
9PAP	PHTR	1779	1975	-36.12	174.25	160	newz001	Waihaha Terrace
9WHH	PHTR	1613	1986	-38.70	175.60	575	newz058	Waihora Lagoon
9WHL	PHTR	1650	1985	-38.65	175.67	640	newz057	Waiomu
9WMU	PHTR	1664	1976	-37.03	175.53	61	newz021	Kauri network
1Kauri	AGAU	0	2002	na	na	na	2	Pink pine network
2Pink	HABI	1400	1999	na	na	na	2	South Island silver pine
3Silver	LACO	0	2003	na	na	na	2	

1 <https://researcharchive.lincoln.ac.nz/handle/10182/2141>

2 Private collection

Table C-2 Details of volcanic eruptions between 1400 and 1990 CE selected using the two thresholds of modelled SAOD over New Zealand (> 0.04 or > 0.08), and prior and secondary eruptions with $SAOD > 0.01$. Eruptions within 5 years prior of the target eruption were removed and the baseline period selected as the closest non-volcanically disturbed period. Secondary eruptions occurring within 5 years of the target eruption were also removed prior to averaging the SEA ensemble (Büntgen et al., 2020).

Eruption date (month/year)	Eruption	Locality	Latitude	SAOD threshold	Prior Eruption	Secondary Eruption
1452	Unknown		16.8°S	> 0.04	1448 (-4)	1457 (+5)
1457	Unknown			> 0.08	1452 (-5)	
2/1477	Bárðarbunga	Iceland	64.6°N	> 0.04		
1595	Unknown			> 0.08	1590 (-5)	1600 (+5)
2/1600	Huaynaputina	Peru	16.6°S	> 0.08	1595 (-5)	
1620	Unknown			> 0.04		
†12/1640	Parker	Philippines	6.1°N	> 0.08		
1653	Unknown			> 0.04		
1673	Gamkonora	Japan	1.4°N	> 0.04		
1694	Unknown			> 0.08		
1761	Unknown			> 0.04		
5/1783	Grímsvötn	Iceland	64.4°N	> 0.08		
	Asama	Japan	36.4°N			
1809	Unknown			> 0.08		
4/1815	Tambora	Sundas	8.3°S	> 0.08		
1831	Unknown*	Philippines	19.5°N	> 0.04		1835 (+4)
1/1835	Cosigüina	Nicaragua	13.0°N	> 0.08	1831 (-4)	
†12/1861	Makian		0.3°N	> 0.04		
8/1883	Krakatau	Indonesia	6.1°S	> 0.08		1886 (+3)
10/1902	Santa Maria	Guatemala	14.8°N	not modelled		
3/1963	Agung	Bali	8.3°S	not modelled		
3/1982	El Chicon	México	17.4°N	not modelled		

†Eruptions occurring in December were assigned an eruption year of year+1 in the superposed epoch analysis event list for consistency with the designation of years in the temperature reconstruction (reconstruction year 1641 is Dec 1640 – Feb 1641).

* Location is disputed (Garrison et al., 2018).

Table C-3 Comparison of volcanic event years between 1400 and 1990 CE selected using two different datasets: a) the ice core analysis of Toohey and Sigl (2017) using a regional threshold of SAOD > 0.04 or 0.08 averaged over the New Zealand latitudinal range (30-50°S), and b) the ice core analysis of Crowley and Unterman (2012) using a threshold of SAOD > 0.04 or 0.08 averaged over the Southern Hemisphere (0-90°S). Event selection between the two datasets is largely consistent. Potential reasons for the differences, including the underlying ice core data and differences in methodology, are discussed by Toohey & Sigl (2017).

Eruption date (month/year)	Eruption	Toohey & Sigl threshold	Crowley & Unterman threshold
1441	Unknown	<i>Not selected</i>	> 0.04
1452	Unknown	> 0.04	<i>Not selected</i>
1457	Unknown	> 0.08	> 0.08
2/1477	Bárðarbunga	> 0.04	> 0.08
1588	Unknown	<i>Not selected</i>	> 0.04
1595	Unknown	> 0.08	> 0.08
2/1600	Huaynaputina	> 0.08	> 0.08
1620	Unknown	> 0.04	> 0.04
12/1640	Parker	> 0.08	> 0.08
1653	Unknown	> 0.04	<i>Not selected</i>
1673	Gamkonora	> 0.04	> 0.08
1694	Unknown	> 0.08	> 0.08
1761	Unknown	> 0.04	<i>Not selected</i>
5/1783	Grímsvötn Asama	> 0.08	<i>Not selected</i>
1804	Unknown	<i>Not selected</i>	> 0.04
1809	Unknown	> 0.08	> 0.08
4/1815	Tambora	> 0.08	> 0.08
1831	Unknown*	> 0.04	<i>Not selected</i>
1/1835	Cosigüina	> 0.08	> 0.08
12/1861	Makian	> 0.04	> 0.04
8/1883	Krakatau	> 0.08	> 0.08
10/1902	Santa Maria	not modelled	> 0.04
3/1963	Agung	not modelled	> 0.08
3/1982	El Chicon	not modelled	> 0.04

Table C-4 Coupled Model Intercomparison Project 5 (CMIP5) models used in the analysis.

Model	No. of Ens.	Solar	Volcanic	GHG	Land Use	Reference
GISS-E2-R 121	1	Steinhilber et al	Crowley & Unterman (2013)	Schmidt et al. (2012)	Pongratz et al. (2008)	Schmidt et al. (2014)
GISS-E2-R 124	1	Viera et al. (2011)	Crowley & Unterman (2013)	Schmidt et al. (2012)	Pongratz et al. (2008)	Schmidt et al. (2014)
GISS-E2-R 127	1	Viera et al. (2011)	Crowley & Unterman (2013)	Schmidt et al. (2012)	Kaplan et al. (2010)	Schmidt et al. (2014)
FGOALS-gl	1	Crowley (2000)	Crowley (2000)	Amman et al. (2007)	-	Guo and Zhou (2013)
MRI-CGCM3	1	Delaygue & Bard (2011) + Wang et al. (2005)	Gao et al. (2008)	Schmidt et al. (2012)	-	Yukimoto et al. (2012)
MPI-ESM-P	3	Viera et al. (2011)	Crowley & Unterman (2013)	Schmidt et al. (2012)	Pongratz et al. (2008)	Jungclaus et al. (2014)
MIROC-ESM	1	Delaygue & Bard (2011) + Wang et al. (2005)	Crowley et al. (2008)	Schmidt et al. (2012)	-	Sueyoshi et al. (2013)

Table C-5 Pearson correlations between New Zealand summer temperature reconstructions over the common reconstruction interval (1720-1987 CE): a, b) DJF New Zealand average temperatures (this study) for (a) all and (b) sensitive chronologies; c) January-March temperature at Hokitika, Westland, based on Oroko Swamp silver pine (Cook et al., 2002); d) Annual average New Zealand temperature based on pink pine chronologies (Duncan et al., 2010); e) February-March average New Zealand temperature based on cedar chronologies (Palmer & Xiong, 2004). All correlations are significant at $p < 0.001$ except for pink pine and cedar, which are not significantly correlated.

	NZall	NZsens	Oroko Swamp	Pink pine
a. NZall	-	0.83	0.44	0.62
b. NZsens	0.83	-	0.33	0.52
c. Oroko Swamp	0.44	0.33	-	0.23
d. Pink pine	0.62	0.52	0.23	-
e. Cedar	0.36	0.52	0.36	0.06

Appendix D. Supplementary information for Chapter 5

Introduction

Here we provide a detailed description of the methods used in the development of the Daly catchment streamflow reconstruction as well as additional results.

Contents of this file

- Text D1 to D5
- Figures D1 to D12
- Table D1

D1. Methodological framework

A step-by-step schematic of our streamflow reconstruction approach is illustrated in Figure 5-3 in the main manuscript. Based on a network of hydroclimate-sensitive tree-ring chronologies we reconstructed streamflow at four gauges in the Daly catchment over the past 592 years using a Bayesian hierarchical regression model with a novel predictor variance transform. This section explains the methodology in detail and discusses the methodological choices and data limitations.

D2. Data preparation

D2.1 Daly River streamflow

For the Daly River at Mount Nancar, the gauge nearest to the catchment outlet, the time series was extended from 1961 to 1971 using data from two nearby gauges and a linear regression model. Daily streamflow data from Gauge G8140041 Daly River at Gourley, approximately 12 km upstream, and gauge G8140003, Daly River at Police Station, approximately 7 km downstream, were used to infill missing daily values from the Mount Nancar gauge (Figure D-1). Values from Gourley were used in preference when data from both G8140041 and G8140003 were available. Years missing more than 15% of daily values during wet season months across all three gauges were discarded.

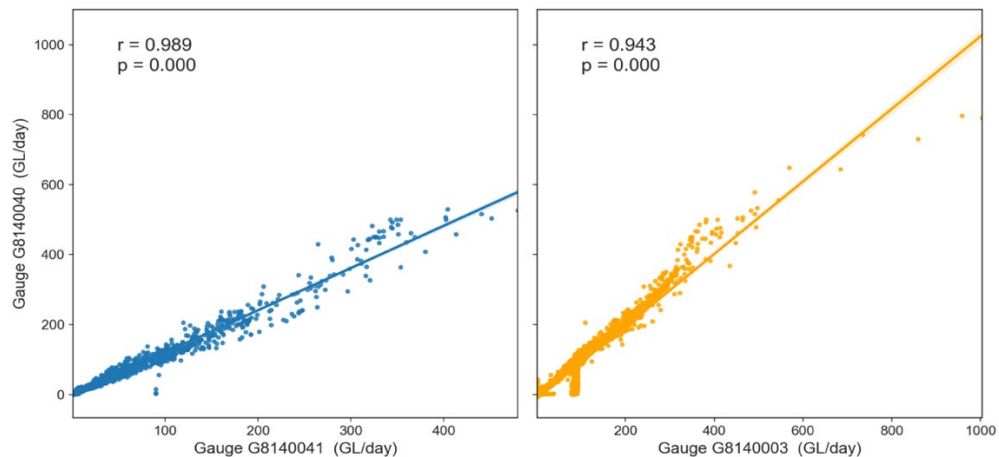


Figure D-1 Relationship between daily discharge at gauge G8140040 Mount Nancar and G8140041 Gourley (left), and G8140003 Police Station (right).

For the remaining gauges, gap-filled daily streamflow data was downloaded from the Australian Bureau of Meteorology (BOM) Hydrologic Reference Stations database. Water year (September to August) streamflow was calculated from the daily data. Figure D-2 shows that streamflow is highly correlated across the four gauges.

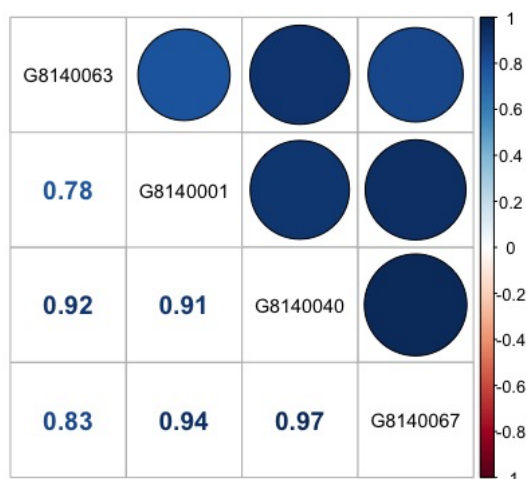


Figure D-2 Water year streamflow correlation between the four gauges in the Daly catchment (1959-2018): Douglas River downstream of the Old Douglas Homestead (G8140063), Katherine River at Railway Bridge (G8140001), Daly River at Mount Nancarrow (G8140040), and Daly River upstream of Dorisvale Crossing (G8140067).

There is a decreasing trend in average annual rainfall from northwest to southeast across the Daly catchment. The relationship between Daly catchment average water year rainfall and water year streamflow at each of the four gauges over the 1959-2018 period is shown in Figure D-3. The correlation with rainfall increases moving toward the catchment mouth as a greater proportion of the catchment contributes to streamflow.

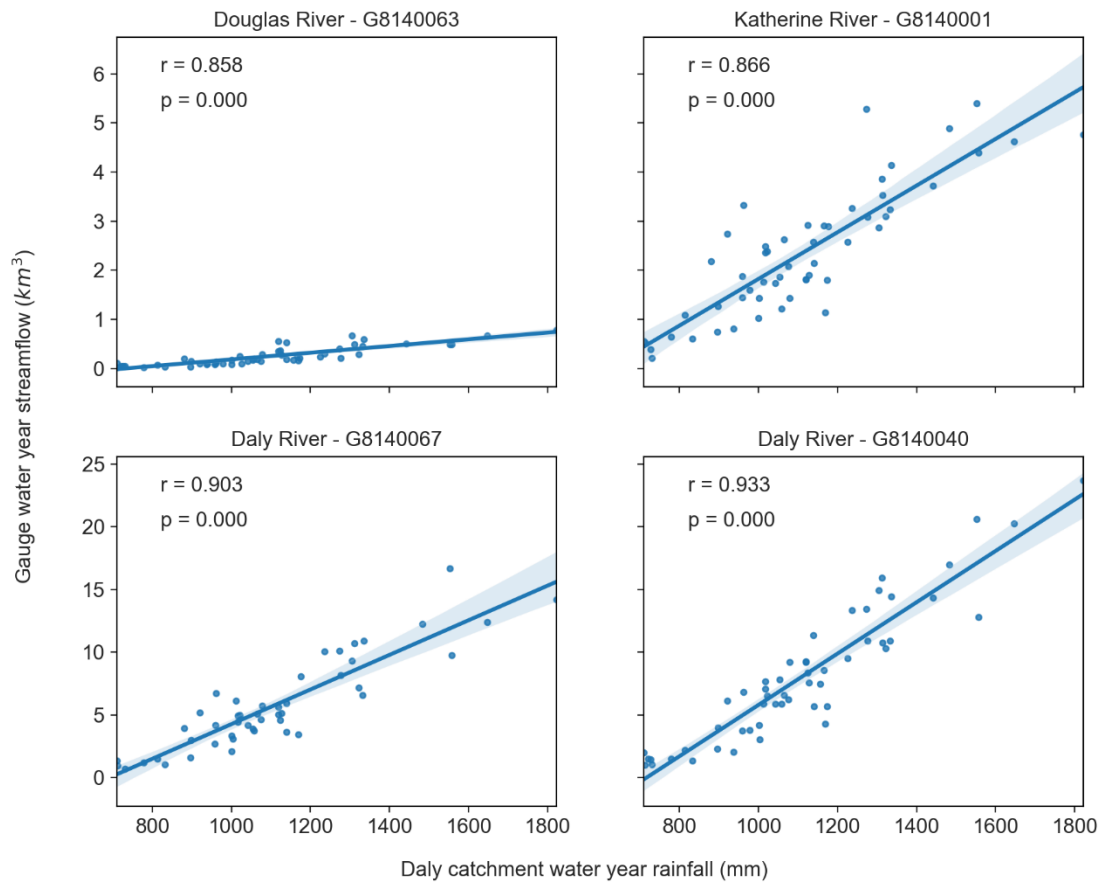


Figure D-3 Relationship between Daly catchment average water year rainfall and water year streamflow at the four gauges in the Daly catchment (1959-2018).

D2.2 Proxy network

Remote proxies were selected from a network of 595 precipitation-sensitive tree-ring chronologies underlying two recently published drought atlases - the Eastern Australia and New Zealand Drought Atlas (Palmer et al., 2015) and the Monsoon Asia Drought Atlas (Cook et al., 2010) – which together encompass the monsoon Asia and Indo-Australian monsoon regions. The end date of the streamflow reconstruction was chosen to maximise both the number of available chronologies and the length of the overlapping data period. Only the 186 chronologies ending at or after streamflow year 2005 were retained for the initial predictor pool (Figure D-4), first accounting for the Schulman shift, in which Southern Hemisphere chronologies are dated based on the year in which the growing season starts (i.e., chronology year 2004 is equal to water year 2005).

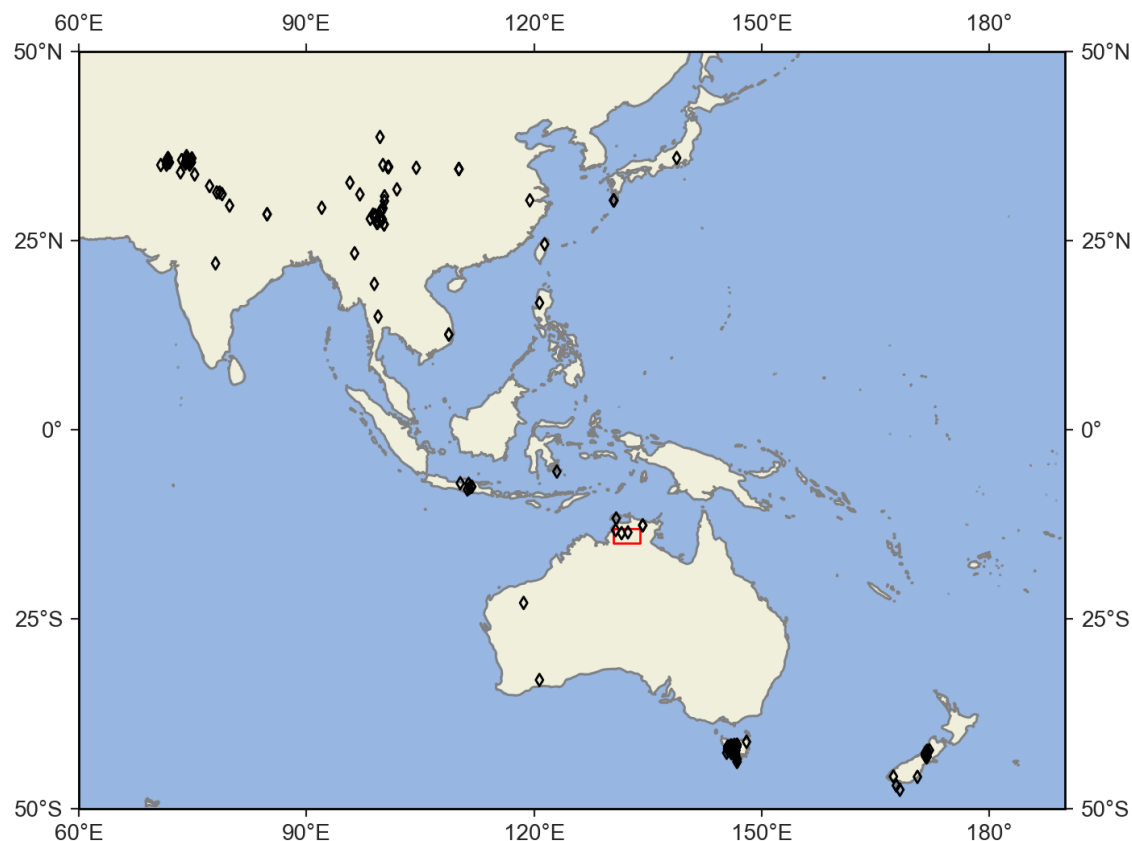


Figure D-4 Distribution of the initial predictor pool of 186 precipitation-sensitive tree ring chronologies (black diamonds) with the approximate extent of the Daly catchment indicated by the red box.

D3. Detailed methods

D3.1 Predictor transformation

For the first time in a paleohydrologic application, we applied a wavelet-based approach (Jiang et al., 2021, 2020) to transform the tree-ring chronologies before reconstruction. In this approach, a unique variance transform is applied to each predictor variable in a predictor suite, transforming their spectral properties to better match the spectral properties of the response variable. This approach mathematically optimises the predictor-predictand match, which improves the modelling of hydroclimatic variables (Jiang et al., 2021). We hypothesise that transforming tree-ring chronologies in the spectral domain will improve the historical prediction of streamflow by maximizing the useful information extracted from multiple noisy proxies predominantly remote from the target catchment.

The Wavelet System Prediction (WASP) R-package (Jiang et al., 2021) was used to calculate a unique variance transformation for each tree-ring chronology, modifying its spectral characteristics to match Daly catchment average annual rainfall. The spectral decomposition of both rainfall and streamflow (Figure D-5) shows that rainfall is a suitable proxy for streamflow to use as a spectral target, and as the rainfall data is much longer than streamflow allows for

greater decomposition of the data. Using catchment-average rainfall also ensures streamflow data later used to verify the model remains independent.

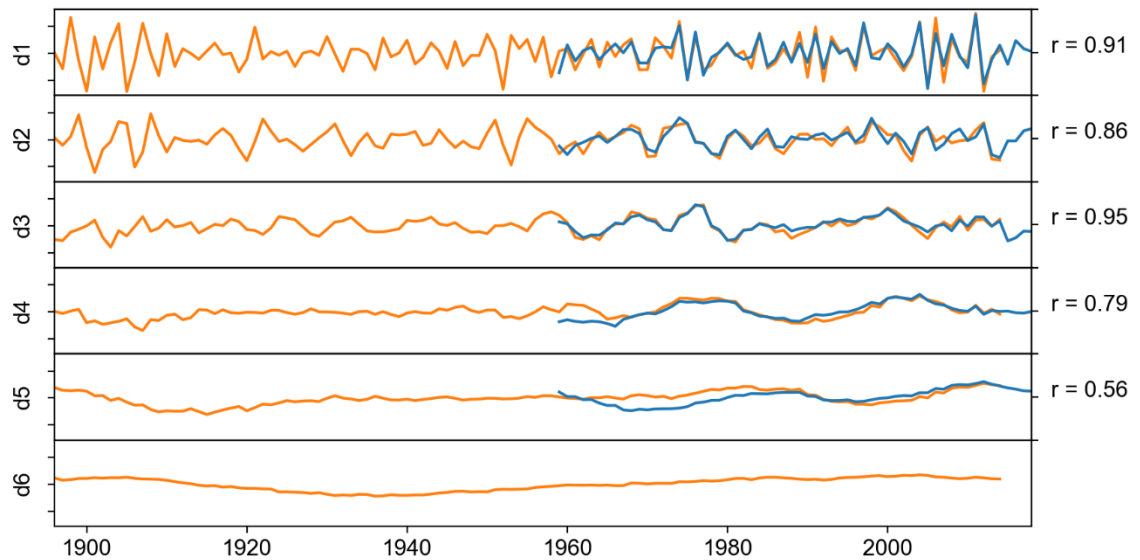


Figure D-5 Comparison between Daly catchment average rainfall (orange) and streamflow at gauge G8140040 (blue) both decomposed using the maximal overlap direct wavelet transform with a Haar wavelet filter and maximum decomposition level $J=6$ and $J=5$ respectively. All correlations are significant at $p < 0.01$. Missing years in the Daly River streamflow record were filled using gap-filled daily streamflow data from the Australian Bureau of Meteorology.

Each tree-ring chronology X_i was decomposed into a matrix of wavelet and scaling coefficients using the maximal overlap direct wavelet transform with a Haar wavelet filter. The decomposition level selected, $J = 6$, is the maximum possible decomposition level based on the constraint of the length of the rainfall data (102 years before 2005). At the maximum level, the number of data after the last subsampling becomes smaller than the wavelet filter length (Jiang et al., 2020). The transformed chronology X_i' was then obtained by redistributing the variance in its spectrum based on the covariance between the coefficients matrix and the rainfall time series (Figure D-6). See Jiang et al. (2020) for the full derivation of the algorithm.

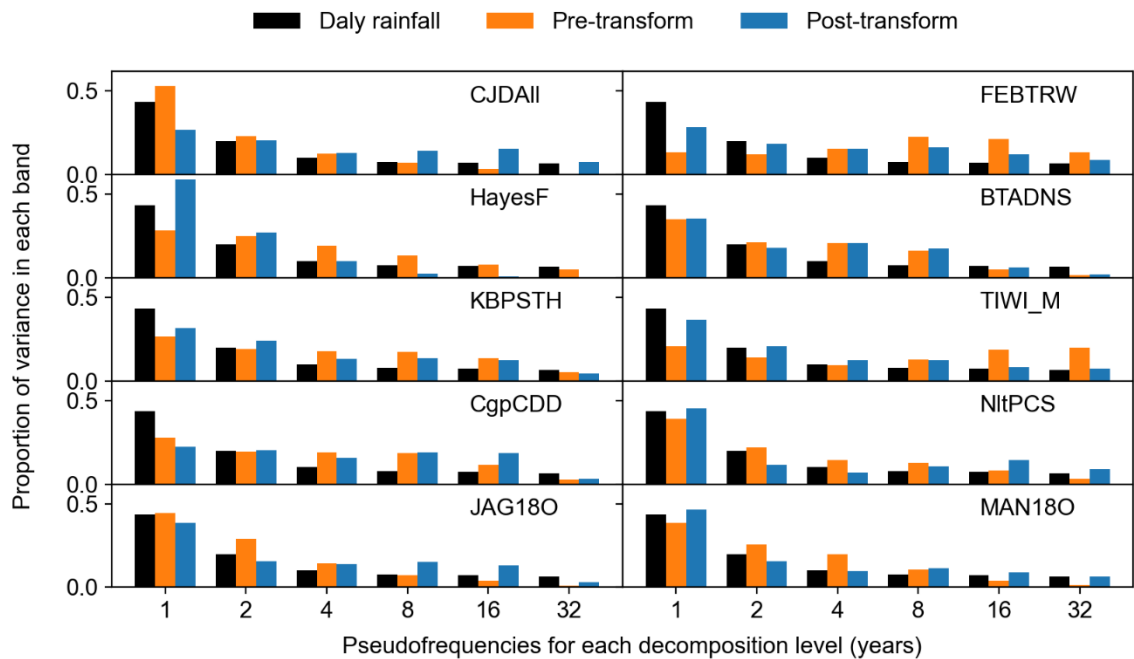


Figure D-6 Proportion of variance in each decomposition level before (orange) and after (blue) variance transformation for ten tree-ring chronologies used in the final model, and the proportion of variance in the Daly catchment-average rainfall series used as the transformation target (black). Tree-ring chronologies representative of the variance transform procedure, and which cover the geographical distribution of the proxy set, were selected for display.

As the maximum decomposition is 32 years, all chronologies were filtered with a 100-year spline that retains 50% variance at frequencies greater than 100 years before variance transformation, retaining the high-to-medium frequency information which can be extracted from a rainfall time-series of length ~100 years. Maximizing long-term variability in tree-ring chronologies is desirable to produce reconstructions that accurately capture low-frequency variability; however, we cannot calibrate the low-frequency information contained in the tree rings based on the much shorter rainfall time series. This is the major drawback of the variance transform methodology for paleohydrologic applications. Future work will focus on addressing this deficiency so that low-frequency information can be retained.

D3.2 Selection of predictors for the model

Variance transformed tree-ring chronologies were initially retained for inclusion in the model if they passed a $p < 0.1$ correlation threshold for at least three of the four streamflow gauges. Principal component analysis was used to reduce the dimensionality of the data, and the number of free parameters to be estimated, with the principal component (PC) scores used as model predictors rather than the variance transformed tree-ring chronologies directly. One decision to be made when undertaking principal components regression is the number of PCs to retain. Often, this decision is based on a cutoff determined by either the eigenvalue (e.g., all eigenvectors with eigenvalues > 1) or a percentage of the explained variance (e.g., 80%), due to the belief that components with small variances are of little use in predicting variations in the dependent variable

(Artigue & Smith, 2019). However, as the eigenvector weights depend solely on the correlations among the explanatory variables and not the dependent variable (Artigue & Smith, 2019), arbitrary cut-off values may discard PCs highly correlated with the predicted variable, while retaining uncorrelated PCs (Hadi & Ling, 1998).

Here, we employed the partial information correlation (PIC; (Sharma & Mehrotra, 2014)) as an alternative method to decide which PCs to retain for the final model. Only significant PCs were retained, where significance was determined based on the PIC between measured streamflow and the candidate PCs with a significance level of $p < 0.01$. After selecting the initial PC predictor, the PIC algorithm (Sharma et al., 2016) selects additional PCs based on their ability to characterise the residual streamflow information after accounting for the effect of the pre-selected PCs. The choice of the significance level is still a somewhat arbitrary decision, as is the choice of the initial correlation threshold. Both thresholds were selected via trial and error and represent a balance between maximizing the useful information from the tree rings (assessed via model calibration-validation statistics) while decreasing model noise (assessed via the ensemble spread).

D3.3 Ensemble modelling approach

We used a nested reconstruction approach in which the initial model was based on all the tree-ring predictors with shorter tree-ring series sequentially dropped and a new model developed for the remaining predictors (a predictor ‘nest’). The nest was dropped, and no further nests added if less than two significant principal components were retained as model predictors. The reconstructions for each nest were scaled to the variance of the calibration period and appended to the initial nest to create the longest possible reconstruction. The final reconstruction incorporates 14 nests and covers the period from 1413 to 2005 CE.

We used a weighted ensemble method (Cook et al., 2010) to produce the reconstruction. The ensemble method explicitly incorporates the covariance between streamflow and the tree-ring series, while acknowledging that noise in the data means there is no optimal correlation threshold for the inclusion of a tree-ring predictor in the model. Each weighted ensemble was created by multiplying the variance transformed tree-ring predictors by a power of their correlation with the streamflow data during the calibration period prior to principal component analysis. The weighting took the form r^w where w ranged from 0.0 to 2.0 (0.0, 0.1, 0.25, 0.5, 0.67, 1.0, 1.25, 1.5, 1.75, 2.0). As w increases, predictors highly correlated with streamflow are given progressively more weight in the principal component analysis.

D3.4 Hierarchical Bayesian model

We used a Bayesian hierarchical regression model with partial pooling (Devineni et al., 2013; Rao et al., 2018) as our reconstruction method due to its ability to handle both short data records and data gaps. Annual streamflow is not normally distributed (Shapiro-Wilk normality test $p <$

0.05), therefore we power-transformed the data prior to modelling with an exponent of 0.425 to ensure minimal skew. As streamflow is highly correlated across the gauges (Figure D-2), we modelled the regression coefficients by drawing them from a common multivariate normal distribution (MVN). By sharing information across the gauges, the partial pooling framework can result in lower uncertainty in estimated parameters and reconstructed discharge, as well as improved final model skill (Devineni et al., 2013).

In the model described below, streamflow y at each gauge i in year t was based on multiple linear regression of the predictor vector X_t :

$$y_{i,t} | \alpha_i \beta_i = \alpha_i + \beta_i \times X_t + \varepsilon_{i,t}$$

$$\beta_i \sim \text{MVN}(\mu_B, \Sigma_B)$$

With non-informative priors modelled as:

$$\alpha_i \sim N(0, 10^4)$$

$$\varepsilon_{i,t} \sim N(0, 10^4)$$

$$\mu_B \sim \text{MVN}(0, 10^4 I)$$

$$\Sigma_B \sim \text{Inverse} - \text{Wishart}_{v_0}(\Lambda_0)$$

The matrix X contains the principal components (PCs) for all variance-transformed tree ring predictors that met the threshold for that nest; β_i is a vector with the corresponding regression coefficients for the predictor PCs; and α_i and ε_i are the intercept and error term respectively. Pooling of information across sites was implemented by drawing the covariance structure of the regression coefficients β_i from an MVN. Parameter β_i is described by two hyperparameters, μ_B and a dispersion matrix Σ_B , leading to the hierarchical framework in our model (Gelman & Hill, 2006). For the prior of the covariance matrices, we assumed an inverse-Wishart distribution with scale matrix Λ_0 , specified to be an identity matrix I and v_0 degrees of freedom set to be one more than the total number of principal component predictors used in that nest (Devineni et al., 2013). We modelled the associated prediction error terms, or residuals, $\varepsilon_{i,t}$ be derived from a normal distribution and not from a MVN as the gauges span a different range of years, meaning the spatial covariance of the error term cannot be computed (Rao et al., 2018).

D3.5 Moving block validation

We chose the 46 years between 1959 and 2005 CE for calibration and validation to maximise both the length of the calibration period and the number of tree-ring predictors available. Conventionally, tree-ring reconstruction models use a split-sample cross-validation scheme in which the model is initially calibrated with the first half of the data and validated with the second half, then calibrated with the second half and validated with the first (e.g., D'Arrigo et al., 2011).

However, our Daly catchment gauge records are too short for split-sample validation, as only 20-25 data points would be available for calibration.

Instead, we implemented a moving-block calibration/validation approach (Nguyen et al., 2020), a modification of a k-fold validation scheme in which k contiguous blocks of data are withheld. This method retains the independent verification period of split-sample validation, while keeping enough data for calibration, and improving the model's ability to capture a regime shift by maintaining contiguous data blocks (Briffa et al., 1988). The length of the validation block was selected to be larger than the largest number of significant autocorrelation lags for any chronology in the predictor pool.

In each iteration, 7 consecutive years (~15% of instrumental time span and ~20% of the span of the shortest gauge) were withheld and the model was calibrated on the remaining years. The selection of significant predictors via PIC (Section 3.2) was also only undertaken on the calibration set to maintain the complete independence of the validation set. In total, 40 moving block iterations were run for each of the 10 ensemble members described in Section S3.3. The final reconstruction and verification statistics described below were calculated as Tukey's biweight robust mean (Mosteller & Tukey, 1977) of the 400 ensemble members with uncertainty intervals calculated as the 5th and 95th percentile results. The robust mean was found to limit the effect of outliers more robustly than the median of the ensemble.

Model validation was determined by calculating the calibration period coefficient of multiple determination (CRSQ or R^2), the Bayesian R^2 (Gelman et al., 2019), the validation period reduction of error (VRE) and the verification period coefficient of efficiency (VCE) (E. R. Cook & Kairiukstis, 1990) for each iteration. The Bayesian R^2 is a data-based estimate of the proportion of the variance explained for new data, where:

$$R^2 = \frac{Var_{\mu}}{Var_{\mu} + Var_{res}}$$

Var_{μ} is the variance of modelled predictive means, and Var_{res} is the modelled residual variance calculated for the set of posterior simulation draws. VRE is a measure of the performance of a model relative to the mean of the calibration period where:

$$VRE = 1 - \left[\frac{\sum (X_i - \hat{X}_i)^2}{\sum (X_i - \bar{X}_c)^2} \right]$$

X_i and \hat{X}_i refer to the observed and simulated value at i , and \bar{X}_c is the mean value over the calibration period. VRE ranges from $-\infty$ to $+1.0$ with $VRE > 0$ indicating that the model is more successful at predicting omitted values than the calibration mean. Similarly, VCE compares the model fit to the verification period mean \bar{X}_v :

$$VCE = 1 - \left[\frac{\sum (X_i - \hat{X}_i)^2}{\sum (X_i - \bar{X}_v)^2} \right]$$

Unless $\bar{X}_c = \bar{X}_v$, VCE will always be less than VRE and is therefore considered a more rigorous statistic. $VCE > 0$ indicates some model skill. The Sign Test (E. R. Cook & Kairiukstis, 1990) was also used to calculate the number of years in which the reconstruction correctly (+) or incorrectly (-) tracks the sign of change between consecutive observations during the calibration period with significance tested against the normal approximation to the binomial distribution.

D3.6 Superposed epoch analysis (SEA)

Superposed epoch analysis (Haurwitz & Brier, 1981) is a compositing technique very commonly used in paleoclimate reconstruction studies to identify volcanic impacts (e.g., Adams et al., 2003; Higgins et al., 2020; Rao et al., 2019), but with wider applications, including identifying flood events in streamflow reconstructions (Rao et al., 2020). SEA requires two independent datasets. The first is a discrete list of events, such as years when historical floods occurred. The second variable is a long, continuous, and evenly sampled timeseries, such as reconstructed streamflow. SEA assumes that ‘key events’ of interest are either a cause or response to a characteristic of a timeseries; and that the identification of the sign, magnitude, and timing of such a response can be optimised by averaging across all events. To test this assumption, a ‘composite matrix’ is created by drawing fixed windows of consecutive observations from the timeseries that span years before, during, and after the event. The statistical significance of the mean of this composite matrix (the ‘epochal response’) can then be tested. Figure D-7 represents the compositing procedure.

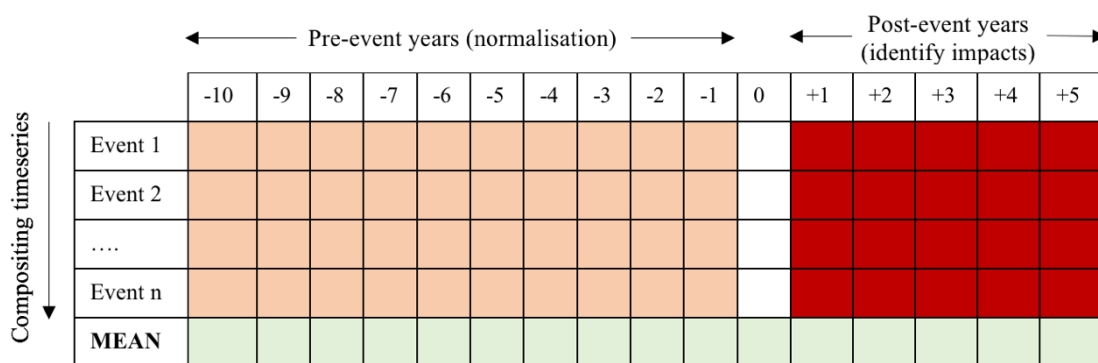


Figure D-7 Schematic representation of a SEA composite matrix, where fixed windows of consecutive observations spanning events of interest are aligned, then averaged to create an epochal mean response.

D4. Additional results

D4.1 Predictor selection

Table D-1 shows the names, species, and coordinate locations of the tree-ring chronologies retained for the regression model. Only chronologies meeting the initial threshold of a significant ($p < 0.1$) correlation with Daly catchment streamflow were retained. Some sites have multiple

chronologies produced from different wood properties. In these cases, only the most highly correlated chronology was retained. The mean of the correlation coefficients between each chronology and the four streamflow gauges are also provided in the table. Correlations greater than ~0.34 are significant at $p < 0.05$ and greater than ~0.42 are significant at $p < 0.01$. The nests to which each chronology contributed are also shown, where nest 1 is the most recent nest (1898-2005, all chronologies contribute).

Table D-1 Metadata for tree-ring chronologies significantly correlated (Pearson r , $p < 0.1$) with Daly catchment streamflow (1959-2005) after variance transform, and the reconstruction nests to which each chronology contributes.

Country	ID code	Species	Lat	Lon	r	Nests	Description
Australia	AUSL046	PHAS	-42.3	146.6	-0.50	1 - 6	TNE
Australia	AUSL038	ATCU	-41.8	146.7	-0.49	1 - 14	Mickey Creek
Australia	Speroa	LGFR	-42.7	145.4	-0.44	1 - 14	Spero River
Australia	LTYMAS	CACO	-33	120.7	-0.43	1 - 8	Lake Tay
Australia	BCHMRD	LGFR	-42.3	145.8	-0.42	1 - 14	Buckleys Chance
Australia	TPKDHP	LGFR	-41.9	145.6	-0.35	1 - 14	Teepookana
Australia	SWCTRW	PHAS	-42	146.6	-0.34	1 - 10	Southwest Celery Top
Australia	AUSL036	LGFR	-42.2	145.5	0.30	1 - 4	Butters
Australia	AUSL047	ATSE	-43.8	146.8	0.33	1 - 5	Mesa
Australia	KBPSTH	ATSE	-43.8	146.8	0.33	1 - 14	King Billy South
Australia	AUSL057	CAIN	-13.6	131.5	0.35	1	Hayes farm
Australia	KBSTRW	ATSE	-42.9	146.6	0.38	1 - 8	King Billy Saddle
Australia	AUSL056	CAIN	-13.5	132.4	0.38	1, 2	El Sharana
Australia	AUSL049	ATCU	-41.8	146.3	0.40	1 - 14	The Walls of Jerusalem
Australia	AUSL060	CAIN	-11.7	130.8	0.40	1	Tiwi Islands
Australia	CODNCT	PHAS	-42.4	146.5	0.42	1 - 7	CO (north Florentine)
Australia	AUSL039	ATSE	-41.6	146.8	0.43	1 - 12	February Creek
Australia	AUSL007	ATCU	-41.8	146.7	0.44	1 - 14	Pine Lake
Australia	AUSL040	ATCU	-42.7	146.6	0.45	1 - 14	Mt Field
Australia	AUSL037	CACO	-22.9	118.6	0.50	1 - 4	Juana Downs Gully
Australia	AUSL048	ATSE	-43.3	146.6	0.51	1 - 14	Lake Riveaux/ Abtotonella Rise
Australia	AUSL042	ATCU	-41.6	146.4	0.56	1 - 14	Lake Mackenzie
China	CHIN017	JUTI	28.9	99.8	-0.41	1 - 13	Xiangchen, Sichuan
China	ZHANGX		34.6	104.5	-0.36	1 - 9	Zhangxian, Gansu
China	CHIN019	ABFO	29.2	99.9	-0.30	1 - 11	Xiangchen Maxiong Valley
China	CHIN020	PIFL	30.2	100.3	0.36	1 - 14	Litang, Sichuan
China	CHIN021	PIFL	29.0	99.9	0.39	1 - 14	Xiangchen, Sichuan
China	CHIN026	ABFO	27.6	99.8	0.39	1 - 10	Shangri La, Yunnan
China	CHIN081	PITW	30.3	119.4	0.41	1 - 8	Tianmu Mountain Forest
China	CHIN024	JUTI	28.4	99	0.42	1 - 7	Baimang Snow Mountain
China	CHIN028	PIFL	27.3	99.3	0.48	1 - 14	Weixi County, Yunnan
China	GOUQIN	JUPR	34.7	100.8	0.48	1 - 14	Hebei, Qinghai
China	CHIN040	TSDU	28.0	99.0	0.52	1 - 14	Hengduan Mountains 13YE
China	CHIN057	JUSP	34.5	110.1	0.58	1 - 11	Huashan HSS
China	CHIN018	JUPR	29.3	100.1	0.61	1 - 10	Docheng
Indonesia	INDO005	TEGR	-5.5	123	-0.55	1 - 9	Muna, Sulawesi
Indonesia	INDO008	TEGR	-7.1	111.4	0.36	1 - 6	Bekutuk

Country	ID code	Species	Lat	Lon	r	Nests	Description
India	22550	CDDE	29.6	79.9	-0.49	1 - 7	Jageshwar D180 Chronology
India	22549	ABPI	32.2	77.2	-0.45	1 - 3	Manali, NW India D180 Chronology
India	INDICD	CDDE	31.4	78.6	0.29	1 - 14	India All Cedrus Deodora
India	BHAICD	CDDE	31.2	78.9	0.32	1 - 4	Bhairoghathi Cedrus Deodora
India	JANGCD	CDDE	31.4	78.2	0.46	1 - 10	Jangla Cedrus Deodora
Japan	JAPA020	CMJA	30.3	130.5	-0.46	1 - 4	Yakushima
Japan	CCB	FACR	35.9	138.8	0.31	1 - 6	Yasue Chichibu Beech
Nepal	NEPA046		28.5	84.8	0.31	1 - 3	Kalchuman Lake
New Zealand	NEWZ052	NOSO	-43.2	171.8	-0.53	1 - 3	Rata Creek
New Zealand	NEWZ053	NOSO	-43.1	171.6	-0.34	1 - 4	Windy Creek
New Zealand	NEWZ124	LIBI	-42.7	171.6	0.34	1 - 14	Camp Creek
Philippines	PH001	PIKE	16.8	120.7	-0.44	1 - 5	Bakun, Philippines
Pakistan	PAKI033	PIGE	35.5	74.8	0.30	1 - 14	Mushkin
Pakistan	PAKI024	PCSM	35	74.6	0.33	1 - 14	Chera (Gilgit)
Pakistan	PAKI039	CDDE	35	70.8	0.43	1 - 9	Tangi-Kamdesh Nuristan
Pakistan	CDACDD	CEDE	35.5	71.5	0.44	1 - 6	Afganistan Cedrus Deodora
Pakistan	PAKI027	CDDE	35.4	71.9	0.46	1 - 11	Islam Baiky
Pakistan	PAKI023	CDDE	35.9	71.7	0.46	1 - 10	Chitral-Gol NP
Pakistan	PAKI040	CDDE	35.4	71.8	0.50	1 - 12	Zairat Chitral
Pakistan	PAKI018	PIWA	35.3	74.8	0.53	1 - 14	Astore-Rama
Pakistan	PAKI021	PIGE	35.7	71.6	0.56	1 - 14	Kalash Valley Bumburet
Pakistan	PAKI036	PCSM	36.2	74.2	0.58	1 - 14	Naltar Gilgit
Tibet	CENTIB	JUTI	29.4	92	-0.28	1 - 14	Central Tibet Juniper
Tibet	CHIN046	JUTI	31.1	97	0.37	1 - 14	Qamdo
Thailand	TH001	TEGR	19.3	98.9	0.42	1 - 9	Mae Hong Son Teak
Thailand	TH004	PIME	15	99.4	0.43	1 - 6	Phu Toei

D4.2 Tree ring-climate relationships

We examined the relationship between monthly Daly catchment rainfall and water year (September to August) streamflow (Figure D-8a) and tested for both contemporaneous and lagged relationships between climate and streamflow. We found water year streamflow to be positively correlated with current year December through March precipitation ($p < 0.01$), which covers the peak rainfall period of the Indo-Australian monsoon. Correlations between streamflow and rainfall in all other individual months were not significant.

We then examined the tree growth response to the climate of the predictor suite used in the first nest for the streamflow reconstruction (Figure D-8b). In our reconstruction model, we used the PIC algorithm to determine which principal components (PCs) should be retained in the model based on their relationship to instrumental streamflow. Six PCs were retained for the first nest, PC1, PC3, PC5, PC13, and PC22. We used the first PC, which represents 34% of variance amongst the chronologies, to test tree ring-climate relationships. We found that PC1 also shows

a positive correlation with peak monsoon (December through March) precipitation ($\rho < 0.01$, January $p < 0.05$) but also a lagged response to monsoon rainfall in the previous year (December, February $p < 0.05$, January, March $p < 0.1$) representing autocorrelation in the tree-ring series.

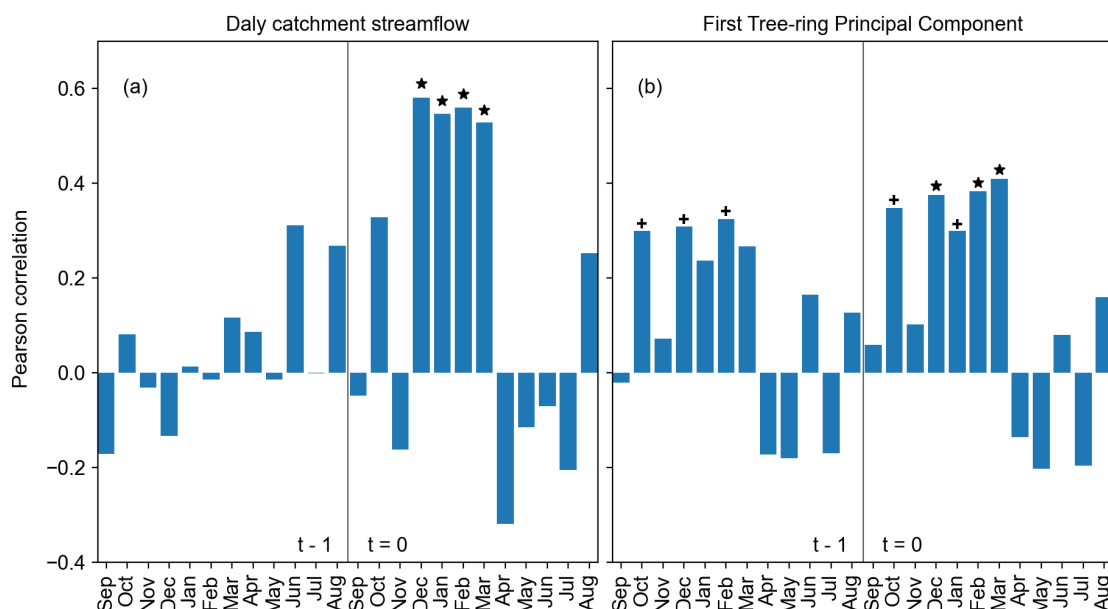


Figure D-8 Pearson correlations between a) instrumental water year discharge at Daly River gauge G8140040 (1961–2005) and month-by-month precipitation (blue; +, $p < 0.05$ and *, $p < 0.01$) for months between prior year ($t - 1$) September through current year ($t = 0$) August; b) same figure as a) but for PC1 of the initial nest.

D4.3 Calibration and validation

The reconstruction fit to the instrumental data during the calibration period is shown in Figure D-9. The full calibration and validation statistics for each gauge over all nests, along with the number of tree-ring predictors contributing to the reconstruction model over time are provided in Figure D-10. A summary table is provided in the main article. Figure D-10 shows that despite the decreasing number of tree-ring predictors moving back in time, the statistical results remain strong for the earliest part of the record. The 5th percentile VRE and VCE values are above zero throughout the reconstruction period, indicating that the reconstruction contains meaningful information over its entire length.

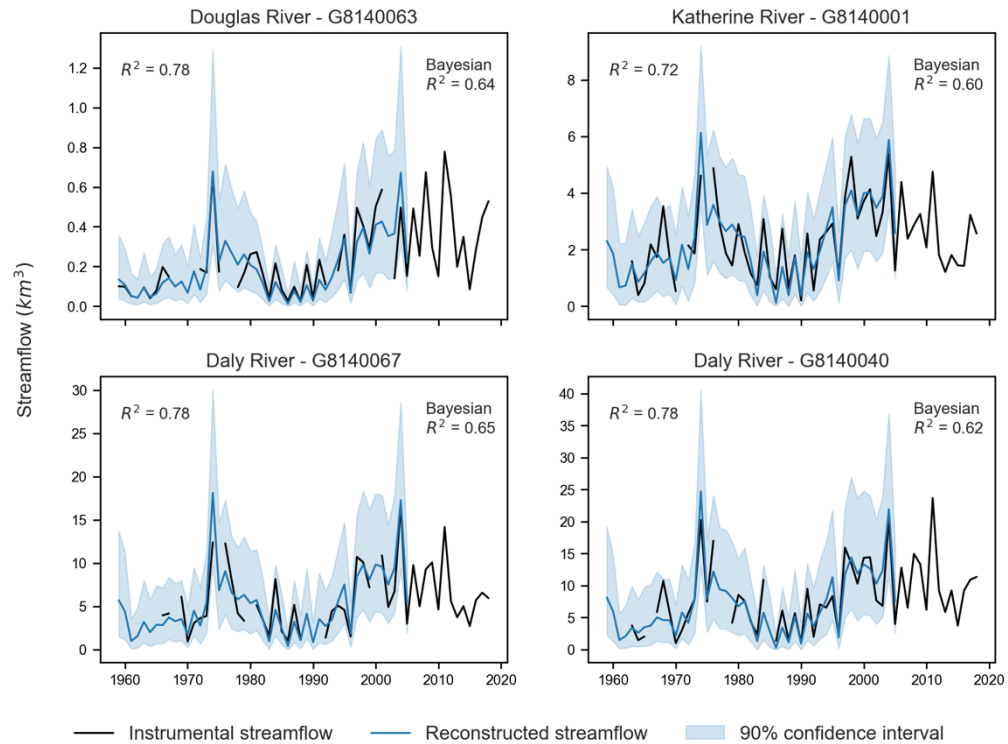


Figure D-9 Instrumental (black) versus reconstructed (blue) streamflow in km³/year for the four Daly catchment streamflow gauges over the instrumental period 1959–2018.

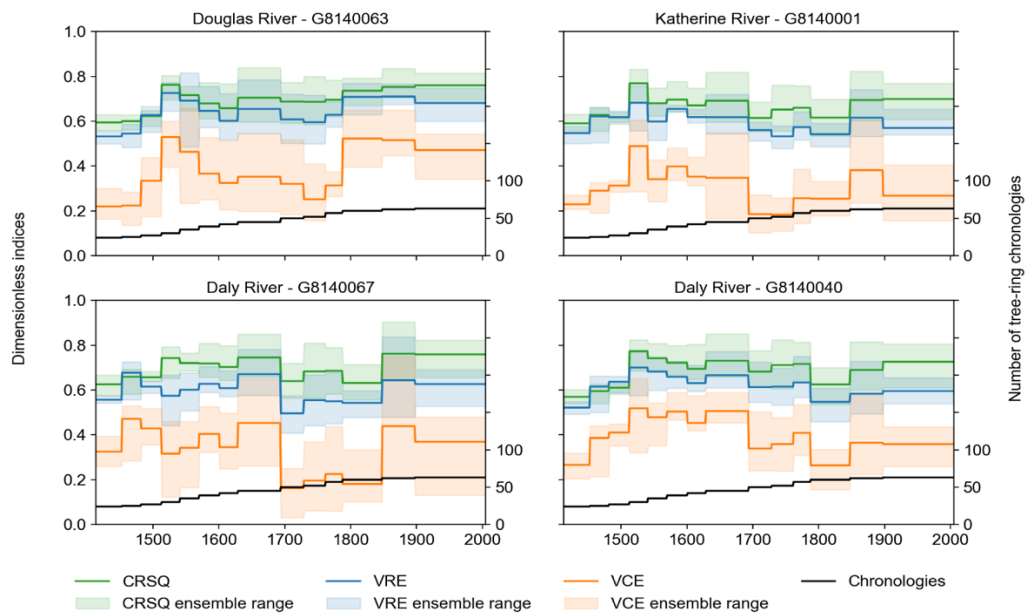


Figure D-10 Verification statistics for each reconstruction nest from 1413 to 2005 CE, for each of the four Daly catchment streamflow gauges. The number of tree-ring chronologies contributing to each reconstruction nest is plotted in black.

D4.4 Links between El Niño and low flow extremes

Differences in the relationship between warm Pacific SSTs and monsoon rainfall have been identified when considering the different ‘flavours’ of El Niño. Canonical El Niño events, characterised by peak SST anomalies in the eastern Pacific, result in a lower-than-average monsoon rainfall. El Niño Modoki events, however, with warmer SSTs in the central-western

Pacific, tend to result in shorter but more intense peak monsoon season, with little impact on total monsoon rainfall (Taschetto et al., 2010). The lack of a significant relationship between El Niño events and low Daly streamflow (see the main article) may therefore be due to the confounding influence of El Niño Modoki, which has become more prevalent since the 1970s.

Too few low flow extremes co-occurred with El Niño events to assess the impact of different types of El Niño on streamflow using only instrumental SST data. We tested the influence of El Niño types by repeating the bootstrap significance testing using the coral-based Canonical/Modoki event classification of Freund et al. (2019) and reconstructed Daly streamflow from 1619 to 2005 CE. Three low flow thresholds were examined, the 5th, 10th and 25th percentile flow. While under each threshold Daly River low flow extremes were found to be more likely to occur during a canonical than an El Niño Modoki event, none of the relationships were significant (Figure D-11).

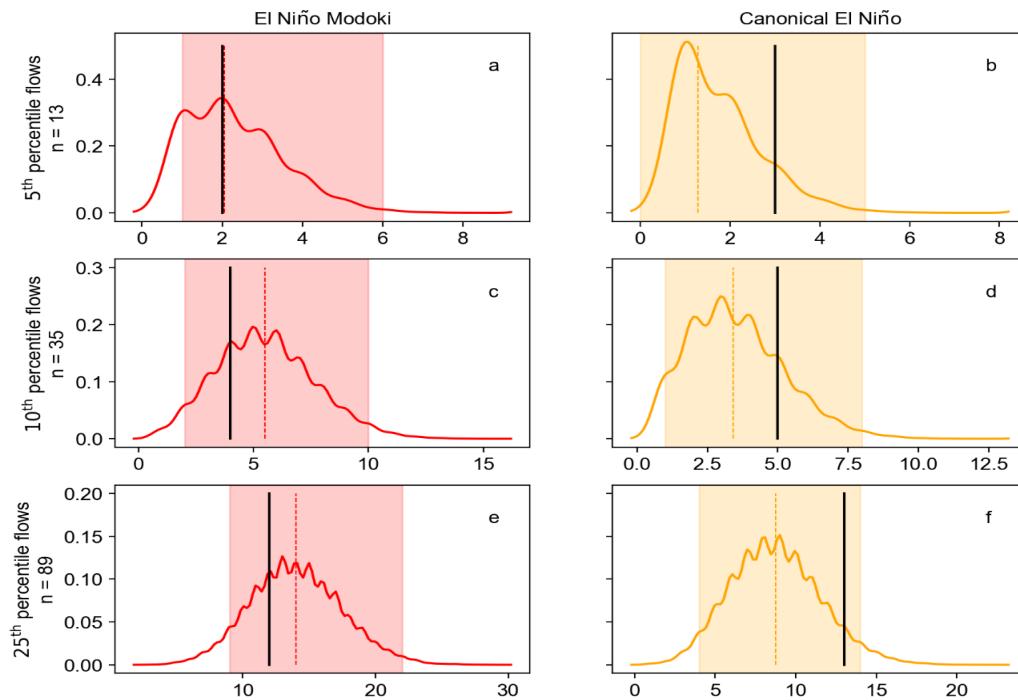


Figure D-11 Kernel density estimate plots of 30,000 bootstrapped replications of canonical/Modoki events from 1619 to 2005 CE showing the co-occurrence of El Niño events with low flow extremes in the reconstructed streamflow at the 5th percentile (a, b), 10th percentile (c, d), and 25th percentile (e, f). The number of extreme low flow events in the reconstruction associated with each ‘flavour’ of El Niño are shown in black and compared to the bootstrap mean (dashed lines); no values lie outside the 95% bias-corrected bootstrap confidence interval.

D4.5 Trends in extreme events

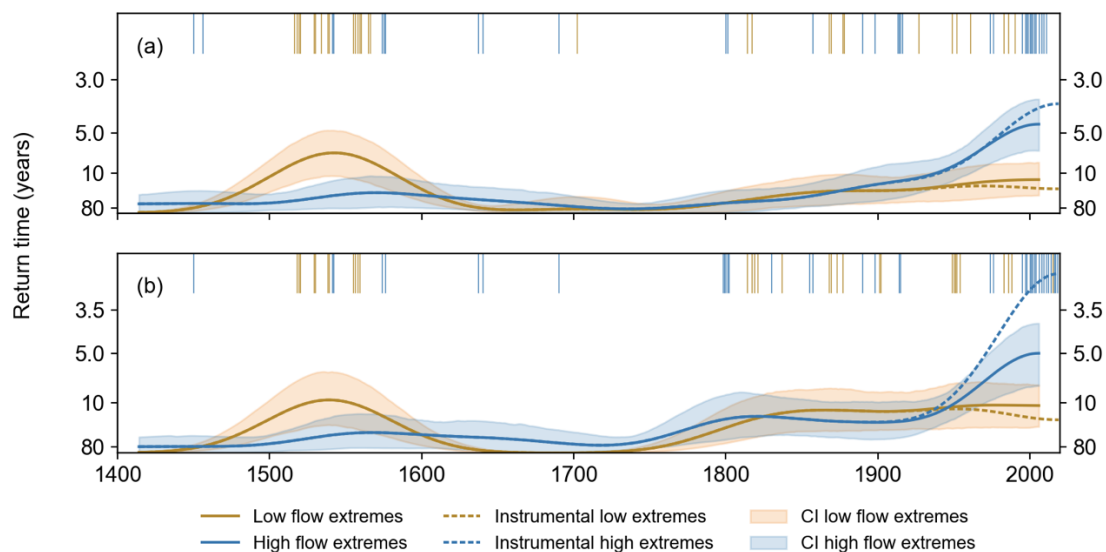


Figure D-12 Extreme high flow/low flow event years and the time-varying frequency of their occurrence of these events between 1413 and 2018 for the a) Daly River at G8140067 and b) Douglas River at G8140063. A kernel smoothing method was used with a bandwidth of 38 years (solid lines), with dashed lines showing the adjusted frequency curve if instrumental data is appended to the reconstruction after 2005.

Appendix E. Supplementary information for Chapter 6

Table E-1 CMIP5 models used in this analysis, including the modelling group, number of ensemble members from each model, and spatial resolution before reprojection to a $2^\circ \times 2^\circ$ grid. Continuous runs from the historical+RCP8.5 experiments were used (years 2000 – 2099).

Model	Modelling centre (or Group)	# Runs	Lat/Lon resolution
CanESM2	CCCMA ^a	5	$2.8^\circ \times 2.8^\circ$
CCSM4	NCAR ^b	6	$0.94^\circ \times 1.25^\circ$
CSIRO-MK3.6.0	CSIRO-QCCCE ^c	5	$1.87^\circ \times 1.87^\circ$
GFDL-CM3	NOAA GFDL ^d	1	$2.0^\circ \times 2.5^\circ$
GFDL-ESM2G	NOAA GFDL ^d	1	$2.0^\circ \times 2.5^\circ$
GFDL-ESM2M	NOAA GFDL ^d	1	$2.0^\circ \times 2.5^\circ$
GISS-E2-R	NASA GISS ^e	1	$2.0^\circ \times 2.5^\circ$
INMCM4.0	INM ^f	1	$1.5^\circ \times 2.0^\circ$
IPSL-CM5A-LR	IPSL ^g	4	$1.9^\circ \times 3.75^\circ$
MIROC5	MIROC ^h	1	$1.4^\circ \times 1.4^\circ$
MIROC-ESM	MIROC ^h	1	$2.8^\circ \times 2.8^\circ$
MIROC-ESM-CHEM	MIROC ^h	1	$2.8^\circ \times 2.8^\circ$
MRI-CGCM3	MRI ⁱ	1	$1.1^\circ \times 1.1^\circ$
NorESM1-M	NCC ^j	1	$1.9^\circ \times 2.5^\circ$

^aCanadian Centre for Climate Modelling and Analysis

^bNational Center for Atmospheric Research

^cCommonwealth Scientific and Industrial Research Organization in collaboration with Queensland Climate Change Centre of Excellence

^dNOAA Geophysical Fluid Dynamics Laboratory

^eNASA Goddard Institute for Space Studies

^fInstitute for Numerical Mathematics

^gInstitut Pierre-Simon Laplace

^hAtmosphere and Ocean Research Institute (The University of Tokyo), National Institute for Environmental Studies, and Japan Agency for Marine-Earth Science and Technology

ⁱMeteorological Research Institute

^jNorwegian Climate Centre

Table E-2 CMIP5 models used in the Australia Water Outlook projections, including the modelling group and the spatial resolution, before downscaling to ~5 km grid. A single run was used from each model.

Model	Modelling centre (or Group)	Lat/Lon resolution
ACCESS1-0	CSIRO-BoM ^a	$1.25^{\circ} \times 1.875^{\circ}$
CNRM-CM5	CNR-CERFACS ^b	$1.4^{\circ} \times 1.4^{\circ}$
GFDL-ESM2M	NOAA GFDL ^c	$2.0^{\circ} \times 2.5^{\circ}$
MIROC5	MIROC ^d	$1.4^{\circ} \times 1.4^{\circ}$

^aCommonwealth Scientific and Industrial Research Organization and the Bureau of Meteorology

^bCentre National de Recherches Météorologiques / Centre Européen de Recherche et Formation Avancée en Calcul Scientifique

^cNOAA Geophysical Fluid Dynamics Laboratory

^dAtmosphere and Ocean Research Institute (The University of Tokyo), National Institute for Environmental Studies, and Japan Agency for Marine-Earth Science and Technology

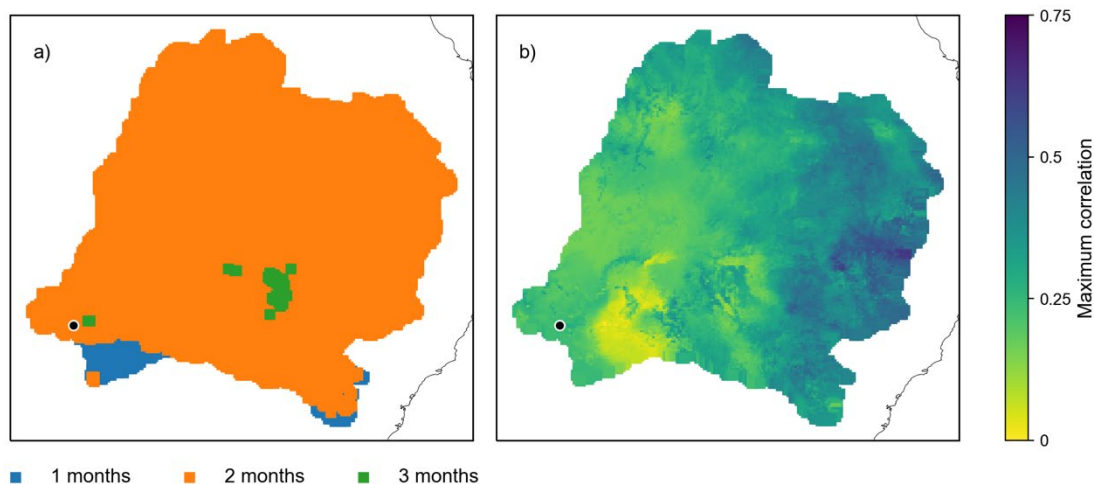


Figure E-1 a) Lag in months for maximum correlation between AWRA-L runoff and Darling streamflow (1960-2018) for each grid cell; b) Maximum correlation between AWRA-L monthly runoff and Darling monthly streamflow (1960-2018) for each grid cell. The black dot indicates the location of the gauge at Wilcannia.

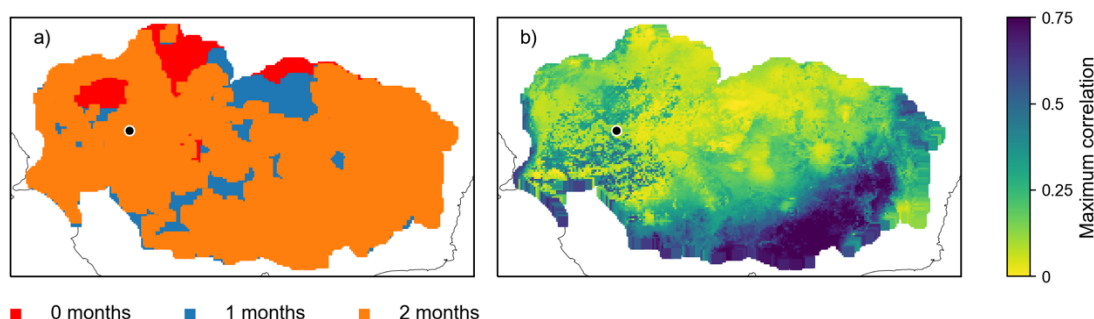


Figure E-2 a) Lag in months for maximum correlation between AWRA-L runoff and Murray streamflow (1960-2018) for each grid cell; b) Maximum correlation between AWRA-L monthly runoff and Murray monthly streamflow (1960-2018) for each grid cell. The black dot indicates the location of the gauge at Lock-7.

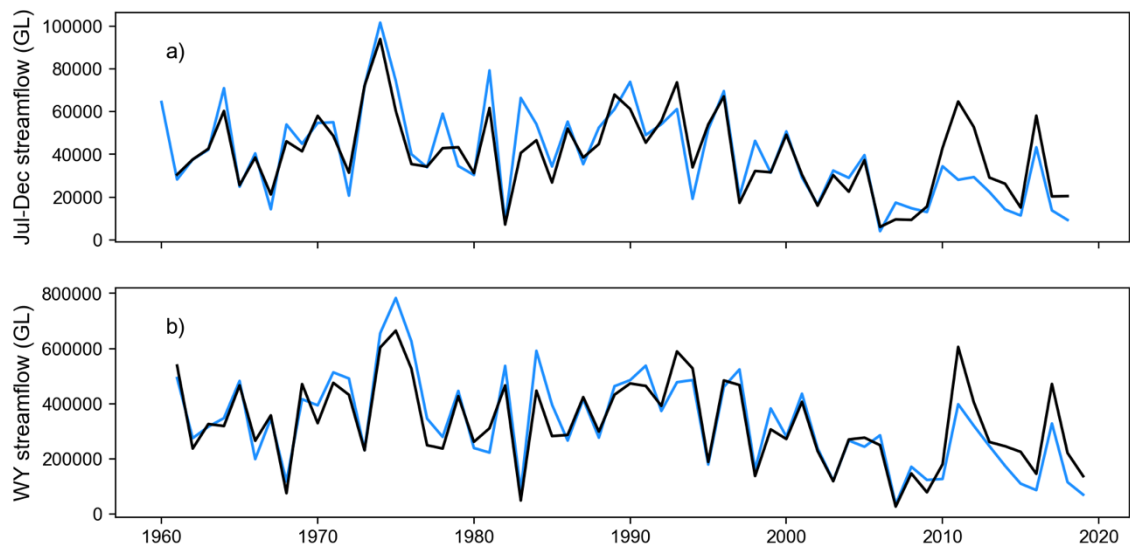


Figure E-3 Streamflow (black) derived from averaging AWRA-L runoff over the entire catchment with a two-month lag compared to modelled pre-development streamflow (blue) during the historical period (1960-2018) for a) Darling River at Wilcannia (July-Dec average), and b) Murray River at Lock-7 (water year average).

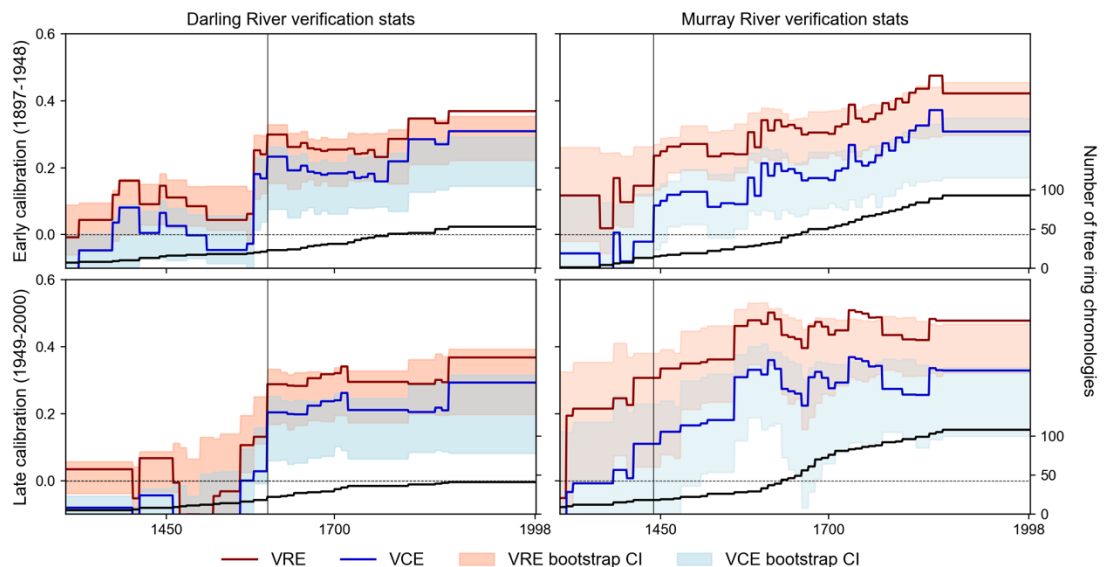


Figure E-4 Verification statistics, the reduction of error (VRE; red line) and coefficient of efficiency (VCE; blue) across all nests for the tree-ring chronology-based reconstructions calibrated to the early period (1897-1948; top row) and late period (1949-2000; bottom row) for the Darling and Murray rivers. The confidence intervals were based on 300 maximum entropy bootstrap replications. The number of tree-ring chronologies contributing to each nest is shown on the right-hand axis (black line). Based on these statistics, the vertical black line indicates the first year of the skilful reconstruction.

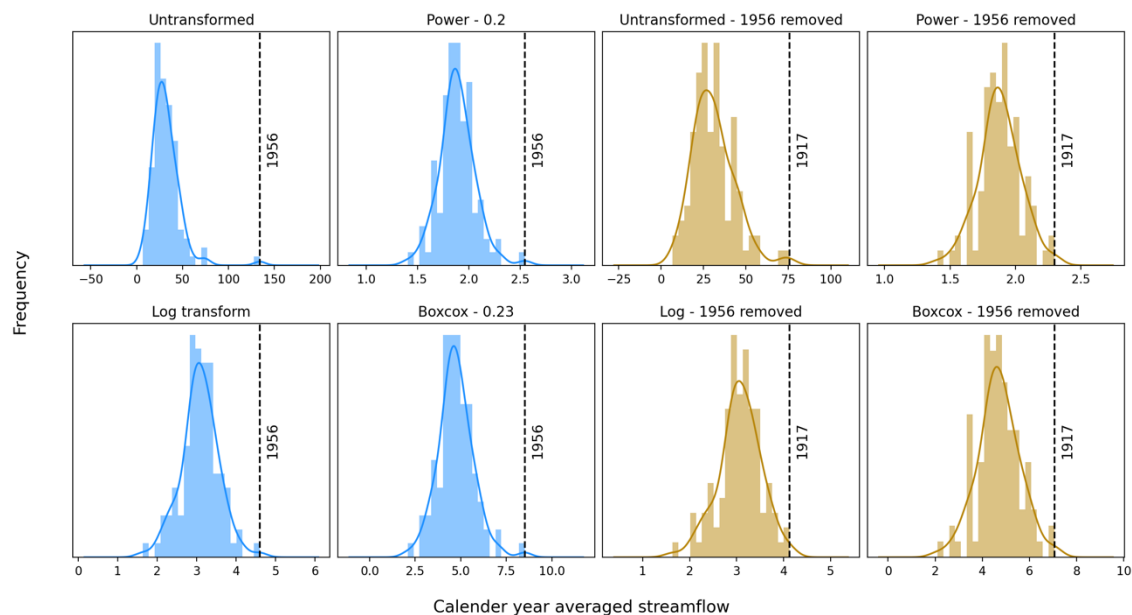


Figure E-5 Distributions of water year streamflow (1897-2019) in the Murray River after standard streamflow transformations (power weighting, log-transform, Box-Cox transform) and showing the extreme 1956 flood year outlier effect.

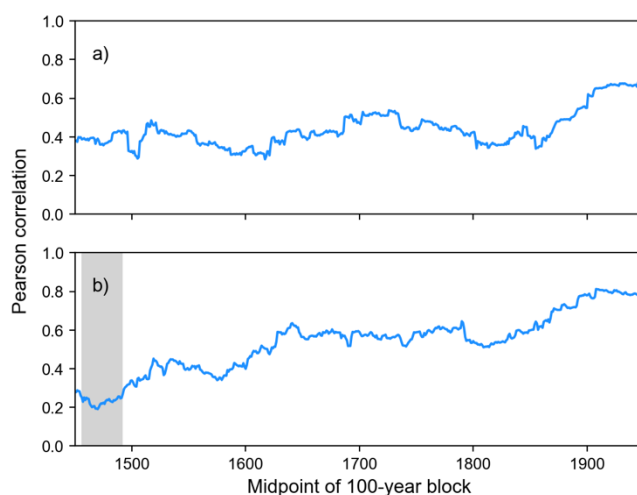


Figure E-6 Running Pearson correlations in 100-year blocks between the reconstructions developed using the tree rings directly and using gridded PDSI for a) Darling July-Dec streamflow and b) Murray water year streamflow. The grey band in b) indicates correlations not significant at $p < 0.01$.

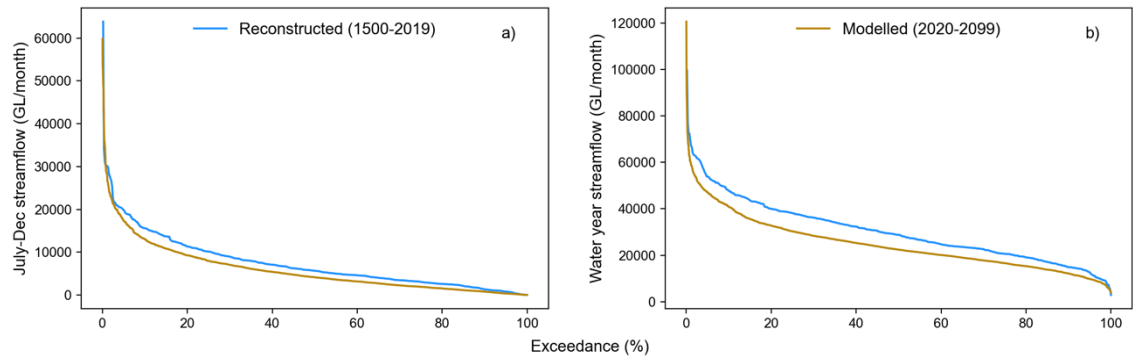


Figure E-7 Flow-duration curves for a) the Darling River at Wilcannia and b) the Murray River at Lock-7, comparing the reconstruction from 1500-2019 (blue line) with the full model ensemble over 2020-2019 (brown line).

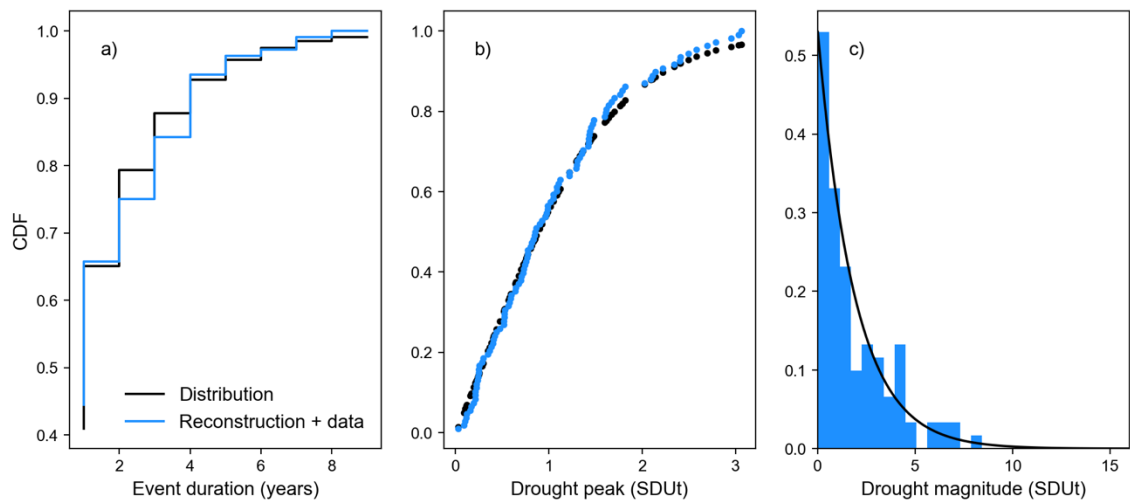


Figure E-8 Marginal distributions fitted to event characteristics for the Darling July-December streamflow reconstruction. a) Empirical (blue line) and hypothesised (black line) geometric cumulative density function (CDF) of drought duration; b) Empirical CDF of peak drought values and the fitted truncated logistic model; c) Probability histogram and fitted exponential distribution for drought magnitudes.

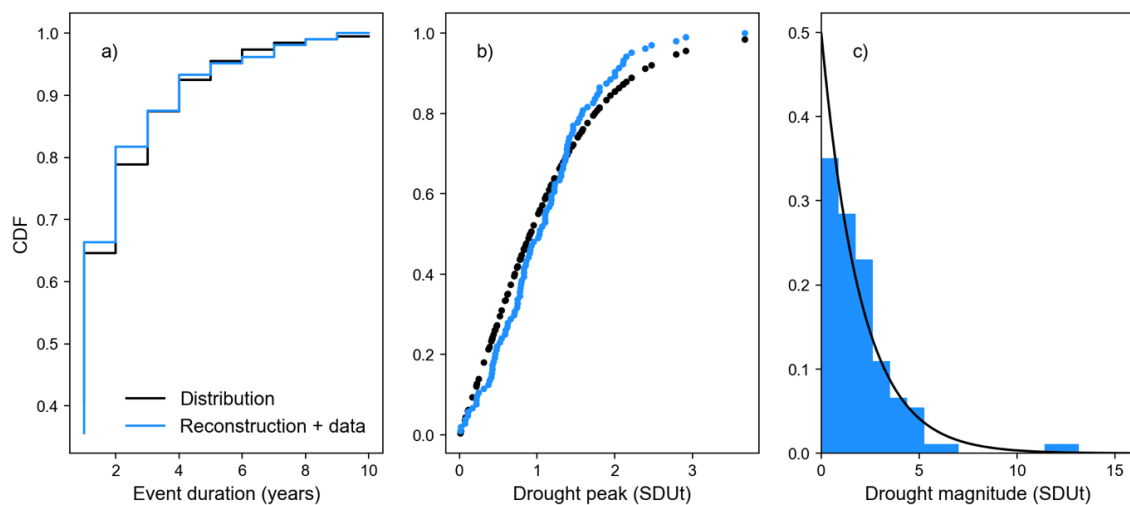


Figure E-9 Marginal distributions fitted to event characteristics for the Murray water year streamflow reconstruction. a) Empirical (blue line) and hypothesised (black line) geometric cumulative density function (CDF) of drought duration; b) Empirical CDF of peak drought values and the fitted truncated logistic model; c) Probability histogram and fitted exponential distribution for drought magnitudes.

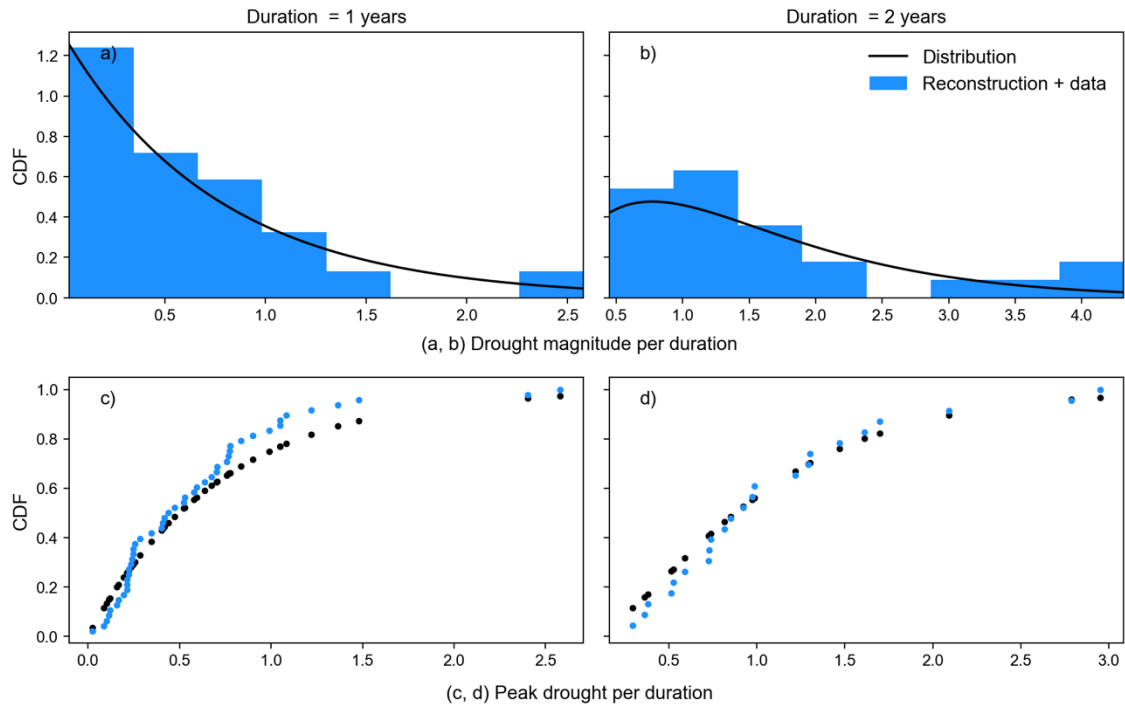


Figure E-10 (a-b) Conditional distribution of drought magnitude given drought duration of 1 (n=48) and 2 (n=23) years for the Darling July-December streamflow reconstruction. The data histogram is overlaid with the model gamma density with estimated parameters $\hat{p} = 0.41$ and $\hat{\beta} = 1.40$. (c,d) Conditional distribution of drought peak given drought duration of 1 (n=48) and 2 (n=23) years for the Darling July-December streamflow reconstruction. The empirical cumulative distribution function (CDF; blue) closely follows CDF (black) model.

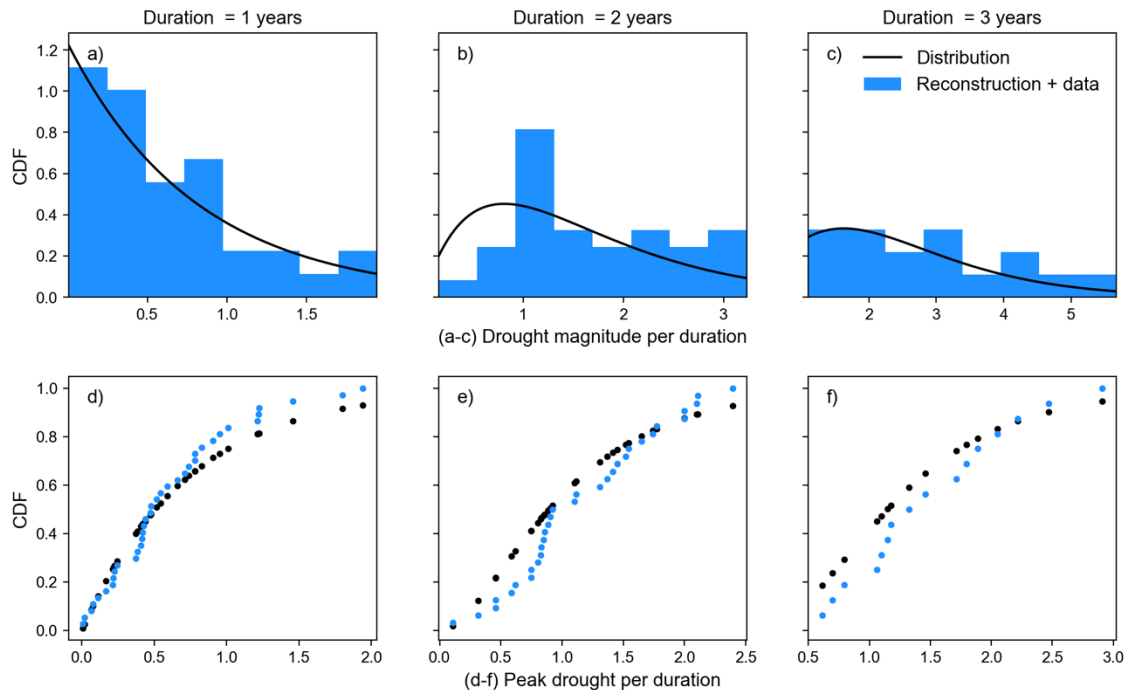


Figure E-11 (a-c) Conditional distribution of drought magnitude given drought duration of 1 (n=37), 2 (n=32), and 3 (n=16) years for the Murray water year streamflow reconstruction. The data histogram is overlaid with the model gamma density with estimated parameters $\hat{p} = 0.40$ and $\hat{\beta} = 1.34$. (d-f) Conditional distribution of drought peak given drought duration of 1 (n=37), 2 (n=32), and 3 (n=16) years for the Murray water year streamflow reconstruction. The empirical cumulative distribution function (CDF; blue) closely follows CDF (black) model.